THE DETERMINATION OF THE STRUCTURE OF SOME CHALCOGENIDE GLASSES BY EXTENDED X-RAY ABSORPTION FINE STRUCTURE

by

ROBERT F. PETTIFER

A thesis submitted to the University of Warwick
for admission to the degree of
Doctor of Philosophy

MAY 1978

EXAFS and its use in the determination of the structure of Glass

A brief introduction to the theory of EXAFS is given together ith an analysis of the important parameters which affect the structure etermination. Methods of extracting the structural information are lso reviewed.

A survey of instrumentation to record this effect is made including ossible topics for future development such as flourescence detection, armonic suppression, and sample preparation.

A review is presented of a range of glass forming systems which ave been measured. These include chalcogenide,elemental, and oxide lasses whose behaviour is contrasted.

In the light of the examples quoted, conclusions are reached concerning he type and reliability of information that can be obtained using this echnique.

CONTENTS

Page No.

CHAPTER 1: GENERAL INTRODUCTION

CHAPTER 2: THE THEORY OF EXAFS AND ITS INTERPRETATION

CHAPTER 3: PHASE SHIFT CALCULATIONS

Page No.

CHAPTER 4: APPARATUS FOR MEASURING EXAFS

CHAPTER 5: CHALCOGENIDE MATERIALS - BACKGROUND AND RESULTS

CHAPTER 6: DISCUSSION AND CONCLUSIONS

LIST OF TABLES

LIST OF FIGURES

Acknowledgements

I wish to thank the following people for their help throughout the work for this thesis. I was sponsored as a student by grants from the Science Research Council and the University of Warwick and to these bodies I owe my thanks. Professor Forty was instrumental in allocating some of this money as well as giving invaluable guidance on the initial draft of this manuscript. Dr. McMillan was my supervisor and I owe him my thanks for finding finance for the project, together with his faith in me and the work, especially during the lean years. Malcolm Gutteridge and Alan Draper applied their skill in constructing various pieces of apparatus which all worked well. Some of the references of this thesis were hard to find, and I have been fortunate in that often obscure journals have been traced and translations of foreign text have been found by Messrs. Bulmer and Davies of Warwick University Library. The major part of the computational work was carried out on the University's Elliot 4130 computer, which at the time was ending its useful life. I must commend the staff of the Computer Unit who exercised much patience and diligence in operating a temperamental machine. The program advisory staff of the Computer Unit have shown me special kindness in locating faults in my software.

I am indebted to Dr. B.W. Holland who has always been a willing adviser and a model of clear thinking. I have had fruitful discussions with Dr. J.B. Pendry who has been kind enough to allow me to use his computer software. Dr. S. Gurman has also contributed software and helped me in understanding some of the theoretical work. Dr. Gurman has made useful comments after reading Chapters 2 and 3 of this thesis, and has also allowed me to reproduce some of his results. For these kindnesses I express my sincere appreciation.

DECLARATION

This thesis is submitted to the University of Warwick in support of my application for admission to the degree of Doctor of Philosophy. It contains an account of my work carried out principally at the School of Physics in the University of Warwick under the general supervision of Dr. P.W. McMillan. No part of this thesis has been used previously in an application submitted to this or any other university. The work described is the result of my own independant research except where specifically acknowledged in the text.

R.Pettifer

SUMMARY

The process of Extended X-ray Absorption Fine Structure is described and the associated theoretical non-structural parameters are calculated. These parameters indicate the sensitivity of the phase and amplitude of the fine structure to the model potential and type of atom involved.

An apparatus is described which was built to utilise the bremstranlung radiation of a conventional X-ray tube to measure X-ray absorption spectra. A full analysis of the factors affecting the resolution of the spectrometer is given. This apparatus was used to measure a variety of crystals and glasses belonging to the chalcogenide family. Details of the method of preparation of these materials are described together with the X-ray powder pattern of a new phase of arsenic telluride. The spectra are analysed using the theoretical non-structural parameters to provide absolute calculations of bond-length. The spectra of glasses are also evaluated by comparison with the corresponding crystal spectra.

It is found that the fine structure is best described by theoretical factors calculated from a potential using Slater's exchange approximation rather than Hartree-Fock theory. The approximation of a plane electron wave interacting with the scattering atom becomes progressively more incorrect with increasing atomic number for the scatterer. The use of a more correct theory which takes into account the curvature of the photo-electron wave is essential to the interpretation of the arsenic telluride data.

It is concluded that in arsenic oxide glass the difference in mean As-O bond length is <0.06 Å and in the shortest As-As bond <0.03 Å relative to the crystal arsenolite. The data is consistent with the absence of large concentrations of discrete arsenolite molecules in the glass.

For arsenic sulphide the difference in the first shell bond length between crystal and glass is 0.0 ± 0.014 Å. The influence of the nearest arsenic shell disappears in the arsenic edge spectrum of the glass. This can be explained by a root mean square variation of As-S-As bond angles which is $<5^\circ$ from the crystal values. The absolute value of bond length calculated is 2.25 ± 0.03 Å.

In the case of arsenic selenide the difference of first shell bond length between crystal and glass is 0.00 ± 0.01 Å and the difference in the mean square variation of this distance is $(0.0 \pm 0.5) \times 10^{-3}$ A^2. In absolute terms the first shell bond length is 2.405 ± 0.01 Å.

A three component chalcogenide glass was measured with the formula $As_2S_3Se_3$. Using both the arsenic and selenium edges, it was found that arsenic bonded to both sulphur and selenium in the ratio 2:1, also selenium avoids bonding to sulphur.

A comparison has been made between measurements of the fine structure of arsenic telluride glass using both synchrotron and bremstrahlung radiation sources. It is found that the data is best described by arsenic sharing its bonding to two tellurium atoms and another arsenic atom.

CHAPTER 1

General Introduction

1.1 Glass: A general survey and the need for glass structure

The word "glass" is usually understood to describe a transparent, brittle, hard substance which is based on our common experience of everyday objects such as bottles and window panes. Glassy materials do however, extend over a range of materials with a wide variety of properties. In this thesis, the word glass refers to a non-crystalline solid formed from the melt. Some authors include in the term glass, non-crystalline solids formed from the vapour phase or some other technique of rendering a solid amorphous. Therefore, caution should be exercised, because it is not yet clear that materials formed by different techniques should have the same properties and structure. Thus, the definition of glass used here refers to a subset of non-crystalline solids, but still manages to include such diverse substances as rapidly cooled salts in solution, (e.g. LiCl in water) organic materials (e.g. tar), metallic alloys (e.g. Ni-Nb), oxides (e.g. SiO_2), chalcogenides (e.g. $As_2 S_3$) and many other groups (e.g. fluorides, phosphates). The range of physical properties exhibited by glass is remarkable, varying from high melting point transparent insulators to metallic flexible glasses. The range of bonding exhibited by glasses spans the entire spectrum of atomic cohesion, and classification according to the type of bond present has yielded little information about why glasses form. Thermodynamic approaches to glass formation emphasise the inability of glasses to to crystallise, and split this failure into two parts which are a) the failure to nucleate and b) a failure to grow. Both of these processes require the material to overcome an activation energy; however, the identification of the specific atomic process associated with the activation process is difficult and has not yielded many results. A good review of glasses and their properties has been given by Rawson (1967) and papers dealing with specific properties of the various types of glass can be found in the books edited by Douglas and Ellis (1970), Pye, Stevens and LaCourse (1972) and Gaskell (1977). These references all deal with the broad aspects of glasses; however, there are clear subdivisions within the field of glass which have occurred quite naturally owing to the possible commercial exploitation of their properties. One obvious subdivision consists of the oxide glasses. These glasses are usually based on silica or boric oxide. However even within this subdivision, it is clear that silicates and borates behave quite differently. It is thought that silicates maintain the basic structural unit of a silicon atom surrounded by four oxygen atoms in a tetrahedral or near-tetahedral arrangement. Boron, on the other hand, can change its coordination. The possible modification of just the first coordinating shell of silicon and boron does have implications in the important properties of thermal expansion and viscosity. It should be clear therefore, that structural information can thus be put immediately to very good use to tailor the properties of industrial glasses.

The same immediate applicability of structural information is not as forthcoming from structural studies of another subdivision of glasses, namely the chalcogenide glasses. The term chalcogenide refers to materials which contain a chalcogen atom and these atoms are members of group VIA of the periodic table, that is sulphur, selenium and tellurium. The type of chemical bond present in chalcogenide glasses is predominantly covalent rather than the highly ionic bonds formed in oxide glasses. The other important property of this class of materials is its semiconducting nature which has led to its widespread use in photocopying machines, in this case an arsenic-selenium alloy. It is very difficult to link structural information with electrical properties, and theoretical studies of transport properties are still at a very rudimentary level. However, one important point may emerge from structural work on non-crystalline semiconductors. This is the relative importance of long-range periodicty in determining such parameters as the density of states of a material, see for example Greenwood (1973). This in turn, may help to weld together the physicists view of bands of electron states and the chemists' simpler, but highly effective concept of the chemical bond.

The properties of chalcogenide glasses have been reviewed in the book by Mott and Davis (1971) and in the volumes edited by LeComber and Mort (1973) and Tauc (1974). Recent applications of chalcogenide glasses have been reviewed by Adler (1977). The oxide glasses and chalcogenide glasses are by far the most heavily studied from a structural point of view. However, these studies tend to take place in isolation owing to the completely different natures of the materials. In fact, some chalcogenide glasses are probably much more closely related to organic polymers than to oxide materials. For example, it is known that long-chain hydrocarbon polymers such as polythene can be given anisotropic properties by stretching them and this is also true of selenium.

The role of solid state physics is to explain the macroscopic properties in terms of microscopic construction of the material. Clearly, a good starting point is to gain some knowledge of the atomic structure from which, ultimately, we would like to answer such questions as - why do some solids fail to crystallise?, and, what is the origin of the mechanical and electrical properties of the solid? Also, the study of the structure of glass should enlighten us on the nature of the liquid-state, which is the least understood state of matter.

1.2 Techniques of structural investigation

Unlike most studies of the crystalline state, the investigation of structure is not confined to X-ray or neutron diffraction studies. In fact, it seems clear that a large amount of structural evidence must be amassed from a number of differing techniques to gain a good idea of the structure. The tools of structural research can be described under three categories:-

a) Scattering studies

b) Indirect structural information

c) Trend analysis.

The type of information obtained, together with the limitations of each technique are discussed briefly below.

Scattering techniques usually employ mono-energetic X-rays, neutrons, or high energy electrons. Usually the angular dispersion of the scattered rays is studied. Energy dispersive techniques have also been used for neutron scattering to extend the momentum transfer to larger values and thus improve the quality of real space information about the structure that can be obtained. Energy dispersive X-ray techniques have also been tried,but this type of measurement presents the problem of removing inelastic components of the beam. Reviews of scattering studies on glass have been given by Wright (1973) and Wright and Leadbetter (1976), together with useful summary tables of the principal conclusions of the published structure determinations by this technique. The interaction of X-rays, neutrons, and, to a lesser extent, high energy electrons with matter, is well understood and consequently, the structural information gathered by these techniques should be regarded as the most reliable. One great drawback is the limited nature of the information obtained and this can be summarised in two parts:-

a) the real-space information is essentially one-dimensional and provides no angular distribution, merely a radial structure.

b) The real-space information is a pair distribution function, thus, in a binary compound, A B peaks in the pair distribution function may contain contributions from A-A, A-B and B-B pairs. Clearly, the situation gets much worse when considering more than two components.

Nothing can be done to resolve limitation a) and thus we must recognise that if a model satisfies the scattering experiments, then this is a necessary but not sufficient condition for the validity of the model. Efforts have been made to overcome limitation b) by exploiting the change of scattering properties of atoms or nuclei with energy or isotope number. This procedure, in the case of neutrons, involves measuring the scattered intensity of the material as a function of the isotopic composition of the material. By performing three experiments the partial distribution functions in a binary Cu-Sn alloy has been established (see Enderby (1974)). Bondot (1974) has also used the change in atomic scattering factor near an absorption edge for X-rays to deduce the structure of Ge O_2. Although appearing to overcome limitation b) these techniques are restricted because they cannot be extended to situations where one constituent is in a dilute state in an alloy, and also they become very complicated when the number of components becomes greater than two.

Another technique which falls under the general heading of scattering is electron microscopy. The main advantage of this technique is that it provides a two-dimensional picture in real space of the solid, however, there are difficulties in allowing for instrumental artefacts and in preparing specimens characteristic of the bulk glass. These difficulties have been discussed by Freeman, Howie, Mistry and Gaskell (1977). At present, the resolution of these experiments is ~ 3 Å which, although it does not permit detailed structural parameters to be evaluated, does allow a search for ordered regions in the glass such as crystallites.

Extended X-ray Absorption Fine Structure (EXAFS) can also be regarded as a scattering process and in this case the scattering projectiles are low energy electrons. This technique is the one used in this thesis and the general physics of the process is given later in section 1.3.

The second major group of experiments used to deduce the structure of a glass can be termed indirect, because they do not monitor the positions of an atom but assess properties of the solid which are structure-dependent. One such property is the phonon spectrum of the solid, and this can be sampled by infra-red or Raman experiments. In general, the lower the frequency of the mode excited, the greater the structural unit which can be identified. It is very tempting to assign structural features to modes observed in glassy solids by identifying them with the corresponding modes excited in a molecular group. Unfortunately, the modes of vibration are properties of the entire crystal and so some simplifying assumptions must be made, otherwise the interpretation of the spectrum of the glass requires a large amount of computational effort. In the classic work of Bell and Dean (1970) on silica, it was found that the degree of localisation of the modes varied throughout the frequency range and, in a few high frequency bands, could be assigned to specific types of motion of a structural feature. We should expect that the ease of identification of a particular molecular mode should vary with the degree of connectivity of the atoms in a solid. Therefore, it should be progressively easier to assign vibrational modes to two- and one-dimensional solids. Examples of the latter are to be found in chalcogenide systems typified by As_2S_3 and Se respectively. In the case of As_2S_3 Lucovsky and co-workers (1974) have stressed that the system can be regarded as composed of units consisting of an arsenic atom with three attached sulphur atoms in a pyramidial arrangement with arsenic at the apex. The units appear independent owing to the weak As - S - As coupling between units. The molecular model of Lucovsky has however been contested by Taylor, Bishop, Mitchell and Treacy (1974) who find that the infra-red and Raman modes display features characteristic of the existence of layers present in the glass. The application of the molecular model to a range of glasses has been reviewed by Lucovsky (1974), and a general review has been given by Tauc (1974). It is worthwhile pointing out that to infer the existence of certain molecular groupings in glass based merely on the similarity of the vibrational spectra of known crystals and glasses is a hazardous procedure. Two examples relevant to the work of this thesis are worth mentioning. The first is that of As_2O_3 in which the Raman spectrum of the cubic crystalline form has modes similar to those found in the glass (Cheremisinov (1968)). However, a closer theoretical examination of the spectra together with experiments on other crystals of As_2O_3 indicate that molecular units of As_4O_6 do not exist in the glass. Secondly, the vibrational modes of the monoclinic rather than the chains found in hexagonal Se coincide with those found in the glass. This is a result of the disappearance of the inter-chain coupling in the hexagonal selenium crystal rather than due to the existence of rings in the glass, Lucovsky (1967) and

Lucovsky and White (1973). Thus, structural information from this source should only be accepted after exhaustive experimental and theoretical work.

Further indirect evidence of glass-structure comes from the study of nuclear effects which can be divided into two parts. The nuclear energy levels may be sampled by either inducing transitions between split levels of a nucleus of a given spin by exciting nuclear magnetic resonance (NMR) or nuclear quadrupole resonance (NQR), or by inducing transitions between different split nuclear levels belonging to different spins which can be monitored via the Mössbauer effect. The principal information derived from both of these effects comes from the measurement of chemical shifts which give a measure of the ability of the valence or conduction electrons to shield the nucleus from any applied magnetic field,and it can be related to the degree of ionicity/covalency of bonding present in the system. Further, the nuclear levels may be split by the interaction of electric-field gradients with the nuclear quadrupole moment. The latter type of information is the principal interaction used in glass studies and gives a measure of the site symmetry of the nucleus. The quadrupole interaction is particularly important in chalcogenide glasses where the bonding is covalent, since this type of bonding produces large electric field gradients at the nucleus. This type of interaction has been studied in As_2S_3 crystal and glass by Rubinstein and Taylor (1974) and a review of the use of the nuclear resonance techniques has been given by Bishop (1974) and Wong and Angell (1976). Mössbauer studies of chalcogenide glasses are rare owing to the difficulties of finding suitable radioactive isotopes, however, we will refer later to a Mössbauer study of Te in As_2Te_3 by

Seregin and Vasil'ev (1972). The studies of nuclear properties are comparatively few relative to those of infra-red and Raman spectroscopy; this is due in part to the weak nature of the magnetic resonance effect. With improvements in experimental apparatus and the use of isotopic enrichment, this situation is expected to change.

So far we have considered the direct structural information obtained by scattering studies which can be regarded as the most reliable experimental data. This has been followed by a discussion of indirect evidence which is quite reliable for determining the local structure out to the first coordination shell, but needs careful analysis if further information is to be obtained. The final type of information is based on observations which have no well established connection to the atomic structure of materials, but nevertheless can be scrutinised for trends in behaviour. Examples of these measurements are the behaviour of electrical conductivity, viscosity, glass transition temperature, micro-hardness and density as a function of composition. Anomalies often occur in these properties at well defined compositions and reflect compound formation in the material. A dramatic example of this is given by the variation of electrical conductivity with composition in the evaporated alloys of thallium-tellurium studied by Ferrier, Prado and Anseau (1972) which show anomalies in the conductivity for the compositions $Tl_2 Te_n$ (n = 1 → 7) as well as $Tl_3 Te_2$ and $Tl_5 Te_3$. Anomalies also exist in the electrical conductivity in the As-Se and As-S alloys at the composition which corresponds to the crystal $As_2 X_3$ where X is the chalcogen. This is a clear pointer to the preponderence of heteropolar bonding in these systems. Often the anomalies are reflected for the liquid alloy, many examples of which have been given by Glazov, Chizhevskaya and Glagoleva (1969). The anomalies of the electrical conductivity is also mirrored in the other properties mentioned above and detailed reference will be made to those measurements of particular interest to the materials studied in this thesis in a later chapter.

It is clear that no single experiment on the structure of glass gives a unique solution and every piece of evidence must be considered in order to build a reliable picture of the material. The non-uniqueness of experiments also applies to the EXAFS technique, although it does possess important advantages over the other structural tools discussed here.

1.3 X-ray absorption and EXAFS

X-rays undergo both scattering and absorption by matter which results in the removal of flux from an incident beam. Fortunately, for all except the very light elements, the true absorption process is dominant. The X-ray beam is attenuated in its passage through matter according to the familiar absorption law

$$I = I_o \exp(-\mu x) \qquad (1.1)$$

where I_o is the incident beam intensity, I is the transmitted intensity, μ is the absorption coefficient and x is the thickness of the specimen. Absorption of the X-ray photon results principally in the excitation of the core electrons of the solid. Depending on the energy, different core states of the atom can be excited giving rise to sudden discontinuities in the absorption coefficient with wavelength. The energy of the photon at one of these discontinuities corresponds to the energy needed to promote the system into an allowed excited state. The energy of the photon, together with the energy required to transfer an electron from an inner shell to a state of the excited system, satisfies energy conservation to within ΔE given by the uncertainty principle

$$\Delta E \Delta t = \hbar \qquad (1.2)$$

where Δt is the lifetime of the excited states, which for 1 Å X-rays is dictated by the radiative de-excitation of the core hole. For this process Hedin (1974) gives ΔE approximately by:-

$$\Delta E = 0.952 \times 10^{-8} E^2 \qquad (1.3)$$

1 eV (for 12 KeV photons)

This results in the broadening of both emission and absorption features by a Lorentzian function with half width ΔE. The general form of an absorption edge is given in Fig. 1.1.

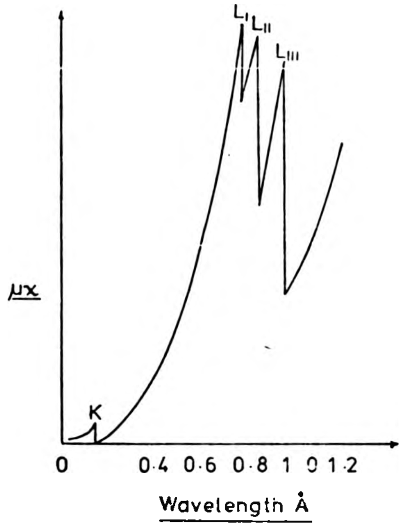

Fig. 1.1 The Absorption of Lead

The K edge corresponds to excitation of a 1s shell, the deepest level of the atom. This is followed by the L_I, L_{II} and L_{III} in progressively less energetic transitions which involve the excitation of 2s, $2p^{\frac{1}{2}}$, and $2p^{3/2}$ electrons (the superscript refers to the total angular momentum quantum number j). The L levels have their degeneracy removed mainly by relativistic and spin-orbit effects. As the atom increases in charge, so the splitting of the L levels increases. For example, the L levels of lead in Fig. 1.1 differ by quite large energies ($L_I - L_{II}$ = 650 eV) $L_{II} - L_{III}$ = 2155 eV. In general, absorption increases with increasing energy. If we define the atomic cross section for absorption μ_a by

$$\mu_a = \frac{\mu A}{\rho N} \qquad (1.4)$$

where A is the atomic weight, ρ the density and N Avogadros' number, then μ_a is given approximately by (Azaroff (1974))

$$\mu_a \propto Z^4\lambda^3 \tag{1.5}$$

Another useful relation is given by the additivity of the mass absorption coefficients $\left(\mu/\rho\right)_i$ such that

$$\left(\frac{\mu}{\rho}\right) = \sum_i g_i \left(\frac{\mu}{\rho}\right)_i \tag{1.6}$$

where g_i is the mass fraction of atomic component i and approximate values of $\left(\mu/\rho\right)_i$ can be found in tables in International Tables for X-ray Crystallography Vol. III (1962).

When examined in greater detail however, the absorption edges appear to possess structure which usually lies within ~ 1000 eV of the edge. Close to the absorption edge, there is quite sharp structure, further away from the edge,on the high energy side,the structure becomes increasingly weaker and broader. The sharp structure close to the edge has been found to be present in all forms of matter including monatomic gases and is also insensitive to temperature. This type of structure has been called Kossel structure after the scientist who explained its origin on the basis of transitions of the excited electron to unoccupied optical levels which exist in the excited atom (Kossel (1920)). More recently, these Kossel lines have been attributed to the Rydberg-like states formed by the binding of the emitted photo-electron to the core hold (Parratt (1939)), unbound resonances existing above the ionisation threshold (Cauchois and Mott (1949)), molecular or solid state band levels (Dehmer (1972), Beeman and Friedman (1939)) or more complicated final-state effects (Nozière and Dominicus (1969)).

All of these effects may be important, depending on the material studied. The structure in the immediate vicinity of the absorption edge is thus a very complicated process. However, Lytle (1967) has used this absorption region to gain information about the atomic structure in the vicinity of the absorber. By noting that a peak in the absorption, occurring below the main edge, depended on the symmetry of the environment of an absorbing atom, in this case vanadium, he was able to distinguish between the existence of a VO_4 rather than CrO_4 radical in the compound $CrVO_4$. This information could not be obtained from the X-ray scattering,owing to the similarity of the atomic scattering factor of chromium and vanadium.

A further type of structure-related information comes from studies of the shift of the absorption edge with the coordination of the absorber. This shift has been correlated with charge on the surrounding atoms assessed by using electro-negativity values (Cramer. Eccles, Kutzler, Hodgson and Martenson (1976)). Earlier work by Agarwal and Verma (1968) concerned the chemical shift of arsenic compounds. Although this work was not undertaken with very high resolution, it did point to increasing negative shift of the absorption edge with increasing electro-negativity of the absorber. The position of the edge is very ill-defined experimentally, and theoretically it involves the difference between the final state, which may be a mixture of effects mentioned above,and also shifts of the core-levels. It therefore seems likely that the process of putting edge shifts on a firm theoretical basis may take a considerable effort.

So far, we have discussed phenomena which contribute to the X-ray structure close to the absorption edge, say within 10 eV. Beyond this energy region, structure is found in absorption spectra measured on molecules, liquids and solids, but not on monatomic gases. This structure has been called Kronig structure after Kronig (1931, 1932) who first proposed its origin. Later, the phenomenon has been re-christened EXAFS (Extended X-ray Absorption Fine Structure). Despite the re-naming of the effect, the basic physics of the process has remained unchanged since the early description of the effect. The EXAFS structure is caused by the interference between the primary emitted photo-electron wave and the secondary scattered waves from surrounding atoms. This interference changes the transition probability for absorption via a changing overlap between the final state wave-function and the perturbed initial state. The dominant scattering comes from the backscattering of the surrounding atoms. Thus the absorption fine structure is sensitive to the local environment of the atom. A readable account of this process has been given by Stern (1976). Because the oscillations of the absorption coefficient arise from an interference phenomenon, the periodicity of the oscillations gives information about the distance of the scatterer from the emitter. Further, the amplitude of the oscillations is related, as we shall see in the next chapter, to the number and type of atoms surrounding the absorber and also to their distribution from a discrete radius caused by either static (for glasses) or dynamic (temperature) effects. These are clearly highly desirable structural parameters to obtain. The importance of EXAFS however, lies in its ability to sample the environment of a particular type of atom because the absorption edges for different elements differ in energy. Thus,one can obtain from a single experiment the radial structure about a single type of atom in a multiple component system. This is in contrast to conventional scattering techniques which require several sets of experimental data to obtain this information. Further, the number or dilution of a component is not a severe limitation. With the recent availability of X-ray continuous wavelength sources producing ~ 10^5 times the intensity of the conventional source, experimental techniques employing the detection of characteristic fluorescent radiation from a particular type of atom can be used to enhance the signal-to-noise ratio of the absorption measurement. The limitations of this technique have not been fully assessed, but it seems clear that concentrations of impurities <1% in a host material of similar atomic absorption should be easily measured. A further development of the EXAFS technique which has been suggested by Lee (1976) is the use of Auger electrons in a similar way to the fluorescence technique. The real advantage of this however, is that it renders to EXAFS the power of a surface sensitive technique.

Despite the rapid improvements which have, and still are being made in experimentation, the major influence has been the impact of a better theoretical understanding of the phenomenon. This has been based on earlier work on a closely related problem, namely that of low energy electron diffraction (LEED). Many of the ideas and formalism of LEED theory have been used to place EXAFS on a much sounder footing. The leading contributions have been made by Ashley and Doniach (1975) and Lee and Pendry (1975). The work of this thesis relies heavily on the theory put forward in the latter paper.

The EXAFS effect is useful provided the X-ray absorption edges are well separated. The K edges of materials such as arsenic and selenium are separated by ~ 700 eV which provides enough data of use for structure determination. The L edges for a single element are not well spaced except for the very heavy elements and thus this makes them potentially less useful than the K-edges. X-ray spectra obey the same selection rules as optical spectra and so we should expect L_I and K edges to possess the same EXAFS structure. This is, in fact, the case and the K and L_I structure and also the L_{II} and L_{III} structure of silver have been measured and compared by Anikin, Borovskii and Kozlenkov (1967) who also compared the L_{II} and L_{III} spectra. It was, indeed, found that EXAFS originating from initial states of the same symmetry possess the same structure.

The range of edge energy which exhibits the EXAFS effect has not been fully explored. The lowest energy edge which definitely exhibits the extended structure is the L_{II} L_{III} edge of silicon in SiF_4 starting at 100 eV (Friedrich, Sonntag, Rabe and Schwarz (1977)) and the highest energy known to the author is the K edge of tellurium at 31.8 KeV.

EXAFS studies of glass have been made by several authors. The first was that of Nelson, Siegel and Wagner (1963) who compared the fine structure of GeO_2 in both its crystalline forms and also the glass. A figure from their paper is reproduced below.

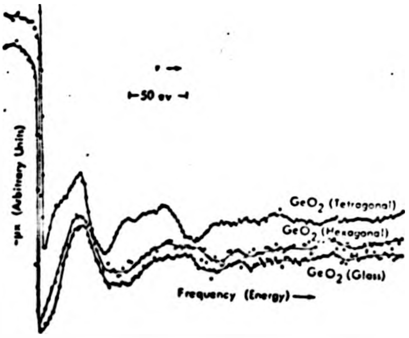

Fig. 1.2 Ge Edge in GeO_2 (after Nelson, Siegel and Wagner).

It is clear that a mere comparison of the EXAFS structure is very valuable. This figure shows at a glance that the glass has a structure much more closely related to the hexagonal form of GeO_2 than the tetragonal modification. Further studies of GeO_2 were made by Lytle (1965), and using a Fourier transform technique on the EXAFS by Sayers, Lytle and Stern (1972). The main conclusion from this paper was that the results could not be explained on the basis of the glass being essentially micro-crystalline. Further measurements have been made by the same group reported in Sayers, Lytle and Stern (1974) who measured amorphous GeSe, $GeSe_2$, As_2Se_3, As_2S_3 and As_2Te_3 and crystalline GeSe and $GeSe_2$. Unfortunately, these papers were written when there was insufficient appreciation of the role of the scattering atom in shifting the phase of the backscattered wave and also of the dependence of the backscattering amplitude on atomic number. Despite this, these authors were able to give a conclusive demonstration of a change in the first coordination distance when GeSe changes from crystal to glass. Other work on glasses have been reported by White and McKinstry (1966) who established from a qualitative examination of their spectra that the environment of Ge in $SiO_2 - CaO - Al_2O_3 - GeO_2$ glasses of a wide range of compositions remained unchanged. More recently, Hayes and Hunter (1977) have analysed amorphous Ge and Se using a comparison method of the Fourier transform of the data. Their results show a complete absence of information beyond the first shell in amorphous germanium but do show higher shell information in amorphous selenium.

1.4 Scope and philosophy of thesis

At the outset of this work it was envisaged that structural studies could be undertaken using the EXAFS technique as one of several experimental tools. On closer examination, it became increasingly obvious that much work needed to be done on the phenomenon of EXAFS itself.

The first task to be tackled was the attainment of reliable measurements on a suitable range of glasses. This was a cautious selection of binary glasses designed to extract as much information about the EXAFS phenomenon as well as the structure of the glass itself. We adopted the conservative view of measuring both crystals and glasses of the same compositions. The definition of the term chalcogenide has been extended to include arsenic oxide. Oxygen is, in fact, a member of the same group of the periodic table as the other chalcogenides, S, Se and Te, but it does have quite different chemical properties owing to its larger electro-negativity. Despite this, some arsenic oxide crystals do show a remarkable resemblance to the sulphides and selenides. In this thesis, we will present measurements of As_2O_3, As_2S_3, As_2Se_3 and As_2Te_3 in both cyrstal and glassy forms. By comparison of the two forms of material, the basic differences in their structure can be determined. This set of materials also provides a wide range of first shell scattering atoms, spanning from the light oxygen atom to the very heavy tellurium atom. This provides a reasonably varied set of data for theoretical examination.

In the next chapter, we present the theory of EXAFS with some comments on the way it can be used to give structural information. This chapter introduces parameters which are dependent on the partial wave phase shifts. In Chapter 3 the parameters which depend on these phase-shifts are calculated and are discussed in terms of the sensitivity to the theoretical models used. These calculations serve to highlight the types of experiment which may prove most profitable. The back-scattering amplitude calculations immediately enable us to understand the basic shapes and behaviour of the EXAFS fine structure. These calculations then permit us to predict what type of atom identification we can most readily make in the scattering pattern.

In Chapter 4 the experimental apparatus is described, which in fact, constitutes the bulk of work for this thesis.

Chapter 5 contains the experimental results together with a semi-quantitative comparison of crystal and glass spectra. Further theoretical calculations of the spectra are also presented using the theory of Chapter 2 and the parameters evaluated in Chapter 3. These allow a partial evaluation of structual parameters. Also included in this chapter is an examination of a three component glass which was measured because the calculations of Chapter 3 suggested that useful structural information could be easily obtained.

Chapter 6 is a discussion of the results and a summary of the outstanding problems that remain.

Before proceeding it is wise to make some comment about the question of units. The work presented here is interdisciplinary in that we have to reconcile information calculated theoretically with experimental measurements and structural data. The theoretical equations have a much simpler form if they are written in atomic units with $e^2 = \hbar^2 = m = 1$. With these transformations the units of length and energy are the Bohr radius (BR), and the Hartree (H). For experimental measurements, the units are usually expressed in electron volts (eV) or the wavelength of the X-ray radiation which is given in Å*. (The Å* is an X-ray unit of length defined in terms of the wavelength of the tungsten Kα_1 characteristic line and is equal to 1.00002 Å.) Structural information has been affected little by the S.I. standardisation of units and measurements of distances are still expressed in Å which is 10^{-10} metres. Fortunately conversion to different units can be easily accomplished using few conversion coefficients and these are summarised below

$$1\text{H} = 27.20\ \text{eV}$$

$$1\text{BR} = 0.5292\ \text{Å}$$

$$1\ \text{Å}^* = 12398.5\ \text{eV}$$

$$2E(\text{H}) = (k(\text{BR}^{-1}))^2$$

$$E(\text{eV}) = \frac{12398.5}{\lambda(\text{Å}^*)}$$

CHAPTER 2

The Theory of EXAFS and its Interpretation

2.1 The General Model

Firstly, we wish to define a quantity which is a measure of the fine structure. This is best accomplished by the fine structure function $\chi(k)$, given by

$$\chi(k) = \frac{\mu(k) - \mu_0(k)}{\mu_0(k)} \qquad (2.1)$$

where $\mu(k)$ is the absorption coefficient of the atom in its environment and μ_0 is the corresponding absorption for a free atom. Both μ and μ_0 refer to the absorption coefficient resulting from excitation of an electron from a single level only, i.e. the K, L_I, L_{II} etc. levels of the atom. The parameter k is the emitted photoelectron wave vector. If we consider an X-ray photon incident on an atom, then the radiation field creates a small perturbation to the electrons in the atom which results in a finite probability for a transition to take place. The transition probability is proportional to the absorption coefficient, and is given by the Golden Rule

$$\mu = \sum_f |\langle f|H'|i\rangle|^2 \quad \delta(E_F - E_i - \hbar w) \qquad (2.2)$$

where $|i\rangle$ and $|f\rangle$ are the initial and final states, H' is the perturbation from the radiation field. In the limit of the exciting radiation having a much larger wavelength than the spatial extent of the initial state, H' can be expressed as $H' = \underset{\sim}{\varepsilon}.\underset{\sim}{r}$ where $\underset{\sim}{\varepsilon}$ is a unit vector in the direction of the electric field of the X-ray photon. Of particular interest in this work is the excitation of 1s electrons whose wavefunction diameter d is given by

$$d \simeq \frac{2a_0}{Z} \qquad (2.3)$$

where a_0 is the Bohr radius and Z the atomic number. For arsenic, d is 0.03 Å and the wavelength for arsenic excitation of the K shell is about 1 Å. Therefore the dipole approximation will be good for this edge, although not so good as when applied to optical transitions.

The final state in Eq. (2.2) can be written

$$|f\rangle = |\psi_0\rangle + |\psi_{Sc}\rangle \qquad (2.4)$$

where $|\psi_0\rangle$ is the state which would result if the atom was isolated and $|\psi_{Sc}\rangle$ is the contribution to the final state from scattering processes. Inserting Eq. (2.4) into (2.2) and expanding yields:

$$\mu = \sum_f |\langle\psi_0|H'|i\rangle|^2 + \langle i|H'|\psi_{Sc}\rangle^* \langle i|H'|\psi_0\rangle + \langle\chi_0|H'|i\rangle\langle i|H'|\psi_{Sc}\rangle$$

$$+ |\langle\psi_{Sc}|H'|i\rangle|^2 \quad \delta(E_F - E_i - \hbar w) \qquad (2.5)$$

As the EXAFS oscillations only contribute at the most about 15% of the total oscillator strength, we may neglect the last matrix element in Eq. (2.5). Noting that the final state of an isolated atom is just $|\psi_0\rangle$, then using 2.1 we may write

$$\chi = \frac{\langle i|H'|\psi_{Sc}\rangle\langle\psi_0|H'|i\rangle + cc}{|\langle\psi_0|H'|i\rangle|^2} \qquad (2.6)$$

where cc stands for complex conjugate. We can expand the final state as a sum of spherical waves of angular quantum number ℓ and magnetic quantum number m

$$|\psi_0\rangle = \sum_{\ell m} A_{\ell m}|\ell mc\rangle \qquad (2.7)$$

where the label c denotes that the waves are specified inside the core of the emitting atom. The scattered wave on the other hand can be written

$$|\psi_{Sc}\rangle = \sum_{\ell m} A_{\ell m}\, t_e\, G_0^+\, t_j\, G_0^+\, t_e\, |\ell mc\rangle \quad . \qquad (2.8)$$

The operator t_e represents the effect of the emitter potential on the states $|\ell mc\rangle$. The effect of this operator is to present the effect of the emitting atom as a black box, emerging from which are spherical waves of the correct phase. If we adopt a muffin-tin potential of the solid then the spherical waves which emerge from the potential, $|\ell m\rangle$, will be solutions to Schrödinger's equation in the constant part of the potential. The group of operators $G_0^+ t_j G_0^+$ describe the propagation of the emitted wave as a free wave in the constant part of the muffin-tin potential to a scatterer whose effect is represented by t_j, this is followed by propagation back to the emitter where it is again subject to the scattering of the emitter potential given by t_e. G_0^+ is the propagating Green's operator. Conceptually this operator yields the amplitude of the wave at a given point in space given the amplitude at all other points in space. Thus its effect is closely associated with the Huygen's construction of optics. Again the operator t_j refers to black boxes localised about the j^{th} isolated scatterer. We introduce these operators to clarify the concepts involved. It should also be noted that the t operators are only valid if the individual potentials are separated in real space. Secondly, the Green's operator G_0^+ implies that the particles move as free particles between the scatterers (i.e. we need a muffin-tin potential model) and, thirdly, that only single scattering of the particles is considered. It can be shown (Holland 1977) that the final state wavefunction for a photoelectron emitted from an atom just outside the range of the potential takes the form of a purely outgoing wave.

$$\langle r|\ell m\rangle = \langle r|t_e|\ell mc\rangle = h_\ell^{(1)}(kr)Y_{\ell m}(\Omega(\underset{\sim}{r}))\, e^{i\delta_\ell} \qquad (2.9)$$

$h_\ell(kr)$ is a spherical Hankel function of the first kind and it has the form of an outgoing wave, $Y_{\ell m}(\Omega(\underset{\sim}{r}))$ is a spherical harmonic, $h_\ell^{(1)}(kr)Y_{\ell m}(\Omega(\underset{\sim}{r}))$ is a solution of the Schrödinger equation in a constant potential. In general the operator $G_0^+ t_j G_0^+$ acting on $|\ell m\rangle$ will produce when expanded about the emitter another set of spherical waves. Thus if we define a matrix $Z_{\ell'm',\ \ell m}$ which is the amplitude of a spherical wave $|\ell'm'\rangle$ produced by scattering from an initial wave $|\ell m\rangle$ then

$$|\psi_{Sc}\rangle = \sum_{\ell m} \sum_{\ell'm'} |\ell'm'c\rangle\, e^{i\delta_{\ell'}}\, Z_{\ell'm',\ \ell m}\, e^{i\delta_\ell}\, A_{\ell m} \qquad (2.10)$$

Therefore (2.6) becomes

$$\chi(k) = \sum_{m_0} \sum_{\ell m} \sum_{\ell'm'} \langle c\ \ell_0\ m_0|\underset{\sim}{\varepsilon}\cdot\underset{\sim}{r}|\ell'm'c\rangle e^{i\delta_{\ell'}} Z_{\ell'm',\ \ell m}\, e^{i\delta_\ell}\, |A_{\ell m}|^2$$

$$\times \langle c\ell m|\underset{\sim}{\varepsilon}\cdot\underset{\sim}{r}|\ell_0\ m_0\ c\rangle + cc / \sum_{m_0} \sum_{\ell m} |\langle c\ell m|\underset{\sim}{\varepsilon}\cdot\underset{\sim}{r}|\ell_0\ m_0\ c\rangle\ |A_{\ell m}|^2 \qquad (2.11)$$

or more simply

$$\chi(k) = \frac{\sum_{m_0} \sum_{\ell'm'} \sum_{\ell m} P_{\ell_0\ m_0\ \ell'm'}\, e^{i\delta_{\ell'}}\, Z_{\ell'm',\ell m}\, e^{i\delta_\ell}\, P_{\ell m\ \ell_0\ m_0} + cc}{\sum_{\ell_0 m_0} \sum_{\ell m} |P_{\ell m,\ell_0 m_0}|^2} \qquad (2.12)$$

where the amplitudes $A_{\ell m}$ have been incorporated into the atomic matrix elements P. Evaluation of one of the P's yields an angular integral which gives the usual selection rules

$$\Delta \ell = \pm 1$$

$$\Delta m = 0 \text{ or } \pm 1 \qquad . \qquad (2.13)$$

for any general direction of the polarisation vector $\underset{\sim}{\varepsilon}$. For an initial state of s-symmetry and the electric field vector aligned along the z-axis, the emitted wave will have p-symmetry and $\Delta m = 0$, thus the lobe of the wavefunction will also point along the z-axis. Thus for s-states

$$\ell_0 = m_0 = 0$$

$$\ell' = \ell = 1$$

$$P_{\ell_0 m_0 \ell m} = P_{\ell_0 m_0 \ell' m'} \quad . \qquad (2.14)$$

If we assume that the material is polycrystalline then Lee and Pendry (1975) have shown that by averaging over all directions of polarisation Eq. (2.12) reduces to

$$\chi = \frac{2}{3} \operatorname{Re} \sum_m Z_{1m,\,1m}\, e^{2i\delta_1} \qquad (2.15)$$

We wish to note here, that the assumption of an unpolarised beam is not equivalent to the assumption of a polycrystalline absorber, as the electric-field vector must be at right-angles to the direction of propagation. Hence, we must note that the EXAFS phenomenon will exhibit preferred orientation effects similar to those found in X-ray diffraction.

2.2 Calculation of the Matrix Z

From Eq. (2.15) of the previous section, we note that the EXAFS function χ is given just in terms of the matrix Z and the emitting atom p-wave phase shift. To find the matrix Z, we merely need to consider an outgoing wave from the emitter $h_\ell^{(1)}(kr)Y_{\ell m}(\Omega(\underset{\sim}{r}))$ being scattered by the surrounding atoms and then returning. Remembering that the wavefunction of the photoelectron is of the form of a purely outgoing wave, we only have to select the part of the returning wave of the form $h_{\ell'}^{(1)}Y_{\ell' m'}(\Omega(\underset{\sim}{r}))$ and its amplitude is the matrix element $Z_{\ell' m',\ell m}$. To give an example of the calculation of Z, we consider the special case of a wave emitted from the origin which, when it reaches the scattering atom, looks like a plane wave with the correct amplitude and phase. This derivation follows from the work of Lee and Pendry (1975). The definitions of the spherical waves and the expansions can be found in Pendry's book (1974) on LEED. If we consider a single spherical wave

$$\psi(\underset{\sim}{r}) = h_\ell^{(1)}(kr)Y_{\ell m}(\Omega(\underset{\sim}{r})) \qquad (2.16)$$

then at the scatterer at $\underset{\sim}{R}_j$, this wave is of the form of a plane wave with the correct amplitude and phase so

$$\psi(\underset{\sim}{r}) \simeq h_\ell^{(1)}(k\,R_j)Y_{\ell m}(\Omega(\underset{\sim}{R}_j))\ \exp(i\,\underset{\sim}{k}\cdot(\underset{\sim}{r}-\underset{\sim}{R}_j)) \qquad (2.17)$$

where the $\underset{\sim}{k}$-vector of the wave is in the direction of $\underset{\sim}{R}_j$. Expanding the plane wave by noting that

$$e^{i\underset{\sim}{k}\cdot\underset{\sim}{r}} = 4\pi \sum_{\ell'' m''} i^{\ell''}\ j_{\ell''}(kr)\ Y_{\ell'' m''}^{*}(\underset{\sim}{k})\ Y_{\ell'' m''}(\underset{\sim}{r}) \qquad (2.18)$$

where $j_{\ell''}(kr)$ is a spherical Bessel function.

Equation (2.17) then becomes

$$\psi(\underset{\sim}{r}) = h_{\ell}^{(1)}(k\ R_j)\, Y_{\ell m}(\Omega(\underset{\sim}{R}_j)) \sum_{\ell''m''} 4\pi\ i^{\ell''}\ j_{\ell'}(k|\underset{\sim}{r}-\underset{\sim}{R}_j|)\, Y^{*}_{\ell''m''}(\Omega(\underset{\sim}{k}))\, Y_{\ ''m''}(\Omega(\underset{\sim}{r}-\underset{\sim}{R}_j)) \qquad (2.19)$$

The scattered wave is found by multiplying the coefficients of the incident spherical waves by the t matrix which, for the definitions of j_{ℓ} used here, is given by

$$T_{LM\ \ell''m''} = \delta_{L\ \ell''}\ \delta_{M\ m''}\ \frac{1}{2}(e^{i2\delta_L} - 1) \qquad (2.20)$$

(see Lee and Pendry 1975), and again selecting the outgoing part gives

$$\psi_{sc}(\underset{\sim}{r}) = h_{\ell}^{(1)}(k\ R_j)\, Y_{\ell m}(\Omega(\underset{\sim}{R}_j)) \sum_{LM} 4\pi\ i^{L}\ h_{L}^{(1)}(k|\underset{\sim}{r}-\underset{\sim}{R}_j|)\, Y^{*}_{LM}(\Omega(\underset{\sim}{k}))$$

$$\times\ Y_{LM}(\Omega(\underset{\sim}{r}-\underset{\sim}{R}_j))\ \frac{1}{2}\ (e^{2i\delta_L} - 1) \qquad (2.21)$$

Replacing this wave by a plane wave at the origin gives

$$\psi_{sc}(\underset{\sim}{r}) = h_{\ell}^{(1)}(k\ R_j)\, Y_{\ell m}(\Omega(\underset{\sim}{R}_j)) \sum_{LM} 2\pi\ i^{L}\ h_{L}^{(1)}(k\ R_j)\, Y^{*}_{LM}(\Omega(\underset{\sim}{k}))\, Y_{LM}(\Omega(-\underset{\sim}{R}_j))$$

$$\times\ (e^{2i\delta_L} - 1)\ e^{-i\ \underset{\sim}{k}\cdot\underset{\sim}{r}} \qquad (2.22)$$

Using (2.18) we may expand the plane wave about the origin to give

$$\psi_{sc}(\underset{\sim}{r}) = h_{\ell}^{(1)}(k\ R_j)\, Y_{\ell m}(\Omega(\underset{\sim}{R}_j)) \sum_{LM} 2\pi\ i^{L}\ h_{L}^{(1)}(k\ R_j)\, Y^{*}_{LM}(\Omega(\underset{\sim}{k}))\, Y_{LM}(\Omega(-\underset{\sim}{R}_j))$$

$$(e^{2i\delta_L} - 1) \sum_{\ell'm'} 4\pi\ i^{\ell'}\ j_{\ell'}(kr)\, Y^{*}_{\ell'm'}(\Omega(-\underset{\sim}{k}))\, Y_{\ell'm'}(\Omega(\underset{\sim}{r})) \qquad (2.23)$$

again selecting the outgoing part by noting that

$$2j_{\ell'} = h_{\ell'}^{(1)} + h_{\ell'}^{(2)}\ . \qquad (2.24)$$

Thus, our original,wave quantum number ℓm,has been transformed into another outgoing wave with quantum number $\ell' m'$ and so the coefficient of the new wave must be the element of the Z matrix,$Z_{\ell' m', \ell m}$. Thus

$$Z_{\ell' m', \ell m} = h_{\ell}^{(1)} (k\, R_j) \sum_{LM} 4\pi^2\, i^{L + \ell'} (e^{2i\delta_L} - 1)\, h_L(k\, R_j)$$

$$\times\, Y_{LM}^{*} (\Omega(\underset{\sim}{k}))\, Y_{LM}(\Omega(-\underset{\sim}{R}_j))\, Y_{\ell' m'}^{*}(\Omega(-\underset{\sim}{k}))\, Y_{\ell m}(\Omega(\underset{\sim}{R}_j)) \quad . \qquad (2.25)$$

We can simplify this by remembering that the direction of $\underset{\sim}{k}$ is the same as $\underset{\sim}{R}_j$. Therefore

$$Y_{LM}^{*}(\Omega(\underset{\sim}{k})) = Y_{LM}^{*}(\Omega(\underset{\sim}{R}_j)) \quad , \qquad (2.26)$$

and

$$\sum_{LM} Y_{LM}^{*}(\Omega(\underset{\sim}{R}_j))\, Y_{LM}(\Omega(-\underset{\sim}{R}_j)) = \sum_{L} \frac{2L+1}{4\pi}\, P_L(\cos(\pi)) \qquad (2.27)$$

so

$$Z_{\ell' m', \ell m} = h_{\ell}^{(1)} (k\, R_j)\, i^{\ell}\, Y_{\ell' m'}(\Omega(-\underset{\sim}{R}_j))\, Y_{\ell m}(\Omega(\underset{\sim}{R}_j))$$

$$\times \sum_{L} 2\pi i (2L+1) P_L(\cos(\pi))\, i^{L} \sin\delta_L\, e^{i\delta_L}\, h_L^{(1)} (k\, R_j) \quad . \qquad (2.28)$$

We can invoke a further level of approximation here, in that we can replace the spherical Hankel function by its asymptotic form

$$h_{\ell}^{(1)}(z) = - \frac{i}{Z}\, e^{iz} (-i)^{\ell} \quad . \qquad (2.29)$$

Inserting this into Eq. (2.28) gives

$$Z_{\ell' m'\, \ell m} = - \frac{i}{k\, R_j} (-i)^{\ell}\, e^{i\, k\, R_j}\, i^{\ell'}\, Y_{\ell' m'}^{*} (\Omega(-\underset{\sim}{R}_j))\, Y_{\ell m}(\Omega(\underset{\sim}{R}_j))$$

$$\times\, 2\pi\, \frac{e^{i\, k\, R_j}}{R_j} \sum_{L} \frac{1}{k} (2\ell + 1)\, e^{i\delta_{\ell}} \sin\delta_{\ell}\, P_L(\cos(\pi)) \qquad (2.30)$$

We see that the term inside the summation of (2.30) is the familiar form of the scattering amplitude f(θ) for backscattering which appears in the Faxen-Holtzmark equation for scattering Eisberg (1961)

$$f(\theta) = \frac{1}{k} \Sigma(2\ell+1)\ e^{i\delta_\ell} \sin\delta_\ell\ P_\ell(\cos(\theta)) \tag{2.31}$$

Using (2.1) which applies for a polycrystalline absorber and an initial slate of s-symmetry with $\ell = \ell' = 1$ we get

$$\chi(k) = \frac{2}{3} \mathrm{Re} \left[-2\pi i \frac{e^{2ikR_j}}{k\ R_j^2} f(\pi)\ e^{2i\delta_1} \sum_{m'} Y^*_{1\ m'}(\Omega(-\underset{\sim}{R}_j)) Y_{1\ m'}(\Omega(\underset{\sim}{R}_j)) \right]. \tag{2.32}$$

From (2.27)

$$\sum_{m'} Y^*_{1\ m'}\ (\ (-\underset{\sim}{R}_j)) Y_{1\ m'}(\ (\underset{\sim}{R}_j)) = -\frac{3}{4\pi}\ . \tag{2.33}$$

Writing

$$f(\pi) = |f(\pi)|\ e^{i\eta_{II}} \tag{2.34}$$

and the emitting atom phase-shift as η_I gives

$$\chi(k) = -\frac{|f(\pi)|}{k} \frac{1}{R_j^2} \sin(2k\ R_j + 2\eta_I + \eta_{II})\ . \tag{2.35}$$

We note here, which is the point of this derivation, that Eq. (2.35) differs from the corresponding formulae in Lee and Pendry (1975) and Ashley and Doniach (1975) by a factor of -1. It does however agree in sign with the expressions derived by Schaich (1973) and Stern (1974).

Although Eq. (2.35) is very simple in form, there have been some drastic assumptions made in its derivation, particularly the replacement of the Hankel functions by their asymptotic forms.

The calculation just performed can, however, be repeated without using the plane-wave or asymptotic assumptions by using the expansions of spherical waves about different origins (Pendry 1974). In this case, the matrix Z can be expressed by the matrix equation

$$Z_{\ell'm'\ \ell m} = V(-R_j)\ S^{\ell'm'}\ T\ R^{\ell m}\ V(R_j) \tag{2.36}$$

where

$$[V(R_j)]_{LM} = h_L^{(1)}(k\ R_j)\, Y_{L-M}(\Omega(\underset{\sim}{R}_j))$$

$$[S^{\ell'm'}]_{LM\ L'M'} = 2\pi\ i^{L'-L\ \ell'}\ (-1)^{M+m}$$

$$\times \int Y_{L'M'}\ {}_{LM}\ Y_{\ell'-m}\ d\Omega$$

$$T_{L'M'\ L''M''} = (e^{2i\delta_{L'}} - 1)\ \delta_{L'L''}\ \delta_{M'M''}$$

$$[R^{\ell m}]_{L''M''\ L'''M'''} = 4\pi\ i^{\ell - L''' - L''}\ (-1)^{M''' + M''}$$

$$\times \int Y_{\ell m}\ Y_{L'''\ M'''}\ Y_{L''\ M''}\ d\Omega \tag{2.37}$$

Equation (2.36) we shall call the curved wave (CW) equation. The extent to which this formula differs from the asymptotic plane wave (APW) case is discussed in Chapter 5.

2.3 Inelastic Loss

In this chapter so far, we have used the variable k, which is the photoelectron wavevector, without relating this to the energy of the photon. The wavevector can be written in atomic units as

$$k^2 = 2(E_f + \Sigma\ (E)) = 2E \qquad (2.38)$$

Here the energy E is measured relative to the constant part of the muffin-tin potential. The term $\Sigma(E)$ is a correction term, which results from the interaction of the photoelectron with the other electrons in the solid. $\Sigma(E)$ is energy dependent and in general decreases with increasing energy. Unfortunately, it is not easy to identify the zero of energy E in terms of the photon energy because the onset of absorption may correspond to ejection of the photoelectron into different states depending on the nature of the material. The X-ray edge may be a result of electron ejection into an excitonic level which is bound and below the muffin-tin zero, or it may correspond to ejection into a level several electron volts above the muffin-tin zero because the states below the Fermi level are occupied. Thus in general, we cannot specify the zero of energy without identifying some of the features close to the absorption edge. This is only possible for a few materials and thus the zero of energy remains a problem. We note that the self-energy Σ is also complex. In the picture given by scattering theory, the photoelectron may induce both virtual and real excitations of the valence band or core electrons. The virtual excitations give a real part to Σ and the real excitations result in its imaginary components. If we have a wave with an imaginary k-vector, then this represents a damped wave in the crystal. It is precisely this effect which limits the range of the photoelectron in the solid. It was recognised that the electron wave was damped inside a solid for energies above the Fermi level as long ago as 1937 by Slater who, interestingly enough, concluded his paper with a note that this did not invalidate Kronig's (1931) long-range order theory. The long-range order theory attributes the EXAFS oscillations to the variations in the density of states. The reason for Slater's conjecture was not, however, made plain and indeed this is an essential parameter which limits the amount and sharpness of the structure observed. In the asymptotic plane wave formula, 2.36, the inelastic effects can be represented by a term written in atomic units as $\exp\left(-\frac{2E_i R_j}{k}\right)$, where E_i is the imaginary part of $\Sigma(E)$ and k is the real part of the wavevector. The factor 2 enters this formula because the wave suffers losses on both its outgoing and returning propagation. In the curved wave expression for χ, the effect of a complex energy may be included by defining complex phase-shifts given to first approximation by a Taylor expansion of the real phase-shifts. Pendry (1974) has suggested that E_i is a constant which is, for most materials, given by $E_i = 4$ eV. The inelastic loss can be written in terms of a mean-free-path λ such that

$$\frac{k}{2E_i} = \lambda \ . \qquad (2.39)$$

Here the mean-free-path refers to intensity rather than the amplitude of the wavefunction. Mean-free-paths have been tabulated for a number of materials by Lindau and Spicer (1974) whose results show that for electron energies in excess of 50 eV, the results based on a constant $E_i = 4$ eV part of the self energy are in reasonable agreement with experiment. Below 50 eV, the mean-free-path starts to increase and tends to infinity at the Fermi level. The assumption of a constant imaginary self energy arises theoretically when considering the interaction of an incident electron with the conduction electrons which is thought to be the dominant process. This produces a slight decay in E_i which is bolstered by the much less probably excitation of core-electrons (Ing and Pendry 1975). Fortunately, electron energy loss measurements have been made for materials similar to those studied here, namely As-Se alloys by Rechtin and Averbach (1973). The results of their measurements show a large plasmon loss peak at 19 eV and small maxima at 6 eV and 55 eV. The 6 eV transition is due to valence band excitation, whereas the 55 eV peak arises from excitation of the 3d electrons from Se, however, the dominant mechanism is clearly the coupling of the incident electron to the valence electrons and thus we expect a model in which the imaginary part of the self-energy is a constant to hold for this work also.

2.4 Temperature Effects

As the electron propagates from the emitter, it does not interact with a static array of scatterers. However, the transit time for an electron sampling the lattice is ~10^{-3} - 10^{-4} times the period of oscillation of a pair of atoms (Shmidt 1961). The absorption will measure an average displacement of all of the atoms. Thus, clearly we can include with the temperature effect the frozen-in positional disorder in the glass. It is important to realise that the type of disorder seen by the photoelectron is a relative disorder, i.e. the technique will sample both the deviations of the scatterers and the emitters from their equilibrium positions calculated along the vector, joining the emitter to the scatterer. The temperature dependence of EXAFS has been examined by Shmidt (1961) (1963) and Beni and Platzman (1976). Their analysis leads to an additional term multiplying the plane wave expression which is of the form of a Debye-Waller factor $e^{-2\sigma_j^2 k^2}$ where σ_j^2 is not the mean-square vibrational amplitude of an atom, but it is the mean-square relative displacement of the emitter and scatterer. To include the temperature effects in the case of the curved wave calculations we can appeal to a device used for low energy electron diffraction (LEED) which is to replace the phase shifts calculated for a static scatterer by temperature dependent phase shifts, (Pendry 1974). The result is that the T matrix defined in (2.37) becomes

$$T_{L'M'\,L''M''} = \left(e^{2i\delta_{L'}(T)} - 1\right)\delta_{L'L''}\,\delta_{M'M''}\cdot\frac{1}{2} \qquad (2.40)$$

with the temperature dependent phase shifts given by

$$e^{i\delta_L(T)} \sin(\delta_L(T)) = \sum_{L'} \sum_{L''} i^{L'} \exp(-2\alpha k^2) j_{L'}(-2i\alpha\, k^2)$$

$$\times\, e^{i\delta_{L''}} \sin(\delta_{L''}) \left[\frac{4\pi\ (2L'+1)(2L''+1)}{2L+1} \right]^{\frac{1}{2}} B^{L''}(L'0,L0) \qquad (2.41)$$

where

$$\alpha = 2\sigma_j^{\,2} \qquad (2.42)$$

and

$$B^{\ell}(\ell'm',\ell''m'') = \int Y_{\ell m}\, Y_{\ell'm'}\, Y_{\ell''m''}\ d\Omega \qquad (2.43)$$

Thus the thermal effects can all be easily incorporated within the calculation. The only problem that remains is the calculation of $\sigma_j^{\,2}$. We note here that the parameter $\sigma_j^{\,2}$ is shell dependent. Except for very short wavelength phonons, the atomic vibrations will be correlated. In general, a calculation of $\sigma_j^{\,2}$ requires a knowledge of the phonon spectrum of the solid which is usually not known, and thus we must treat $\sigma_j^{\,2}$ as an adjustable parameter. Some model calculations will, however, provide clues to the type of behaviour to be expected. Beni and Platzman (1976) have performed calculations for a monatomic lattice using the Debye approximation to determine the mean-square displacement (MSD) and the displacement correlation function (DCF). If the atomic motions were completely uncorrelated then

$$\sigma_j^{\,2} = 2(\mathrm{MSD}) \quad . \qquad (2.44)$$

However, in the presence of correlation, then

$$\sigma_j^{\,2} = 2(\mathrm{MSD}) - 2(\mathrm{DCF}) \ . \qquad (2.45)$$

For the first shell in an fcc lattice Beni and Platzman (1976) have found that correlations are most important at high temperatures where the ratio DCF/MSD saturates at ~0.36 for $T/\theta_0 > 0.7$, where θ_0 is the Debye temperature. Similar behaviour is expected for a body-centred cubic material. It can also be seen from their calculations that σ_j^2 changes little below 50° K, which results from the dominance of the zero-point motion of the lattice below this temperature. For materials with weak bonding, for example inter-layer and inter-molecular bonding, we can expect that the phonons will not be in their ground state and so these materials may well show a temperature dependent fine-structure below 50° K.

It should be emphasised here, that these calculations are based on a very idealised model; the real situation, especially for the materials studied in this work, is quite unknown, and probably highly anisotropic. The calculation of Debye-Waller factors is a serious limitation on any empirical approach to interpreting EXAFS spectra because the values of σ_j^2 will not, in general, be transferrable from one material to another, unless those materials are very similar in nature.

2.5 Multiple Scattering

Over most of the energy range of EXAFS signal, the backscattering can be assumed to be weak. This does not, however, imply that the same is true for forward scattering. It has been recognised for some time that much of the structure in LEED data can be assigned to multiple scattering effects. Owing to the similarity between the EXAFS and LEED phenomena, we should expect the same to be true for the former also. LEED does, however, produce structure by sampling the translational symmetry of the solid which is present in all crystals. EXAFS, on the other hand, is sensitive to radial symmetry which is often not present in crystals, and indeed most of the crystals studied here do not possess radial order. Two salient points emerge, however, concerning multiple scattering. The first is that the path length for the multiple scattering process should be larger than the dominant first shell interaction. Secondly, multiple scattering may become important when an atom shadows or lies close to a path to an outer shell atom. These are the main conclusions drawn by Lee and Pendry (1975) and Ashley and Doniach (1975). Multiple scattering can be incorporated into the Z matrix introduced into Eq. (2.11), but this requires large computational effort. Ashley and Doniach (1975) have introduced a parameter A_j which is a shell penetration term and this is an attempt to partially accommodate multiple scattering into a single scattering scheme.

To summarise, we note that multiple scattering may be important in materials of high radial symmetry, and it is identified by its frequency, which is higher than that from the first shell and also possibly phase shifted by the forward scattering event.

2.6 Relationships to Other Theory

To begin this section we will write down the single scattering asymptotic plane wave (APW) expression for the EXAFS function $\chi(k)$ including the additional terms discussed in the previous sections:

$$\chi(k) = -\sum_j \frac{|f(\pi)_j|}{k} \frac{N_j}{R_j^2} \exp\left(-\frac{2E_i R_j}{k}\right) \exp\left(-2\sigma_j^2 k^2\right)$$

$$\times \sin(2k R_j + 2\eta_I + \eta_{II,j}) A_j \qquad (2.46)$$

This expression, although approximate, does contain the various physical processes involved in separate, easily identifiable terms. The summation over j is made over the number of shells containing N_j atoms at a radius R_j. The factor $|f(\pi)_j|$ and $\eta_{II,j}$ are the backscattering amplitude and phase of the type of atom in the j^{th} shell. Calculations of these parameters were performed many years ago by Hartree, Kronig and Petersen (1934) who integrated numerically the radial Schrödinger equation to yield the phase-shifts from which $f(\pi)_j$ can be found (see equation 2.36). The effect of the emitter potential in shifting the phase by η_I was recognised by Kostarev (1941) who also was the first person to apply a short range order theory to solids, although he did not appreciate the crucial role of inelastic effects in limiting the range of the photo-electron. A review of the theory of EXAFS, contrasting the long-range order and short-range order approaches, has been given by Azaroff (1963), and Schaich (1973) has pointed out that the difference between the two approaches lies merely in the inelastic loss factor which limits the multiple scattering events. If a full multiple scattering calculation is performed in a régime where the inelastic loss is negligible, then the EXAFS structure reflects the density of states of the appropriate symmetry monitored at the nucleus of the emitter. Inelastic losses were first included in the calculations of Shiraiwa, Ishimura and Sawada (1958) who also included multiple scattering, although they concluded that the latter was of no importance in copper. This is contrary to other more accurate calculations by Lee and Pendry (1975) and Ashley and Doniach (1975).

The main investigations of EXAFS have all been based on Eq. (2.46) with the one exception of Lee and Pendry who showed that the phase, if not the amplitude of scattering from copper differed significantly from that predicted by Eq. (2.46). In Chapter 5 we will compare the fine structures calculated with the APW equation (2.46) and the more accurate CW equation (2.36).

2.7 Extracting Structural Information from EXAFS

Encouraged by the potential of the EXAFS technique to extract structural information from the data, but disuaded from performing theoretical calculations owing to their difficulty, various empirical schemes of calculations have been introduced. These are mainly based on the APW equation (2.46). Owing to its form, it is clear that a Fourier transform of this equation will produce structure in real space. If the phase factors η_I and η_{IIj} were both zero, then the sine transform of Eq. (2.46) would produce peaks at the atom positions. Unfortunately the theory becomes uncertain at low energies and so the Fourier transform, instead of extending from 0 to ∞ for ideal measurements, extends from a value $k_{min} \approx 2 \rightarrow 4$ Å^{-1} to $k_{max} \approx 20$ Å^{-1}. This not only produces the usual high frequency cut-off ripples (Bragg and West 1930), but also a slowly varying modulation caused by the low frequency cut-off. In fact, the real spectrum is convoluted with the Fourier transform of the window function W

$$W = 1 \qquad k_{min} < k < k_{max}$$

$$W = 0 \qquad \text{otherwise.} \tag{2.47}$$

This follows immediately from the convolution theorem of Fourier transforms

$$FT(A \times B) = FT(A) * FT(B) \tag{2.48}$$

where * denotes convolution. A simple way to view this is to note that

$$FT(W) = FT(W_2) - FT(W_1) \tag{2.49}$$

where

$$\begin{array}{lll} W_1 = 1 & 0 < k < k_{min} & \\ \quad = 0 & \text{otherwise} & \\ & & (2.50) \\ W_2 = 1 & 0 < k < k_{max} & \\ \quad = 0 & \text{otherwise} & \end{array}$$

The Fourier transforms of W_1 and W_2 are of the form $\frac{\sin k_0 r}{k_0 r}$ where k_0 is the upper limit of W_1 or W_2. Thus

(2.51)

FT(W_2) FT(W_1) FT(W)

As well as the window effects, the Fourier transform of the amplitude terms in Eq. (2.46) will also be convoluted into the real structure plus a term resulting from a lack of knowledge of the background absorption μ_0 defined in Eq. (2.1), and also the noise of the spectrum. To sharpen the Fourier transform in real space, an attempt is usually made to compensate for the amplitude terms by multiplying the spectrum by a factor k (Lytle, Sayers and Moore 1974), k^2 (Cramer, Eccles, Kutzler, Hodgson and Doniach 1976), or k^3 (Stern, Sayers and Lytle 1975). Fortunately, we may expect that the factors $\frac{|f(\pi)|}{k}$ and $\exp - \frac{2R_j E_i}{k}$ will remain constant when comparing materials of similar structure and composition and so comparative measurements can still be made. One assumption which has been made, is that the values of $\frac{|f(\pi)|_j}{k}$ are the same regardless of the atom in the j^{th} shell. In the next chapter, we will see that this is totally incorrect. Thus the peak heights in the Fourier transform will be a function of the window in k-space chosen. Comparison of data presented in a Fourier transform thus becomes very difficult.

So far, we have assumed that the phase shift functions η_I and η_{II} are zero. If we can approximate by allowing

$$2\eta_I + \eta_{IIj} = - ak + b \qquad (2.52)$$

which is a formula first introduced by Mott (1963) then the structural features in the Fourier transform are shifted to r-a and, depending on the constant b, will be peaks, dips, or something in between. Sometimes, the features are forced into being peaks by adjusting the zero energy point E (Sayers, Lytle and Stern 1974). Of course, this situation is further complicated if the phase-shifts are non-linear, a situation found empirically for molecules by Citrin, Eisenberger and Kincaid (1976). The breakdown of Eq. (2.51) has also been noted by Stern, Sayers and Lytle (1975) in GeO_2 and its range of applicability has not yet been tested. We present some theoretical calculations of these phase factors in the next section. It seems therefore, that the Fourier transform technique has many drawbacks, and as the equation (2.46) has easily recognisable parameters whose form we know, it is thus clearer to examine the fine-structure function directly in energy space.

Finally, we should point to a method of extracting structural information from the EXAFS structure which appears at first sight to be a Fourier transform technique. This method has been introduced by Gurman and Pendry (1976) to analyse the fine structure of copper.

The method starts by calculating the transform $\phi(r)$ given by

$$\phi(r) = r^2 \left| \int_{k_2}^{k_1} \left| \frac{\chi(k)k}{f_1(\pi,k)} \right| \frac{\exp[i(-2kr - \eta_{tot}(k))]}{\exp(-2\alpha(k)R_1)\exp(-2\sigma_1{}^2k^2)} \times \exp[-a(k-k_0)^2] \right| dk. \tag{2.53}$$

We note here that the fine-structure has been divided by the first shell amplitude parameters calculated theoretically; also the phase $\eta_{tot}(k)$ of the transform has been corrected by using theoretical values. The modulus of the transform has been used to ensure that a peak will occur at the atom position. Termination effects have also been reduced by multiplying by the window function $\exp[-a(k-k_0)^2]$. This transform then provides the starting point for the analysis. The first peak distance is then noted and the theoretical contribution of the first shell is calculated and subtracted from the experimental spectrum. This difference is then retransformed and the first peak is monitored. The theoretical parameters are then adjusted to remove the first shell contribution to the Fourier transform. This, of course, has the advantage of also removing the termination effects from the first shell. Thus the technique can proceed, shell by shell, to analyse the structure. Originally the technique was used for a monatomic solid and for calculations using the plane wave expression of Eq. (2.40). However, it is clear that this method can be generalised to include different types of atoms, by multiplying the transform by the appropriate amplitude functions for the shell under consideration. Also the more accurate curved wave calculations can be included easily. The major drawback of this technique, however, is the use of theoretical parameters which limited the accuracy of Gurman and

Pendry's shell radii to ~ 0.05 Å.

It is clear that Fourier transform techniques have many drawbacks, and the use of empirical techniques has not been justified by full theoretical calculation. In some cases empirical techniques are impossible to apply. A good example is the case of $As_2 Te_3$, dealt with later in this thesis. Thus it seems logical to proceed by doing full theoretical calculations to gain confidence in our physical models. Only when we are satisfied that we understand the physical processes involved, will it be possible to use the quicker methods of interpretation.

CHAPTER 3

Phase shift calculations

3.1 General remarks

From the previous chapter it can be seen that the frequency of the EXAFS signal depends not only on the distance of the emitter from the scatterer, but also on the emitted photo-electron phase shift η_I and the phase of the backscattering amplitude η_{II}. The amplitude of the EXAFS signal is also a function of the type of atom doing the scattering. Thus, for the structural information which we seek, it is important to understand how these parameters behave. In particular, if we wish to find the distance of one scattering atom from the emitter then we must have a knowledge of the phases η_I and η_{II}. Also the behaviour of η_{II} and $|f(\pi)|$ will give some indication of the sensitivity of these factors to differing atoms and thus enable us to anticipate the likelihood of atom identification under various conditions. Further, by examining the behaviour of $|f(\pi)|$ we can establish the range of energies over which we can observe the EXAFS oscillations. It is clearly important to evaluate $|f(\pi)|$, η_I and η_{II} as this will reduce the number of unknowns in the EXAFS equation and leave us with parameters for which we have little knowledge, such as the shell-dependent Debye Waller factors and the inelastic loss function.

We have seen in the previous section that the amplitude and phase of the signal may also depend on the distance of the scattering atom from the emitter via the wave curvature effect. However, we anticipate that the general features of the amplitude and phase will be reproduced when we use the plane wave equation (equation ?.46). Examples of the error of the phase and amplitude of the wave resulting from the asymptotic plane wave approximation will be given later. Here it is expedient to draw attention to the range of energies discussed in the context of EXAFS. If this technique is to be generally useful as a structural tool then the calculations of scattering properties of an atom should not be sensitive to the environment of the scatterer (a situation which is largely true for X-ray scattering). The photo-electron is scattered by the potential of the atom and we know that parts of the potential are sensitive to the atom's environment. This arises when free atoms are aggregated into a condensed form, the outer electrons redistribute themselves to form bonds which are responsible for the cohesive energy of the system. The redistribution of charge may well be anisotropic. Despite these apparent difficulties we can take comfort from band-structure calculations of the augmented plane wave variety which have achieved much success by using spherically symmetric potentials, Loucks (1967). Band structure calculations are performed for electron energies which are within a few electron volts of the Fermi level, and here the kinetic energy of the electron is comparable to the potential variation created by the valence charge redistribution. Thus we expect that if we restrict our attention to photo-electron energies in excess of 50 eV, say, then we can be content to construct reliable potentials on a somewhat cruder level than those used for band structure calculations.

To avoid confusion, we will clarify the use of the term phase-shift. Unfortunately this is used in two contexts. The first corresponds to the usual scattering theory meaning of phase shift and is referred to by the symbol δ_ℓ. The simplest way to view this function is to note that at large distances from the spherical potential the solution of Schrodinger's equation for a wave of angular momentum ℓ outside the range of a potential differs from the solution of the equation if the potential were everywhere zero by a phase factor δ_ℓ. This is not to be confused with the phase-shift $\eta_{II,j}$ which is the argument of the backscattering amplitude, and is itself a function of the δ_ℓ s.

3.2 Calculation of the Phase Shifts δ

The phase shifts δ_ℓ are given by comparing the solutions of the Schrödinger equation in the presence of the potential with those obtained when the potential is absent. If the muffin tin potential is truncated at a radius r = R then the phase-shift is given by

$$\exp(2i\delta_\ell) = \frac{L_\ell\, h_\ell^{(2)} - h_\ell^{(2)\prime}}{h_\ell^{(1)\prime} - L_\ell\, h_\ell^{(1)}} \qquad (3.1)$$

where L is given by

$$L_\ell(R) = \frac{\phi_\ell'(R)}{\phi_\ell(R)} \qquad (3.2)$$

and here the prime denotes the derivative with respect to the radius r, and $h^{(1)}$ and $h^{(2)}$ are spherical Hankel functions of the first and second kind (see Pendry (1974)). The equation to be solved in atomic units for the wavefunction ϕ_ℓ of the incident electron with angular momentum ℓ is

$$-\frac{1}{2}\frac{1}{r^2}\frac{d}{dr}\left[r^2\frac{d\,\phi_\ell(r)}{dr}\right] + \frac{\ell(\ell+1)}{2r^2}\,\phi_\ell(r)$$

$$+ V_H(r)\,\phi_\ell(r) + \int V_{ex}^{(\ell)}(r,r')\,\phi_\ell(r')\,r'^2\,dr' = E\,\phi_\ell(r) \qquad (3.3)$$

The first two terms result from expressing Schrödinger's equation in spherical polar coordinates and then separating the radial part from the angular part. The term $V_H(r)$ is the Hartree potential and is given by

3.2 Calculation of the Phase Shifts δ

The phase shifts δ_ℓ are given by comparing the solutions of the Schrödinger equation in the presence of the potential with those obtained when the potential is absent. If the muffin tin potential is truncated at a radius r = R then the phase-shift is given by

$$\exp(2i\delta_\ell) = \frac{L_\ell\, h_\ell^{(2)} - h_\ell^{(2)'}}{h_\ell^{(1)'} - L_\ell\, h_\ell^{(1)}} \qquad (3.1)$$

where L is given by

$$L_\ell(R) = \frac{\phi_\ell'(R)}{\phi_\ell(R)} \qquad (3.2)$$

and here the prime denotes the derivative with respect to the radius r, and $h^{(1)}$ and $h^{(2)}$ are spherical Hankel functions of the first and second kind (see Pendry (1974)). The equation to be solved in atomic units for the wavefunction ϕ_ℓ of the incident electron with angular momentum ℓ is

$$-\frac{1}{2}\frac{1}{r^2}\frac{d}{dr}\left[r^2\frac{d\,\phi_\ell(r)}{dr}\right] + \frac{\ell(\ell+1)}{2r^2}\,\phi_\ell(r)$$

$$+ V_H(r)\,\phi_\ell(r) + \int V_{ex}^{(\ell)}(r,r')\,\phi_\ell(r')\,r'^2\,dr' = E\,\phi_\ell(r) \qquad (3.3)$$

The first two terms result from expressing Schrödinger's equation in spherical polar coordinates and then separating the radial part from the angular part. The term $V_H(r)$ is the Hartree potential and is given by

$$V_H(r) = -\frac{Z}{r} + \frac{1}{r}\int_0^r 4\pi\,\rho(r')\,r'^2\,dr' + \int_r^\infty \frac{4\pi r'^2\,\rho(r')\,dr'}{r'} \qquad (3.4)$$

Here $\frac{Z}{r}$ is the potential of the nucleus and the other terms give the potential due to the charge distribution of the other electrons present in the muffin-tin. The term $V_{ex}(r,r')$ is called the exchange potential. This results from the application of the Pauli Exclusion Principle which requires the total wavefunction of all of the electrons of the system to be anti-symmetric to a change of coordinates of any two of the electrons. Because the potential depends not just on a potential at the point r but is dependent on two coordinates r and r', it is called a non-local potential. The expression used for the exchange potential can be calculated to be (Pendry (1974)),

$$V_{ex}^{\ell}(r,r') = -\sum_{\ell\ell'} \psi_{\ell'}(r)\,\psi_{\ell'}(r')\,\frac{r_<^{\ell''}}{r_>^{\ell''+1}}\,C(\ell',\ell'',\ell) \qquad (3.5)$$

where ψ_ℓ is a core wavefunction angular momentum ℓ, $r_<$ and $r_>$ are the lesser and greater of r and r' and $C(\ell',\ell'',\ell)$ is given by

$$C(\ell',\ell'',\ell) = \frac{2\ell'+1}{2}\int_0^\pi P_{\ell'}(\cos\theta)\,P_{\ell''}(\cos\theta)\,P_\ell(\cos\theta)\,\sin\theta\,d\theta \qquad (3.6)$$

the C's can be expressed using a single formula given by Gaunt (see Slater (1960)). Using equation (3.5) for V_{ex} in equation (3.3) defines the Hartree-Fock equation.

Two sets of phase shifts were calculated for the atoms under study here. The construction of the potentials were as follows:-

a) The Hartree potential V_H was calculated by solving Poisson's

Equation. The charge density was obtained from the core wavefunctions tabulated by Herman and Skilman (1963). The charge density was truncated at the edge of the muffin-tin radius and the deficiency of charge inside the muffin-tin which resulted, was then distributed uniformly over the atomic volume. The exchange potential was that given in equation (3.6). The calculation was carried out using a program which is listed in Pendry (1974). This program was modified to calculate fifteen phase-shifts, the limit being set by floating point overflow when calculating factorials in the Gaunt integral, see equation (3.6). The radii chosen for the muffin-tin are shown in table 3.1.

Table 3.1

Atom	Muffin-tin radius (Å)	Atom	Muffin-tin radius (Å)
O	0·63	Te	1·35
S	1·02	Ge	1·22
Se	1·16	As	1·19

b) These calculations were carried out by B.W. Holland using a program of Pendry (1977, unpublished) which constructs the Hartree potential by a method described by Loucks (1967). In this case, the charge density is formed by superimposing the charge density taken from the wavefunctions of Clementi and Roetti (1974) of the atom under consideration with the charge distribution from the neighbouring potentials which are arranged on a lattice of given symmetry. The charge distribution is then spherically averaged. Again, the electrostatic problem is solved using Poisson's equation. The lattice used was a simple cubic lattice with the atom whose phase-shifts are to be calculated surrounded by six arsenic atoms. The lattice constant was chosen so that the nearest neighbour was a distance 2.0, 2.2, 2.4 and 2.6 Å for oxygen, sulphur, selenium and tellurium . Clearly

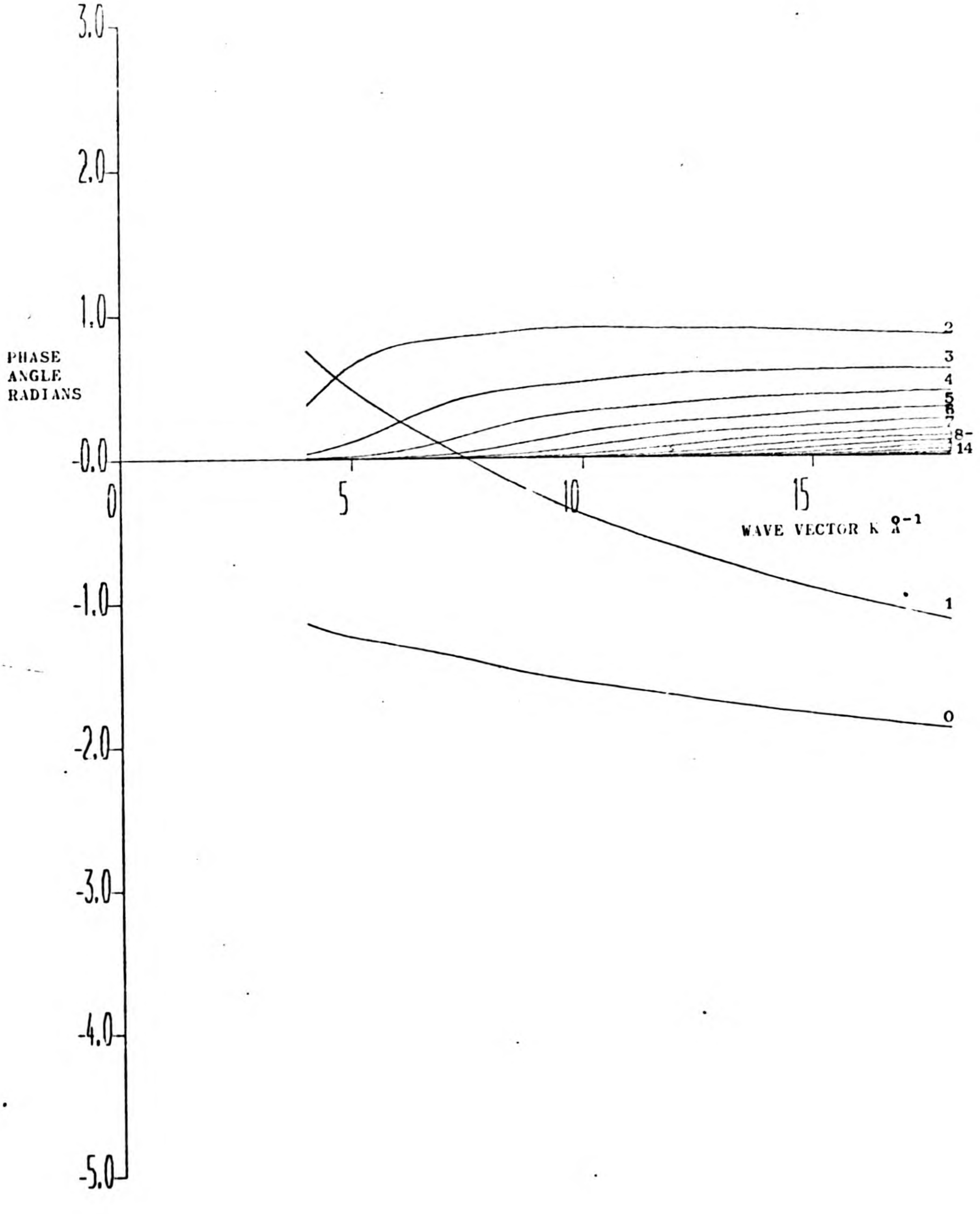

Fig.3.1. Fifteen Oxygen Phase Shifts.

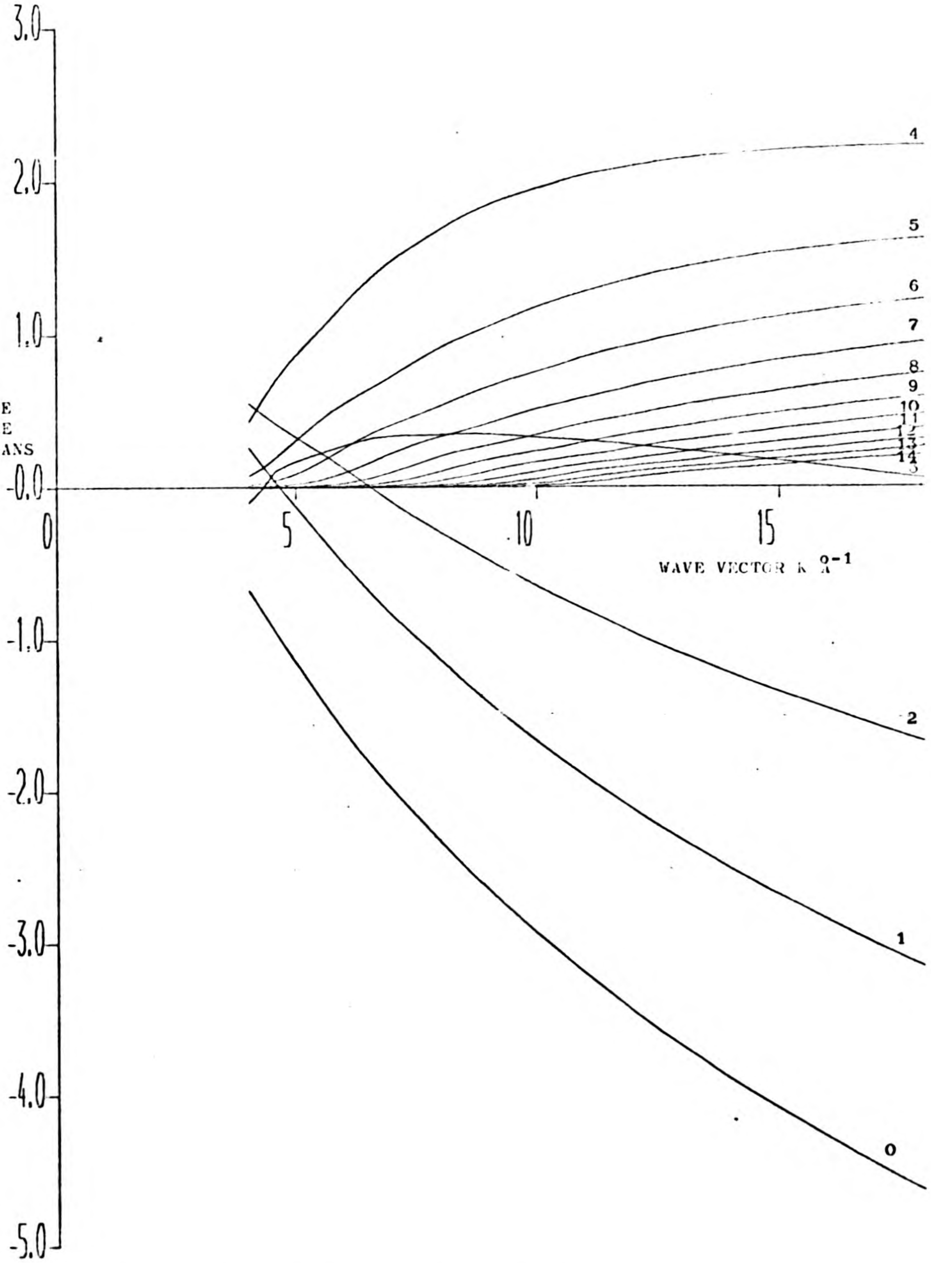

Fig.3.2. Fifteen Tellurium Phase Shifts.

this is an idealised situation because the atoms in the materials studied here have very asymmetric coordination. The exchange potential was approximated by a Slater (1968) type free electron approximation where the non-local operator V_{ex} is replaced by a local potential which varies as $(\rho)^{1/3}$.

Fifteen phase-shifts were calculated for each atom and the two extreme sets, one for oxygen and one for tellurium, are shown in figures 3.1 and 3.2. These phase-shifts have been calculated using the Slater exchange approximation; the Hartree-Fock phase-shifts behave in an analagous manner. The values of δ_ℓ are arbitrary to a factor of $n\pi$. The absolute values of phase-shift can be calculated using Levinson's theorem which states that $\delta_\ell(E = 0) = m\,\pi$ where m is the number of bound states of the atom with angular momentum ℓ, although this is not necessary for the following calculations. The general behaviour shows that the oxygen phase-shifts vary much more slowly than those of tellurium and also for tellurium the higher partial waves are active at lower energies than in the case of oxygen. This is a consequence of the larger core of the tellurium atom relative to that for oxygen. The situation for sulphur and selenium is intermediate between these extremes and follows the same trends.

3.3 Calculation of the factor $\frac{|f(\pi)|}{k}$

The quantity $\frac{|f(\pi)|}{k}$ is a term which represents the contribution to the amplitude of the EXAFS signal dictated by the properties of the scattering atom. The factor $^1/_k$ comes from the recognition that we are scattering spherical waves and arises when replacing the Hankel function by its asymptotic form. This parameter can be calculated from equation (2.31) repeated here.

$$f(\pi) = \frac{1}{k} \sum_0^\infty (2\ell + 1) \ (-1)^\ell \ \sin \delta_\ell \ e^{i\delta_\ell} \qquad (3.8)$$

Note that the Legendre polynomial reduces to $(-1)^\ell$ for backscattering. The factor $(2\ell + 1)$ ensures that the higher partial waves are weighted more than the small partial waves, and so we must be cautious in evaluating the sum over a finite set of phase-shifts if we suspect that the phase-shifts for partial waves greater than the maximum ℓ value calculated are finite. Fortunately, the factor $(-1)^\ell$ ensures that their magnitude is alternately added and subtracted from the sum and this will help to reduce the errors in a premature termination of the sum.

From the phase-shifts of oxygen (figure 3.1) we can see that the restriction to fifteen phase-shifts will cause a negligible error over the entire energy range. On the other hand, the phase-shifts for tellurium (figure 3.2) behave in a manner which suggests that the phase-shifts for $\ell > 14$ are quite large. From a limited number of calculations which extend to 25 phase-shifts we can conclude that the amplitude of backscattering is unaffected to within 5% by truncation of the phase shifts at $\ell = 14$ for tellurium provided the energy is below 500 eV (~ 11.5 $Å^{-1}$), and for arsenic below 800 eV (~ 14.5 $Å^{-1}$).

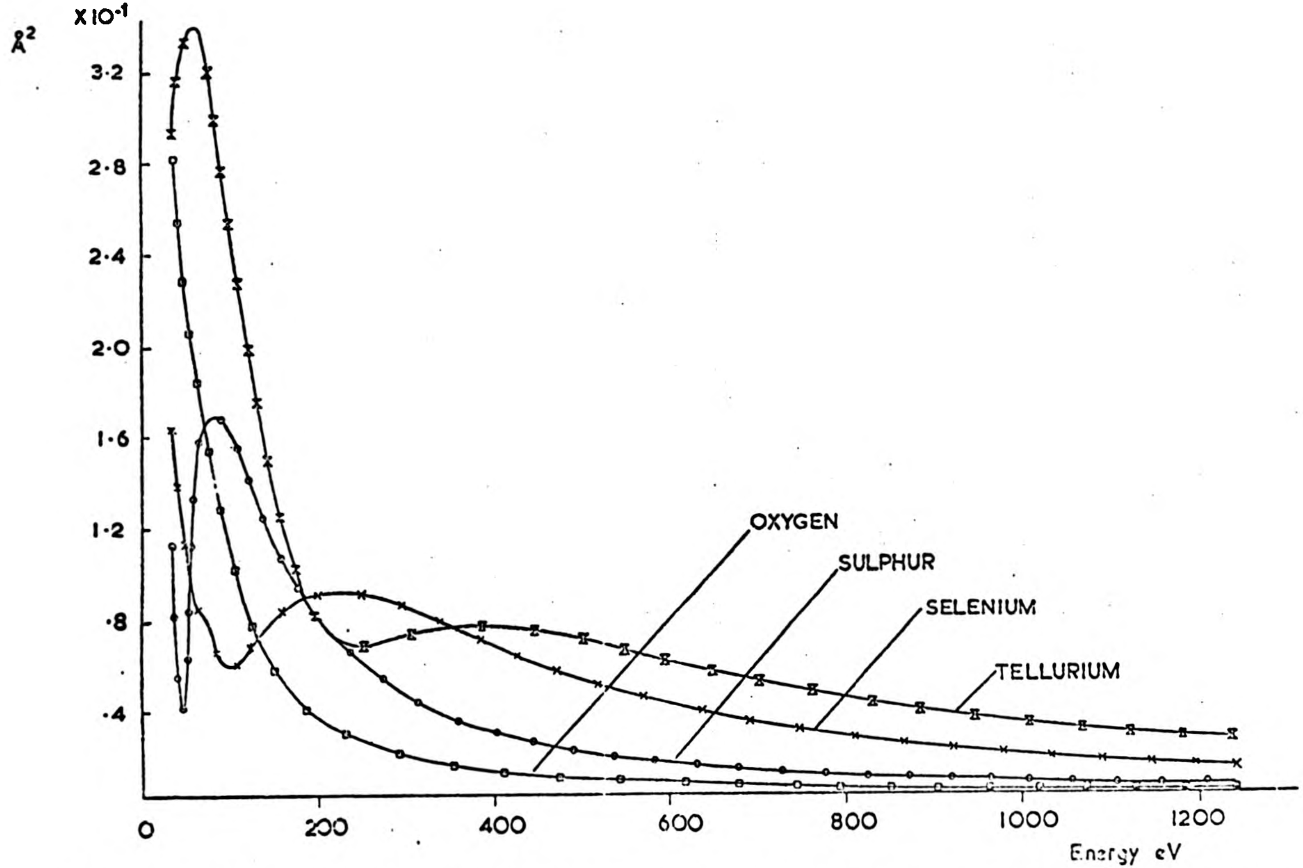

Fig.3.3. The factor $\frac{|f(\pi)|}{k}$ for the chalcogen family using the Hartree-Fock phase shifts.

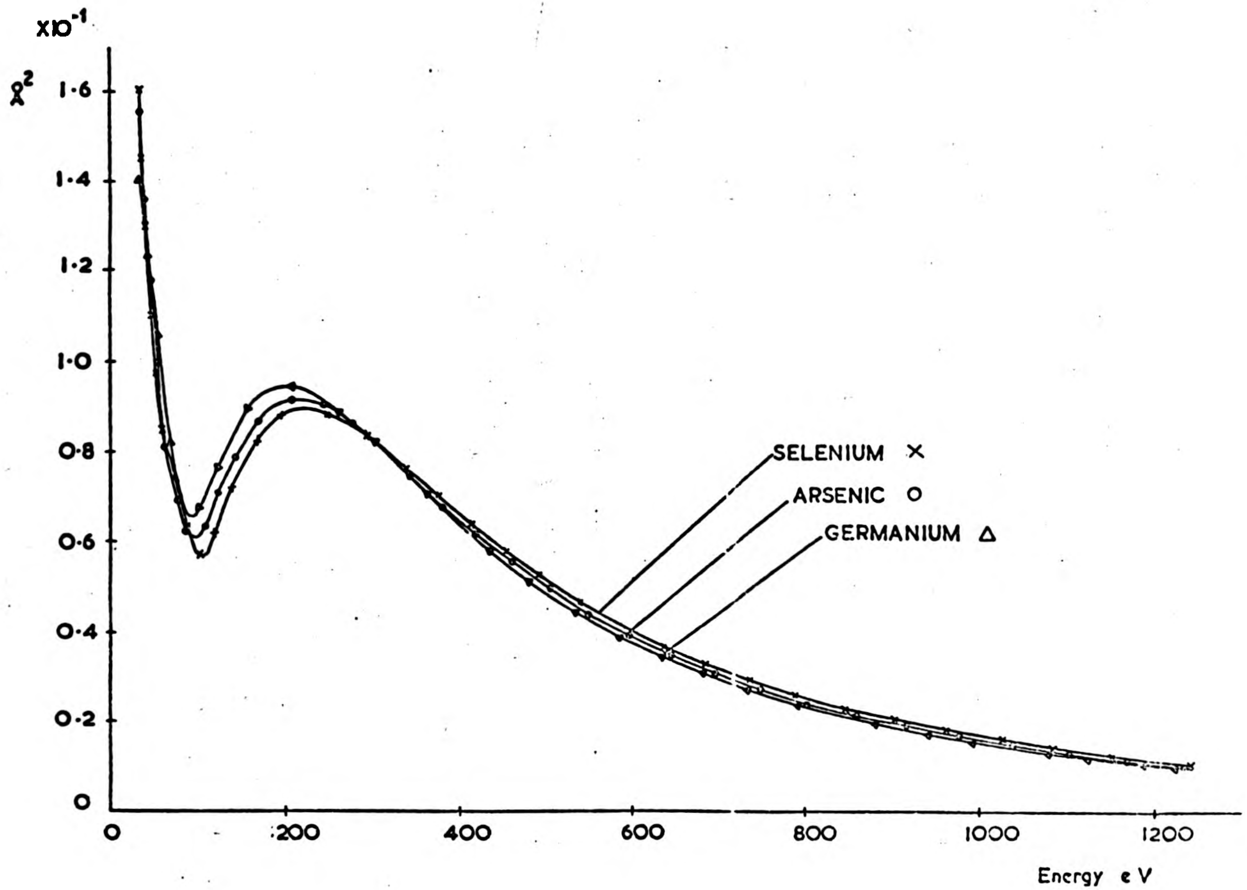

fig.3.4. The factor $\frac{|f(\pi)|}{k}$ for Ge, As and Se using Hartree-Fock phase shifts.

Figure 3.3 shows the quantity $\frac{|f(\pi)|}{k}$ plotted as a function of energy for the members of the chalcogen family calculated using the Hartree-Fock phase-shifts. The striking feature of these curves is the variety of structure which is exhibited for large changes in the atomic number. It is clear also that the size of the nuclear charge dictates the strength of scattering at energies in excess of 400 eV. If we had calculated the factor $|f(\pi)|$ using the Born approximation then we would obtain a bell-shaped function centred at E = 0 (Doyle and Turner (1968)). The Born approximation is valid when scattering is weak and the particle is scattered once by the potential. The varied structure of the curves in figure 3.3 can be interpreted in terms of multiple scattering within the atom.

The function $\frac{|f(\pi)|}{k}$ also shows that the range in energy of the lighter atom scattering is limited and thus it is more difficult to obtain information about bond-distances for oxygen than tellurium (say). Also, as the amplitude of scattering from oxygen diminishes quickly, then it may be possible to isolate the major contributions to the EXAFS function in energy. An example of this effect can be seen later in Chapter 5 in the material As_2O_3. The curves also suggest that because of the distinctive behaviour of the scattering for atoms of quite different atomic number, then these atoms can be identified from their backscattering behaviour. Again this point is taken up in Chapter 5.

Turning to a comparison of the amplitude behaviour of atoms of similar atomic number shown in figure 3.4, also calculated from the Hartree-Fock equation, we see that there are only slight differences

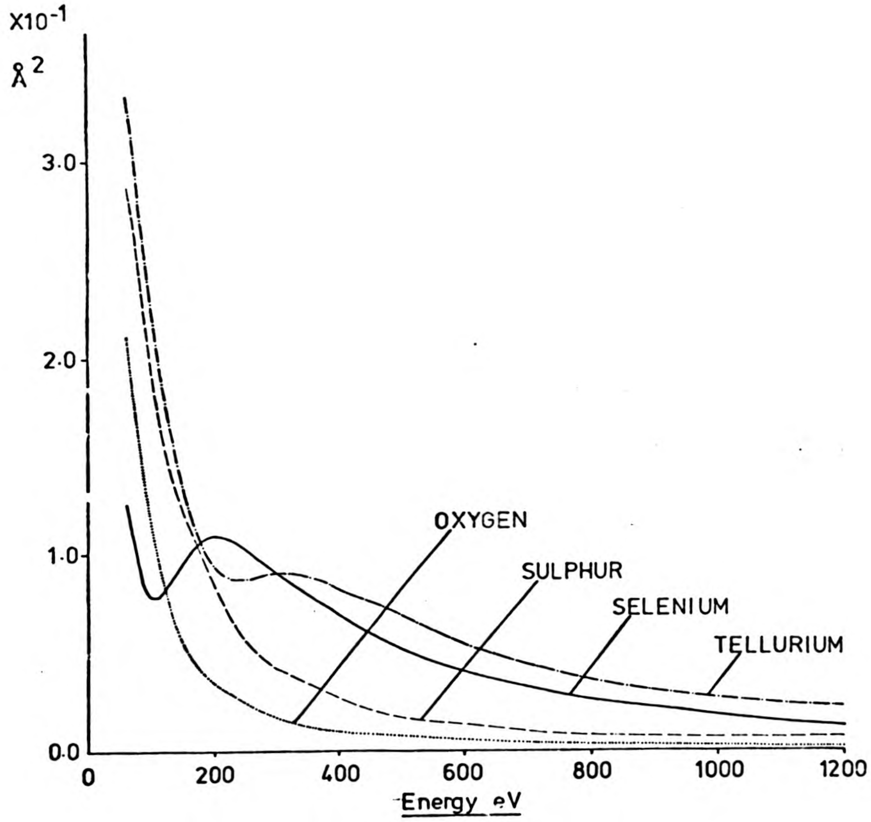

Fig.3.5. The factor $\frac{|f(\pi)|}{k}$ for the chalcogen family using Slater's local exchange approximation.

in the behaviour of backscattering from Ge, As and Se. This suggests that it will be difficult to distinguish between atoms adjacent to each other in the periodic table on the basis of the amplitude of the EXAFS signal alone. However it can be seen that the major differences occur at low energies, i.e. less than 200 eV.

Figure 3.5 shows the function $\frac{|f(\pi)|}{k}$ for the chalcogens calculated using the $\rho^{1/3}$ exchange approximation, and in general we can see that the curves have the same basic shape above 100 eV. Below 100 eV the differences become very noticeable and are most apparent for sulphur which does not show a large dip at 50 eV. Quantitatively the magnitude of the signal is larger at low energies for the Slater $\rho^{1/3}$ exchange than for the Hartree-Fock case and the amplitudes agree at high energies. This effect could be caused by

a) The different electro-static model used, or

b) The different exchange potential adopted.

As the exchange potential is itself an electro-static potential, at present it is difficult to identify the cause of the differences.

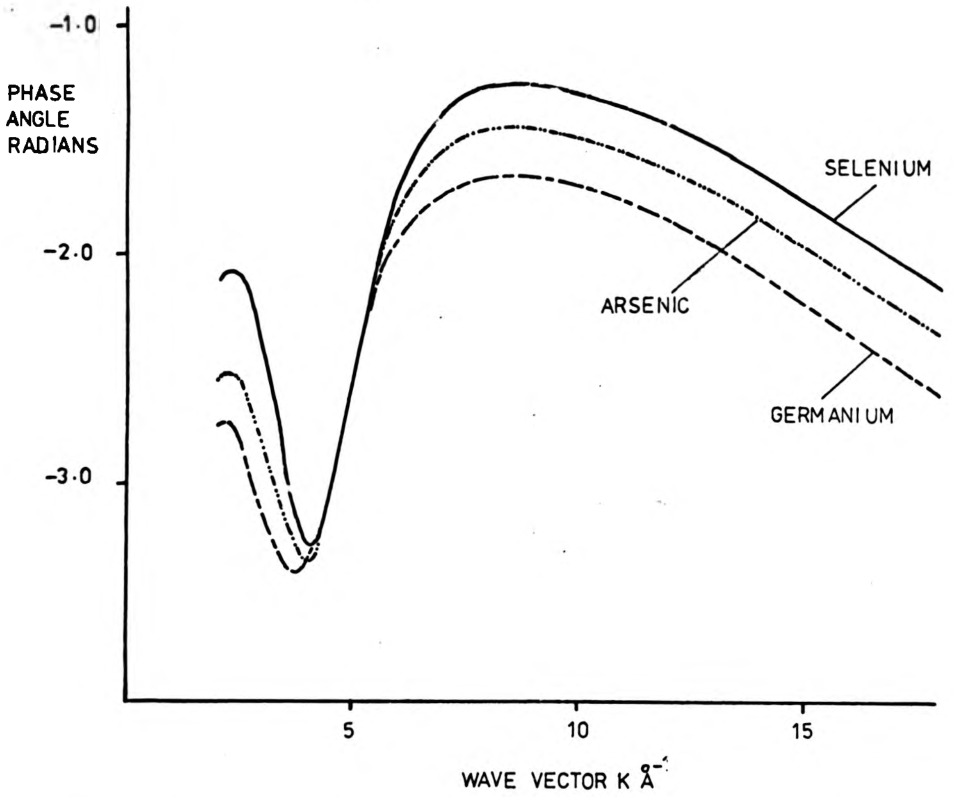

Fig.3.6. The factor η_{Π} for Ge, As and Se using Hartree-Fock phase shifts.

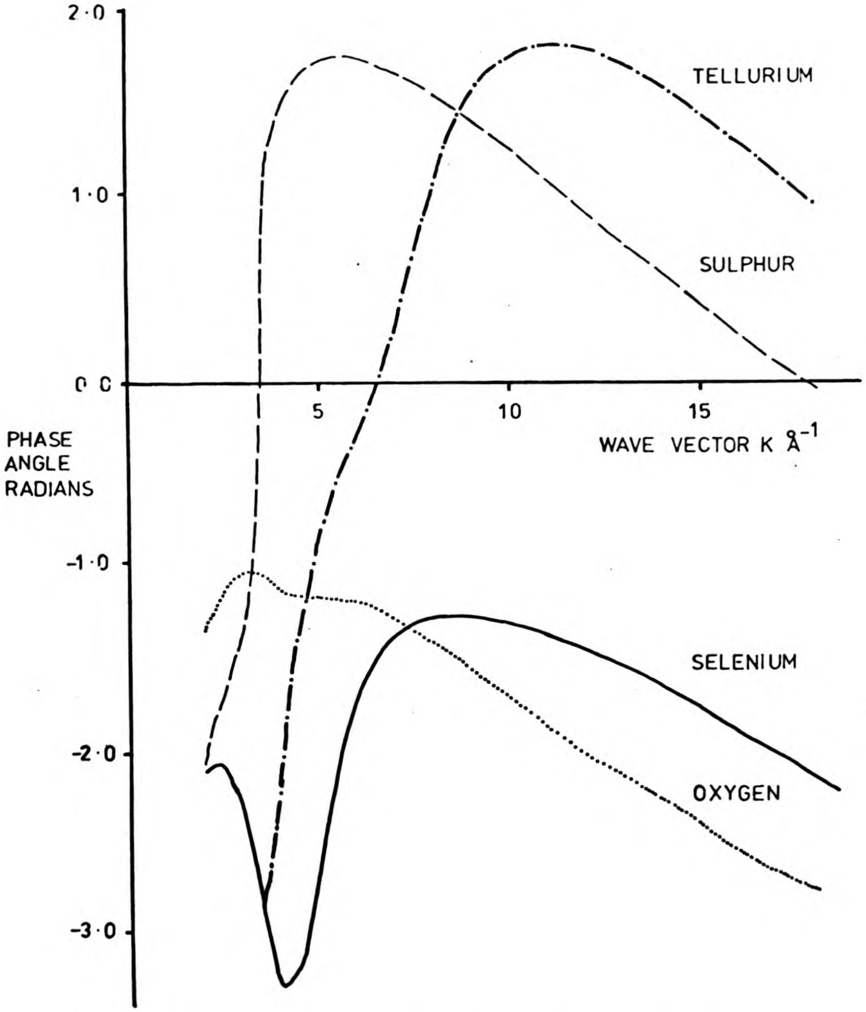

Fig.3.7. The factor η_l for the chalcogen family using Hartree-Fock phase shifts.

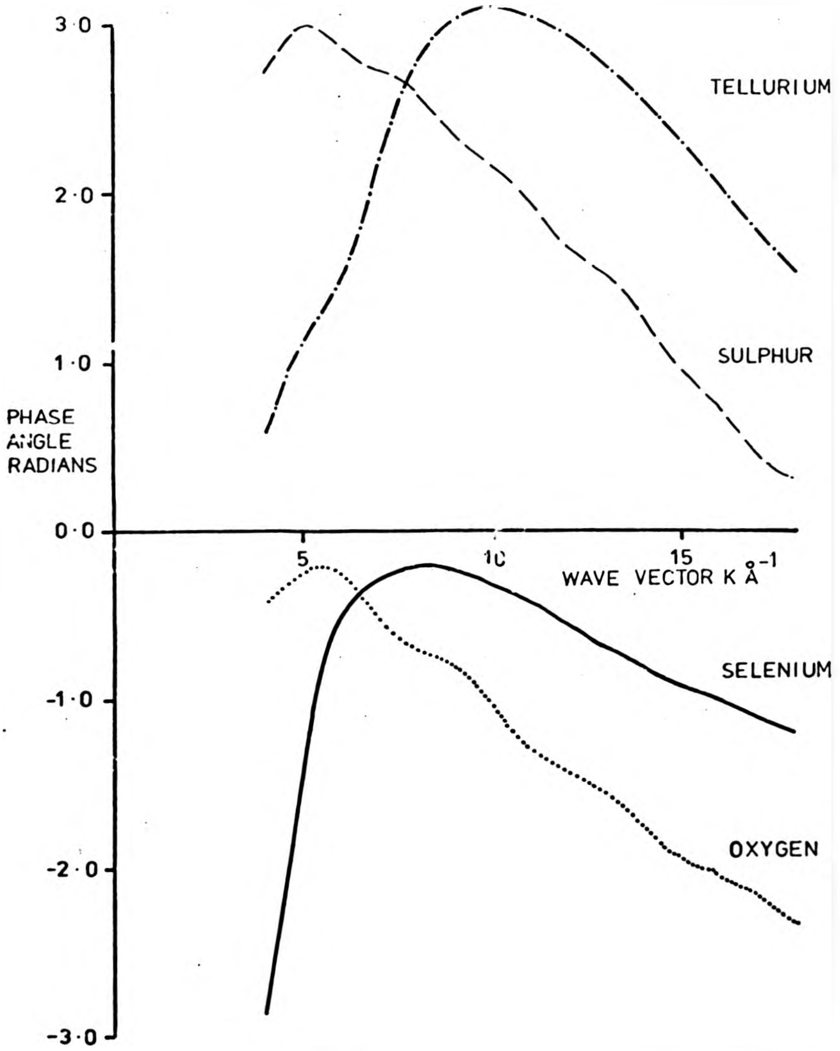

Fig.3.8. The factor η_{II} for the chalcogen family using Slater's local exchange approximation.

3.4 Calculation of the factor η_π

The parameter η_{II} is the total phase-shift of the scattered wave and is given by the argument of f(π) in equation (3.8). Again we note that the value of this phase may vary as a function of the distance of the scattering atom from the emitter; however we wish to examine the general trends in its behaviour. Figure 3.6 shows the variation of the phase η_{II} for the atoms germanium, arsenic and selenium using the Hartree-Fock phase-shifts, again systematic behaviour is evident. Over a large part of the range of K-vector from 7 Å^{-1} (~ 190 eV) to 17 Å^{-1} (1100 eV) the phase difference between these atoms is roughly constant at about 0.2 radians. Again this difference is small when viewed in the context of the other uncertainties, for example the position of the zero of energy. Thus it is at present difficult to identify atoms of similar atomic number. We note here that the curvature of the function η_{II} is negative.

The behaviour of the backscattering phase η_{II} for the chalcogen group is shown in figure 3.7. As for the case of the amplitude, the phases are quite different. It can be seen that, as we move down the periodic table, the magnitude of the phase alternates approximately by a factor of π.

The factor η has also been calculated for the chalcogens using the phase-shifts based on the Slater $\rho^{1/3}$ approximation and these results are given in figure 3.8. Again the same basic behaviour is evident above 5 Å^{-1} (~ 100 eV). However, above this energy the values of η_{II} are greater than the Hartree-Fock η_{II}'s by about 1 radian. It should therefore be quite easy to detect which set of phase-shifts best represent the true situation. If we were to compensate for an error of 1 radian in the phase-shift by adjusting the radius of a shell to match a peak at 10 $Å^{-1}$ (380 eV) say, then the error in the radius would be about 0.05 Å.

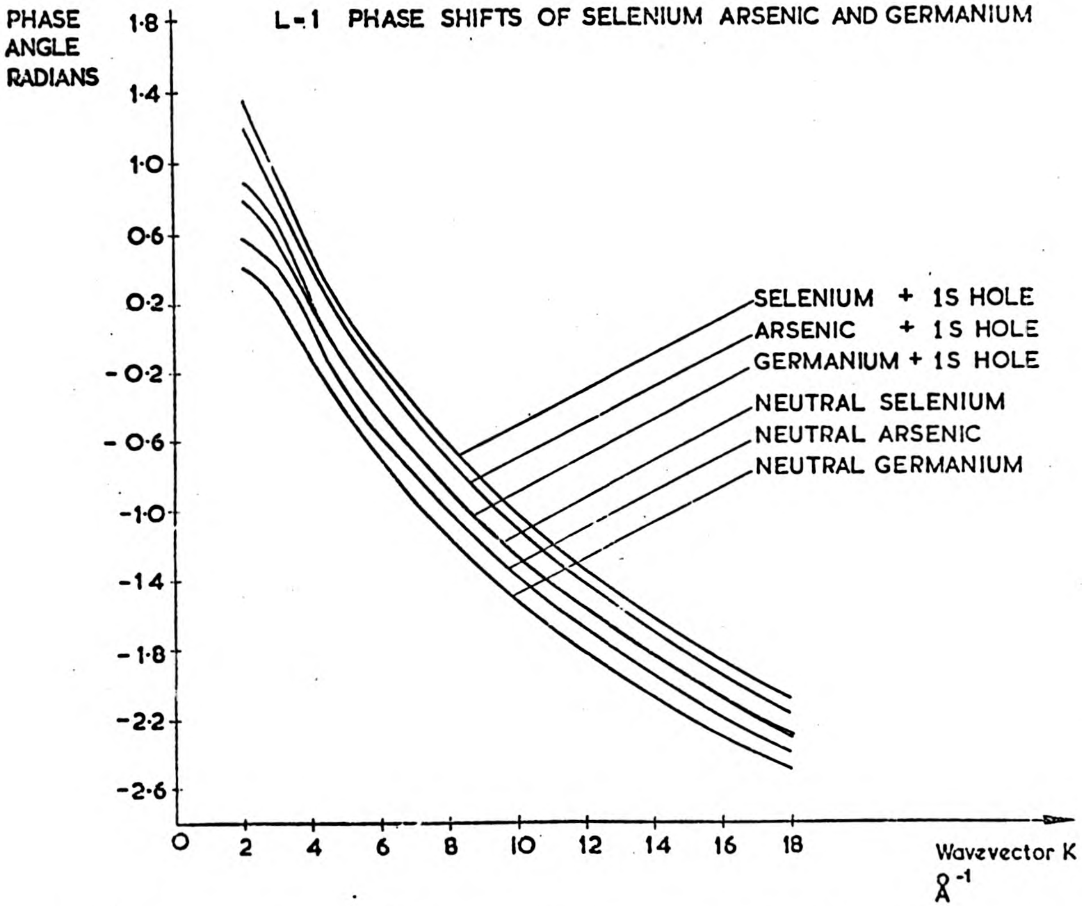

Fig.3.9. The out-going p-wave phase shift η_1 using Hartree-Fock exchange.

3.5 Calculation of the emitting atom phase-shift

If we assume that we are exciting a K-state in the absorption process then the final state must have p symmetry and so the $\ell = 1$ phase-shift δ_1 will be the emitting atom phase-shift which has the symbol η_I. The value of η_I was calculated for the atoms germanium, arsenic and selenium which are of particular interest in chalcogenide glasses and which also have their K-absorption edges accessible to our spectrometer.

One model adopted for the emitter potential was of an atom with a hole in the 1s state. The wavefunctions of the other electrons were assumed to be unchanged. An alternative model to this is to assume that the electrons relax under the influence of the apparent increase in atomic number caused by the absence of an electron in the 1s state. The appropriate wavefunctions are those of the next atom in the periodic table. Thus a fully relaxed arsenic atom will possess a potential similar to that of selenium. In figure 3.9 both the unrelaxed and the neutral atom $\ell = 1$ phase-shifts are given. The most striking feature is that they all possess the same shape and differ by a near constant phase angle. All curves show the same positive curvature, and this is compensated to some extent by the negative curvature of η_{II}, which explains the success of the linear phase-shift approximation equation (2.53) used by Sayers, Lytle and Stern (1971) for germanium. However, from figure 3.9 it can be seen that the linear phase-shift approximation is not, in general, valid.

Just as for the other parameters the values of η_I calculated using the Slater $\rho^{1/3}$ exchange gives the same general behaviour. The difference lies in the magnitude of the phase-shift and not in its energy dependence. These results show an increase of ~ 0.5 radians over the Hartree-Fock values. Remembering that η_I is multiplied by 2 in the sine term of equation (2.47), we note that this will also produce a difference in phase of one radian with respect to the Hartree-Fock values. The combined effect is additive to yield a shift in phase of two radians.

In conclusion, we can note that the phase-shift parameters are sensitive to the type of electro-static potential and/or the exchange expression used. However, the calculations are valid in providing a pointer to the type of experiment in which the interpretation of EXAFS can be most readily obtained. On the basis of the errors in the phases alone, calculated from two approximations, we can expect errors in the phase of the EXAFS signal of two radians. By comparing calculated EXAFS structure with measured structure for materials of known coordination, we can determine which of these approximations gives the best results.

3.6 Environmental sensitivity of the factors $\frac{|f(\pi)|}{k}$, η_I and η_{II} for arsenic

The program which calculates the phase-shifts using the local exchange potential also allows us to make a few comparisons of the factors investigated in this chapter as a function of the environment of the atom.

The phase-shifts for neutral arsenic in a simple cubic lattice with nearest neighbour coordination either oxygen or tellurium atoms at 2.0 and 2.6 Å respectively, provides a test of the type of environmental sensitivity of these parameters.

The factor η_I for arsenic in an oxide lattice shows a reduction over that in the telluride lattice by 0.15 radians at 50 eV, reducing to a constant 0.1 radians at energies in excess of 150 eV. The phase factor η_{II} for arsenic in an oxygen environment is less than that calculated for a tellurium environment by ~ 0.6 radians at 50 eV, but this difference is reduced to 0.3 radians at 150 eV, and eventually becomes approximately constant at 0.2 radians above 400 eV. For the amplitude $\frac{|f(\pi)|}{K}$ the trend of environmental sensitivity at low energies continues with differences reaching about 30% excess for the Te environment at 50 eV, but dropping rapidly to about 4% for energies in excess of 100 eV.

To summarise these results, we find that the effect of each of the phase factors η_I and η_{II} on the phase of the EXAFS parameter $\chi(k)$ will contribute approximately the same amount for high energies, remembering that the emitter phase is multiplied by a factor of two in equation (2.47). In excess of 150 eV we can expect differences in phase of about ½ radian resulting from using environmentally independent phase-shifts. However, these differences are small when compared to the effects of the exchange potential which may well contribute a difference of about two radians.

CHAPTER 4

Apparatus for measuring EXAFS

4.1 General requirements

There have been many reported measurements of X-ray absorption spectra and these fall roughly into two categories. Firstly, high resolution measurements have been made, usually with a double crystal spectrometer, see for example Mott (1963), Shaw (1946), Doran and Stephenson (1957), Beeman and Friedman (1939). However,this type of measurement is usually restricted to energies close to the absorption edge and/or in the statistical accuracy of the magnitude of the absorption fine structure. Secondly, many measurements of absorption have been made using photographic recording. This technique has the advantage of simplicity whilst simultaneously accumulating the spectrum over its entire range, and examples of these measurements can be seen in the work of Cauchois and Mott (1949), Coster and Klamer (1934), Hannawalt (1931), Padalia and Krishnan (1975) amongst many others. The drawback of this technique, however, results from the non-linear response of the films used, both to wavelength and intensity, thus although the positions of maxima and minima in the EXAFS region may be known accurately, the magnitude of the fine structure is not. To obtain a feel for the type of instrument suitable for EXAFS measurements we must consider the size of the structure to be expected and also its fineness.

As a general rule, for scattering atoms with atomic number $Z \sim 30$ then the EXAFS structure contributes a maximum amplitude of 1% per nearest neighbour atom. This accounts for the extensive study of the fine structure of many face centred cubic metals, notably copper, which have twelve nearest neighbours, see Krogstad (1955), Hayasi (1949), Klems, Das and Azaroff (1963), Lytle (1963), Beeman and Friedman (1939), Coster and Veldkamp (1931) and Shiraiwa, Ishimura and Sawada (1958). It should be noted that the magnitude of the EXAFS structure is normalised to the size of the K-abosrption edge for the element under study. The fraction which is contributed by the K-edge of a particular type of atom is dictated by its concentration and by the absorption of other atoms in the material. Thus it is considerably more difficult to measure the arsenic edge in As_2Te_3 rather than in As_2O_3 owing to the Z^4 dependence of the atomic absorption coefficient. Where possible,the absorption thickness product μx was chosen to be greater than one but less than two, although in practice, difficulty in preparing exactly the right thickness of material strongly affects the choice of μx. The upper limit is set by a realistic time for the measurement and also to minimise the distortion of the spectra by the so-called thickness effect (Parratt, Hampstead and Jossem (1957)). For a constant number of counts N for both I and Io the fractional error in μx is given by

$$\Delta\mu x = \sqrt{\frac{2}{N}} \qquad (4.1)$$

and for a total of 10^6 counts this gives $\Delta\mu x = 0.0014$. For the case of Se with two nearest neighbours, the error in the maximum fine structure is ~ 7%, if the change of absorption at the K-edge is ~ 1. It is clear from this calculation that the number of counts collected per point must be ~ 10^6 if the magnitude of the fine structure even for the contributions from the first shell are to be measured accurately. The total counts required thus preclude the use of a high resolution spectrometer and therefore a single crystal spectrometer, whose resolution can be sacrificed for count-rate, is the obvious choice if quantitative measurements are to be made.

The resolution requirement on the other hand can be estimated from typical values. A peak in the EXAFS of $As_2 S_3$ at about 50 eV above the edge has a full width at half maximum of 14 eV, but the periodicity increases as one goes to higher energies; further, the frequency is mainly dominated by the $2kR_j$ factor in the sine term equation 2.46, and thus the EXAFS is finer for $AS_2 Te_3$ than for $As_2 O_3$. Note however that this periodicity relates to nearest neighbours only, and a correspondingly higher resolution is required for information from shells with a larger radius.

The general features of X-ray spectrometers have been reviewed by Compton and Alison (1935) and Sandstrom (1957). Single crystal instruments have been described specifically to measure EXAFS from a conventional source by Nagasima (1966), White and McKinstry (1966), Klems, Das and Azaroff (1963) and Nordstrand (1960), however, the best experimental results obtained with this type of equipment have been those of Lytle (1965) and Lytle, Sayers and Stern (1975). The instrument described here is very similar to the instrument described in the previous two references.

A single crystal spectrometer has many features in common with a diffractometer. The performance of the latter instrument has been extensively discussed by Klug and Alexander (1974) and Wilson (1970). Thus many of the ideas, particularly concerning the resolution of diffractometers, can be adapted for the case of a single crystal spectrometer. The following sections outline the important parts of the apparatus with particular reference to the attainment of maximum intensity, adequate resolution, and reliability, within the confines of performing the experiments in a realistic time.

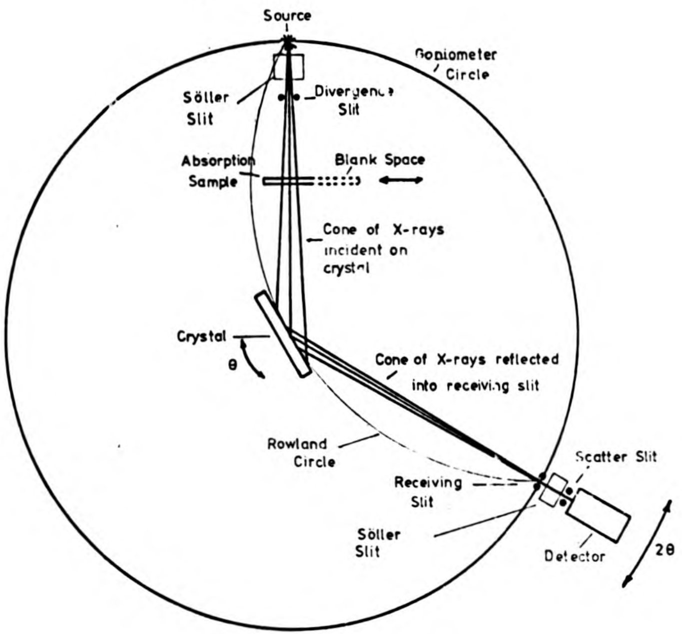

SCHEMATIC DIAGRAM SHOWING THE
GEOMETRY OF THE SPECTROMETER

Fig.4.1. General Layout of the X-ray Spectrometer.

4.2 General Layout of the Apparatus

Fig. 4.1 shows the general geometry of the EXAFS spectrometer. A source of X-rays illuminates a crystal which is mounted on a horizontal goniometer (Phillips 1380). The horizontal cone of X-rays incident on the crystal is limited by a divergence slit which was chosen to be ½°. The effect of this slit is merely to limit the background scattered radiation. The vertical divergence of the X-rays is controlled by Söller Slits, such that only radiation subtending an angle of less than ± 2° from the horizontal was allowed to pass. Radiation, having a vertical component, will be incident on the crystal at an angle differing slightly from the Bragg angle, subtended by a horizontal ray. This discrepancy s between the true and apparent Bragg angle for the ray, is given in terms of the angle ψ that the beam makes with the horizontal plane by

$$s = \frac{1}{2}\psi^2 \tan\theta \qquad (4.2)$$

where θ is the Bragg angle (Thomsen (1974)). Now considering the flux transmitted by the Söller Slits and received by the receiving slit for a beam with vertical component ψ, yields an expression for the line profile distortion produced by vertical divergence given by

$$\begin{aligned} g(\varepsilon) &= \left(1 - (\varepsilon/\tan\theta\delta^2)^{\frac{1}{2}}\right)\left(1 - (\varepsilon/\tan\theta\delta^{*2})^{\frac{1}{2}}\right) && 0 < \varepsilon < \varepsilon \text{ max} \\ &= 0 && 0 > \varepsilon > \varepsilon \text{ max} \end{aligned} \qquad (4.3)$$

$\delta = \tan^{-1}(\ell/L)$ where ℓ and L are the Söller Slit width and length respectively.

$\delta^* = h/2R$ where h = source and receiving slit height assumed to be equal and R is the goniometer radius.

$\varepsilon_{max} = \delta^2_{min} \tan\theta$ where δ_{min} is the lesser of δ and δ^* and ε and δ's are expressed in radians. ε is a variable in 2θ space.

Having undergone Bragg reflection at the crystal, the X-rays pass through a receiving slit which for this study was of width W_2 = 50 μr. This in turn produces a distortion to the spectrum given simply by

$$\begin{aligned} g(\varepsilon) &= 1 \qquad -\varepsilon_m < \varepsilon < \varepsilon_m \\ &= 0 \qquad -\varepsilon > \varepsilon > \varepsilon_m \end{aligned} \tag{4.4}$$

where $\varepsilon_m = \frac{W_2}{2R}$ radians.

The X-rays then pass through a scatter slit to the detector. Given the geometry of figure 4.1,it is always possible to draw a circle through the crystal axis, source and receiving slit,such that the flat crystal surface will always be tangential to the circle. If a mosaic crystal surface were curved to the radius of this circle, then any ray from the source would be brought to a focus at the receiving slit. This circle is called a parafocusing circle. However, because the crystal is flat, a perfect focus is not obtained, and thus this will introduce an aberration into the measured line shape, Klug and Alexander (1974).

$$\begin{aligned} g_{\text{flat crystal}}(\varepsilon) &= |\varepsilon|^{-\frac{1}{2}} \qquad 0 > \varepsilon > \varepsilon_m \\ &= 0 \qquad 0 < \varepsilon < \varepsilon_m \end{aligned} \tag{4.5}$$

where $\varepsilon_m = -\frac{\xi^2 \cot\theta}{114.6}$.

ε_m and ξ are in degrees, ξ is the angle of horizontal divergence, and for a spectrometer ξ is the lesser of either a) the horizontal divergence defined by the crystal or b) defined by the scatter or divergence slits.

From figure 4.1 it can be seen that the sample is positioned between the source and the crystal. Alternatively, the sample could have been placed after the crystal and this would considerably reduce the flux hitting the specimen, and thus lessen the possibility of creating radiation damage. The latter arrangement suffers two drawbacks. Firstly, the complexity of the sample moving device increases as it also has to scan with 2θ, and secondly, the detector is not shielded from fluorescent radiation from the specimen.

Both the goniometer and source were positioned on a steel plate to minimise relative movements between the two with temperature, and the entire system was surrounded by lead sheets for radiation shielding.

4.3 The X-ray Source

The X-ray source is required to produce a continuous distribution of X-ray intensity of the spectral range of interest. This can be achieved by using the bremsstrahlung radiation which is produced when electrons are decelerated as they hit a target. Alternatively, there is a new source of continuous X-ray flux available from a synchrotron in which the electrons are accelerated in a circular path and produce a continuous spectrum of radiation which results from relativistic effects. The essential point about this source is that the intensity may be greater than 10^6 times larger than a conventional source. For details of the properties of this source, the reader is referred to Codling (1973). Examples of spectra taken with synchrotron radiation can be seen in Chapter 5.

The source used principally in this study was a standard 1 kW X-ray tube. The properties of continuous radiation from this type of source have been reviewed by Stephenson (1957). The bremsstrahlung is partially polarised ~ 10% for wavelengths $3/2\ \lambda_c$ or longer (λ_c is the shortest wavelength excited), however the polarisation can become much stronger for $\lambda \approx \lambda_c$. It was found experimentally that the intensity of bremsstrahlung emission at 1Å taken at an angle of 3° from the surface varied roughly as $(V - V_c)^{\frac{1}{2}}$ which is a milder dependence on voltage than the total integrated intensity which has been reported to vary as ZV^2 (Stephenson 1957). The characteristic radiation, which is undesirable as it requires detectors which have a linear response over a large dynamic range, varies in intensity as $(V - V_c)^{3/2}$. It is interesting to note here, that the conventional X-ray tube uses the projection of the focal spot at a shallow angle to produce an effective fine image. However, the use for most

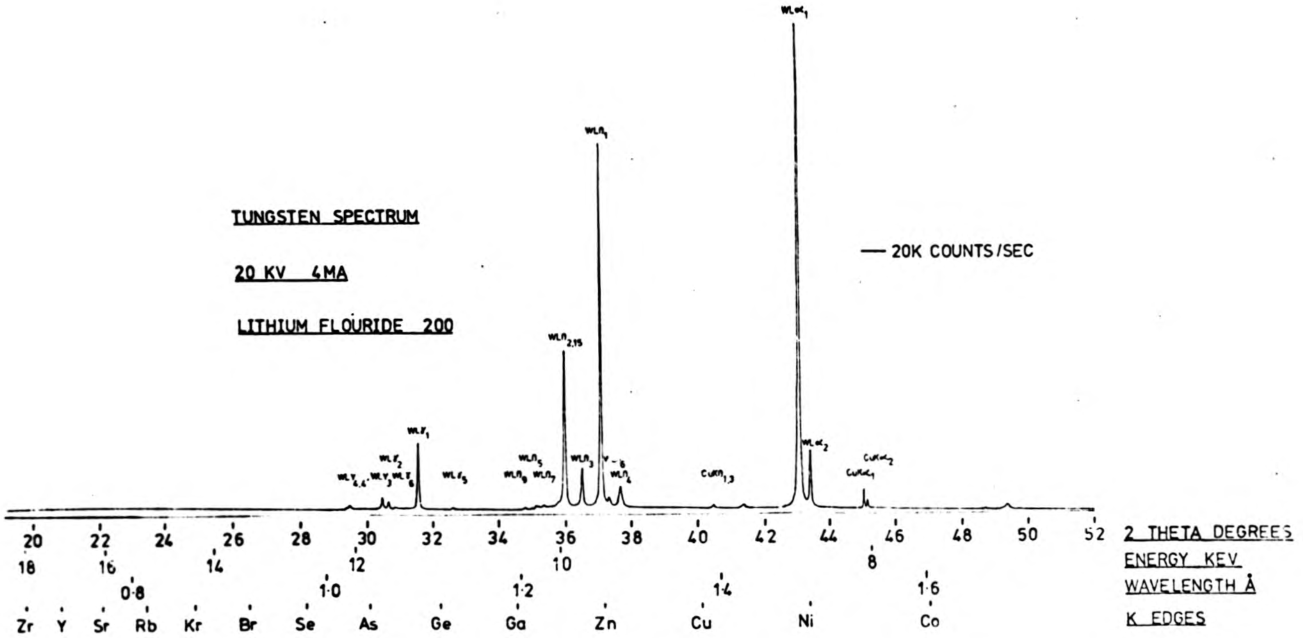

Fig.4.2. The emission spectrum from the tungsten tube including the elements covered by the spectrometer

diffraction tubes is in the production of characteristic radiation and this has been found to peak at 90° to the target by Green (1964). Thus if, for the present study, the characteristic radiation is regarded as noise and the continuous radiation as signal, then the conditions for the best signal-to-noise ratio are fulfilled when a small take-off angle is used. Note that the opposite is the case if the source is used in diffractometry.

The dependence of emission varies linearly with Z and so a high atomic weight material should be used for the target, and in this case it was chosen to be tungsten (Z = 74). The focal spot size was 1 × 10 mm, and this, viewed at an angle of 3° from the surface, gives an effective source size $W_1 = 50\ \mu m$. The effect of a broad source produces an aberration (Klug and Alexander (1974)) given by

$$g_{source}(\varepsilon) = \exp\left(-\frac{\varepsilon^2}{1.41\ S^2}\right) \qquad (4.6)$$

where $s = \dfrac{28.65 \times W_1}{R}$.

The spectrum produced by the tungsten tube is shown in fig. 4.2. This figure illustrates the relative intensity of emission lines and bremsstrahlung and also spans the effective range of the spectrometer with an indication of the atoms that can be studied in this range.

The tube was driven by an Elliot GX1 power supply, which provides current up to 40 mA and a potential up to 100 kV although the X-ray tubes are only rated for 60 kV. The generator has both current and voltage stabilisation. Tests on the stabilisation of the equipment showed that variations of intensity over a period of 600 seconds, which is the largest time required for both I and Io measurements were much smaller than the statistical noise, although larger variations in the intensity were noted over periods of a day.

4.4 The Diffracting Crystal

The choice of diffracting crystal is governed, as in many spectroscopy experiments, by the requirements of maximum intensity with maximum resolution. Crystals have been studied in relation to their use for monochromators for X-ray diffraction, X-ray fluorescence spectroscopy, where the maximum intensity is usually the dominant criterion, and for X-ray spectroscopy which has usually been concerned with fine detail in emission and absorption spectra. Corresponding to these two major uses of X-ray crystals, their properties have been reviewed with different criteria in mind. Bertin (1970) and Klug and Alexander (1974) list crystals suitable for high intensity, and Thomsen (1974) is concerned with crystals more appropriate to high resolution studies. It has been known for a long time that the X-ray properties of crystals can be altered by grinding or polishing their surface, see for example Bragg, James and Bosanquet (1921). Vierling, Gilfrich and Birks (1969) and also Lytle (1969) have shown how the properties of LiF can be changed from a nearly perfect crystal for a good quality cleaved specimen, to an almost imperfect crystal when the surface has been ground. The resolution of the spectrometer is not governed solely by the quality of the crystal. As a conventional X-ray tube emits radiation over a distribution of horizontal angles, there are large gains to be made by using an imperfect crystal, owing to the fact that the integrated reflectivity of an imperfect crystal may be more than one order of magnitude greater than its perfect counterpart (Warren (1969)). For an ideally imperfect crystal, monochromatic X-rays incident on the surface of the crystal will be brought to a focus (parafocus) at the receiving slit. At first sight therefore, it appears that most of the radiation incident on the crystal could be used, provided the crystal was in fact a powder with preferred orientation to match the divergence of the incident beam. On the other hand, a perfect crystal will accept from a point source, a horizontal angular aperture of X-rays which can be calculated from the Darwin equation for a perfect crystal reflection profile (Warren (1969))

$$\Delta 2\theta_{\text{perfect}} = 2.12 \left(\frac{e^2}{mc^2}\right) \frac{N \lambda^2 |F|}{\pi \sin(2\theta)} \quad 2\left(\frac{1 + |\cos 2\theta|}{2}\right) \qquad (4.7)$$

$\Delta 2\theta$ is also twice the width of the so-called "rocking curve" which is the response of a crystal reflection to a single wavelength of X-rays as it is rotated through the Bragg angle. For the case of LiF at 1Å this equation yields $\Delta 2\theta = 2.26 \times 10^{-3\circ}$. This shows that the angular acceptance of a perfect crystal is very restrictive.

An examination of Klug and Alexander's analysis of the diffractometer shows that the resolution performance of an imperfect crystal can be assessed by its linear attenuation coefficient μ. For an ideally imperfect crystal μ is dictated for most materials by the photo-ionisation cross-section. The situation for a perfect crystal is entirely different, because here μ is dominated by strong dynamical scattering. The reflected beam from a layer of atoms suffers a 90° phase shift and so a doubly reflected beam travels in the same direction as the incident beam but with a 180° phase shift, thus weakening the intensity of the primary beam. Thus by choosing a perfect crystal, one is enhancing the attenuation of the beam and minimising the crystal penetration distortion. The apparent linear attenuation coefficient for a perfect crystal has been given by Warren (1969) as:-

$$\mu_{app} = \frac{\pi}{2}\left(\frac{e^2}{mc^2}\right) N \lambda |F| \qquad (4.8)$$

F is the structure factor, N is the number of unit cells per unit volume, and the other symbols have their usual meaning. For LiF with $\lambda = 1.098$Å ($WL\gamma_1$), $\mu_{app} = 233$ mm^{-1} and the penetration depth of the crystal is ~ 4.5 µm. The linear attenuation coefficient, nelgecting scattering, can be calculated from the Victoreen coefficients (International Tables for X-ray Crystallography, Vol. III (1962)) and yields a value for an imperfect crystal of 1.19 mm^{-1} i.e. a depth of 840 µm. The line profile distortion by crystal penetration is given by Klug and Alexander (1974) as

$$g(\varepsilon) = \exp\left(\frac{4\mu R \sin 2\theta\ \varepsilon}{114.6}\right) \qquad -\infty < \varepsilon < 0$$

$$= 0 \qquad \varepsilon > 0$$

where θ is the Bragg angle and ε is in $^\circ 2\theta$. This equation yields for the half width in the perfect crystal case, a value of $\Delta 2\theta = 1.4 \times 10^{-3\circ}$ and for the imperfect case $\Delta 2\theta = 0.26^\circ$. If we compare these figures with a typical value of $\Delta 2\theta$ from a receiving slit i.e. $\Delta 2\theta = 1.6 \times 10^{-2\circ}$, then it is clear that an ideally imperfect crystal would sacrifice a lot of resolution, but there is an opportunity to increase the angular acceptance of the crystal from its perfect crystal value as long as extinction effects are still sufficient to maintain μ_{app} to about one order of magnitude greater than for the imperfect case.

Five crystals were tested and the width of the $WL\gamma_1$ line was recorded for each. Three of the crystals were abraded, LiF 200, LiF 220 and Si 111, which, whilst giving a high intensity,also yielded very broad profiles. The other two were both cleaved LiF 200 specimens, free of steps on the surface. The first crystal of unknown origin produced a very asymmetric pattern with a long tail extending to small angles, and it follows from equation 4.9 that this specimen was exhibiting little extinction. The second cleaved LiF crystal was trepanned from the centre of a boule by Nuclear and Silica Products. This crystal produced a sharp, slightly asymmetric profile for $WL\gamma_1$ and as the intensity from the crystal was ~ 3000 counts/sec for the bremsstrahlung at 1Å this crystal was adopted for the absorption studies without any attempt at changing its characteristics. The attenuation and diffraction profile of this crystal are treated in the section on resolution.

It became quite clear from an early stage that the normal mounting post of a diffractometer was inadequate for the type of precision required here, and so a special crystal holder was built. The crystal was held by three screws in an L shape configuration which had three adjustable tension pins facing the screws. The L shaped geometry allowed independent adjustment of the tilt and Bragg angle, and in conjunction with the θ drive, could translate the face of the crystal to the axis of the goniometer. The entire crystal mounting could be removed from the goniometer, if necessary for alignment checks, without the need for readjustment.

4.5 The Detection System

The requirements of a detection system are

1) The efficiency of the detector should be as high as possible

2) The detector should respond linearly with count rate

3) Pulse height discrimination

The efficiency of thallium activated NaI scintillators are > 90% for X-rays in the region 1Å. Proportional counters, on the other hand, have efficiencies ~ 50% although, to counteract this, the speed, pulse height discrimination and noise characteristics of this detector are slightly superior to the scintillator. On balance, however, it was considered that the scintillator was the best detector for this type of measurement.

The detection system consisted of a Phillips PW 1964/30 scintillation detector coupled into the main amplifier, followed by a single channel analyser.

The response of a system described above is, in general, non-linear with count-rate i.e. the number of pulses counted is not directly proportional to the number of photons reaching the detector. In Geiger Müller detectors this phenomenon is associated with a dead-time for the detector itself, however, with scintillation counters, the phenomenon is ascribed to the behaviour of the entire detection system, rather than just the detector. Statistical fluctuations in the operating point of the preamplifier and amplifier system, together with the finite pulse time of the scintillator

(~ 200 ns), cause changes in the distribution of pulse-heights such that the number of pulses falling within the entrance window of the single channel analyser changes with count-rate. Thus the form of the response of the detecting system is complex and in general not known. The detector non-linearity manifests itself in absorption measurements, by causing a dip in the absorption curve as the spectrum is swept across a peak in the incident intensity. The following paragraphs describe the implementation of an appropriate correction formula consistent with the accuracy of the experiment.

The method used is essentially that of Short (1960) which has been simplified by Burbank (1961). The technique is simply to use a single absorbing foil and to measure the ratio of incident to transmitted beam intensity for a range of count-rates, and this method is clearly very suitable for this type of equipment as the absorption measurements can be made automatically. Following Burbank (1961) we note that

$$I_1 + I_1^{loss} = (I_0 + I_0^{loss})R_c \tag{4.10}$$

where I_0 and I_1 are the incident and transmitted intensities and I_0^{loss}, I_1^{loss} their corresponding losses as both the incident and transmitted intensities will be expected to suffer losses. R_c is the constant value of $\frac{I_0}{I_1}$ obtained if there was no loss. Similarly, a set of equations can be defined

$$\begin{aligned} I_1 &= R_1 I_0 \\ I_2 &= R_2 I_1 \\ I_n &= R_n I_{n-1} \\ I_{n+1} &= R_c I_n \end{aligned} \tag{4.11}$$

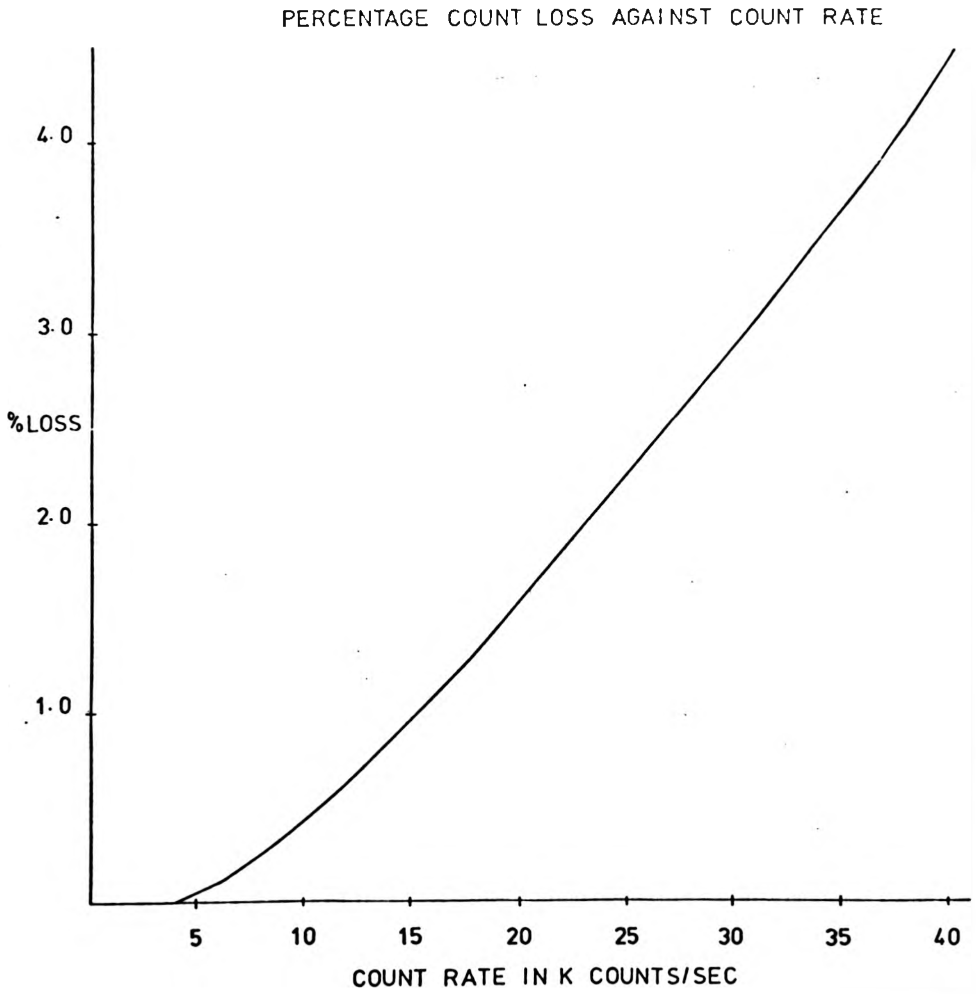

Fig.4.3. Percentage count loss against count rate for the scintillator detector.

where I_{n+1} and I_n both lie in the linear region of detector response. Thus the percentage count loss is given from (4.10) and (4.11) as

$$\frac{I_0^{\text{loss }\%}}{I_0} = \frac{R_n\,R_{n-1}\cdots\cdots R_2\,R_1}{R_c^{\,n}} \times 100\ \% \qquad (4.12)$$

The apparatus was set up exactly as it was to be used for absorption measurements. The detector was set at an angle such as to receive WL_{γ_1} radiation as this was the largest emission line close to the arsenic absorption edge. The single foil absorber was a sheet of aluminium which gave a value of $R_c = 1.47689 \pm 0.0004$. Thirty-three points were taken of the value of R over the full range of count-rates (0.3 → 40 K counts/sec), each point was a mean of roughly 50 readings each measuring a total of 10^5 counts. The count-rate was varied by placing aluminium foils between the crystal and detector. It was found that the response of the detector was linear up to 4 K counts per second. The plot of R against I_0 was smoothed graphically and the values of $\frac{I_0\text{ loss}}{I_0}$ were calculated using (3). For computational purposes a least squares fit to a polynomial of the experimental points was obtained using the NAG routine EO2ABA

$$P(x) = 87.10^{-3} + 3.544.10^{-2}\,x + 6.564.10^{-3}\,x^2 - 2.012.10^{-4}\,x^3 + 2.43.10^{-6}\,x^4$$

$$x = (I - 4.0) \text{ where I is measured in K counts.} \qquad (4.13)$$

Fig. (4.3) shows the percentage loss against count-rate. The total statistical accuracy of the absorption measurements was ~ 0.1% and thus the error in the correction which is 4% maximum of the total counts needs to be in error by less than 3%, and this is well within the accuracy of this correction procedure which is estimated to be in error by 1%.

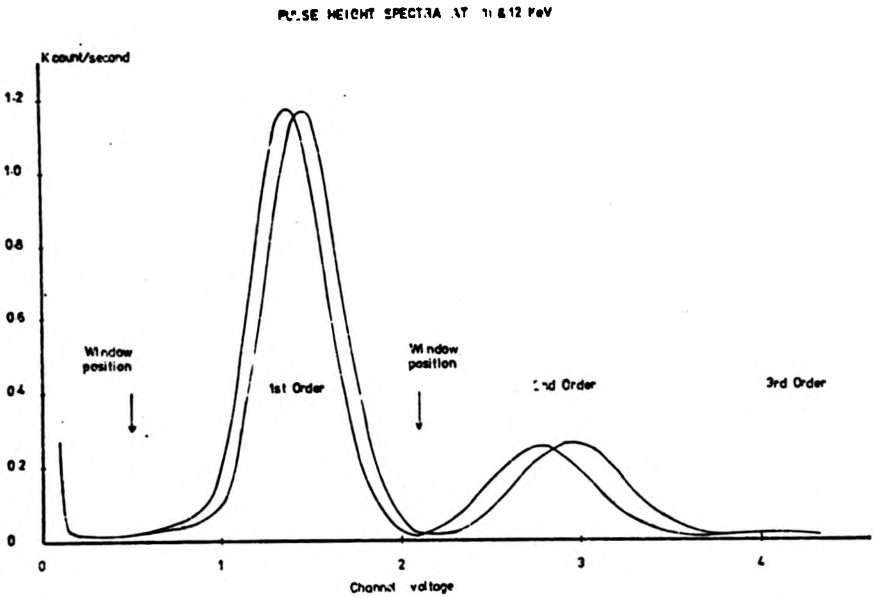

Fig.4.4. Pulse height analysis of scintillator detector.

The detector loss compares favourably with Burbank's (1961) results whose loss at 40 K counts/sec was roughly double that found with this detector. This determination of non-linearity also afforded an ideal opportunity to examine the data for other forms of random error, apart from those associated with randomly arriving signals. For each of the intensities examined, the standard deviation in the value of R was calculated. These were found not to deviate with any statistical significance from a value computed from the formula

$$\frac{S_R}{R} = \sqrt{\frac{2}{N}} \qquad (4.14)$$

where S_R is the error in R and N is the number of counts for both I and I_o. Thus errors may be confidently assigned to absorption measurements based purely on the errors associated with randomly arriving signals.

Together with the ability of the detector to behave linearly, it is required to perform some pulse height discrimination so that second and higher order components can be removed from the X-ray beam. Pulse height analysis from the detector at the beginning and the end of a scan are shown in fig. 4.4. Given that the windows were positioned as shown in the diagram, it can be seen that the 2nd order component is not completely discriminated against. As a result of this,the X-ray tube voltage was adjusted such that 2nd order components were not generated. The sacrifice was not great however,as the X-ray tube was operating at 900 W rather than 1 kW.

4.6 Alignment of the Spectrometer

The initial alignment of the spectrometer can be accomplished by following the alignment procedure specified in the instructions on the PW 1380 goniometer. These adjustments leave the goniometer at the same height as the source with, the axis of the goniometer and source vertical. The illumination of the axis of the goniometer is only approximately correct, but this can be refined by measuring the angle subtended

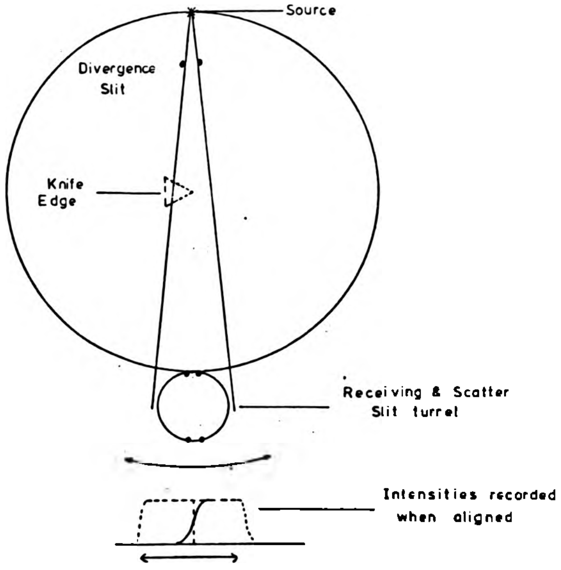

Fig 4.6 The Alignment of the Spectrometer

by the source. A knife edge is then inserted such that the edge is coincident with the axis of the goniometer. The position of the centre of the shadow cast by the knife edge is noted. The knife edge is removed and the counter is placed at this angle and the turret containing the receiving and scatter slits is then rotated for maximum intensity. The goniometer is then moved such as to place the shadow closer to the centre of the illuminated area. The process is then repeated iteratively until the X-rays uniformly illuminate the axis of the goniometer. This then defines the position of zero degrees 2θ. Following this,the crystal is placed in the beam and its surface is adjusted to lie parallel to the goniometer axis. This is achieved by placing a large angle divergence slit in the beam, and removing the scatter slit. The θ drive was operated so that the detector received flux at some angle θ. The θ and 2θ drives were then locked and the profile of the $WL\gamma_1$ line was then recorded. An adjustment was then made to one of the L-shaped configuration screws of the crystal holder which controlled the vertical alignment. The process was repeated until the observed profile had a minimum width. From the sensitivity of the method it is estimated that the crystal surface was aligned parallel to the beam to within 0.1°. This adjustment fixes the axis parallel,but not coincident with the face of the crystal. To achieve coincidence,the divergence and scatter slits were changed to narrow width 50 μm which defined a fine pencil of beam both hitting and taken from the crystal. By the manipulation of one of the screws of the crystal holder and the θ drive,the crystal could be translated to the centre of the goniometer. The estimated accuracy of this procedure was that the crystal was coincident with the axis of the goniometer to within 4 μm. It should be noted that the removal of the very narrow divergence and scatter slits only resulted in an increase of intensity of 20% and thus we can conclude that the rocking curve half width of the crystal was ~ 0.03° and this controls the horizontal beam divergence ξ used in equation 4.5.

Finally, a specimen could easily be positioned accurately in the beam by lining up the divergence slit and the F-centre yellowing of the LiF crystal with the desired portion of the sample.

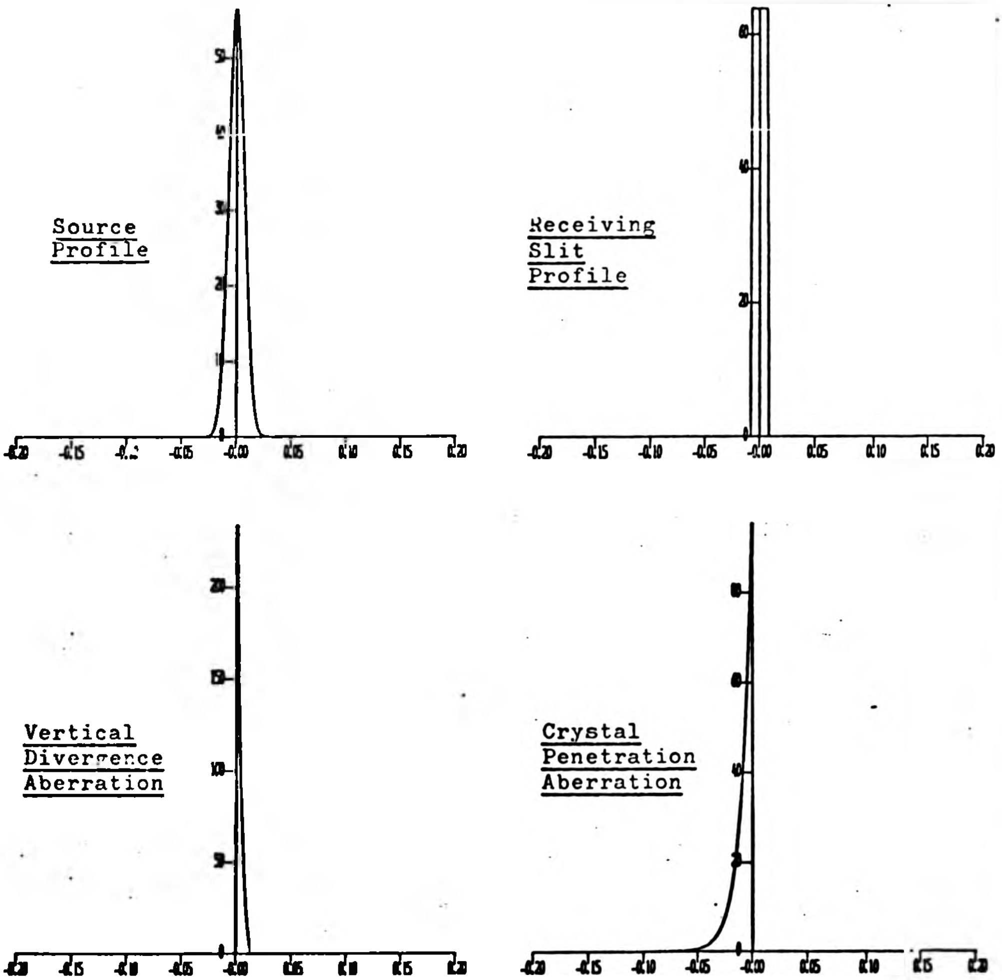

Source Profile

Receiving Slit Profile

Vertical Divergence Aberration

Crystal Penetration Aberration

Fig.4.6a. Aberration contributions to the resolution of the Spectrometer.

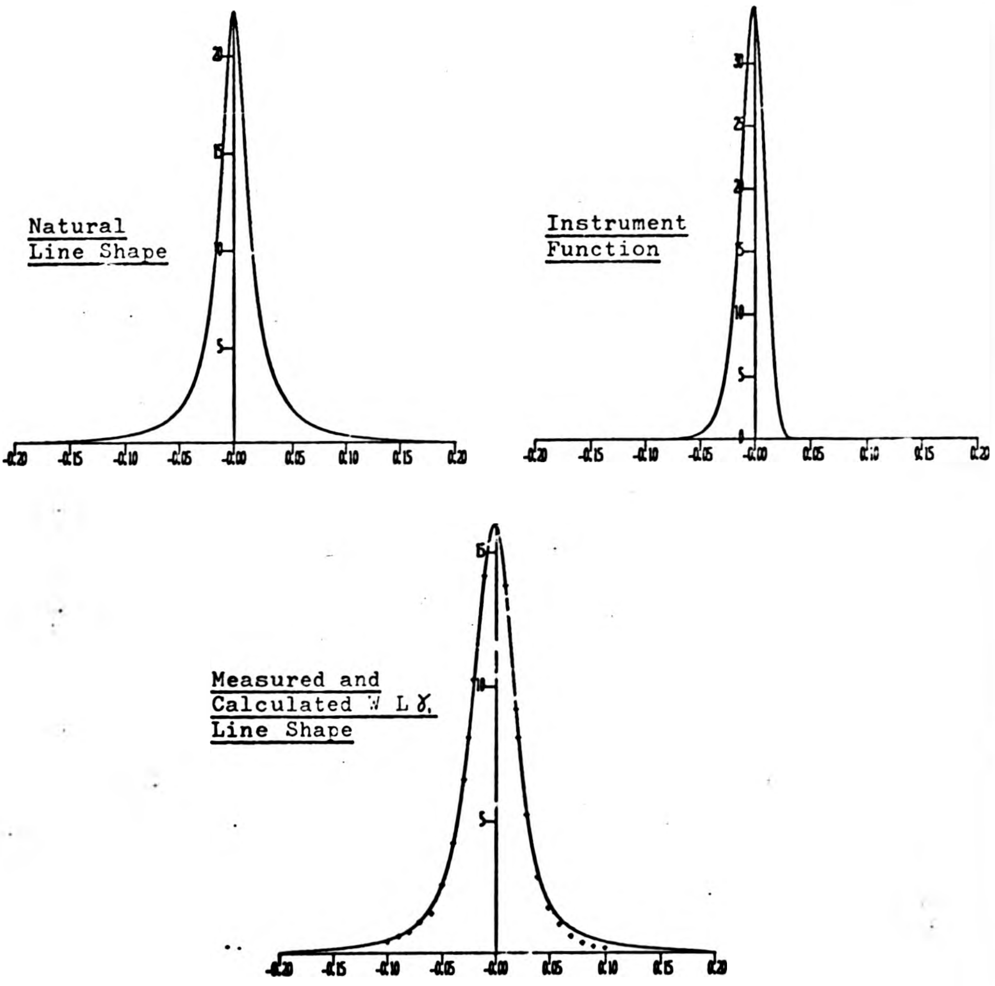

Fig.4.6b. Aberration contributions to the resolution of the Spectrometer.

4.7 Spectrometer Resolution

This section describes the synthesis of the measured WLγ_1 emission line from the aberration functions introduced in the previous sections, and the natural profile of this line (full width at half maximum = 10.4 eV).

Suppose we have a line profile s(y), an aberration function g(ε) and a final line shape h(z). Now h(z) will be a superposition of all the weighted aberrations from each element of s(y) such that

$$d\,h(z) = s(y)\,dy\,g(\varepsilon) \qquad (4.15)$$

where ε is measured from y such that

$$z = y + \varepsilon \qquad (4.16)$$

$$\therefore \quad h(z) = \int_{-\infty}^{+\infty} s(y)\,g(z-y)\,dy \qquad (4.17)$$

This is the convolution integral. By repeated application of this formula, inserting the aberration functions in turn, the final instrument function can be obtained and this gives an accurate measure of the distortion of the spectra recorded. Owing to the small horizontal divergence collected by the crystal, it was concluded that this aberration will not contribute significantly to the total width and hence this convolution was omitted.

The individual contributions to the total instrument function are shown in fig. 4.6 and the formulae and constants used are collected in table 4.1. The only unknown is the apparent linear attenuation of the crystal which has been adjusted for a best fit. The value found was 9.0 ± 0.5 mm^{-1}, an intermediate value between the perfect and ideally imperfect case. The agreement between theory and experiment is surprisingly good, especially in view of the accuracy to which some of the parameters are known. The final calculated instrument function should, however, correspond closely to the true function. This function is slightly asymmetric with a full'width at half maximum of $2.60 \times 10^{-2\circ}$ 2θ. This value yields a resolution r given by

$$r = \left|\frac{\tan\theta}{\Delta\theta}\right| = \left|\frac{E}{\Delta E}\right| \qquad (4.18)$$

or $r = 1100$ and in terms of energy, the resolution is ~ 10 eV at the $\text{WL}\gamma_1$ line.

Table 4.1 Aberration Constants

Constants defined as:-

Z = Conversion factor which converts ° to radians = 57.3/rad.

γ = Vertical divergence angle = 2°.

h = Source and receiving slit height ~ 10 mm.

R = Goniometer radius in mm's = 173 mm.

W_1 = Apparent source width mm = 50×10^{-3} mm.

W_2 = Receiving slit width mm = 50×10^{-3} mm.

ξ = Horizontal beam divergence degrees = 0.03°.

θ = Bragg angle in degrees = 15.828°.

μ = Linear attenuation coefficient mm^{-1} = 9 mm^{-1}.

E = Energy of the emission line ($WL\gamma_1$) = 11285.9 eV.

ΔE = Full width at half maximum of natural line = 10.4 eV.

With this set of constants a subsidiary set of constants can be defined

$\delta = \tan\left(\frac{\gamma}{z}\right)$ $\delta^* = \frac{h}{2R}$ δ_{min} = smaller of δ and δ^*

$C_1 = \frac{zW_1}{2R}$ $C_2 = \frac{zW_2}{2R}$ $C_3 = -\frac{\xi^2}{2\tan(\theta/Z)z}$

$C_4 = \frac{1}{\delta\sqrt{z\tan(\theta/Z)}}$ $C_5 = \frac{1}{\delta^*\sqrt{z\tan(\theta/Z)}}$ $C_6 = z\delta^2_{min}\tan\left(\frac{\theta}{Z}\right)$

$C_7 = \frac{4\mu R}{2z\sin\left(\frac{2\theta}{Z}\right)}$ $C_8 = \frac{E}{\tan\left(\frac{\theta}{Z}\right)\Delta E}$

Source Profile $g(\varepsilon) = \exp - \frac{\varepsilon^2}{1.4\,C_1{}^2}$

Receiving Slit $g(\varepsilon) = 1 \quad |\varepsilon| < C_2$

$= 0 \quad |\varepsilon| > C_2$

Flat Crystal $g(\varepsilon) = |\varepsilon|^{-\frac{1}{2}} \quad C_3 < \varepsilon < 0$

$= 0 \quad C_3 > \varepsilon > 0$

Vertical Divergence $g(\varepsilon) = (1 - |\varepsilon|^{\frac{1}{2}}.C_4)(1 - |\varepsilon|^{\frac{1}{2}}C_5) \quad 0 < \varepsilon < C_6$

$= 0 \quad 0 > \varepsilon > C_6$

Crystal Transparency $g(\varepsilon) = \exp(C_7\,\varepsilon) \quad \varepsilon < 0$

Natural Line Shape $g(\varepsilon) = \frac{1}{1 + C_9{}^2\,\varepsilon^2}$

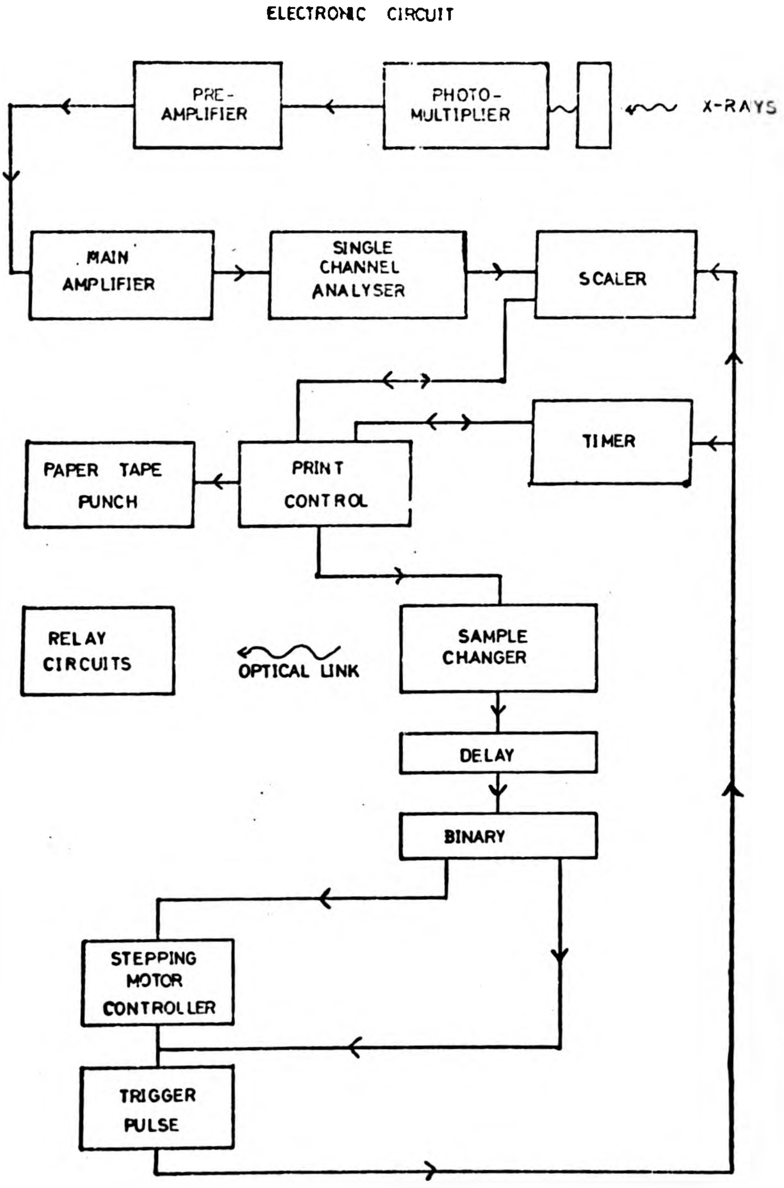

Fig.4.7. The Electronic System.

4.8 Electronic System

A schematic diagram of the electronic system is shown in fig. 4.7. The detector has been discussed in a previous section. This feeds pulses into the main amplifier which a) amplifies the pulses and b) shapes the pulses from a sawtooth form to a near gaussian shape. The time constant for pulse shaping is 200 ns and this results in a gaussian pulse shape with full width at half maximum of ~ 600 ns. After analysis by the single channel analyser, the pulses were counted with a six-digit scaler. The time was recorded by a 5-digit timer, counting in units of 10^{-3} seconds. When a preset number of counts had been reached, both the scaler and timer were interrogated by the print control unit which punched the data onto paper-tape. From the print control unit a gate was set which operated a light emitting diode. This signalled to a set of mains operated relays which controlled the sample changer. A delay was initiated from the gate to allow the sample changer to operate ~ 6s. Following this, a binary was switched,which alternatively activated the stepping motor or by-passed it. The two alternatives correspond to measurement of the transmitted and incident intensities for each new energy of the X-rays. The cycle, once initiated, continues until the stepping motor is inhibited by a micro-switch indicating that the desired final energy of the spectrum has been reached.

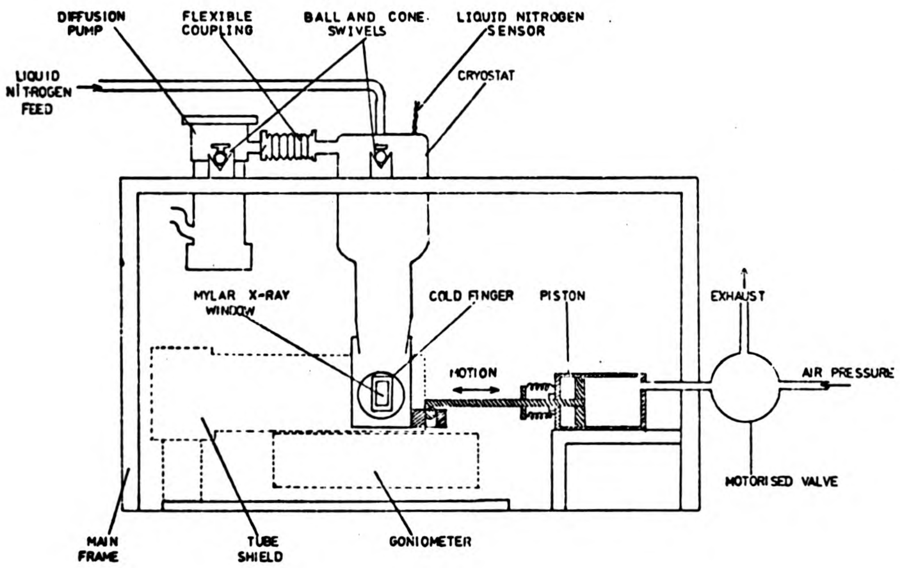

Fig.4.8. Sample Changer Layout.

4.9 The Specimen Chamber

The requirements of a sample changer are that it can sustain the sample at liquid N_2 temperature and is able to move the sample in and out of the X-ray beam reproducibly. The general diagram of the specimen chamber is seen in fig. 4.8. To facilitate movement of the specimen, the cryostat was rocked through a small angle ($\sim 1^{\circ}$). The sample was placed over half of a cold finger, the other half was left blank for the I_0 measurement. The glass dewar was continuously pumped by a diffusion pump which was also allowed to rock, with the cryostat. In turn, the diffusion pump was backed from a rotary pump which had its vibrations decoupled from the diffusion pump by a long flexible vacuum pipe (~ 4 ft.). Sample positioning for I and I_0 measurements was carried out by pushing and pulling on the cryostat with a pneumatic piston driven by a motorised valve. The piston was rigidly attached to a frame which carried the dewar mountings. Originally the dewar was rocked by a device attached to the goniometer, this however produced features in the absorption coefficient proportional to the derivative of the incident intensity. The origin of this effect came from tiny movements of the goniometer (~ 1 μm) which had to transmit the force for rocking the cryostat between I and I_0 measurements. This small movement was easily detected in the absorption owing to the sharpness of the emission lines.

A light-activated switch detected the output of the l.e.d. from the sequencing electronics (see previous section). This signal was amplified and then used to operate the mains relay, which controls the direction in which the motorised valve turned. It was necessary to decouple the counting electronics from the mains switching circuit as it was found that the transients accompanying the relay switching could interfere with the TTL logic of the electronic circuits and upset the sequence of measurements.

The dewar capacity was ~ 3 L and with the pressure in the dewar $<10^{-5}$ torr the nitrogen could last about 12 hours between fillings. However,it was noticed that the position of the cold finger in the dewar was liable to move as the dewar cooled down. Indeed, this movement was visible. To stabilise this movement, the level in the dewar was automatically filled and so the level of nigrogen was maintained ± 2 cms. A further hazard resulted from condensation of water on the 25 μm thick mylar window of the dewar during very humid days. This was eliminated by constantly operating a fan onto the window.

4.10 General Performance of the Apparatus

Measurements of spectra were taken by measuring the incident and transmitted beam approximately every two eV. A total of 10^5 counts were collected for each of the data points which numbered about 800. The time taken for each run of the spectrum varied between one and three days. To improve the statistics of the experiment, several runs were averaged together. The longest time taken to record a spectrum was three-and-a-half weeks, for the $As_2 Te_3$ crystal.

From the higher resolution synchrotron spectrum of $As_2 Te_3$ shown later, it is found that this material exhibits a strong 'white line' at the arsenic edge, which is ~ 2 eV wide. Thus by examining this feature measured by the conventional apparatus, it can be seen to be ~ 10 eV wide, in agreement with the resolution found in section 4.7. Further the relative size of the white line compared to the size of the EXAFS structure can be compared with Sayers, Lytle and Stern's (1974) data, and indeed, this is also comparable. The flux received from the bremsstrahlung radiation was about 3000 counts per second, in reasonable agreement with Lytle, Sayers and Stern's (1975) figure of 1 → 10000 counts per second; so we may conclude that in both resolution and intensity this apparatus is very similar in performance to that of Lytle (1965), Lytle, Sayers and Stern (1975). However, in view of the vast superiority of synchrotron data, resulting from the much higher intensity of continuous radiation, then for anyone who has access to this type of instrument, a conventional source must be regarded as redundant.

CHAPTER 5

Chalcogenide Materials - Background and Results

5.1 Sample Preparation

It is difficult to present a general section on sample preparation owing to the varied properties of the materials studied here. There are, however, some points which are common to most of the materials. The elements used to make glasses and crystals consisted of arsenic and the chalcogens. Arsenic is known to oxidise readily on exposure to the atmosphere and oxygen can be incorporated into chalcogenide glasses quite easily. Further, it is possible that water may also affect the properties of glasses, owing to its ability to donate monovalent hydroxyl ions to the glass. These may act as bond terminators and thus affect the structure. The most noticeable effect of water can be seen in As_2O_3 glass. This material becomes opalescent when exposed to the atmosphere for a few minutes owing to crystalisation, catalysed by the presence of water. Therefore, the material preparation in its initial stages was confined to a glove-box, purchased from SLEE Ltd., Slough, London. The glove-box was flushed with nitrogen gas derived from a liquid nitrogen plant. Unfortunately the gas contained quite large amounts of oxygen, which, at times, exceeded 2000 ppm, therefore the gas was de-oxygenated by passing it over heated (700°C) copper. Once every hour the copper oxide was converted back to copper by automatically flushing via cam-controlled valves with forming gas (15% H_2: 85% N_2). Residual water was removed from the system by passing the gas over potassium hydroxide pellets. The glove-box was equipped with a balance capable of weighing to ± 1 mg. The extreme dryness of the glove-box created its own problems, however, owing to the electrostatic properties of powders under these conditions. The powders, particularly arsenic, readily adhered to non-metallic objects and it was found necessary to discharge the scale-pan of the balance otherwise large errors in weighing could result (> 300 mg). To minimise the errors due to weighing where possible, large batches of glass were made (~ 10-15 gms).

The freshly powdered elements were weighed and sealed in silica ampoules which were approximately 75 mm long and 15 mm outside diameter. The ampoule had a neck which was 1 mm inside diameter which joined onto a 9 mm outside diameter tube, about 90 mm long, through which the ampoule could be evacuated. The ampoules were pumped through a liquid nitrogen cold trap to a pressure which was approximately 10^{-5} torr and then sealed. The glasses (with the exception of As_2O_3 and As_2Te_3) were made by heating the sealed ampoules in a furnace equipped with a device to continually agitate them by eccentric rotation. Details of this furnace can be found in the thesis by Hulls (1970).

Having made the material, specimens suitable for X-ray absorption had to be prepared. Two factors are important for accurate absorption measurements and these are

a) Sample uniformity

b) Lack of preferred orientation.

The latter requirement applies to the crystals other than those of cubic symmetry. Unfortunately for some materials these conditions are mutually exclusive. For glasses the first requirement can be satisfied by polishing the material to the required thickness, ≃ 30 μm. However the materials were mechanically too weak to achieve specimens of the necessary size (> 10 × 2 mm). Fortunately absolute measurements of the absorption coefficient are not required. Thus, all of the materials were powdered. With the exception of As_2O_3 glass and As_2S_3 crystals, which were special cases, the materials were milled in a small agate vibration ball-mill, originally used for preparing infra-red specimens. It is known from X-ray diffraction work that preferred orientation can be minimised by reducing the particle size as much as possible consistent with the retention of undamaged crystallites. The powers were milled in amyl acetate. When a fine slurry had been produced, it was mixed with "Durofix", a glue which is based on cellulose acetate. This mixture was left to stand to remove bubbles. A strip of "Sellotape" was stuck to a glass plate and strips of "P.V.C." insulation tape were laid on either side of the "Sellotape". A film of glue containing the specimen was cast onto the back of the "Sellotape" and uniformity was achieved by levelling with a razor blade supported on the "P.V.C." tape. When dry the absorption film could be easily lifted from the "Sellotape" to form a manageable film. A photograph of three films of glass prepared in this way is shown on the next page.

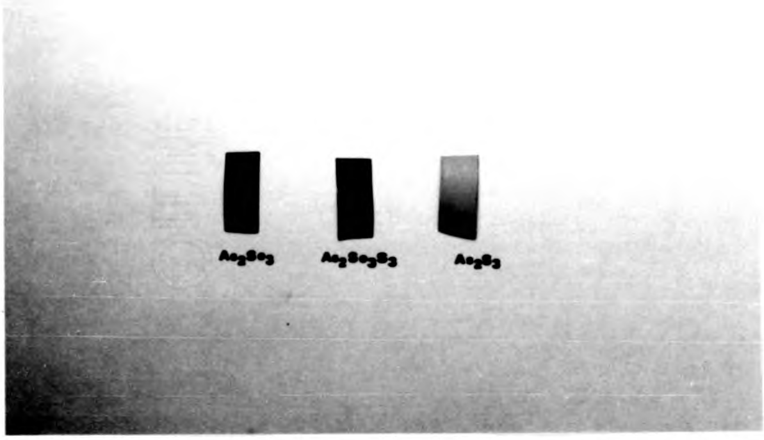

Fig. 5.1 Three absorption specimens studied in this thesis. Milling and casting the specimens in "Durofix" onto the back of "Sellotape" produced uniform, easily-handled specimens for X-ray absorption.

Following a suggestion of Lytle (1965) the films were wrapped in aluminium foil to produce good thermal contact to the cold finger of the cryostat.

5.2 Data Reduction

In this section we will describe the methods used for producing plots of spectra shown in the following sections of this chapter. Four numbers were recorded for each raw data point. These were the number of counts in transmission and absorption, and their respective times. A constant number of counts was accumulated for each point. The measurements were made with an angular increment of 0.0025° θ (~ 2 eV for the arsenic edge and LiF 200 reflection) over an energy region which extended from -200 eV to about 1000 eV above the absorption edge where possible. The starting angle was recorded prior to each run, and from the step-size the energy could be calculated. Each paper tape output was processed by the first three programs, designated by blocks, in fig. 5.2. From the output of the first program, the positions of peaks in the incident intensity could be determined, and from these peak positions the spectrum could be calibrated. In this case the emission lines $WL\gamma_3$ (11674.3 eV) $W(L\gamma_4, L\gamma_4')$ and the $Pb(L\beta_1, L\beta_2)$ were used. The latter peaks were composite peaks owing to the finite resolution of the spectrometer. By measuring the positions of the pure arsenic and selenium edges, these peaks were assigned the energies 12058.9 eV and 12617.7 eV which are intermediate values between $WL\gamma_4'$ (12053.0 eV) $WL\gamma_4$(12063.4 eV) and $PbL\beta_1$ (12613.7 eV) $PbL\beta_2$)12622.6 eV). A linear correction was applied to energies of the spectrum to bring the measured emission lines into coincidence with the values above. The standard deviation of edge positions of different runs of the same material corrected as above was less than 2 eV.

Having corrected each spectrum for energy, the ratio of absorption coefficient for each of the individual runs of the experiment on the same material was calculated over a sample of 200 absorption positions. It was found that small changes of absorption occurred between runs on some occasions. This was possibly associated with slight changes in the position of the absorption film. It was noticed that the changes were apparent when the liquid nitrogen supply to the dewar failed. This may cause vapours to be pumped from the plastic film supporting the specimen and thus cause it to warp. A check was made of the standard deviation of the ratio of absorption between films and if this exceeded three times the value expected on the basis of pure counting statistics, then the run was rejected. The satisfactory spectra were then combined. The result of the combination can be seen later in this chapter in Fig. 5.43 and can be compared with an example of a single run of the same spectrum.

Following the combination of spectra, we have the raw absorption as a function of energy. To obtain the fine structure function $\chi(E)$ we should also know the photoabsorption spectrum of the same atom as that responsible for the absorption in an isolated state. Clearly this is very difficult to obtain experimentally, and so we must be satisfied by approximating the atomic absorption by a smooth curve. Victoreen (1962) has found that the absorption of materials can be approximated over a wide energy range by a formula of the form

$$\mu = A\lambda^3 + B\lambda^4 \qquad (5.1)$$

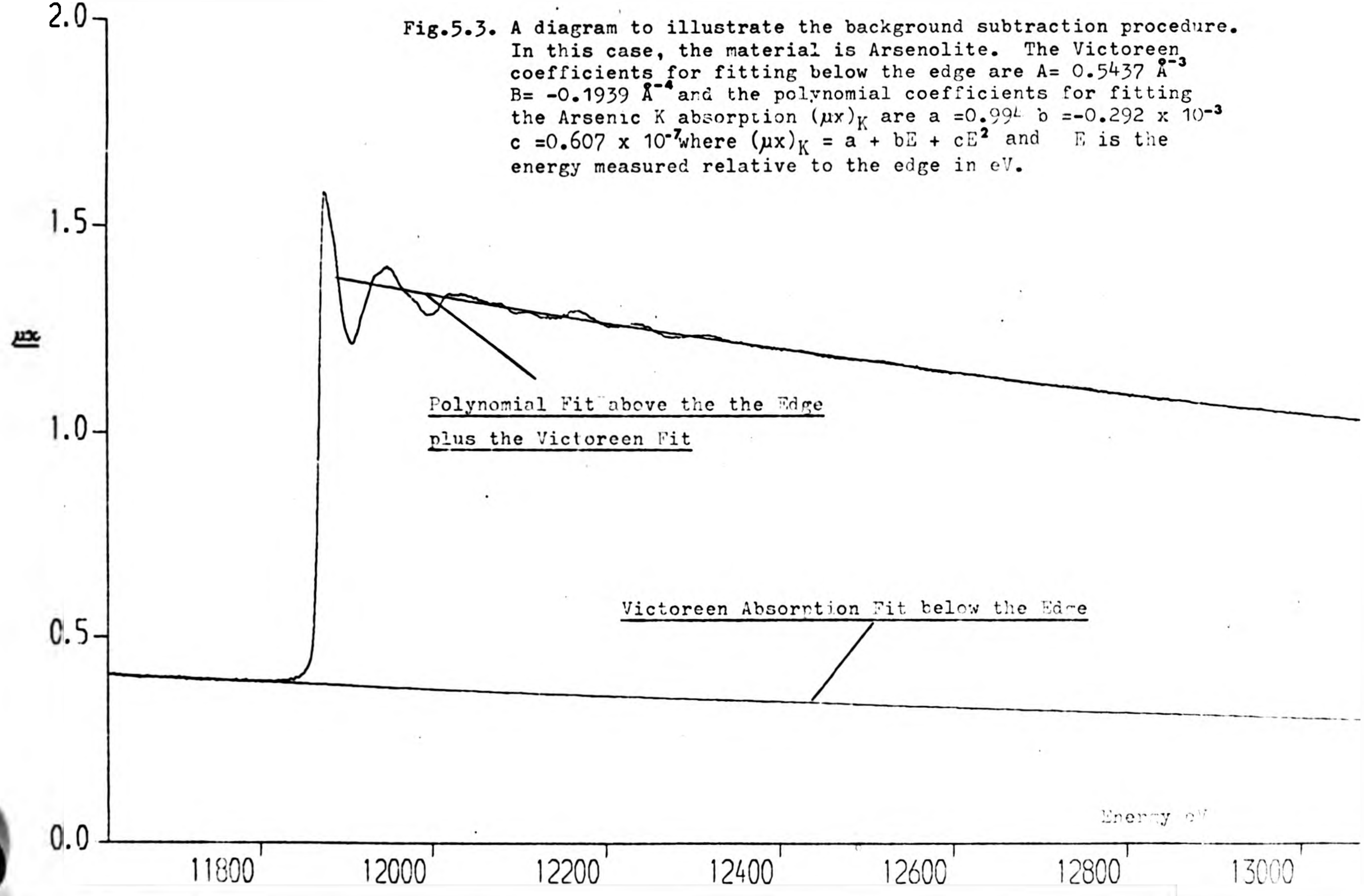

Fig.5.3. A diagram to illustrate the background subtraction procedure. In this case, the material is Arsenolite. The Victoreen coefficients for fitting below the edge are A= 0.5437 $Å^{-3}$ B= -0.1939 $Å^{-4}$ and the polynomial coefficients for fitting the Arsenic K absorption $(\mu x)_K$ are a =0.994 b =-0.292 x 10^{-3} c =0.607 x 10^{-7} where $(\mu x)_K = a + bE + cE^2$ and E is the energy measured relative to the edge in eV.

This formula was used to represent the absorption below the absorption edge. Its use above the absorption edge was, however, less successful and an alternative was tried of fitting a polynomial of maximum degree four to the absorption above the edge. The polynomial was found to be well behaved by weighting the fit as the square of the energy above the edge. The result of this polynomial fit is that the fine structure oscillates about the axis; however, this is still a very unsatisfactory method of subtracting the background absorption, particularly close to an edge which has large amplitude oscillations.

The fitting of the spectrum was carried out from at least - 200 eV from the absorption edge to - 50 eV from the edge for the Victoreen fit, to account for the L, M, etc., processes and the absorption of the matrix material. The polynomial fit is carried out over the energy range from 20 eV above the edge to the end of the data. All of the fine structures calculated have been plotted with error bars which span the range ± standard error, where this is assessed on the basis of pure counting statistics. An example of the background subtraction procedure is given in fig. 5.3 which was performed for the arsenolite (As_2O_3) data.

The data has been taken every 2 eV which is a finer mesh size than the resolution of the spectrometer and so it is desirable to have this additional information, and use it when performing interpolation. Smoothing cubic splines were chosen for this purpose as they are admirably suited for interpolation through noisy curves; further the splines have no built-in bias of an osscillatory nature.

Splines are polynomials which are chosen to fit the data over a small range. The points at which the splines meet each other are called knots. Cubic polynomials g(E) were chosen with knots at every data point and these were fitted to the measured data with the restrictions

$$\int_E g''(E)\, dE = \min \qquad (5.2\ a)$$

$$\sum_i \left(\frac{g(E_i) - \chi(E_i)}{\Delta\, \chi(E_i)} \right)^2 \leqslant n \qquad (5.2\ b)$$

and g(E), g'(E) and g"(E) must be continuous at the knots. $\Delta\, \chi(E_i)$ is the error in the fine structure at the energy E_i and n is the number of data points. Reinsch (1967) has given a computer algorithm to produce the spline fit which assigns knots to every point. One uncomfortable aspect of splines is that if a curve possesses an uneven distribution of curvature then condition (5.2a) forces the curve into a smooth curve at extremaa, thus contributing a disproportionate amount to the sum (5.2 b). Despite these worries splines have been found to give faithful reproduction of the fine structure. Examples of the use of splines together with the use of the Victoreen expression for interpolating above the absorption edge are given later when we wish to plot an interpolated curve.

A table of the materials studied in this thesis is given on the next page together with the errors of each point.

TABLE 5.1

Spectrum	Edge	No. of Counts	Δ μx	Δχ %
$As_2 O_3$ crystal	As	4×10^5	2.2×10^{-3}	0.22
$As_2 O_3$ glass	As	7×10^5	1.7×10^{-3}	0.29
$As_2 S_3$ crystal	As	7×10^5	1.7×10^{-3}	0.15
$As_2 S_3$ glass	As	5×10^5	2.0×10^{-3}	0.20
$As_2 Se_3$ crystal	As	13×10^5	1.2×10^{-3}	0.21
$As_2 Se_3$ crystal	Se	13×10^5	1.2×10^{-3}	0.17
$As_2 Se_3$ glass	As	13×10^5	1.2×10^{-3}	0.45
$As_2 Se_3$ glass	Se	13×10^5	1.2×10^{-3}	0.32
$As_2 Te_3$ crystal	As	11×10^5	1.3×10^{-3}	0.24
$As_2 Te_3$ glass	As	7×10^5	1.7×10^{-3}	0.40
$As_2 S_3 Se_3$ glass	As	4×10^5	2.2×10^{-3}	0.53
$As_2 S_3 Se_3$ glass	Se	4×10^5	2.2×10^{-3}	0.38

Table 5.1 The edges measured for this thesis tabulated against the number of counts per point, the change of absorption at the edge (Δ μx) and the error in the fine structure (δχ).

5.3 Preparation and Properties of As_2O_3

Arsenic sesquioxide exists in three known crystal forms called arsenolite, Claudetite I and Claudetite II. Arsenolite is the usual product of most chemical preparations of As_2O_3, and is the stable phase at low temperatures. The arsenolite lattice is cubic and consists of As_4O_6 molecules arranged on a diamond lattice. Each As_4O_6 molecule consists of an octahedron of oxygen atoms with arsenic atoms attached to four of the faces in a tetrahedral arrangement. A perspective drawing of the structure can be found in the book by Wyckoff (1964). The vapour over As_2O_3 consists almost entirely of As_4O_6 molecules. These molecules have been found by Papatheodorou and Solin (1976) to be stable up to 900° C. Octahedral crystals of arsenolite are formed when the vapour is condensed onto a cool substrate. Arsenolite is also the product of devitrification of the glass. The As_4O_6 molecules retain their individual identity in solid arsenolite, being bonded to other molecules by weak Van der Waals type forces This weak interaction is reflected in a comparison of the Raman and infra-red spectra of the solid and gas which indicate only small perturbations to the vibrational frequencies due to inter-molecular coupling. A general review of the properties of As_2O_3 can be found in the article of Becker, Plieth and Stranski (1962) and recent infra-red and Raman spectra of phases of As_2O_3 have been given by Beattie, Livingston, Ozin and Reynolds (1970), Flynn, Solin and Papatheodorou (1976). The shell radii for arsenolite have been calculated from the crystal structure of Almin and Westgren (1942) and are given on the next page in Table 5.2.

TABLE 5.2

Shell	No. of atoms	Shell radius Å	Type	Position
1	3	1.80	Oxygen	Intramolecular
2	3	3.03	Oxygen	Intermolecular
3	3	3.22	Arsenic	Intramolecular
4	3	3.47	Oxygen	Intramolecular
5	6	3.94	Arsenic	Intermolecular
6	6	4.24	Oxygen	Intermolecular
7	3	4.60	Arsenic	Intermolecular
8	3	5.09	Arsenic	Intermolecular
9	6	5.16	Oxygen	Intermolecular
10	6	5.53	Oxygen	Intermolecular

The radial structure about arsenic in arsenolite.

Claudelite I is found as a mineral and is quite different in crystal structure from arsenolite, having a monoclinic unit cell with space group $P2_1/n$. The complete crystal structure together with a drawing of the lattice can be found in Wyckoff's (1964) book. The lattice is a layer lattice with sheets of atoms normal to the b axis. The layers are not planar, but are heavily convoluted. Within the layers, the usual valencies of arsenic and oxygen, two and three respectively are fully satisfied by heteropolar bonds. The arsenic and oxygen atoms arrange themselves into twelve-membered rings with six arsenic and oxygen atoms alternatively arranged around the ring. The layers are weakly bonded to each other and evidence for this can be found by noting that the layers are easily cleaved. Further, the vibrational properties are in general characteristic of isolated layers. The full layer symmetry is broken by the presence of other layers, and gives rise to a small splitting of the vibrational states (Davydov splitting). One of these split states is infra-red active and the other is Raman active. Observation of this splitting gives a quantitative measure of the strength of the interlayer bonds. Flynn, Solin and Papatheodorou (1976) have measured the splittings and have shown them to be small. The radial structure calculated from the crystal structure reported by Wyckoff (1964) gives values for the interatomic first shell distances ranging from 1.69 to 1.85 Å; however this is inconsistent with the range of values 1.74 to 1.82 Å quoted by this author. Similarly the special positions quoted by Becker, Plieth and Stranski (1962) also yield bond distances which differ from those in arsenolite which, according to these authors, has the same arsenic-oxygen and arsenic-arsenic distances.

During the preparation of Claudetite, Becker, Plieth and Stranski (1962) isolated another crystal which they called Claudetite II. This is also a layer lattice. The complete structure of Claudetite II has been given recently by Pertlik (1975). The radial structure about arsenic, calculated from Pertlik's parameters is shown on the next page in Table 5.3.

TABLE 5.3

Shell	No. of Atoms	Shell radius	Type	Position
1	1.0	1.77	Oxygen	Intralayer
2	1.0	1.79	Oxygen	Intralayer
3	0.5	1.80	Oxygen	Intralayer
4	0.5	1.82	Oxygen	Intralayer
5	0.5	2.94	Oxygen	Intralayer
6	0.5	2.96	Oxygen	Intralayer
7	0.5	2.96	Oxygen	Interlayer
8	1.0	3.13	Arsenic	Intralayer
9	1.0	3.17	Arsenic	Intralayer
10	1.0	3.24	Arsenic	Intralayer

The major difference between this radial structure and that of arsenolite from the point of view of contributions to the EXAFS fine-structure is the variation of radius of the arsenic-arsenic distance, which in arsenolite contributed 3 atoms at 3.22 Å and in Claudetite II will contribute 2 atoms at 3.17 Å, 2 atoms at 3.24 Å and 2 atoms at 3.13 Å, which gives a mean distance of 3.18 Å.

As well as three crystal forms of arsenolite, there are also two glassy forms corresponding to two different methods of making glass. The first method yields glass by condensing arsenic oxide vapour onto a hot substrate. The second method involves cooling molten As_2O_3. The second method of preparation of glass results in a material which is more stable than the first (Becker, Plieth and Stranski (1962)), although X-ray and Raman data (Papatheodorou and Solin (1976)) detect no difference between the two types. X-ray diffraction studies have been made on glassy $As_2 O_3$ by Bottcher, Plieth, Reuber-Kürbs and Stranski (1951), and by Plieth, Reuber and Zshoerper (1969), and the main conclusions are that the glass mostly resembles the Claudetite crystal, with all of the atoms accupying the Claudetite structure up to 3.4 Å but between 3.4 Å and 8 Å only one-sixth of the atoms are discretely distributed, the others are arranged at random. The unusual and interesting anomaly of $As_2 O_3$ glass is that it is only formed by cooling the liquid slowly. Rapid cooling results in crystalline arsenolite.

The crystal studied in this thesis was arsenolite which was purchased as a powder of purity > 99.8%. The glass was made by distilling arsenolite in a quartz ampoule to remove as much water as possible. The ampoule was then sealed with an inside pressure of ~ 10^{-5} torr. The ampoule was heated for two days at 600° C and then slowly cooled over 10 hours to room temperature whilst still in the furnace. The ampoule was opened in a glove-box and the $As_2 O_3$ glass separated easily from the silica tube. The glass remained perfectly stable provided it was not allowed to come into contact with moisture.

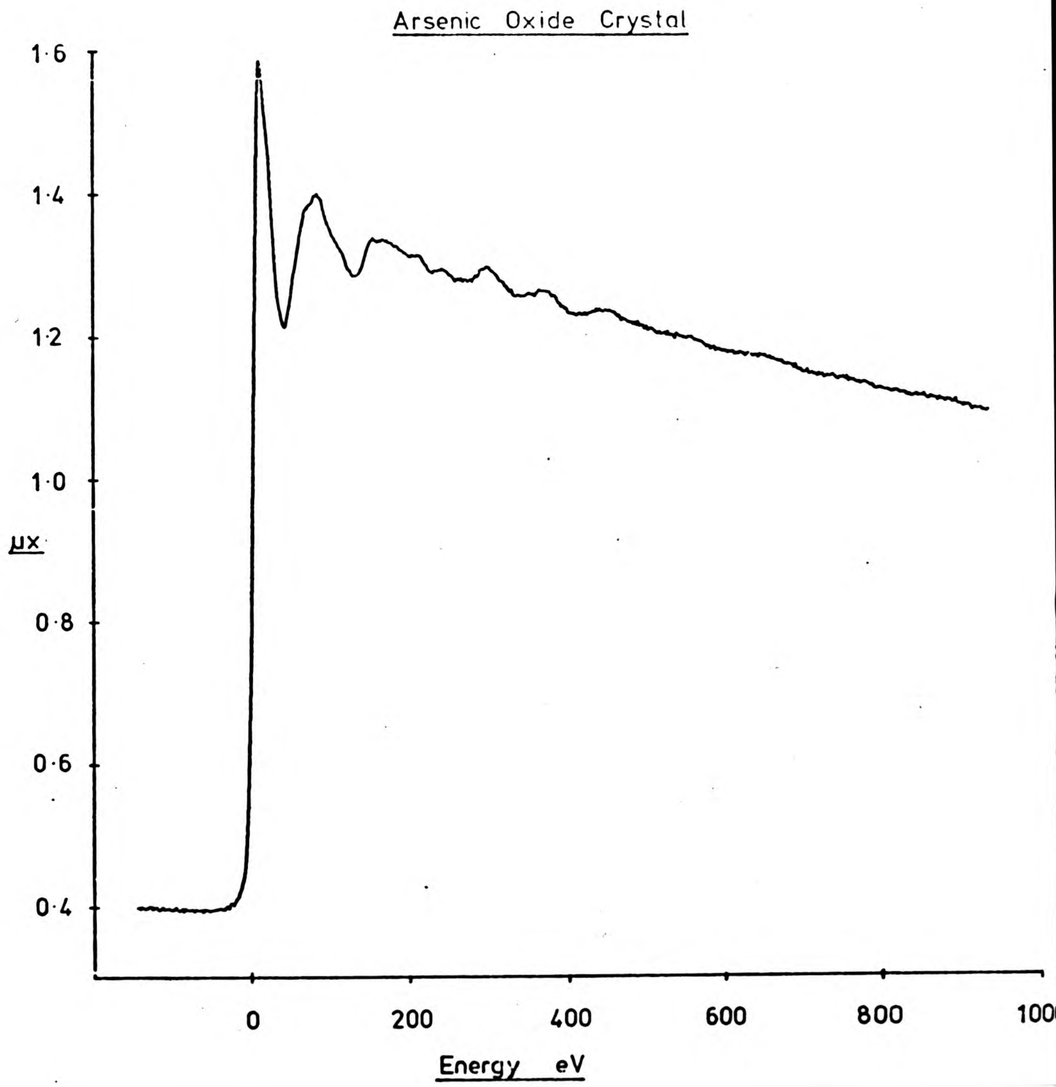

Fig.5.4. The K edge absorption spectrum of Arsenolite taken at liquid nitrogen temperature.

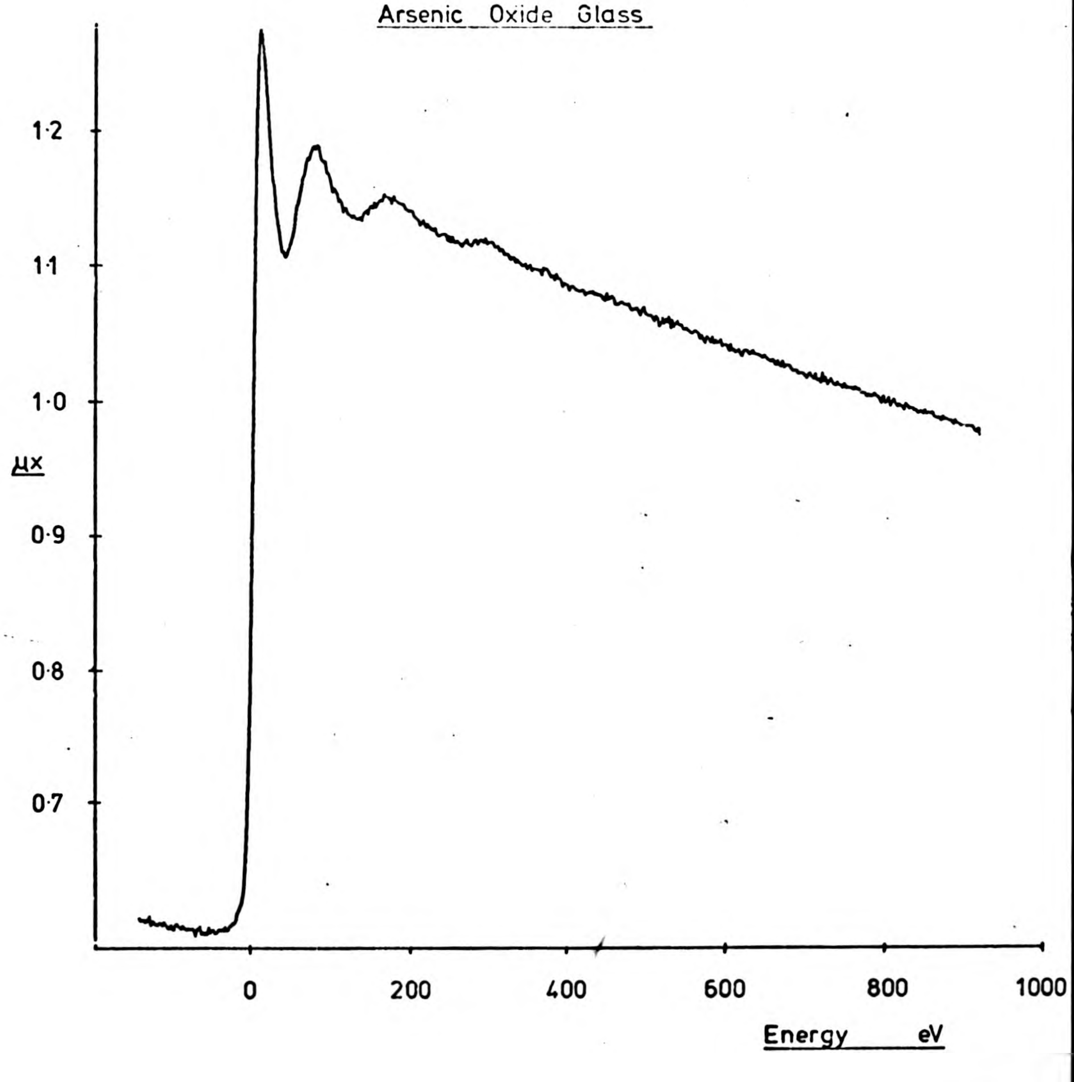

Fig.5.5. The K edge absorption spectrum of As_2O_3 glass taken at liquid nitrogen temperature.

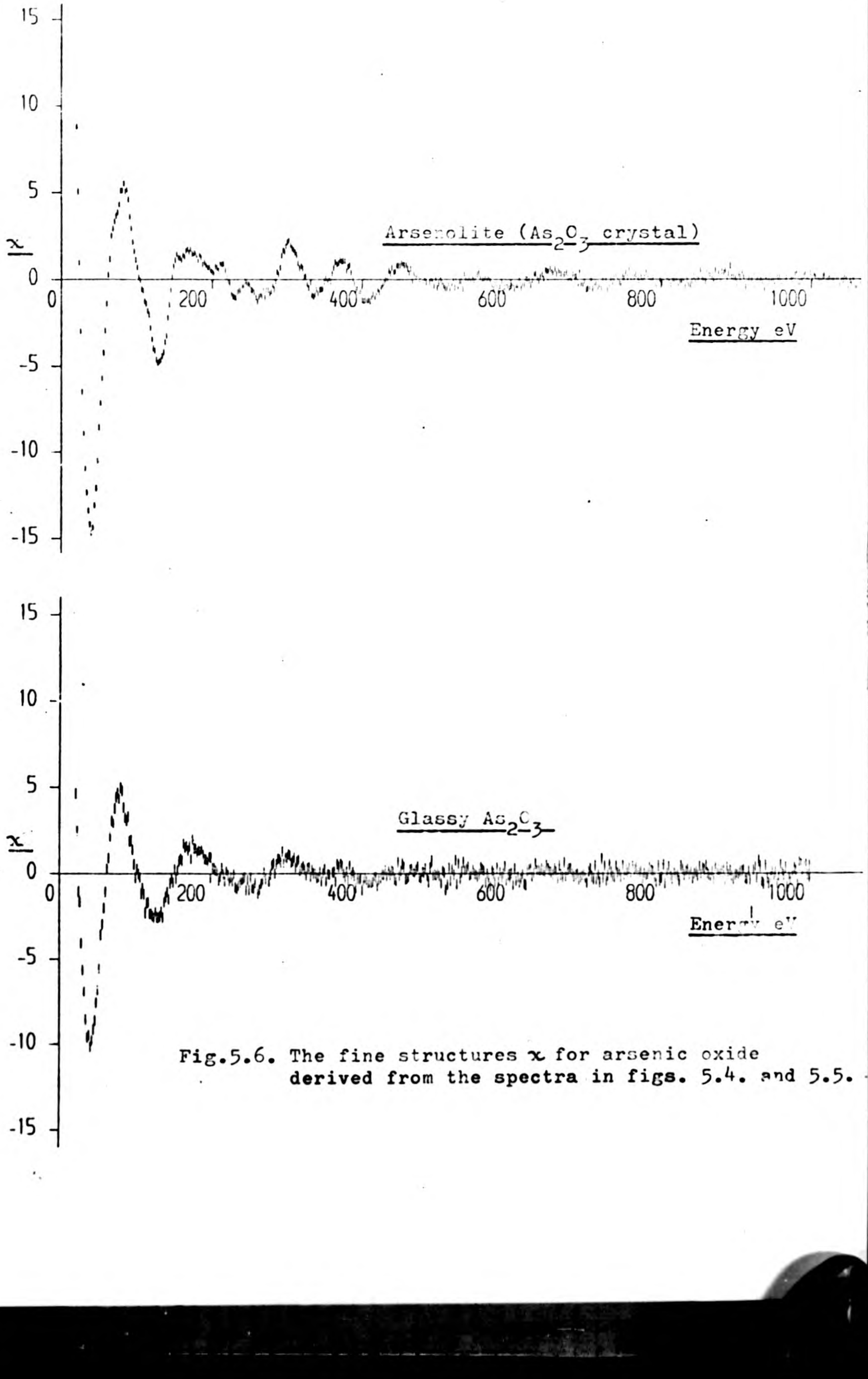

Fig.5.6. The fine structures χ for arsenic oxide derived from the spectra in figs. 5.4. and 5.5.

5.4 Discussion of the As_2O_3 spectra

The K-absorption edge spectrum of arsenolite is presented in fig. 5.4. To the knowledge of the author there is only one other published spectrum of arsenolite by Agarwal and Verma (1968), however the quality of their spectrum is too low to permit any comparison with the results presented here. The spectrum has a spike at the edge which might be attributed to an atomic resonance from the emitter potential, an excitonic level formed by binding the excited photoelectron by the field of the core hole, or a part of the EXAFS effect. Unfortunately the resolution of the measurements is too low to examine this singularity in detail. The absorption spectrum of As_2O_3 glass is shown in fig. 5.5 and this also possesses a spike at the edge although in this case its strength is only about 80% of that of the crystal. This reduction of amplitude is characteristic of sample inhomogeneity as discussed in section 6.1, which is a result of the difficulty of producing very fine powders of the glassy material. The fine structure of As_2O_3 are compared in fig. 5.6. It can be seen that both fine structures look similar with the strong oxygen scattering dominating the spectra at low energies. The glass spectrum is more noisy than the spectrum from the crystal which is a result of the reduced amount of arsenic oxide in the glass specimen compared with that in the crystal. We can see in the crystal fine structure, ripples which extend to almost 1000 eV above the absorption edge. This structure probably does not come from the oxygen first shell because its back-scattering amplitude reduces rapidly as the energy is increased. We can perform a calculation to find the relative contributions to the amplitude of the fine structure from the various shells. The two most dominant shells are the first shell of oxygen scatterers, and the third shell of arsenic atoms. This calculation is shown in Fig. 5.7.

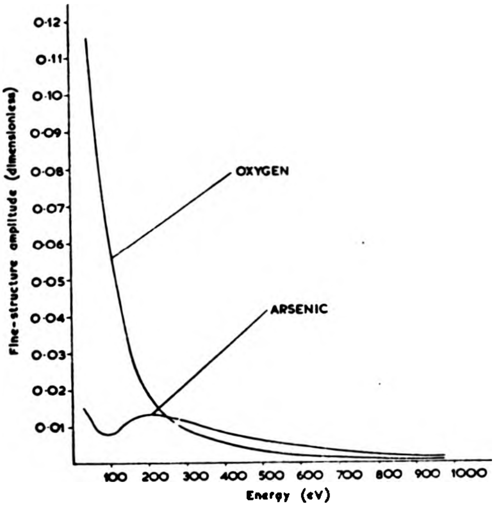

Fig. 5.7 A comparison of the envelope of the fine structure in Arsenolite calculated using the Hartree-Fock phase shifts. The curves relate to the first shell which consists of 3 atoms of oxygen at 1.80 Å and a value $\sigma_1^2 = 2.25 \times 10^{-3}$ Å^2 and a third shell of three atoms of arsenic at 3.22 Å, $\sigma_3^2 = \sigma_1^2$. The imaginary part of the self energy is Ei = 4 eV.

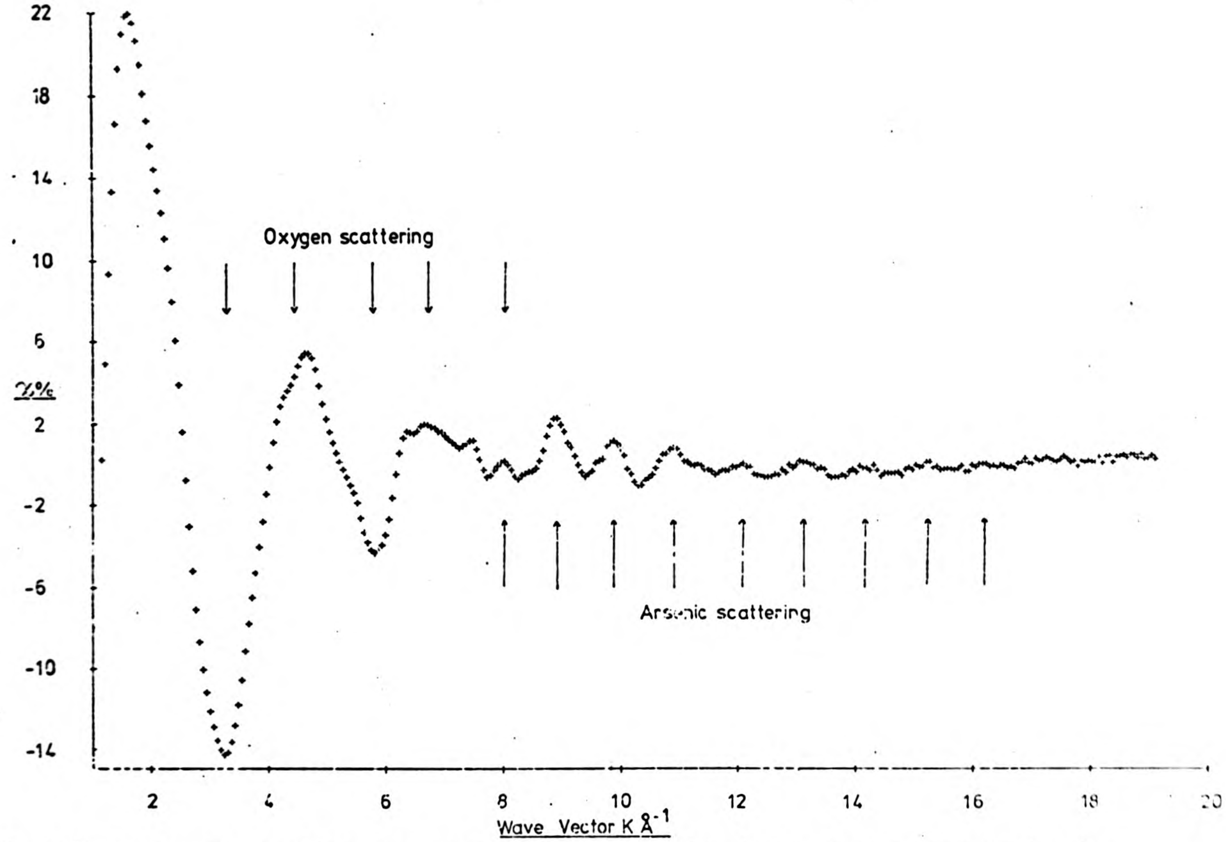

Fig.5.8. A plot of the fine structure $\chi(k)$ against the photo-electron wavevector k. The downward arrows indicate the extremna of the oxygen dominated scattering and the upward arrows indicate the peaks of the arsenic dominated scattering. The curve was generated using smoothing cubic splines and a Victoreen approximation to atomic absorption above the K edge.

From the diagram we can expect that the third shell scattering from arsenic dominates for energies in excess of 250 eV, whilst below this energy we should expect oxygen to be the main contributor. This point can be made clearer if we make the assumption that the sum of $2n_I + n_{II}$ is approximately linear in photo-electron wavevector k, then by plotting the fine structure as a function of k, the peaks belonging to the different shells should be evenly spaced. This has been done for arsenolite and is presented in Fig. 5.8. The curve in this case was produced by using the Victoreen formula for fitting the atomic absorption above the edge and then smoothing and interpolating with cubic splines. From this figure it is clear how the spectrum is split into two halves at $k = 8$ Å^{-1} (244 eV). The arsenic scattering in this case is quite evenly spaced, indicating that a linear phase-shift model is quite reasonable for this atom.

We can discover some structural information from the glass in the light of the previous discussion. Information about the nearest neighbour bond length in the glass is restricted owing to the rapid decay of the fine structure from this atom, also the presence of scattering from other shells makes an accurate estimate of peak position difficult. However the peak in the glass and crystal at 175 eV is the highest energy peak which is clearly dominated by oxygen scattering and there is less than π/4 phase difference in this peak between crystal and glass. This leads us to the conclusion that the difference in mean bond length to the first shell is < 0.06 Å. For the arsenic scattering there is some remnant of a peak at 375 eV which is also present in the glass. The phase difference between these peaks is less than π/6 and this corresponds to a difference of less than 0.03 Å in the radius of this coordination shell between crystal and glass. The fact that there is little arsenic scattering above this energy suggests that an additional positional disorder has smeared out scattering from this shell. The amplitude of the scattering from this peak at 375 eV between crystal and glass is ~ ¼ (allowing for a possible reduction of amplitude owing to inhomogeneity of 80%, see 6.1) which gives an additional Debye-Waller factor, assuming a Gaussian smearing, of $(7 \pm 2) \times 10^{-3}$ Å^2. To estimate the relative smearing of the first shell we have to contend with two difficulties. The first is the uncertainty of the isolated atom absorption which controls the position of the energy axis, and, as we noted before in section 5.2, this is an ill-defined quantity, especially when there is a large amount of scattering close to the edge. Secondly the range of data is too small to produce any reliable estimate. One uncomfortable feature of the fine structure curves is the reduction in amplitude of the first dip of the glass spectrum at 40 eV compared to that of the crystal. We note that a similar reduction of the relative heights of the spike at the edge for these two spectra was also noted earlier. On the evidence from this data alone, this may be due to sample inhomogeneity. This hypothesis is given strength when we note that owing to the reactivity of water with the specimen this sample was prepared without reducing the particle size of the powder by milling. More recent high resolution data has, however, shown that this dip in the glass spectrum is asymmetric and clearly is influenced by higher shell scattering. Therefore we cannot produce any reliable estimate of the relative additional disorder in the glassy material.

5.5 Calculations of the Arsenic Oxide Fine Structure

We anticipate that owing to the small size of the oxygen atom, the asymptotic plane wave expression should be quite a good approximation to the correct curved wave calculation. A comparison has been made of the fine structures from the first shell of arsenolite based on equations 2.37, curved wave and 2.47, plane wave. The curved wave expression was calculated using a program written originally by Pendry (unpublished) and later modified for these calculations by S. Gurman and the author. The emitter potential model adopted was of a neutral selenium atom rather than an unrelaxed excited arsenic atom because the high kinetic energy of the core electrons should relax the potential in a much smaller time than the time of transit of the photo electron to the scattering atoms and back. Fig. 5.9 shows a comparison of the first shell contribution to the fine structure calculated by both methods. It can be seen that the differences are small both in amplitude and phase for energies in excess of 150 eV. However the discrepancies increase as the energy is reduced.

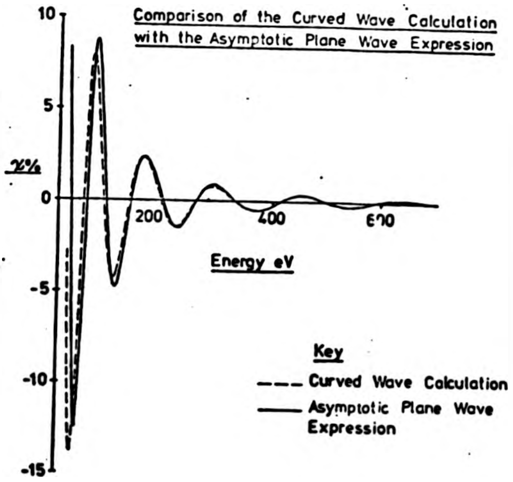

Fig 5.9 A comparison of the fine structure from the first shell of Arsenolite calculated using the asymptotic plane wave approximation and the curved wave calculation. The calculation uses the Slater exchange phase-shifts with three atoms at 1.80Å, Ei = 4eV and $\sigma_1^2 = 2.5 \times 10^{-3}$Å.

Gurman (unpublished) has fitted the arsenolite spectrum using the Hartree-Fock phase shifts of Chapter 3 and the method of Gurman and Pendry (1976) described in Chapter 2. The result of this fit was to yield the following Debye-Waller factors given in Table 5.4. A word of caution is appropriate here, in that the absolute values of σ_j^2 may be affected by other processes not included in the theory. The relative magnitudes are not expected to be greatly changed however. See section 6.2 for discussion.

TABLE 5.4

Shell	σ_j^2 Å^2
1	$(2.5 \pm 0.3) \times 10^{-3}$
3	$(3.9 \pm 0.4)\ 10^{-3}$
5	$(10.4 \pm 0.9)\ 10^{-3}$
2	$(4 \pm 4)\ 10^{-3}$
4	$(5 \pm 4)\ 10^{-3}$

The values of σ_j^2 determined by Gurman for arsenolite

For the first three shells in the table, Gurman reports that the Debye-Waller σ_j^2 can be determined reasonably easily, however for shells 2 and 4 the spectra are not very definitive owing to the weak scattering of oxygen away from the edge. The interesting result from this table is the sudden increase in the Debye-Waller factor for the fifth shell. This results from the weak Van der Waals interaction between molecules, as shell five corresponds to intermolecular scattering.

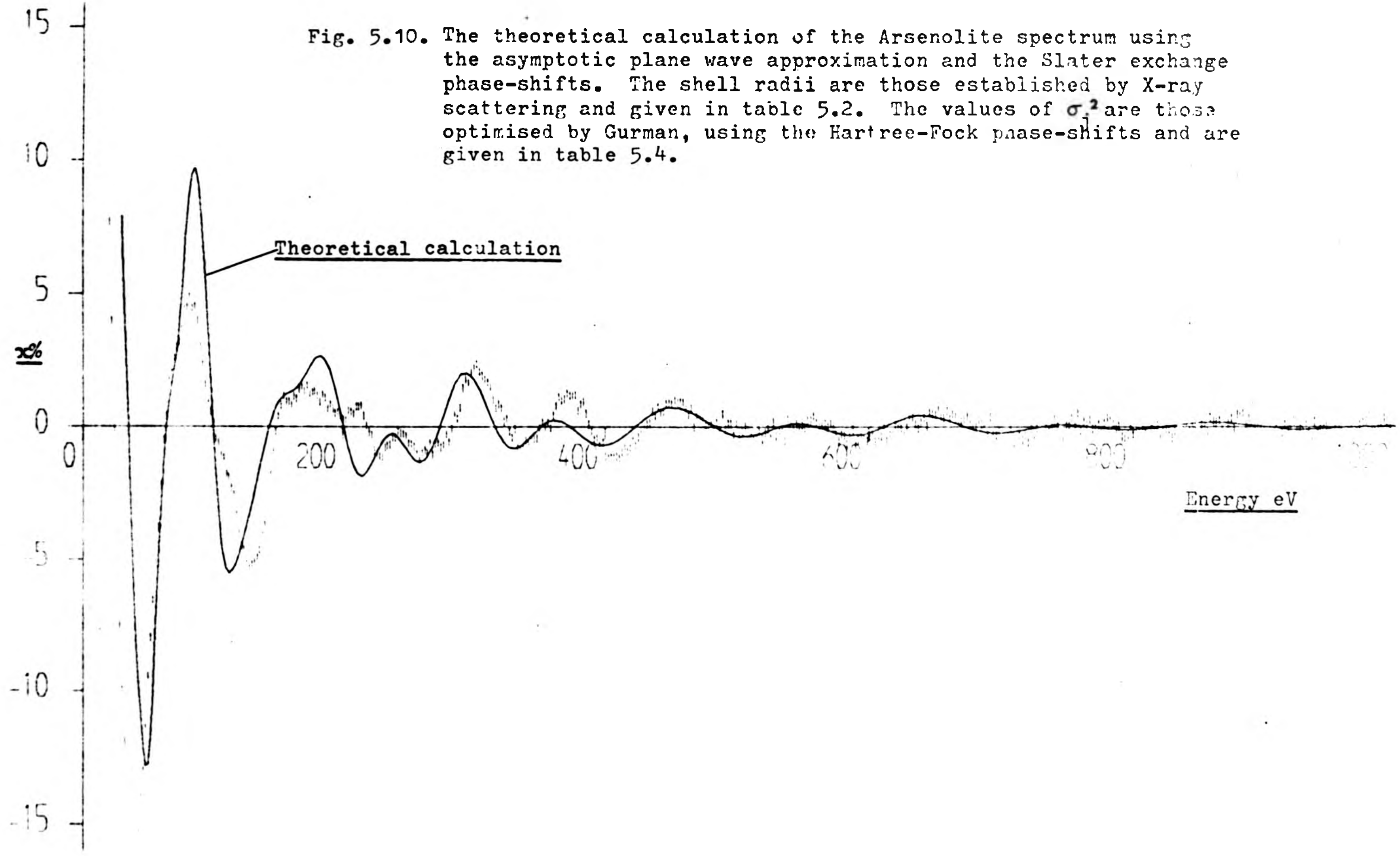

Fig. 5.10. The theoretical calculation of the Arsenolite spectrum using the asymptotic plane wave approximation and the Slater exchange phase-shifts. The shell radii are those established by X-ray scattering and given in table 5.2. The values of σ_j^2 are those optimised by Gurman, using the Hartree-Fock phase-shifts and are given in table 5.4.

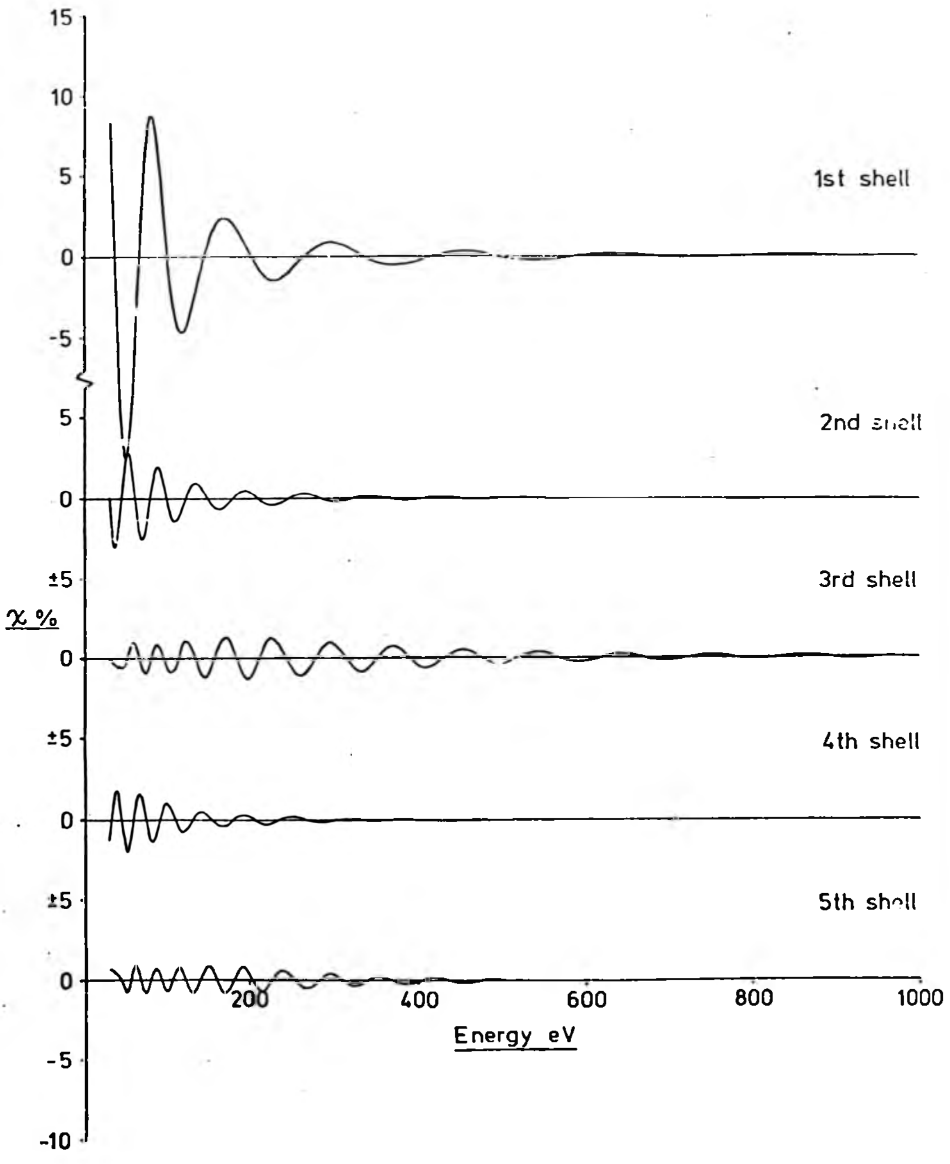

Fig.5.11. The separate contributions to the fine structure of Arsenolite.

We have seen in Chapter 3 that the EXAFS function χ is very sensitive to the phase-shifts. In fact, comparing calculations based on Hartree-Fock exchange and Slater exchange we find that the latter exchange approximation gives much better agreement with experiment than the Hartree-Fock values. Fig. 5.10 shows a comparison between the fine structure calculated by using the five shell crystal radii from table 5.3 and the Debye-Waller factors in table 5.4. We should note that the Debye-Waller factors are not fully optimised for these phase-shifts. The complex part of the self-energy of the photoelectron was chosen to be 4 eV in accord with Pendry's (1974) recommendation. We see from Fig. 5.10 that the agreement in amplitude is difficult to assess owing to the rapid fall-off of $\frac{|f(\pi)|}{k}$ for oxygen. The phase, despite the improved phase-shifts, differs by approximately 0.8 radians for both oxygen and arsenic scattering. If the shell radii were adjusted to optimise the arsenic scattering at about 400 eV, then this would correspond to an error in the radius of about 0.04 Å. It is possible that some of this mismatch could be accounted for by errors in the crystal structure. The error in the As-As distance is 0.02 Å and in the As-O distance, 0.05 Å. In general we can see that the qualitative features of the spectrum are reproduced. The spectrum contributions from each shell in the arsenolite spectrum are shown in Fig. 5.11. We note here that the position of the zero kinetic energy point of the photoelectron has been set at the position of the edge, and the energy variation of the self energy has been ignored. The fit can be considerably improved by moving the energy zero above the centre of the absorption edge. However, there is no

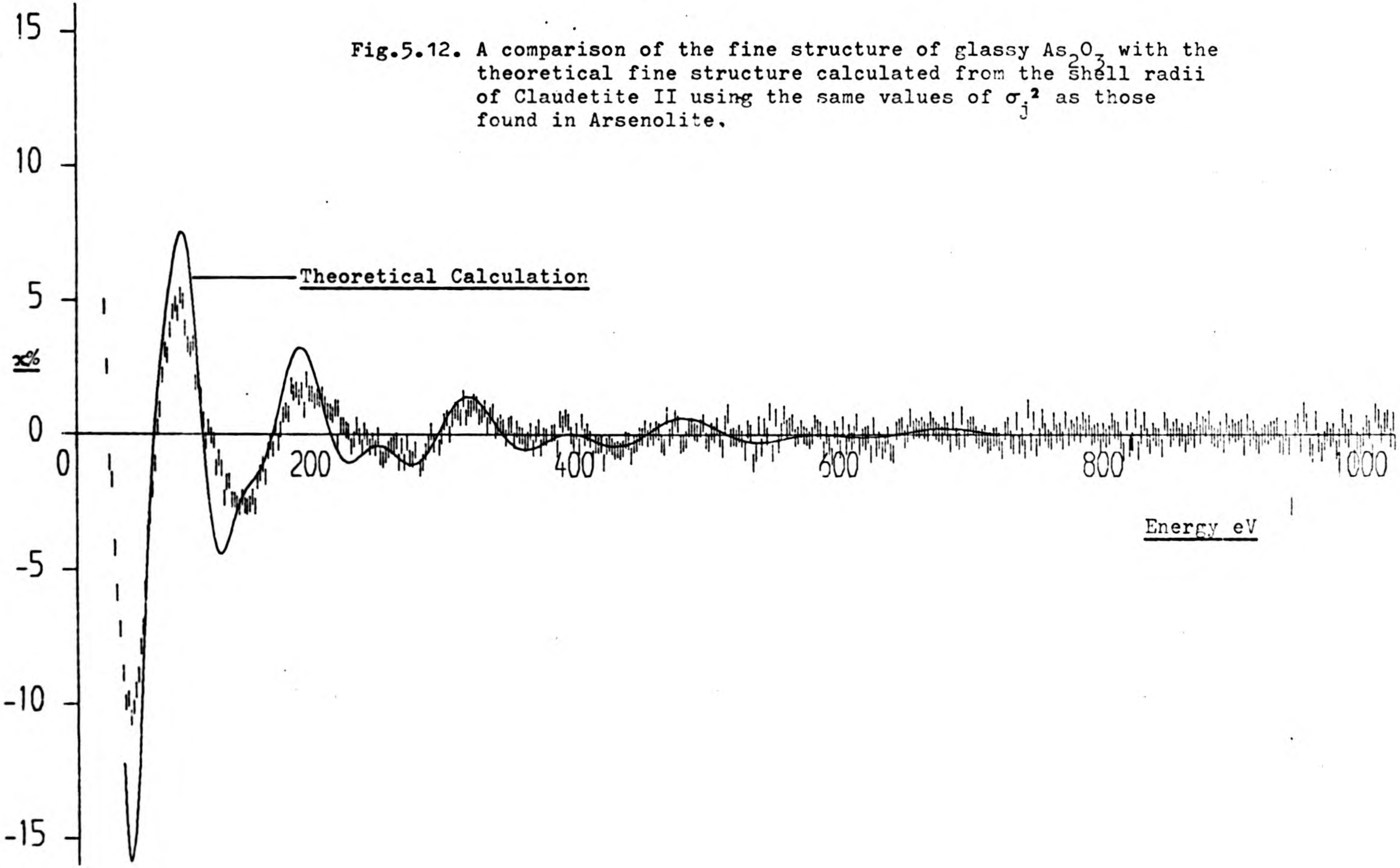

Fig.5.12. A comparison of the fine structure of glassy As_2O_3 with the theoretical fine structure calculated from the shell radii of Claudetite II using the same values of σ_j^2 as those found in Arsenolite.

basis for doing this. Further, the variation of self-energy with energy is also expected to be weak ~ 2 eV (Pendry 1974). Thus the principal mismatch of theory and experiment is probably associated with errors in the phase-shifts.

Turning to the glassy spectrum, we have also compared this spectrum with that calculated from the radial structure of Claudelite II. Just by comparing the fine structures, we know that the arsenic scattering gives rise to peaks at the same energies as those in arsenolite. The better agreement in the phase in Fig. 5.12 is associated with the reduction of the mean As-As distance in Claudelite II by 0.04 Å relative to the same distance in arsenolite. As the discrepancy between experiment and theory for arsenolite was attributed mainly to errors in the phase-shifts, the improvement between theory and experiment for the glass spectrum should be regarded as accidental. The amplitude of the measured arsenic scattering in the glass does diminish with energy indicating an increased Debye-Waller factor over than in arsenolite. It is thus difficult to reconcile this fact with the existence of arsenolite molecules in the glass because we know that the molecules are coupled via weak forces and these are incapable of transmitting the strains necessary to alter the arsenic-arsenic distances. We see from Fig. 5.12 that even the presence of several different As-As distances in Claudetite II is unable to explain the disappearance of structure beyond 450 eV if we assume the same thermal and positional smearing as that which exists in the arsenolite molecule. However, it is felt that this is not a fair test of the existence of Claudetite-like features in the glass because it is very unlikely that the values of

σ_j^2 should be the same between arsenolite and Claudetite. This question can only be resolved by comparing experimentally the spectra of Claudetite and the glass.

In conclusion we can say that the structure of the glass does not contain molecules of $As_4 O_6$ but does possess As-As distances close to those found in this molecule.

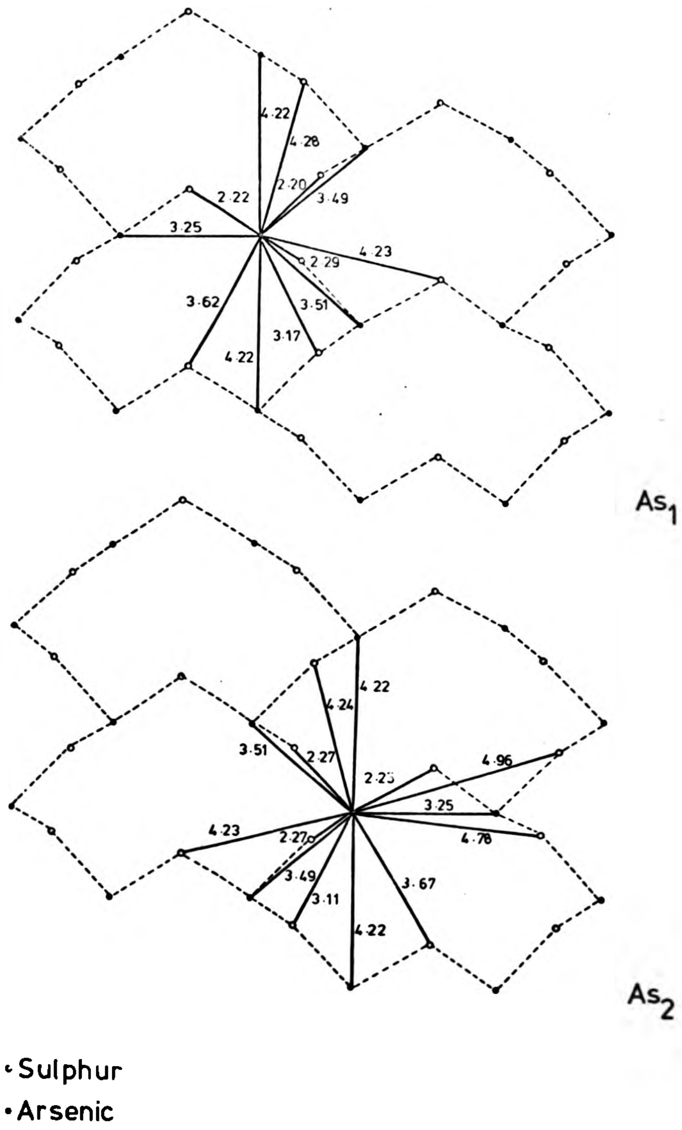

Fig.5.13. A projection of a single layer of Orpiment onto the ac plane. The radial structure is shown about the two non-equivalent sites of the lattice.

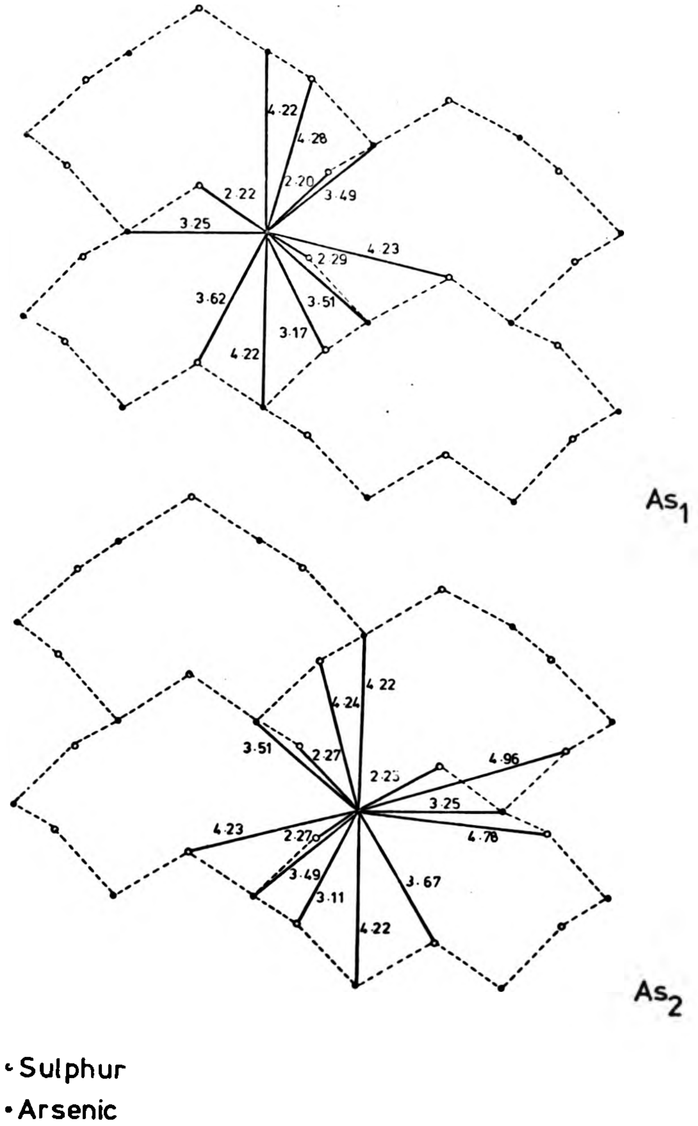

Fig.5.13. A projection of a single layer of Orpiment onto the ac plane. The radial structure is shown about the two non-equivalent sites of the lattice.

5.6 Preparation and properties of $As_2 S_3$

Crystalline $As_2 S_3$ is found as a mineral and is called orpiment. The complete crystal structure has been given by Morimoto (1954) and has been reported by Wyckoff (1964). The structure is similar to that of Claudetite. It is a layer lattice with space group $P2_1/n$ and with the layers arranged normal to the b axis. Each layer consists of twelve-membered rings of atoms with six arsenic and six sulphur atoms alternately bonded together. Each arsenic has its valency fully satisfied by three sulphur atoms. Between layers the bonding is weak and evidence of this fact is given by the easy cleavage and small Davydov splittings of the vibrational spectrum (Zallen, Slade and Ward 1971). The radial structure about arsenic has been calculated from the special positions given by Wyckoff (1964) and is given in Table 5.5. From the table we may expect the principal contributions to come from the nearest neighbour sulphur scattering at a mean distance 2.25 Å, with a mean square variation of radius of 1.5×10^{-3} Å^2, the next pyramidal unit arsenic scattering at a mean distance of 3.42 Å and the cross-ring scattering at 4.22 Å. A projection of the lattice on the ac plane is shown in Fig. 5.13, together with the radial structure about the two non-equivalent As sites.

$As_2 S_3$ forms a very stable glass and will only devitrify after many hours at elevated temperatures. However, crystals formed by this means may well be included in a glassy phase and the degree of crystallinity of the mass may be questioned. Attempts were made to grow orpiment crystals by the method of Boult and Ghosh (1965) and also by the method of iodine vapour transport.

TABLE 5.5

Shell	No. Atoms	Radius	Type	Position	Group
1	0.5	2.20	Sulphur	Intralayer	1
2	0.5	2.22	Sulphur	Intralayer	1
3	0.5	2.25	Sulphur	Intralayer	1
4	1.0	2.27	Sulphur	Intralayer	1
5	0.5	2.29	Sulphur	Intralayer	1
6	0.5	3.11	Sulphur	Intralayer	2
7	0.5	3.16	Sulphur	Intralayer	2
8	1.0	3.25	Arsenic	Intralayer	2
9	0.5	3.46	Sulphur	Interlayer	-
10	1.0	3.49	Arsenic	Intralayer	2
11	1.0	3.51	Arsenic	Intralayer	2
12	0.5	3.55	Sulphur	Interlayer	-
13	0.5	3.62	Arsenic	Interlayer	-
14	0.5	3.62	Sulphur	Intralayer	3
15	0.5	3.67	Sulphur	Intralayer	3
16	0.5	4.00	Sulphur	Interlayer	-
17	0.5	4.17	Sulphur	Interlayer	-
18	2.0	4.22	Arsenic	Intralayer	3

Radial structure about arsenic in orpiment

For the former method the result was glassy, whilst for the latter Realgar ($As_4 S_4$) crystals grew in a rod-like fashion from a glassy condensate. For iodine transport, 1% iodine was added to 3 grams of $As_2 S_3$ glass in a silica ampoule of length 12 cms and internal diameter 8 mm. Growth of realgar ($As_4 S_4$) occurred when the melt was held at 260° C and crystals were deposited in a zone at 128° C.

Owing to these failures, crystals of natural orpiment originating from Nevada were purchased from Gregory Bottley Ltd., 30 Old Church Street, Chelsea. The samples were in the form of an aggregated mass of crystals. X-ray diffraction of the material produced no lines that did not correspond to those of orpiment.

Difficulties were encountered when making films of the material for absorption studies. It was noticed that the X-ray diffraction lines broadened with milling and a rather more intense diffuse halo developed than that usually present from the pyrex support rod. Milling was continued and it was found that eventually the entire specimen became amorphous. This probably results from the layer-like nature of the orpiment crystal being easily cleaved until possibly single layer fragments remain. Accordingly, a rather gentler powdering process was used, consisting of crushing the material in a pestle and mortar. Glassy $As_2 S_3$ can be prepared easily from the elements which in this case were of purity > 99.99%. A 15 gram batch of material was made by sealing the elements in the correct stoichiometric proportions into a silica ampoule. The ampoule was sealed with a vacuum of less than 10^{-5} torr inside and then heated in a furnace at 500° C for 36 hours. The ampoule was air quenched and the resulting glass was yellow with a shiny surface and free from bubbles.

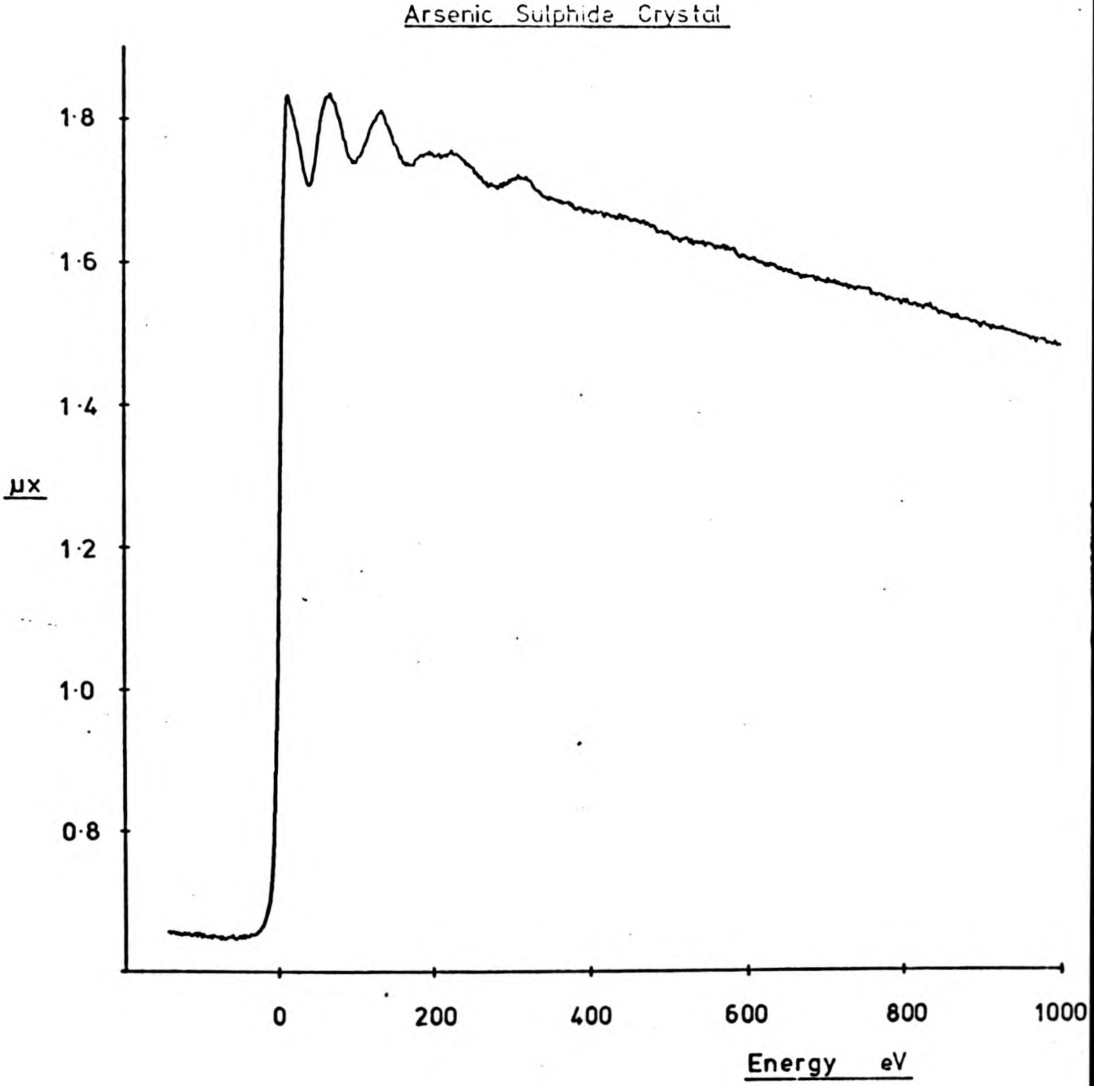

Fig.5.14. The raw Arsenic K absorption edge spectrum of Orpiment, As_2S_3.

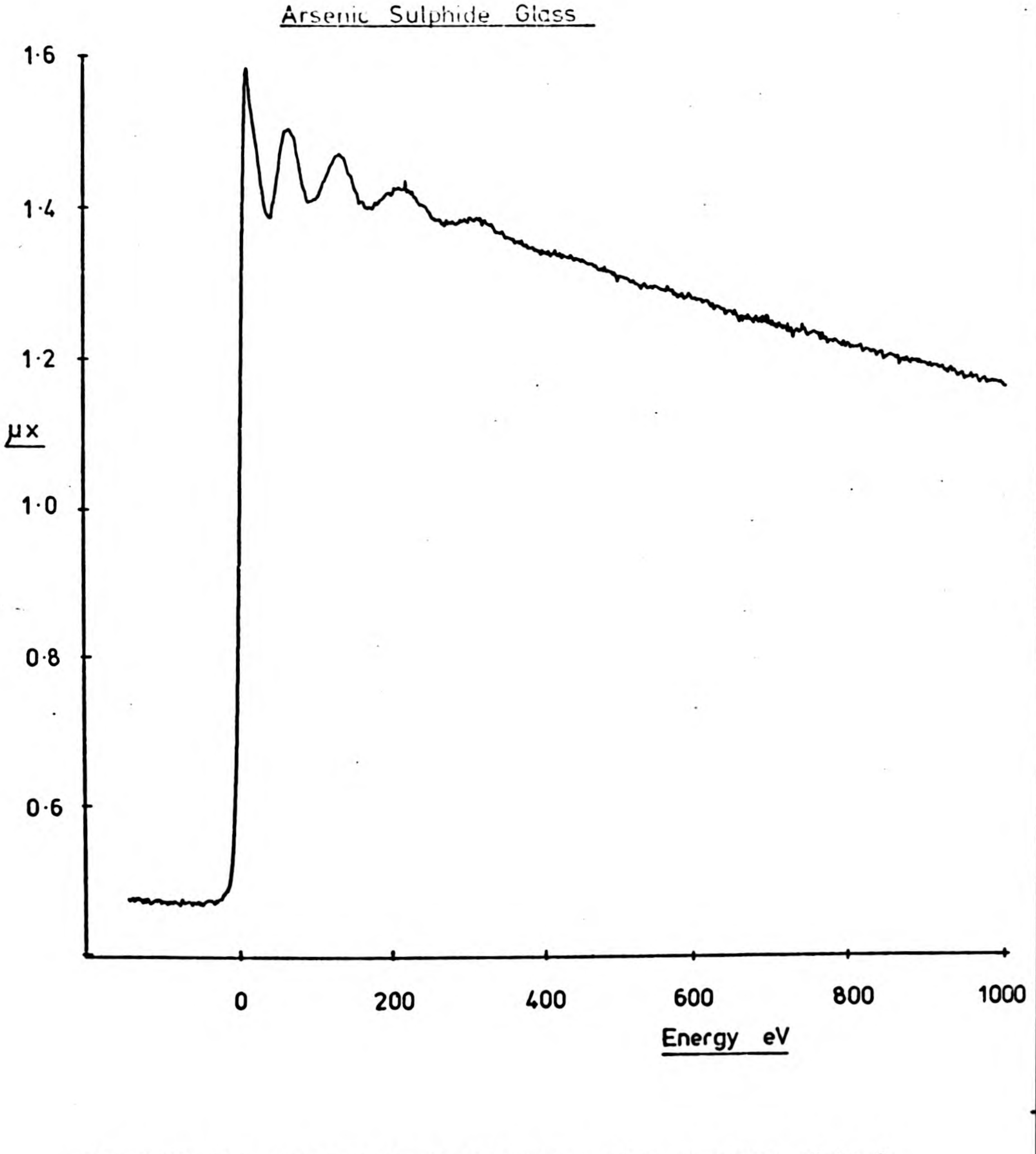

Fig.5.15. The raw arsenic K absorption edge spectrum of As_2S_3 glass.

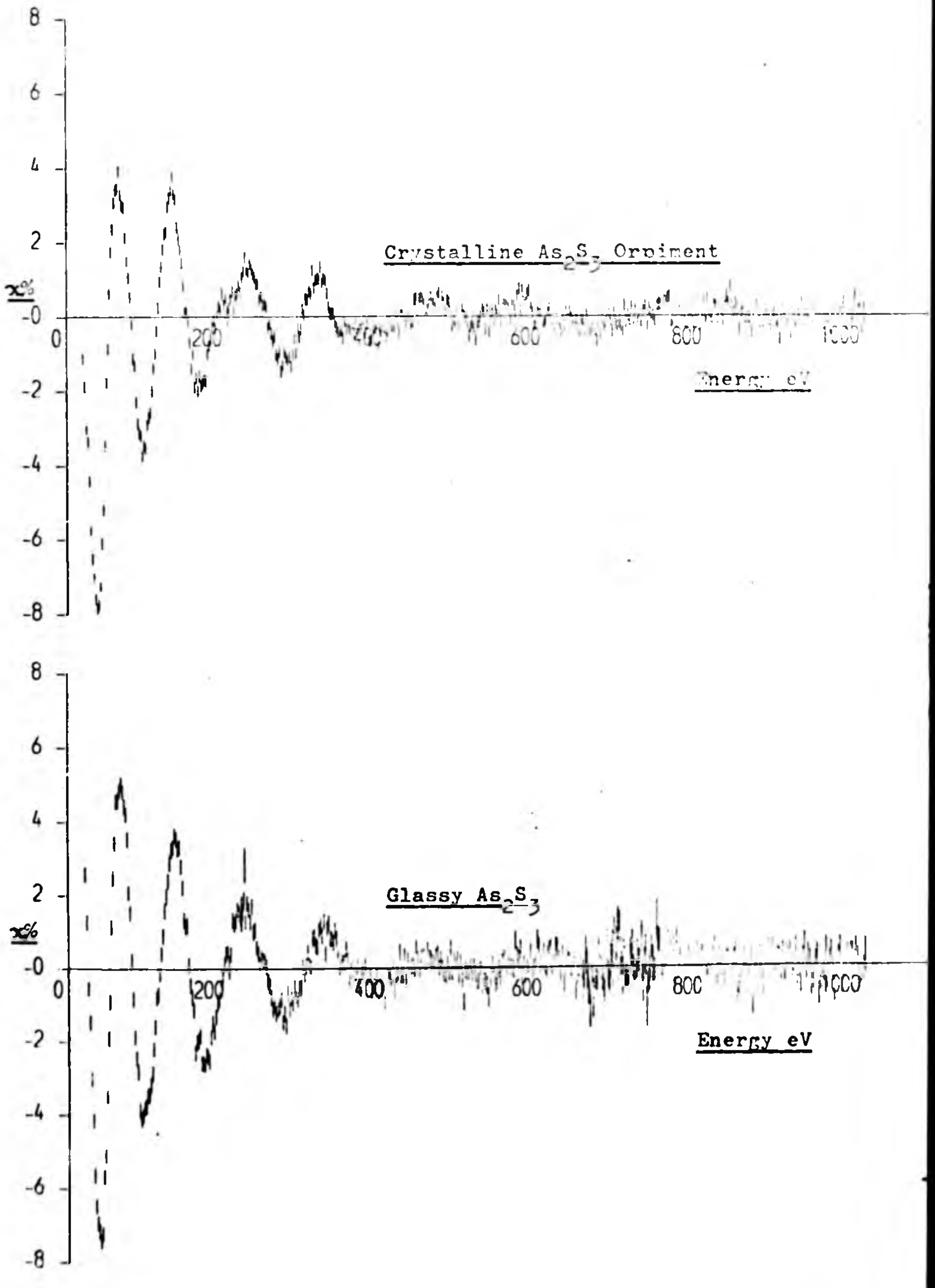

Fig.5.16. The fine structure χ for As_2S_3 crystal and glass.

5.7 Comparison of the $As_2 S_3$ spectra

The raw absorption spectra are presented in Figs. 5.14 and 5.15. The first point to notice is that the glass appears to have a larger spike at the edge than the crystal. Both spectra were recorded under the same condition of resolution discussed in Chapter 4. The only difference between the two measurements is the magnitude of μx above the absorption edge. In this case the crystal absorption has an average value $\mu x \sim 1.8$ and the glass $\mu x \sim 1.5$. It is known that the finite resolution of the spectrometer will distort the spectrum in the vicinity of the absorption edge, and the distortion becomes greater with increasing absorption, and this is the so-called thickness effect. From the resolution calculations performed in Chapter 4,we know that the receiving slit will be accepting some flux from wavelengths transmitted below the absorption edge when the spectrometer setting is up to 15 eV on the high energy side of the edge. Thus the finite instrumental resolution is a possible explanation for the effect. However the difference in maximum absorption $\mu \sim 0.3$ seems small to be fully responsible. Without deconvoluting both the incident and transmitted intensities it is difficult to make any further comment, however it does possibly warrant higher resolution studies. From a comparison of the spectra we can see that the glassy material possesses a much simpler structure than the crystal and thus we must conclude that the crystalline spectrum contains contributions from more shells than the glass. The fine structures are plotted in Fig. 5.6. Both fine structures have the characteristic sulphur scattering which has an envelope which decays smoothly in an exponential-like manner.

This shape is in agreement with that predicted in Chapter 3. The most obvious indication of the influence of higher shells is the shoulder present in the crystal spectrum at 195 eV. Despite the presence of the higher shell structure in the crystal spectrum it is still profitable to perform a crude analysis based on the positions of the extremna in the spectrum.

By noting that the most rapidly varying part of the A.P.W. EXAFS equation (Eq. 2.46) is the sinusoidal term, we can write for the dominant first shell

$$\chi = -A \sin\left(2k\,R_1 + 2\eta(k)\right) \qquad 5.3$$

where the amplitude A is positive and only weakly dependent on the radius. The term $\eta(k)$ contains contributions from the emitter η_I scatterer η_{II} and from wavecurvature η_c and these we expect to be transferable from crystal to glass so long as the difference in first shell radii is small.

$$2\eta(k) = 2\,\eta_I + \eta_{II} + \eta_c \quad . \qquad 5.4$$

Equation 5.4 has been written with a factor 2 proceeding the phase shift so that we may compare our results with those of Sayers, Lytle and Stern (1972). These authors have established that for germanium the parameter $\eta(k)$ can be closely approximated by a linear expression

$$\eta(k) = -\,ak + b \qquad 5.5$$

Extremna positions of the fine structure at k_n then obey

$$2\,k_n(R-a) + 2b = (n + \tfrac{1}{2})\pi \qquad 5.6$$

where n is odd for a maximum.

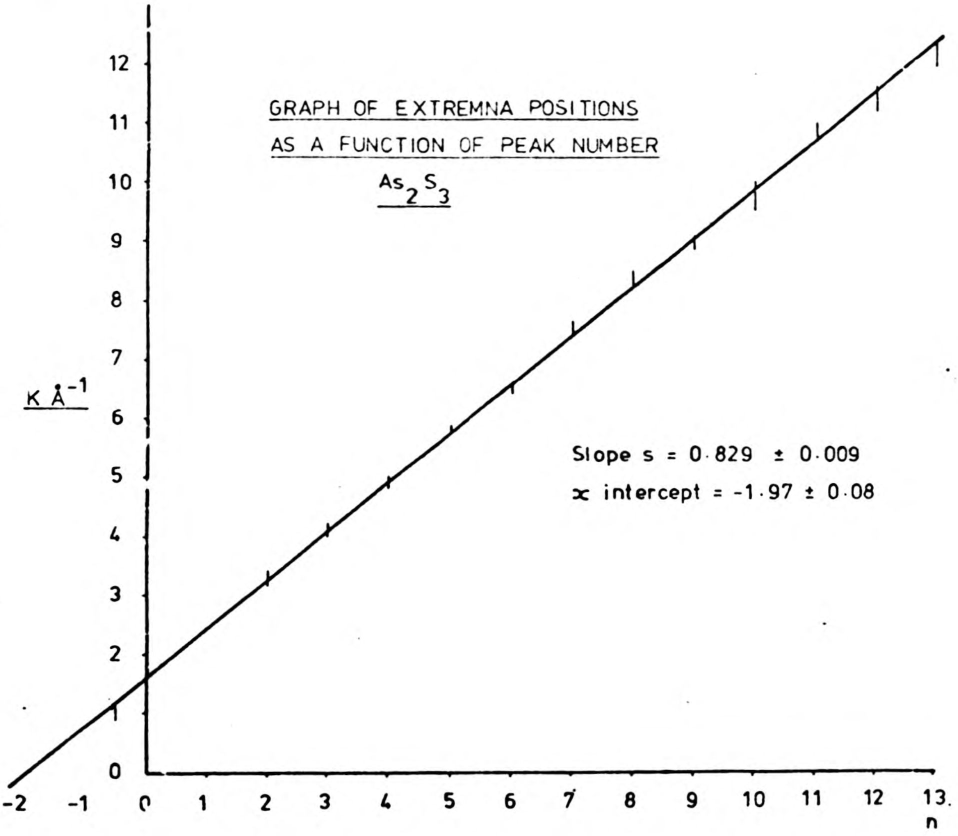

Fig.5.17. A plot of the extremna positions against n, the order of the extremnum, for crystalline As_2S_3.

Rearranging

$$k_n = \frac{n\pi}{2(R-a)} + \frac{(\frac{1}{2}\pi-2b)}{2(r-a)} \qquad 5.7$$

A plot of k_n against n should thus yield a straight line if the linear phase-shift model, Eq. 5.5, holds. The extremna positions for both crystalline and glassy arsenic sulphide are summarised in Table 5.6. The energies of the maxima have been established by ignoring any higher shell effects.

TABLE 5.6

n	Ec (eV)	Kc (Å $^{-1}$)	Eg (eV)	Kg (Å $^{-1}$)	Ec/Eg
2	40 ± 3	3.24 ± 0.12	38 ± 3	3.16 ± 0.12	1.05 ± 0.11
3	65 ± 3	4.13 ± 0.09	64 ± 3	4.10 ± 0.09	1.02 ± 0.07
4	93 ± 4	4.94 ± 0.10	95 ± 3	4.99 ± 0.10	0.98 ± 0.04
5	133 ± 4	5.91 ± 0.09	131 ± 3	5.87 ± 0.09	1.02 ± 0.03
6	169 ± 4	6.66 ± 0.08	165 ± 4	6.58 ± 0.08	1.02 ± 0.03
7	217 ± 4	7.55 ± 0.07	225 ± 4	7.69 ± 0.07	0.96 ± 0.03
8	265 ± 4	8.34 ± 0.06	271 ± 4	8.44 ± 0.06	0.98 ± 0.02
9	318 ± 4	9.14 ± 0.06	312 ± 4	9.05 ± 0.06	1.02 ± 0.02

Table of the extremna positions for the As_2S_3 materials. n the order of the extremnum (odd for a maximum), Ec and Eg the energies of the extremnum position for crystal and glass respectively, measured with respect to the centre of the absorption edge. The weighted mean of Ec/Eg = 1.00 ± 0.015.

The results from the crystal spectrum are shown in Fig. 5.17. From the slope of this graph together with the mean first shell distance of arsenic-to-sulphur of 2.25 Å we find that a = 0.355 ± 0.02 Å. We wish to compare the first shell distance

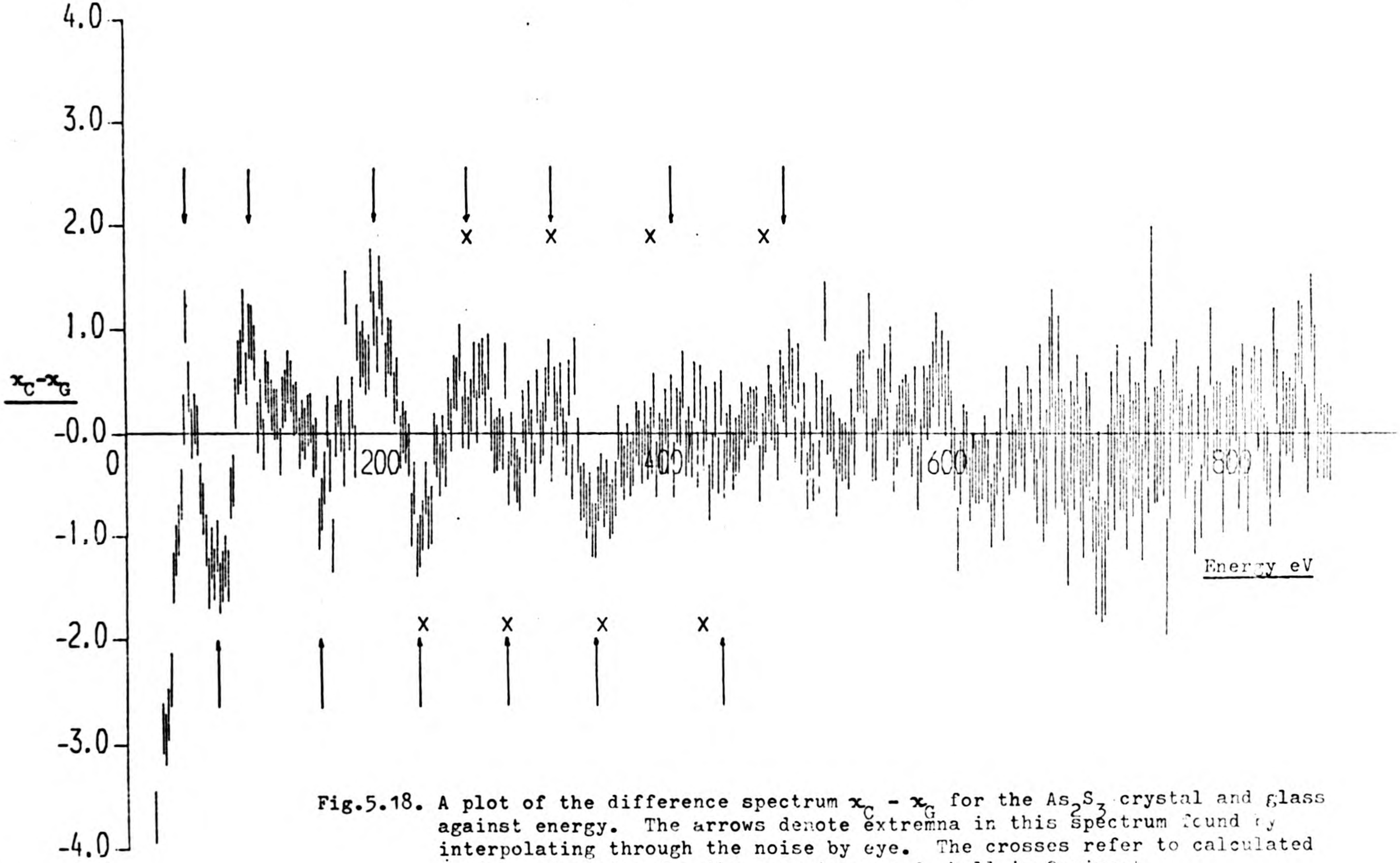

Fig.5.18. A plot of the difference spectrum $x_C - x_G$ for the As_2S_3 crystal and glass against energy. The arrows denote extremna in this spectrum found by interpolating through the noise by eye. The crosses refer to calculated maxima and minima for the arsenic second shell in Orpiment.

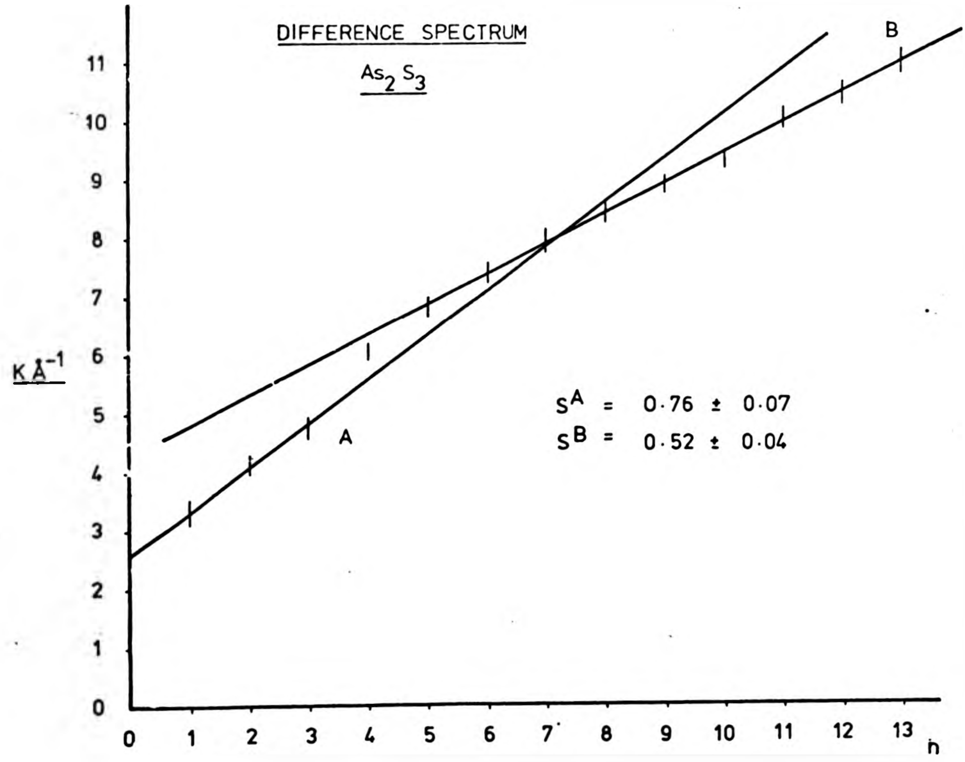

Fig.5.19. A plot of the extremna positions of Fig.5.18. against n.

in both crystal and glass and from Eq. 5.3 we can write

$$\frac{Ec^n}{Eg^n} = \left(\frac{R_g - a}{R_c - a}\right)^2 \qquad 5.8$$

where Ec^n is the energy of the n^{th} extremnum in the crystal

Eg^n is the energy of the n^{th} extremnum in the glass

R_g is the first shell radius in the glass

R_c is the first shell radius in the crystal.

This ratio $\frac{Ec^n}{Eg^n}$ has been established in table 5.6 and a weighted estimate of the mean is calculated to be 1.00 ± 0.015. This yields an estimate of the difference in the mean first shell distance of 0.0 ± 0.014 Å.

Note that because the parameter a appears on both the top and bottom of equation 5.8 so the error is not sensitive to errors in a. If we assume that the first shell radius of the crystal is correct then the first shell radius of the glass is 2.25 + 0.014 Å. This compares with the value of 2.21 Å found by Sayers, Lytle and Stern (1974) on the basis of a linear phase shift η which is independent of scattering atom, and was presumably calibrated from an arsenic emitter and selenium scatterer. It is of interest to examine the difference between the two sets of results from the crystal and glass. The difference $\chi_c - \chi_g$ has been plotted as a function of energy in Fig. 5.18. The arrows indicate the positions of extremna in the difference spectrum. Values of the extremna wavevectors k_n have been plotted against n in Fig. 5.19. This can be seen to be represented by two straight lines. The slopes of these lines yield, for line A R-a = 2.1 ± 0.2 Å and line B R-a = 3.0 ± 0.2 Å. Line A clearly corresponds to the unmatched amplitudes from first shell scattering between crystal and glass. The origin of this effect is not certain. One possible cause is the sample inhomogeneity in the case of the crystal spectrum because this material had been only coarsely powdered owing to its delicate nature. A further discussion of this effect can be found in Section 6.1. Unfortunately it is difficult to quantify this effect. The effect can be important since if it is present then it clearly complicates any analysis of the peak heights. Line B on the graph can be assigned to the second group of atoms of Table 5.5 of which the dominant scattering is contributed by the arsenic atoms at a mean distance of 3.4 Å. The value of 'a' characteristic of an atom of the size of arsenic is ~ 0.28 (see Section 5.10). This value of a then gives the estimated radius 3.3 ± 0.2 Å in good agreement with the expected crystal distance. Thus we can conclude that in the glassy phase the As-As correlation is lost. This is indicative of disorder on a very short range scale. We shall attempt to quantify this smearing of the second coordination sphere in the next section.

Although this empirical analysis is very crude there are two points to consider. Firstly the difference graph Fig. 5.18 emphasises the errors involved in interpreting the spectrum beyond the first coordination sphere. The reliability of higher shell information might well not have been appreciated had a Fourier analysis been performed on the data. Secondly, the analysis is not as crude as it appears at first sight owing to the ability of the eye to interpolate through a noisy spectrum. Thus although we are finding and plotting discrete points, their position is assessed over a range of data surrounding each point.

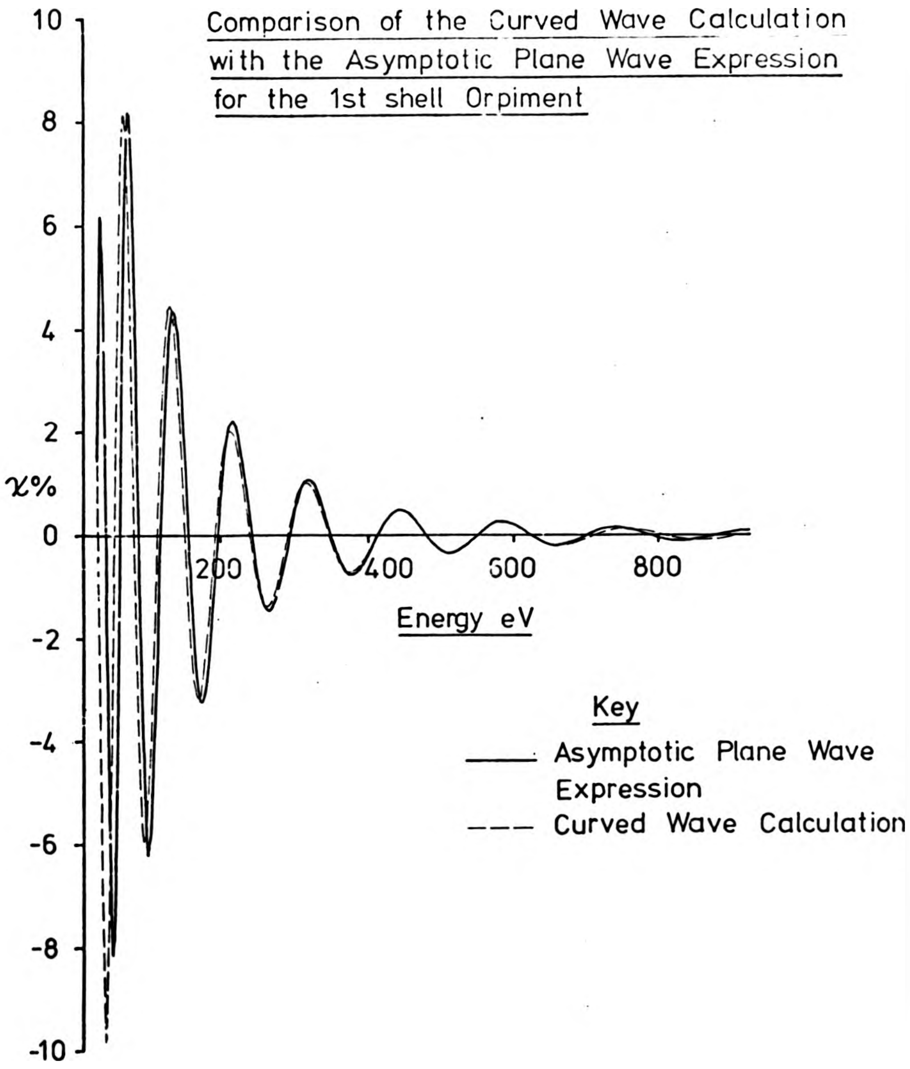

Fig.5.20. The calculated fine-structure from the first shell of sulphur atoms in orpiment using the asymptotic plane wave and curved wave theory. The shell parameters are:- $N_1= 0.5$, $R_1= 2.20$, $N_2= 0.5$, $R_2= 2.22$, $N_3= 0.5$, $R_3= 2.25$, $N_4= 1.0$, $R_4= 2.27$, $N_5= 0.5$, $R_5= 2.29$. with $\sigma_j^2= 2.0 \times 10^{-3}$ Å^2 and Ei = 4eV.

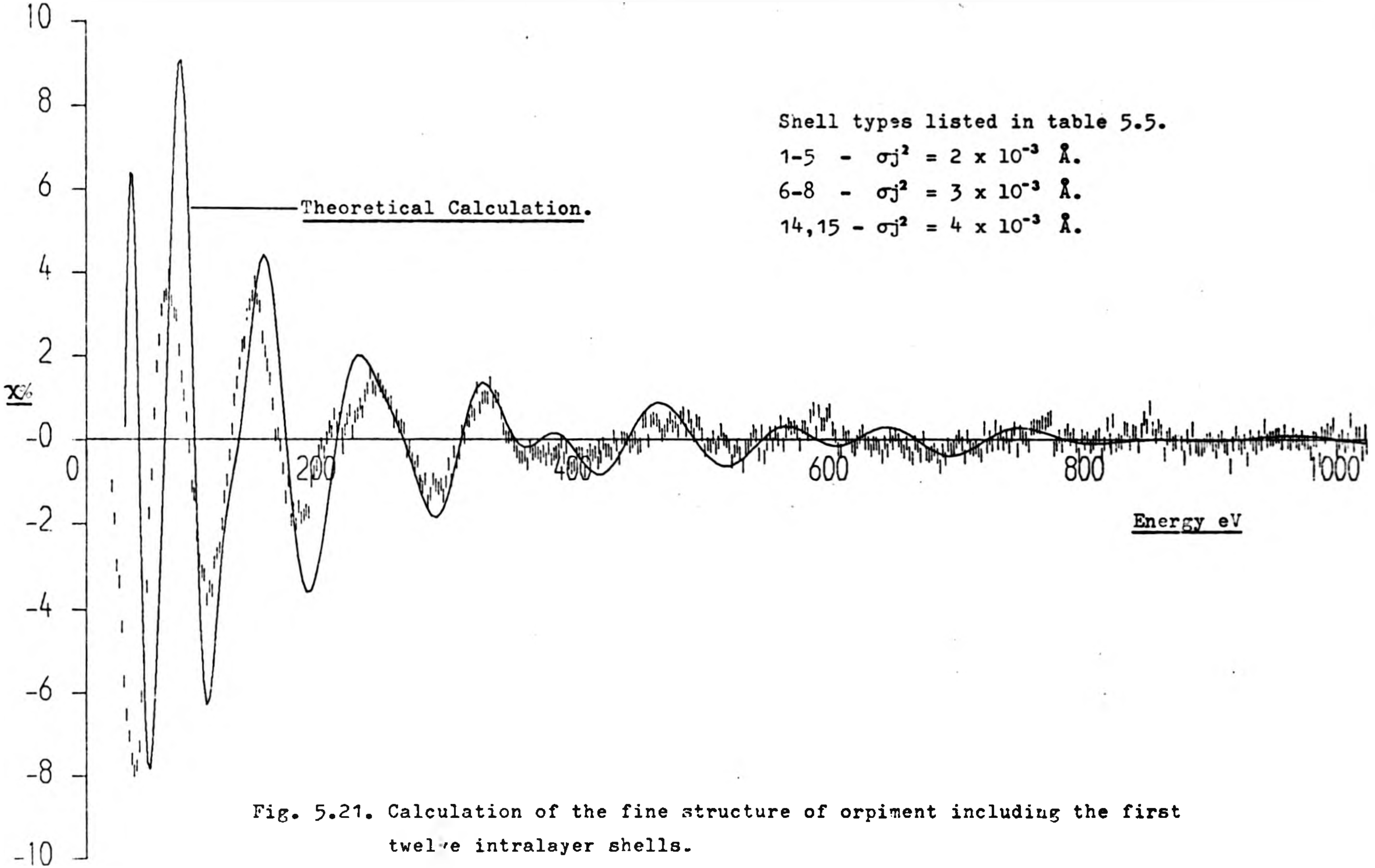

Fig. 5.21. Calculation of the fine structure of orpiment including the first twelve intralayer shells.

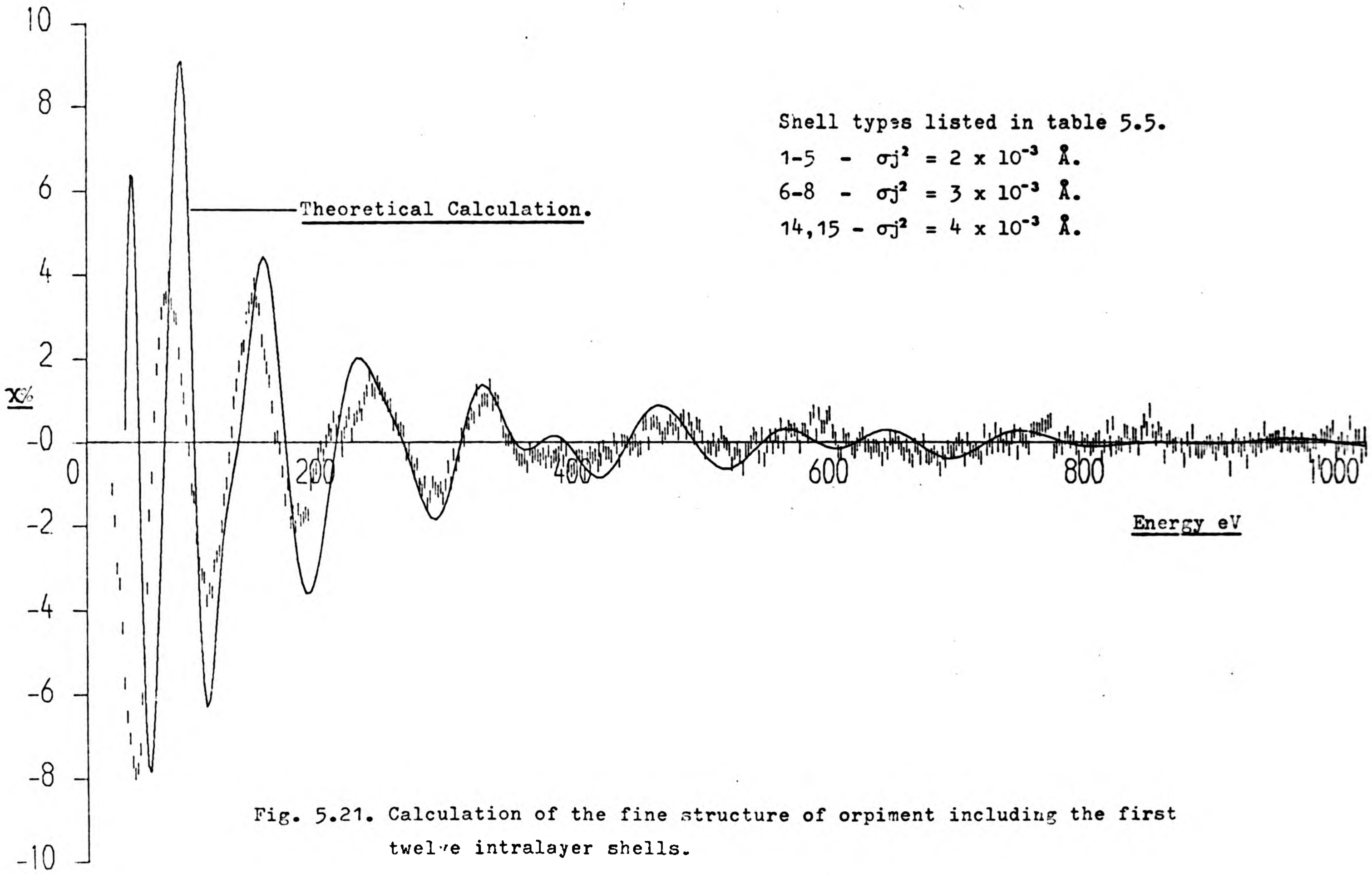

Shell types listed in table 5.5.
1-5 - $\sigma j^2 = 2 \times 10^{-3}$ Å.
6-8 - $\sigma j^2 = 3 \times 10^{-3}$ Å.
14,15 - $\sigma j^2 = 4 \times 10^{-3}$ Å.

Fig. 5.21. Calculation of the fine structure of orpiment including the first twelve intralayer shells.

5.8 Calculations of the $As_2 S_3$ fine structure

Fig. 5.20 shows a comparison of the contribution to the first shell fine structure calculated using the curved wave and asymptotic plane wave theory. The imaginary part of the self-energy was 4 eV. It can be seen that the differences between the two curves is slight and becomes insignificant above 200 eV. The phase of the curved wave calculation is, as in the case of oxygen scattering, advanced with respect to the asymptotic plane-wave case. The differences are, in fact, slightly greater than in the arsenic-oxygen case owing to the larger ion core of sulphur. Thus, we can feel justified in proceeding to calculate the spectrum using the asymptotic plane wave expression for energies in excess of 200 eV. This is just as well, because the radial crystal structure is complex and the application of the curved wave calculation would lead to excessive computing time. Figure 5.21 shows a calculated spectrum including twelve shells from Table 5.5. Again the Slater exchange phase-shifts were used as these produced much better agreement with experiment. The shell dependent σ_j^2 are given in the figure and were derived by guess-work and in no way should they be regarded as optimal. For an initial calculation the σ_j^2 parameters are arranged in ascending order governed by the number of primary bonds between the emitter and the atoms of the appropriate shell. Interlayer scattering is ignored. Above 100 eV the phase and, to a lesser extent, the amplitude from the first shell give progressively better agreement with experiment as the energy increases. Contributions from higher shell scattering which are most evident at energies in excess of 400 eV are too large and correspond to an underestimate of the values of σ_j^2. In particular, the value for the arsenic

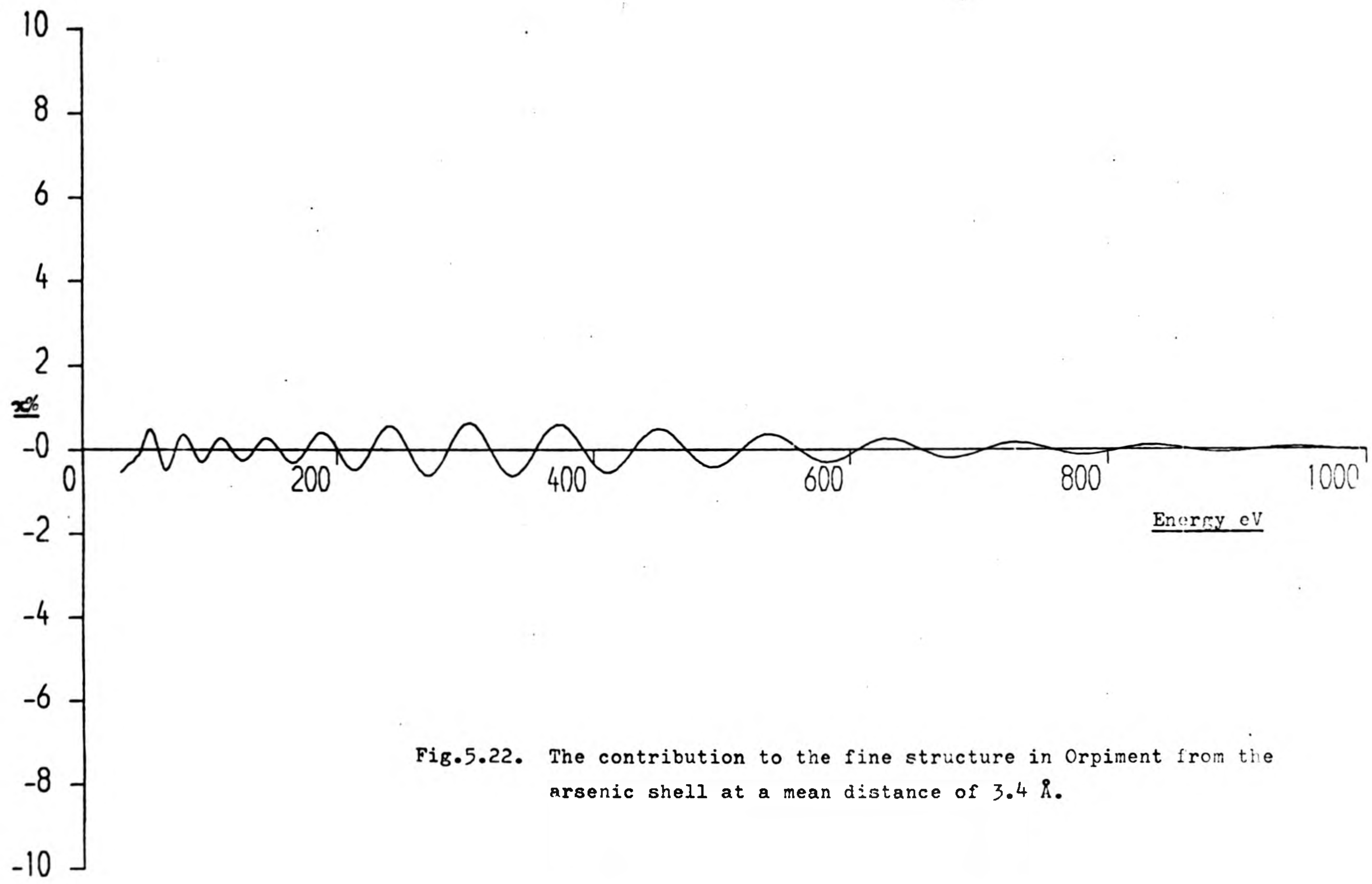

Fig.5.22. The contribution to the fine structure in Orpiment from the arsenic shell at a mean distance of 3.4 Å.

shells at ~ 3.4 Å should yield $\sigma_j^2 < 6 \times 10^{-3}$ Å^2 if the high energy structure is to be suppressed. We note also that the shoulder in the spectrum at 195 eV is also not reproduced. The reason for this arises in two ways:

a) A shell of sulphur atoms (½ atom at 3.11 Å and ½ atom at 3.17 Å) contributes to the signal from the 3.4 Å arsenic shell. Unfortunately this signal beats destructively with the arsenic contribution at about 200 eV. Thus if this feature is to be reproduced then the Debye-Waller factor for the sulphur shell must be large enough to suppress its contribution almost completely at 200 eV, i.e. σ_j^2 (sulphur at 3.11 and 3.17 Å) must be greater than 20×10^{-3} Å^2. This is not unrealistic if we remember that these atoms are connected to the emitter by three bonds. This allows relative displacement via rotation about a bond rather than bond bending which is expected to be much more rigid.

b) Removal of the sulphur scattering leaves the contribution from arsenic shown in Fig. 5.22. We note that the envelope reaches a maximum at ~ 400 eV rather than the expected 200 eV based on the calculations of $\frac{|f(\pi)|}{k}$ in Chapter 3. This is due to the increased effect of the inelastic scattering for a larger shell radius (i.e. longer path length for the photoelectron). Despite the disagreement in amplitude between the theoretical calculation and experiment, we can be consoled by the good agreement in phase and periodicity of the arsenic scattering shown in Fig. 5.22, and the difference spectrum in Fig. 5.18, which includes the positions of the calculated extremna.

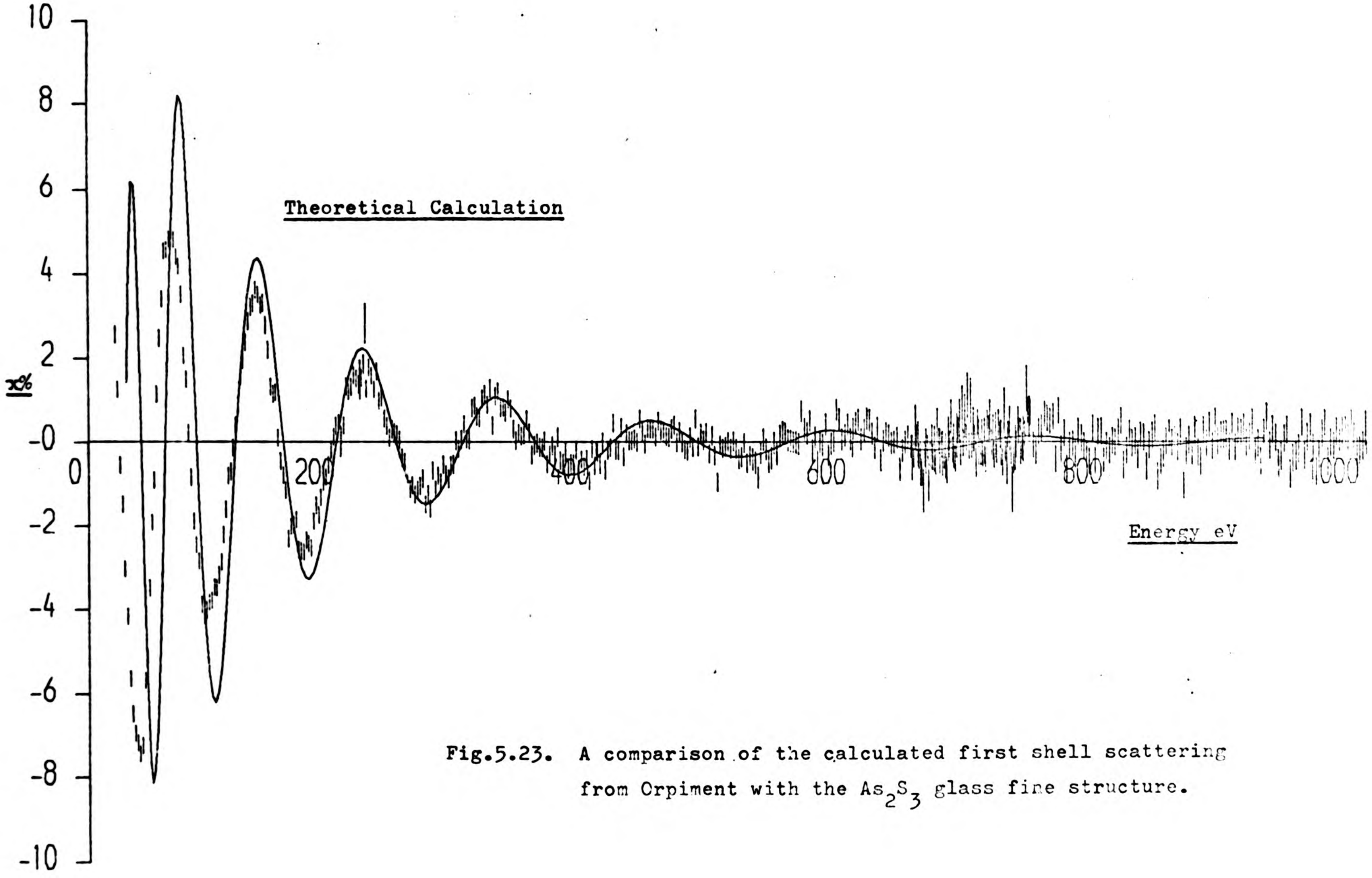

Fig.5.23. A comparison of the calculated first shell scattering from Orpiment with the As_2S_3 glass fine structure.

In Fig. 5.23 the glass fine structure is compared with a calculation performed using the first shell of crystalline orpiment. The periodicity is well reproduced for energies over 100 eV from the edge and indicates that at high energies the maximum error in phase is less than π/6, which for energies ~ 350 eV corresponds to a difference between the calculated shell radius and the experimental radius of less than 0.03 Å. Also we note that the spectrum is fitted well by just considering first shell scattering and there is no sign of the arsenic scattering contribution. Thus, to within the experimental error the increase in σ_j^2 for the arsenic shell from positional disorder must be greater than 22×10^{-3} Å^2. This can be produced, if we assume rigid bond lengths by a root mean square distribution of As - S - As bond angles > 5° from the crystal values. It must be noted that although the phase and periodicity of the fine structure is well reproduced the amplitude of the calculated fine structure is too large. This point is referred to again in Section 6.2.

In summary, we may conclude that:

a) The first shell of As_2S_3 glass has the same bond length as the crystal and consists principally of sulphur atoms;

b) The adjacent arsenic atoms are distorted from their crystalline positions, and this can be explained by a distribution of As - S - As bond angles with root mean square distortion greater than 5°;

c) The Slater exchange phase-shifts provide a good description of the phase and periodicity of the fine structure from the first shell in the crystal for photoelectron energies in excess of 100 eV: however the amplitude from higher shells is too weak to explain the experimental results, although the phase and periodicity are correct.

5.9 Preparation and Properties of $As_2 Se_3$

Arsenic selenide behaves in a similar manner and has similar properties to $As_2 S_3$. The glassy material is easily prepared by melting the elements in the correct stoichiometric proportions in a sealed ampoule under vacuum as we have discussed in Section 5.1. The melt was homogenised for 24 hours at 600° C and air quenched to room temperature. Films were prepared by ball milling the glass and casting into a plastic film. Unlike crystalline $As_2 S_3$, the selenide can be grown by vapour transport. Creveceour and De Wit (1972) have given details of how this can be accomplished. It was found that the nucleating phase of the growth process was not necessary and transport took place between the melt held at 400°-370° C and the crystal growth region at 330°-350° C. It was found that it is necessary to incorporate a weir in the quartz ampoule to prevent the glass from flowing into the crystal growing region. Droplets of glass were however formed in a hot zone of the crystal growing region at approximately 340° C via transport by iodine. These droplets also converted after some time into crystalline material. Other crystals grew apparently directly from the vapour at 330° C. This confirms the results of Crevecoeur and De Wit, who found two distinct types of crystal morphology. The first type of crystal formed in star-shaped clusters radiating from a single point on the surface of the quartz, presumably an imperfection acting as a nucleating centre. These crystals were flat and planar in nature with thicknesses rarely exceeding 0.1 mm. The other type of crystal which grew from the condensed droplets of glass was rod-like and had thicknesses up to 1 mm. A photograph of the largest crystal formed from the liquid phase after a three-month growth period is shown in the photograph below:

Fig. 5.24 Photograph of the largest single crystal of $As_2 Se_3$ formed from crystallisation of glass droplets rather than formed from the vapour.

The crystals were crushed and milled to form an absorption film. X-ray diffraction of the material showed no signs of amorphisation from milling in contrast to the behaviour of the As_2S_3 crystals. The crystal structure of $As_2 Se_3$ has been determined by Vaipolin (1966) and Renninger and Averbach (1973). Both authors quote the same reliability factor for their measurements but the data of Vailpolin is preferred as this is a single crystal study. The structure is isomorphous with orpiment with the space group $P2_1/n$. The radial structure about arsenic is given in table 5.7,

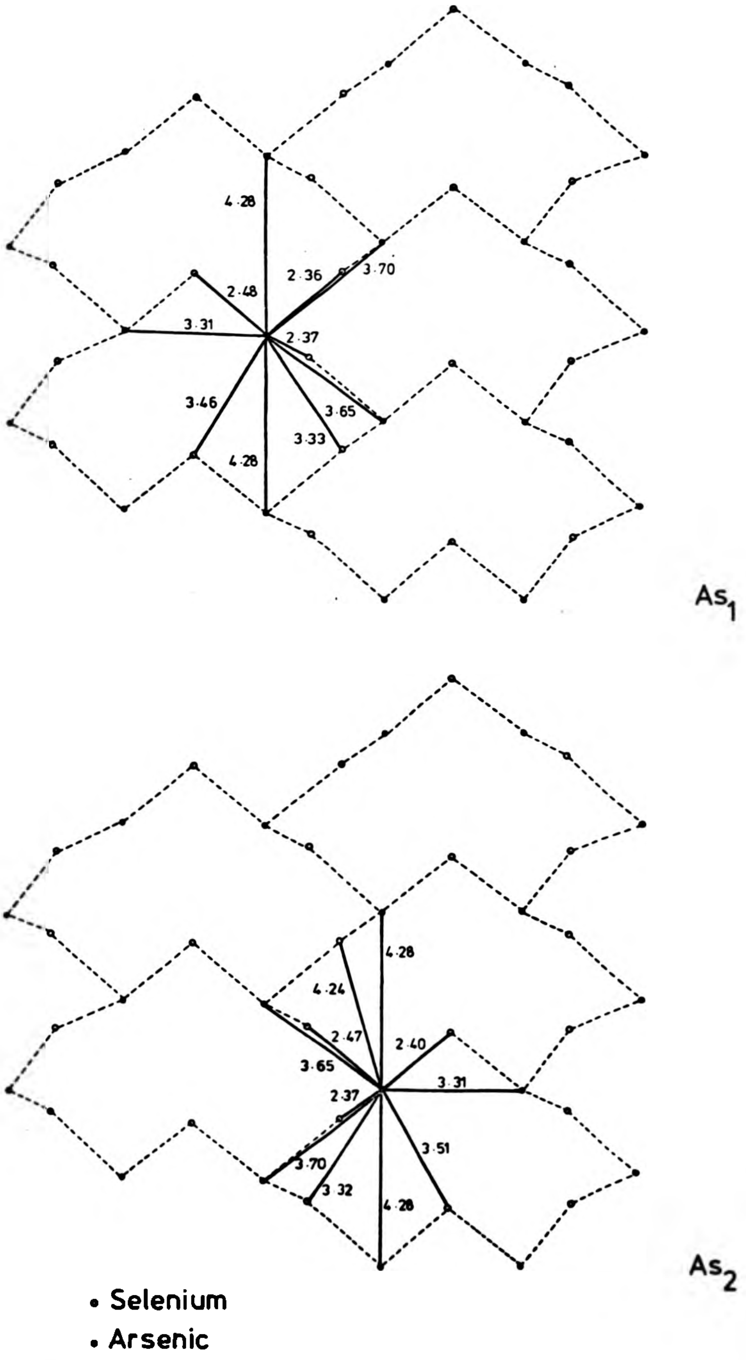

Fig.5.25. A projection of the intra-layer distances from arsenic crystalline As_2Se_3

and a projection onto the ac plane is shown in Fig. 5.25. The crystals are black and exhibit the same ease of cleavage and small Davydov splitting of the infra-red lines as observed in $As_2 S_3$ (Zallen, Slade and Ward 1971). The expected shells which will contribute to the fine structure are similar to those for $As_2 S_3$, however the similarity of atom size complicates the different atom contributions, but the main contribution to the arsenic edge fine-structure should be made by the first shell of selenium atoms at a mean distance from the emitter of 2.41 Å.

TABLE 5.7

N	Radius Å	Type	Position
0.5	2.36	Se	Intralayer
1.0	2.37	Se	Intralayer
0.5	2.40	Se	Intralayer
0.5	2.47	Se	Intralayer
0.5	2.48	Se	Intralayer
1.0	3.31	As	Intralayer
0.5	3.32	Se	Intralayer
0.5	3.33	Se	Intralayer
0.5	3.46	Se	Intralayer
0.5	3.52	Se	Intralayer
0.5	3.61	Se	Interlayer
1.0	3.65	As	Intralayer
0.5	3.69	As	Interlayer
1.0	3.70	As	Intralayer
0.5	3.72	Se	Interlayer
0.5	4.06	Se	Interlayer
0.5	4.17	Se	Interlayer
0.5	4.24	Se	Intralayer
2.0	4.28	As	Intralayer

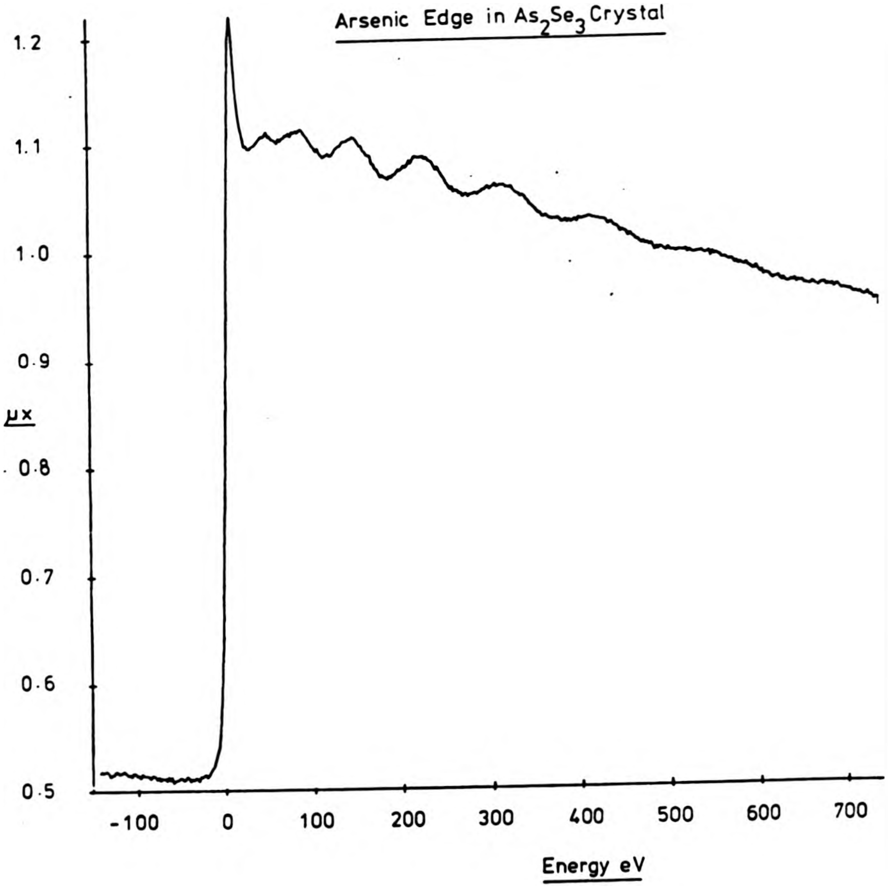

Fig.5.26. The arsenic K absorption spectrum in As_2Se_3 crystal.

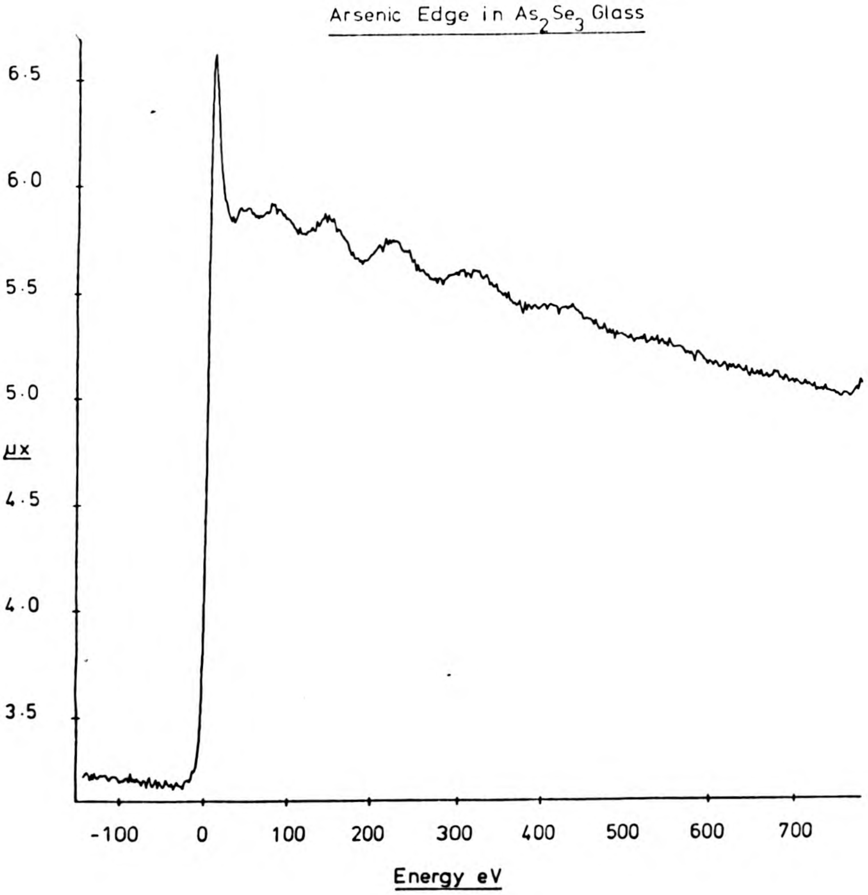

Fig.5.27. The arsenic K absorption spectrum in As_2Se_3 glass.

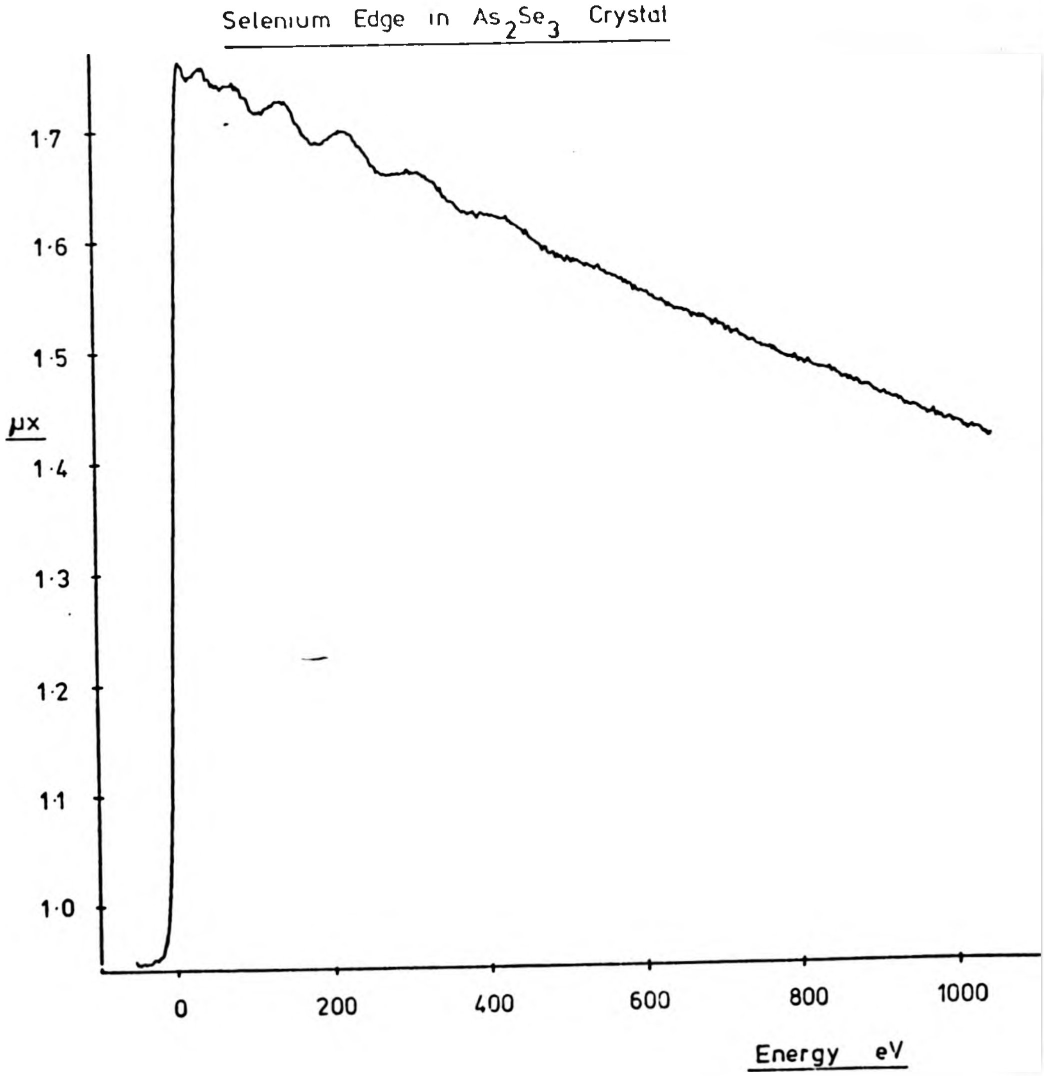

Fig.5.28. The selenium K absorption spectrum in As_2Se_3 crystal.

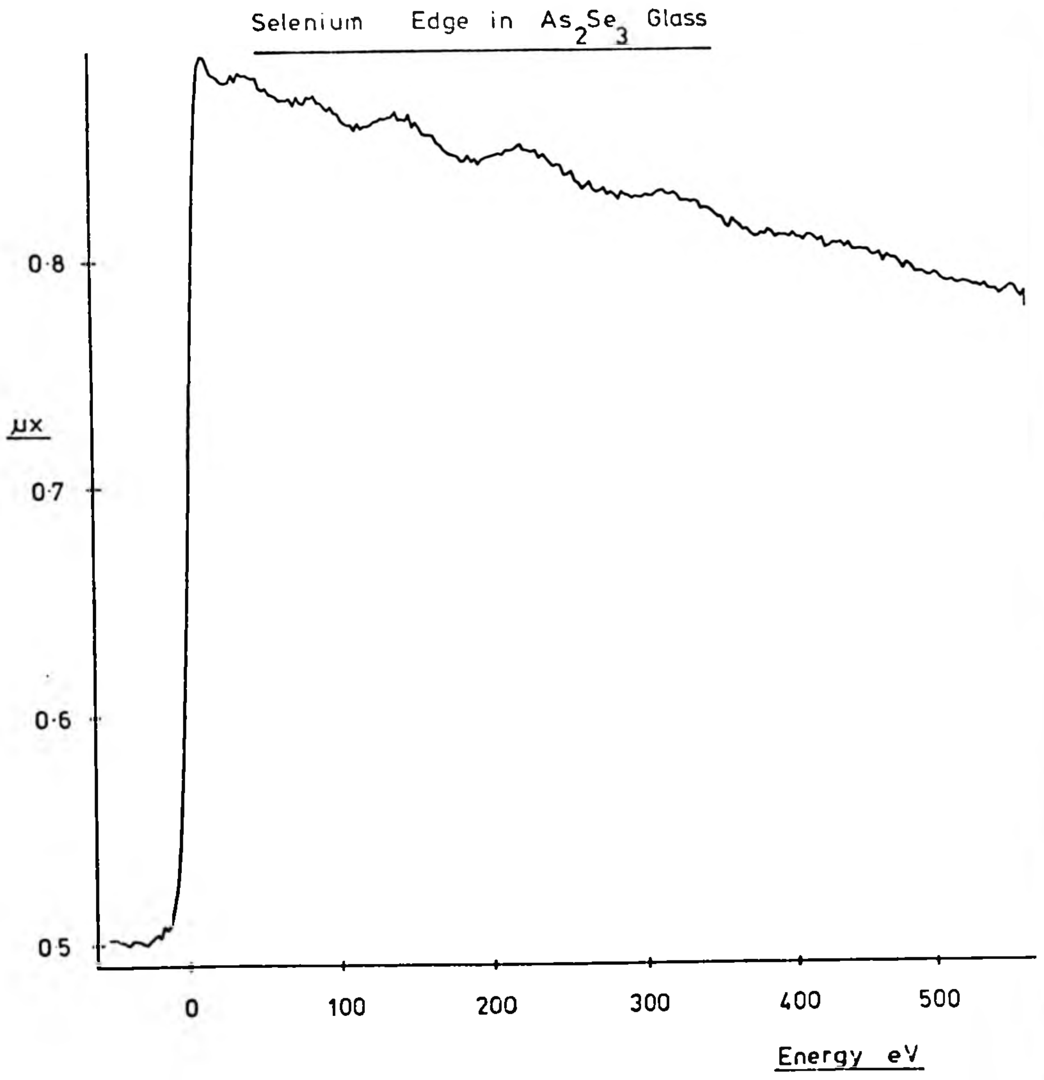

Fig.5.29. The selenium K absorption spectrum in As_2Se_3 glass.

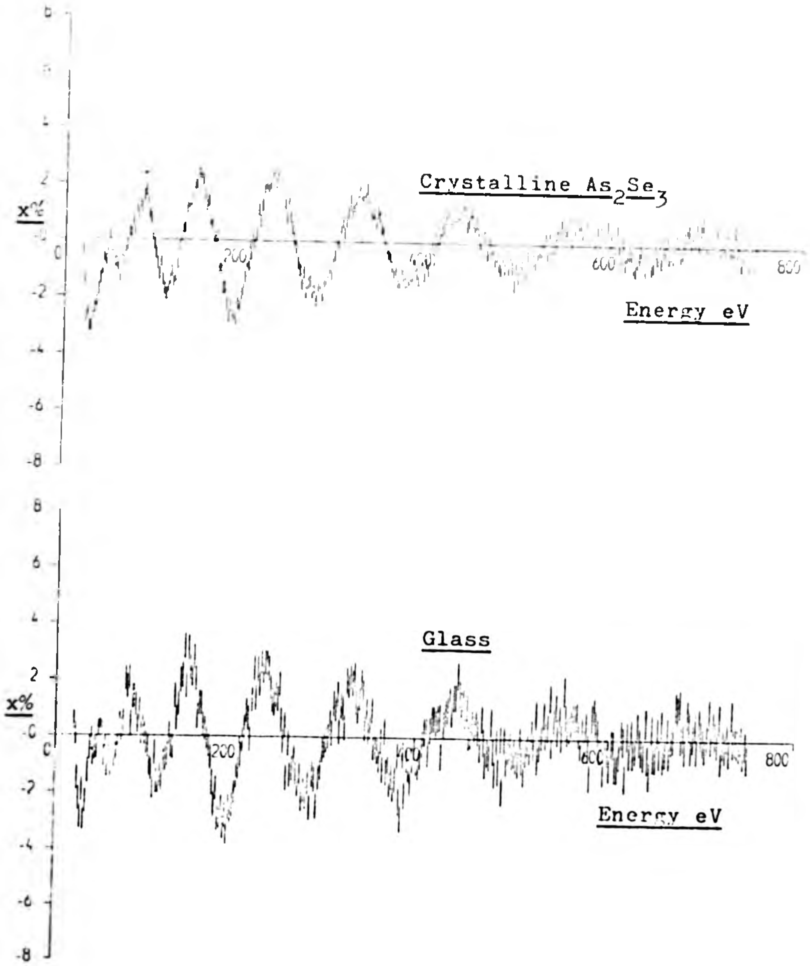

Fig.5.30. The arsenic edge fine-structure in crystalline and glass As_2Se_3.

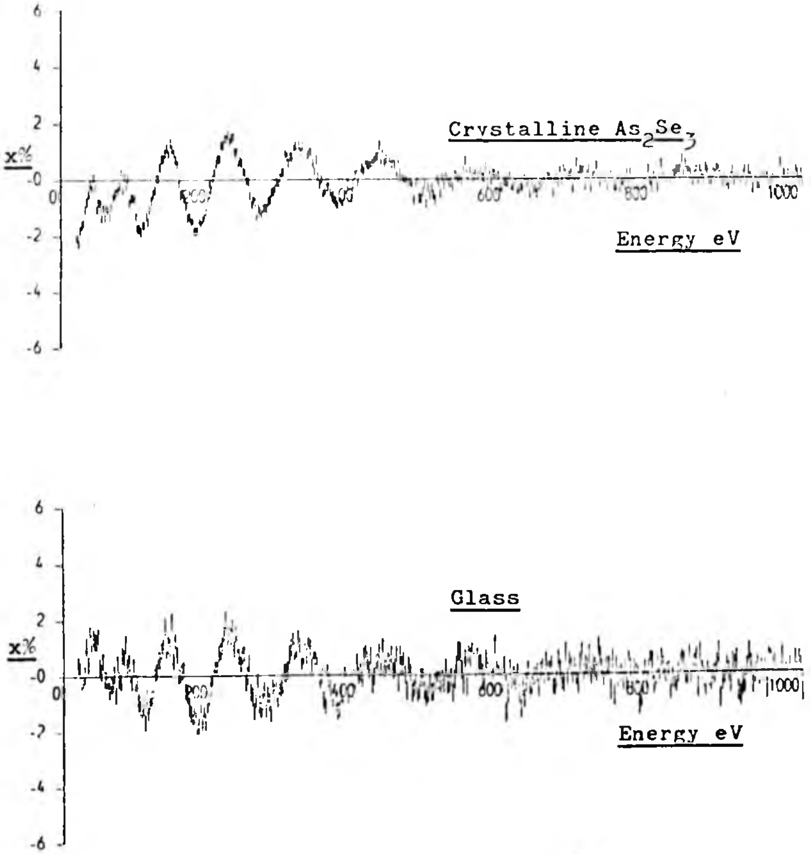

Fig.5.31. The selenium edge fine-structure in crystalline and glass As_2Se_3.

5.10 Discussion of the $As_2 Se_3$ Spectra

We are fortunate in the case of $As_2 Se_3$ to be able to examine both the arsenic and selenium edges in the same material. The raw absorption spectra are shown in Figs. 5.26-5.29. The most striking feature is the presence of a spike at the absorption edge for the arsenic edge in each material. In contrast, the selenium edge appears not to possess this feature; however, higher resolution synchrotron studies have shown that selenium also possesses a spike but this spike is followed by a dip. The finite resolution of the spectrometer used in this study smears both of these features to yield a structureless edge. The fine structures of these edges are plotted in Figs. 5.30 and 5.31. The envelopes of both curves show a rise to a maximum at approximately 200 eV; however, the low amplitude of the fine structure close to the edge is not that predicted by the $\frac{|f(\pi)|}{k}$ curves shown in Fig. 3.3.

From an analysis of the difference between the spectra of both the Se and As edges in these materials we cannot find any difference of statistical significance. The data also possesses smooth variations in amplitude and phase and thus it appears that scattering from higher shells is very small and contributes χ (shells > the first) < 0.3%. The general shape of the EXAFS structure is reproduced by the measurements of Sayers, Lytle and Stern (1974) although a more detailed comparison is not possible with their data. Their crystalline data does show a peak in the Fourier transform at 3.66 Å compared with a mean next-nearest neighbour (in terms of bond counting) peak of 3.55 Å. Also this peak is comparable in height with structure found in the

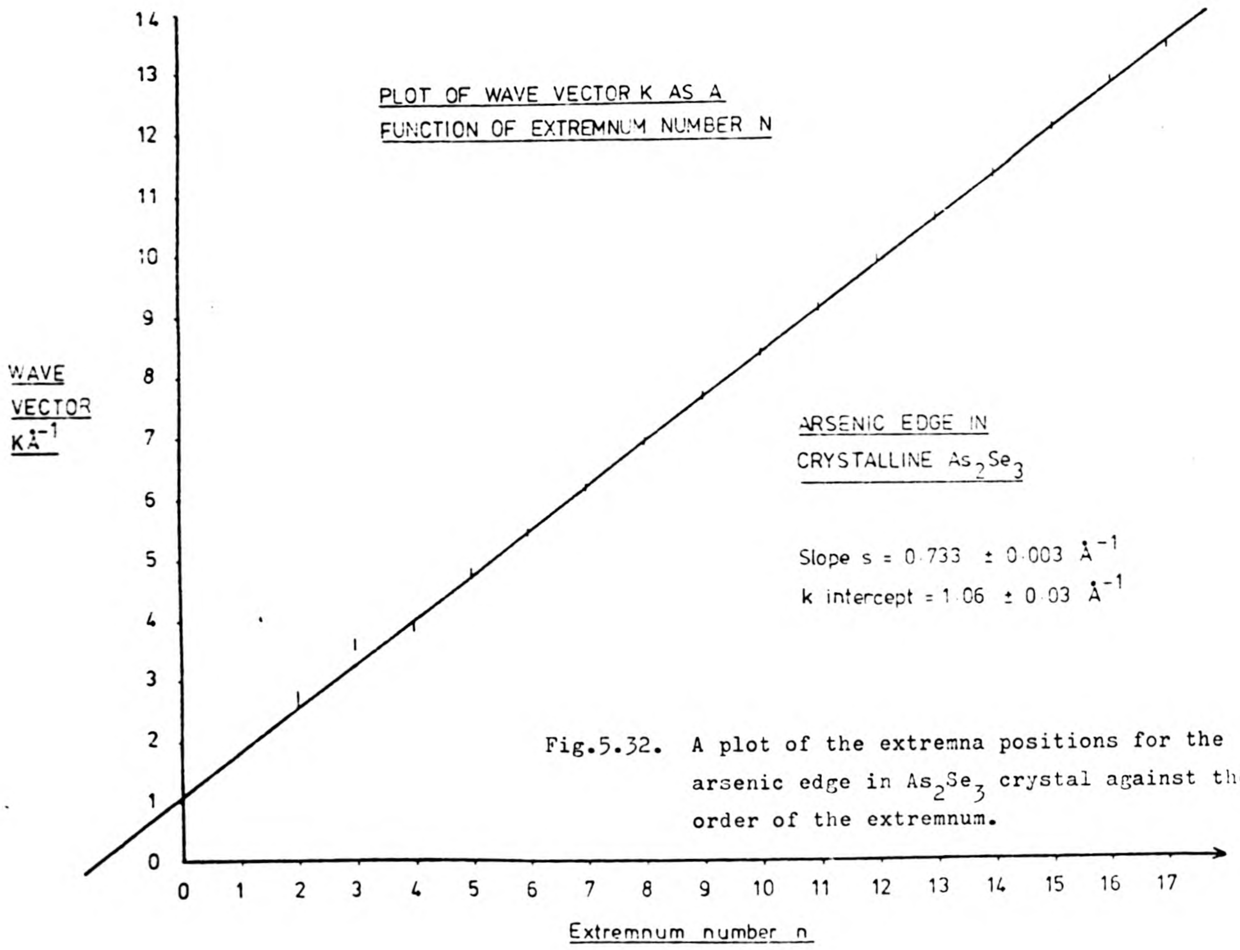

Fig.5.32. A plot of the extremna positions for the arsenic edge in As_2Se_3 crystal against the order of the extremnum.

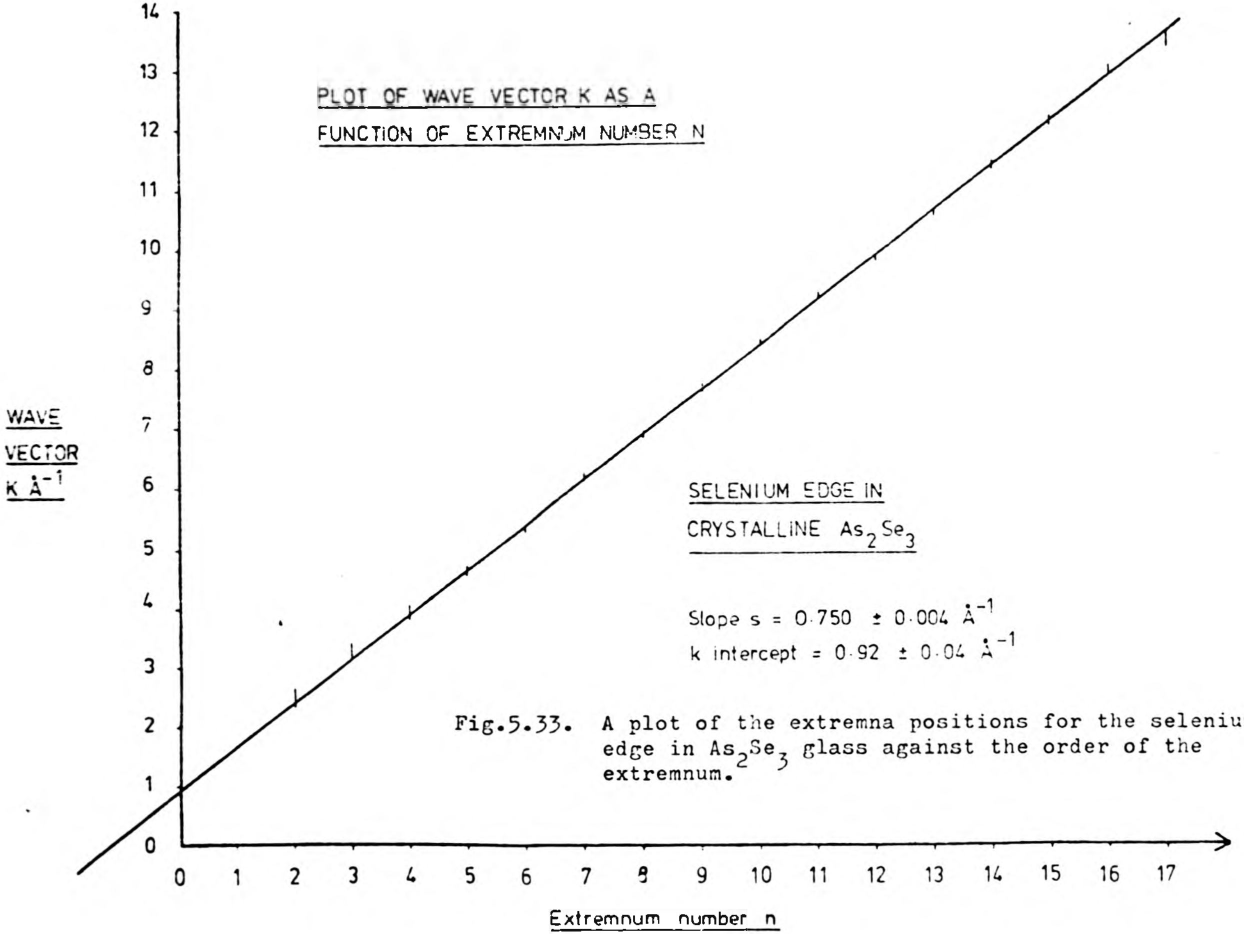

Fig.5.33. A plot of the extremna positions for the selenium edge in As_2Se_3 glass against the order of the extremnum.

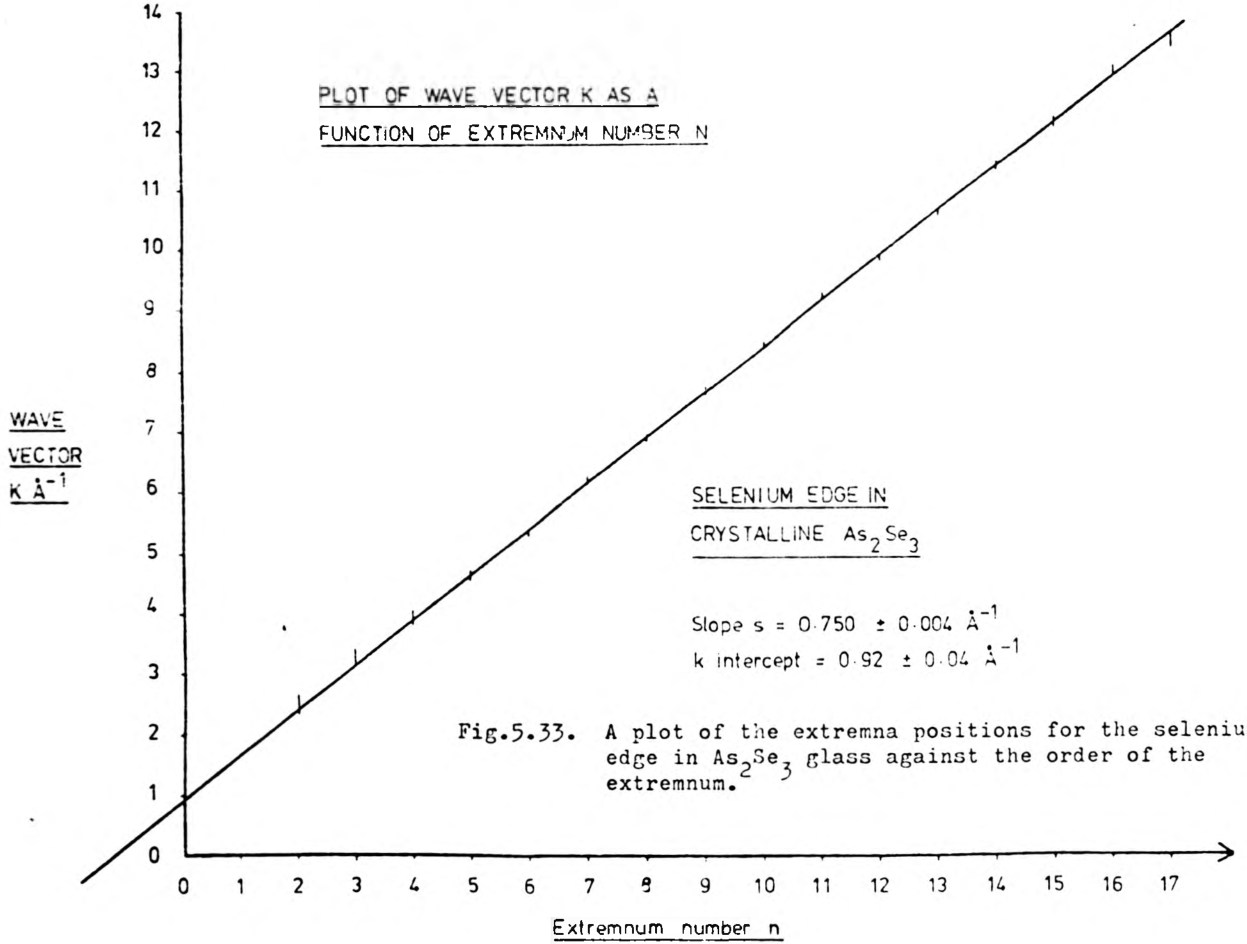

Fig.5.33. A plot of the extremna positions for the selenium edge in As_2Se_3 glass against the order of the extremnum.

transform of $As_2 S_3$ glass data, which, to within our experimental error (which is comparable to Sayers, Lytle and Stern) could be accounted for by just first neighbour scattering.

The first type of analysis which can be performed is a verification of the composition of the material. Although we have no reason to suspect that the material is non-stoichiometric, as it was formed in a sealed silica ampoule, we can perform a test using the ratio of the heights of the arsenic and selenium edges between crystal and glass. Assuming that the crystal is perfectly stoichiometric this analysis yields a value of the composition of the glass as $As_2 Se_{3.1}$ ± 0.1 which is, to within experimental error the anticipated composition.

It is convenient at this point also to test the linearity of peak position measured in $Å^{-1}$ against the order of the peak n as we performed for $As_2 S_3$. The wide energy range of data and the absence of any discernable higher shell structure makes this an easy task. The energies of the extremna of the fine structure are summarised in Table 5.8 for both crystal and glass, and the results of this analysis are plotted for both edges in Figs. 5.32 and 5.33. For both the arsenic and selenium edges the results are remarkably linear with some small deviation below 4 $Å^{-1}$ (60 eV) for both materials. If we assume that the first neighbour bond length is 2.41 Å from Vailpolin's results this yields for "a" in the case of an arsenic emitter and selenium scatterer a value 0.267 ± 0.01 Å, and for a selenium emitter and arsenic scatterer a = 0.316 ± 0.01 Å. The difference is small owing to similarity of the potentials of the arsenic and selenium atoms. From a comparison of the extremna energies in the same manner

TABLE 5.8

Arsenic Edge			Selenium Edge		
n	Crystal (eV)	Glass (eV)	n	Crystal (eV)	Glass (eV)
2	27.0 ± 3.0	30.0 ± 3.0	2	23.0 ± 3.0	25.0 ± 3.0
3	49.5 ± 3.0	48.5 ± 3.0	3	41.5 ± 3.0	41.0 ± 3.0
4	59.0 ± 3.0	59.5 ± 3.0	4	59.0 ± 3.0	63.0 ± 3.0
5	87.0 ± 3.0	82.0 ± 3.0	5	83.0 ± 3.0	81.0 ± 3.0
6	112.0 ± 3.0	112.0 ± 3.0	6	108.0 ± 3.0	111.0 ± 3.0
7	146.0 ± 3.0	146.0 ± 4.0	7	146.0 ± 3.0	142.0 ± 3.0
8	182.0 ± 3.0	185.0 ± 4.0	8	181.0 ± 3.0	182.0 ± 3.0
9	225.0 ± 4.0	226.0 ± 4.0	9	225.0 ± 3.0	225.0 ± 3.0
10	268.0 ± 4.0	272.0 ± 4.0	10	270.0 ± 3.0	275.0 ± 3.0
11	318.0 ± 4.0	319.0 ± 5.0	11	324.0 ± 3.0	321.0 ± 4.0
12	373.0 ± 6.0	373.0 ± 5.0	12	373.0 ± 4.0	372.0 ± 4.0
13	428.0 ± 6.0	433.0 ± 5.0	13	431.0 ± 5.0	429.0 ± 5.0
14	488.0 ± 6.0	491.0 ± 6.0	14	495.0 ± 6.0	497.0 ± 5.0
15	553.0 ± 7.0	549.0 ± 7.0	15	561.0 ± 7.0	553.0 ± 6.0
16	627.0 ± 7.0	622.0 ± 9.0	16	641.0 ± 8.0	614.0 ± 8.0
17	687.0 ± 9.0	693.0 ± 13.0	17	689.0 ± 15.0	699.0 ± 11.0

Energies of the extremna of the fine structure measured relative to the centre of the absorption edge. The extremnum number n is even for a dip.

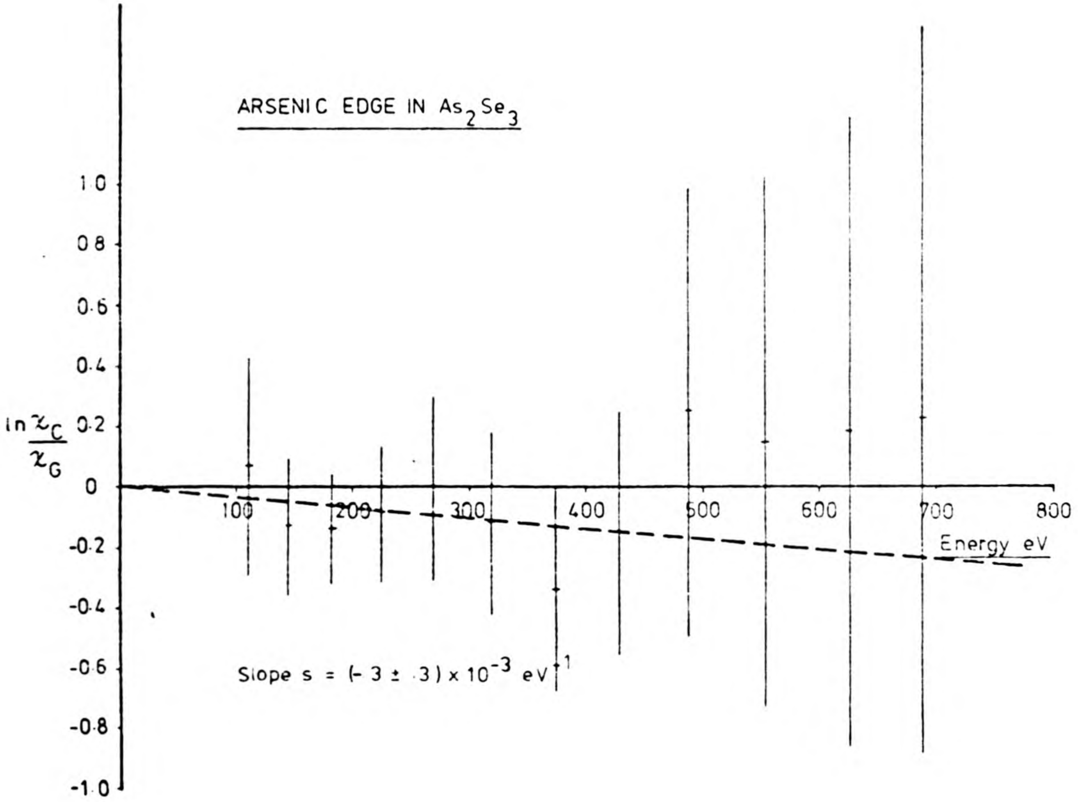

Fig.5.34. A graph of $\log_e$ of the amplitude ratio between crystal and glass for As_2Se_3. ($\ln \frac{x_C}{x_G}$) against photo-electron energy.

Data from the arsenic edge.

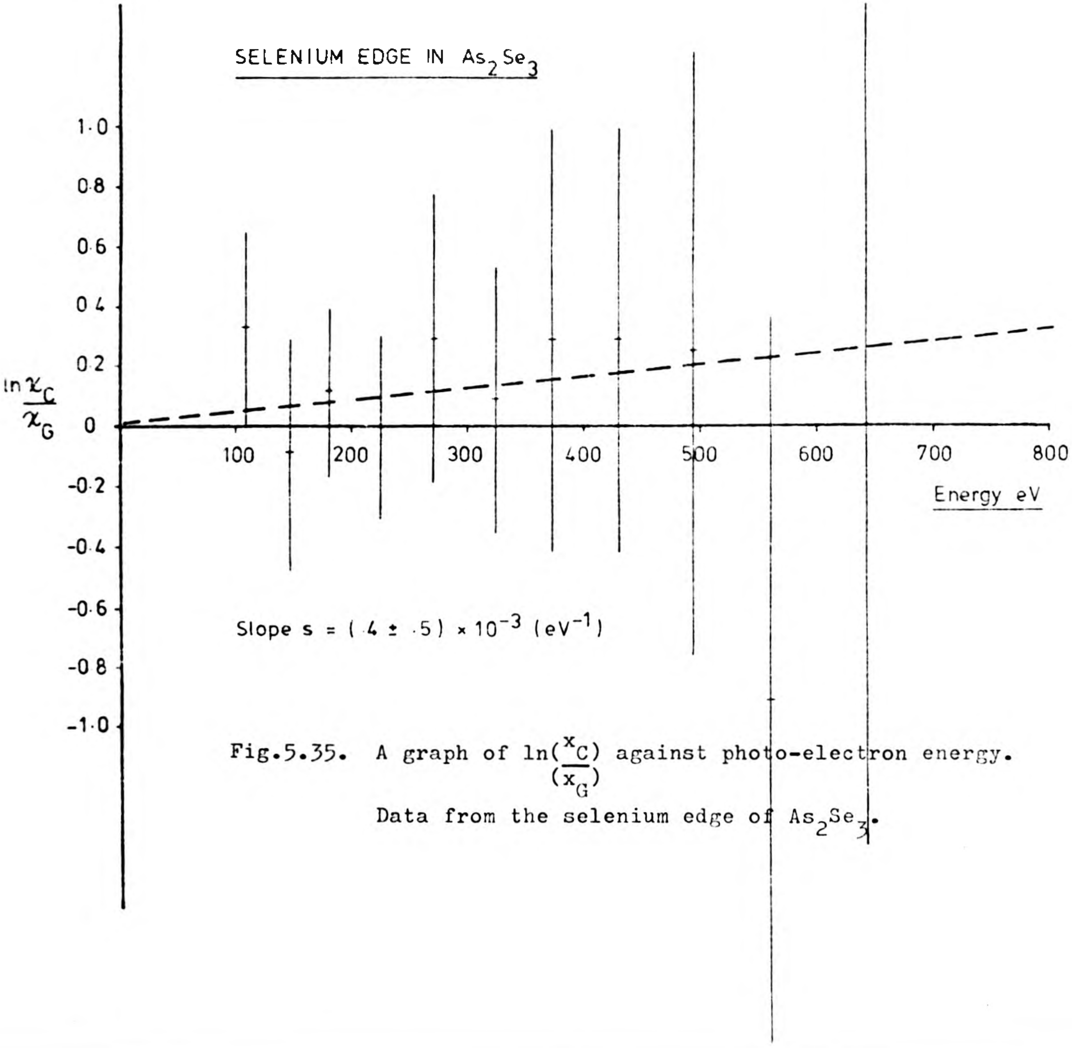

Fig.5.35. A graph of $\ln\left(\frac{x_C}{x_G}\right)$ against photo-electron energy.

Data from the selenium edge of As_2Se_3.

as performed for $As_2 S_3$ we find a value

$$\frac{E_c}{E_g} = \left(\frac{R_G - a}{R_c - a}\right)^{\frac{1}{2}} = 0.997 \pm 0.006$$

which yields a change in bond length ΔR of + 0.01 ± 0.01 Å. The results for the Se edge in the same material gave a value of $\Delta R = 0.00 \pm 0.01$ Å. Thus, to within 0.01 Å, the mean bond length in both crystal and glass is the same.

Both the arsenic and selenium edges in these materials contain enough information and freedom from higher shell contamination to analyse the peak heights. If we assume that the phase shifts and inelastic loss are transferrable between crystal and glass then knowing that the bond lengths are the same and also that the valency of each atom is unchanged and fully satisfied, then

$$\ln\left(\frac{\chi_c}{\chi_G}\right) = -2\,\Delta\sigma^2\, k^2 \qquad 5.9$$

where $\Delta\sigma^2$ is the change in positional smearing between crystal and glass, and χ_c and χ_G are values of the fine structure for crystal and glass respectively.

A plot of $\ln \frac{\chi_c}{\chi_G}$ as a function of energy in eV then gives a slope s such that

$$\Delta\sigma^2 = 1.90\ s\ \text{Å}^2. \qquad 5.10$$

This analysis has been performed for the peaks above 50 eV for both edges and is shown in Figs. 5.34 and 5.35. From the analysis we can conclude that the change is $\Delta\sigma^2 = (-0.5 \pm 0.5)\times10^{-3}$ Å^2 for the arsenic edge and $(0.5 \pm 0.5)\times10^{-3}$ Å^2 for the selenium edge.

This is much less than the expected thermal contribution of $\sigma_T^2 \approx 2 \times 10^{-3}$ Å^2.

In conclusion we can say:-

a) The glass has the same first shell radius as the crystal

b) the additional first neighbour disorder in the glass is less than four times the thermal contribution

c) above 60 eV in energy the linear phase shift model is adequate to describe experiments of the statistical accuracy shown here.

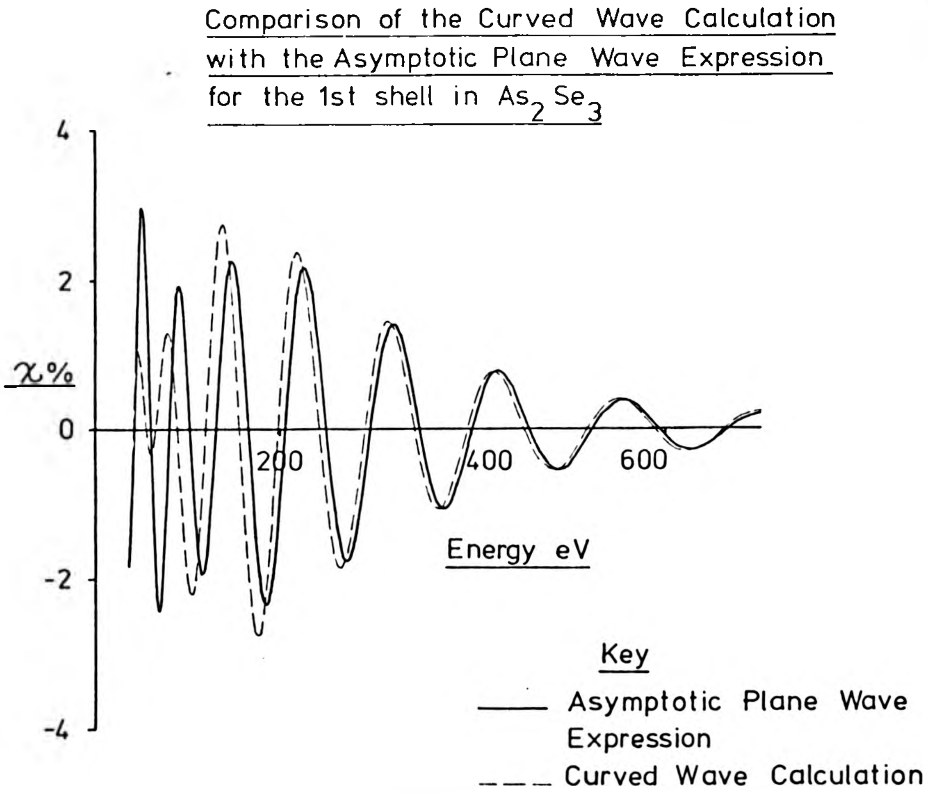

Fig.5.36. A comparison of the fine structure from the first shell of As_2Se_3 calculated from the asymptotic plane wave and curved wave theory.

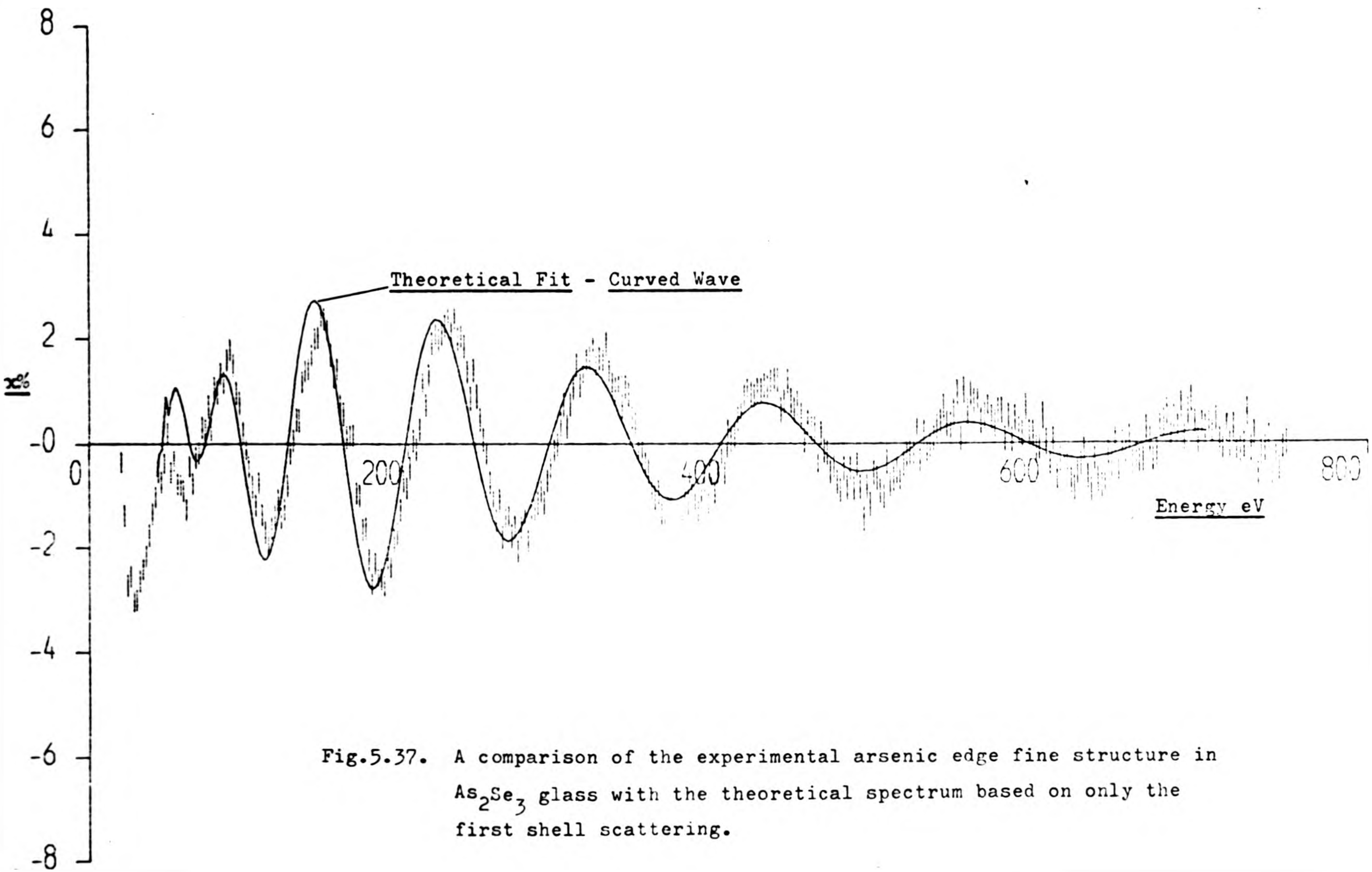

Fig.5.37. A comparison of the experimental arsenic edge fine structure in As_2Se_3 glass with the theoretical spectrum based on only the first shell scattering.

5.11 Calculation of the As_2 Se_3 fine structure

We have seen in the previous section that there is no detectable difference in the spectra of crystalline and glassy As_2 Se_3 so we will concentrate on the crystal spectrum. Figure 5.36 shows a comparison of the calculated fine structure of the arsenic edge from the first shell of selenium scatterers using the curved wave and asymptotic plane wave theory. Unlike the previous comparisons, the effects of wave curvature has a significant influence in the energy region < 200 eV. These effects are comparable in magnitude to those found for the first shell of copper by Lee and Pendry (1975) owing to the similar size of the ion core potential of copper and selenium. The origin of the reduction of amplitude of the fine structure close to the edge compared to that expected from the $\frac{|f(\pi)|}{k}$ plots can now be seen as a consequence of the wave curvature effect.

As an initial attempt, the first shell of As_2 Se_3 was taken and with the values of σ_i^2 of 2.5×10^{-3} Å^2 and radii given in Table 5.7. A comparison of the theoretical calculations based on the curved wave theory is given in Fig. 5.37. We note here, the excellent agreement of the phase and periodicity with experiment. This can be made even better by a small shift of the zero of the optical potential to lie approximately 5 eV above the centre of the absorption edge. This brings most of the peaks into alignment with the experimental data. The experimental data are well described by theory even below 100 eV. Allowing for the 5 eV shift, then the phase of the EXAFS structure is reproduced to within $\pi/10$ radians at high energies which corresponds to an accuracy in bond length of 0.01 Å.

It is worth noting that the success of the linear phase-shift model for all extremna found in the previous section above 60 eV comes from the cancellation of curvature in the sum of the emitter potential phase-shift η_I, the phase of the backscattering amplitude and the modification of the phase by the wave curvature effect. In the region below 150 eV the phase-shifts and amplitudes of the structure are thus not transferrable to higher shells owing to curvature effects. This is important because it is in this low energy that effects of shells,other than the first are likely to be observed. The amplitude presents special problems which have not been treated so far and a full discussion can be found in Section 6.2.

5.12 The Structure of $As_2 S_3 Se_3$ Glass

In this section we wish to use the very powerful aspect of EXAFS which is its ability to determine the local environment of a given atom. We have seen from the previous sections that the environment of arsenic in $As_2 S_3$ and $As_2 Se_3$ is changed very little in moving from the crystal to the glass and this can be attributed to the rigidity of the covalent bond length. Thus, it seems a reasonable assumption that the As-S and the As-Se bond lengths are not likely to vary when in a three component material made up of arsenic sulphur and selenium. Further, from the calculations of Chapter 3, it is quite clear that both the phase and the backscattering amplitude from sulphur and selenium are quite distinctive and thus we should expect good discrimination between As-S and As-Se bonds. The composition of the glass was chosen to be $As_2 S_3 Se_3$ as this gives arsenic an equal opportunity to bond to sulphur or selenium. This composition also lies in the centre of a large glass forming region (Flaschen, Pearson and Northover 1959, 1960). Naively, we might expect that the heteropolar bonding is stronger than homopolar bonding because in the former we have a certain degree of ionic component. On the Pauling electronegativity scale the As-S bond will have a 6% ionic character and the As-Se bond is 4% ionic. It has been suggested by Rechtin, Renninger and Averbach (1974) that the distribution of bond types should be weighted according to a Maxwell Boltzmann factor involving the difference in bond energy. If we adopt this model then small differences in bond energy ~3 K cal/mole are sufficient to cause one bond to dominate the first shell coordination. The cohesive energy for other more

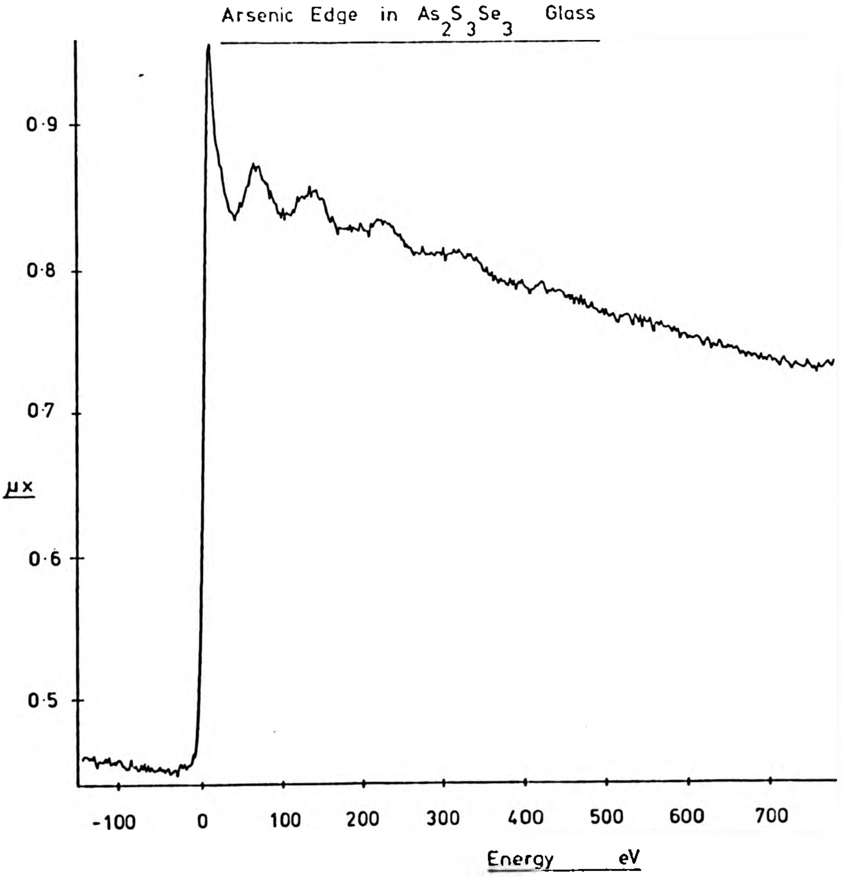

Fig.5.38. The arsenic K absorption edge in $As_2S_3Se_3$.

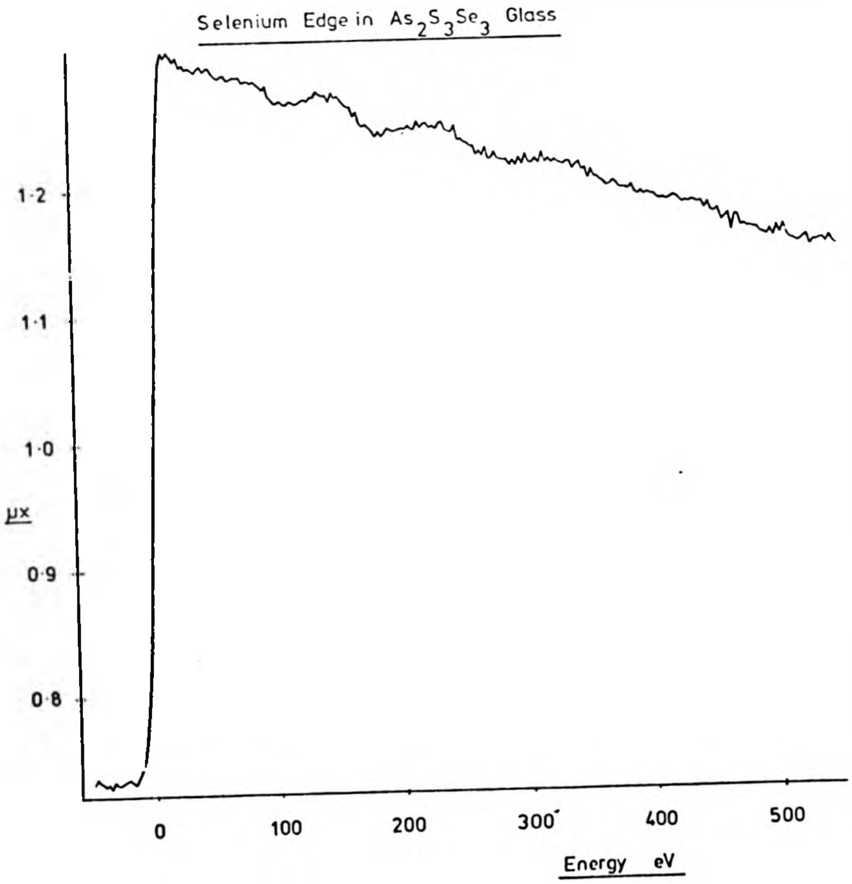

Fig.5.39. The selenium K absorption edge in $As_2S_3Se_3$.

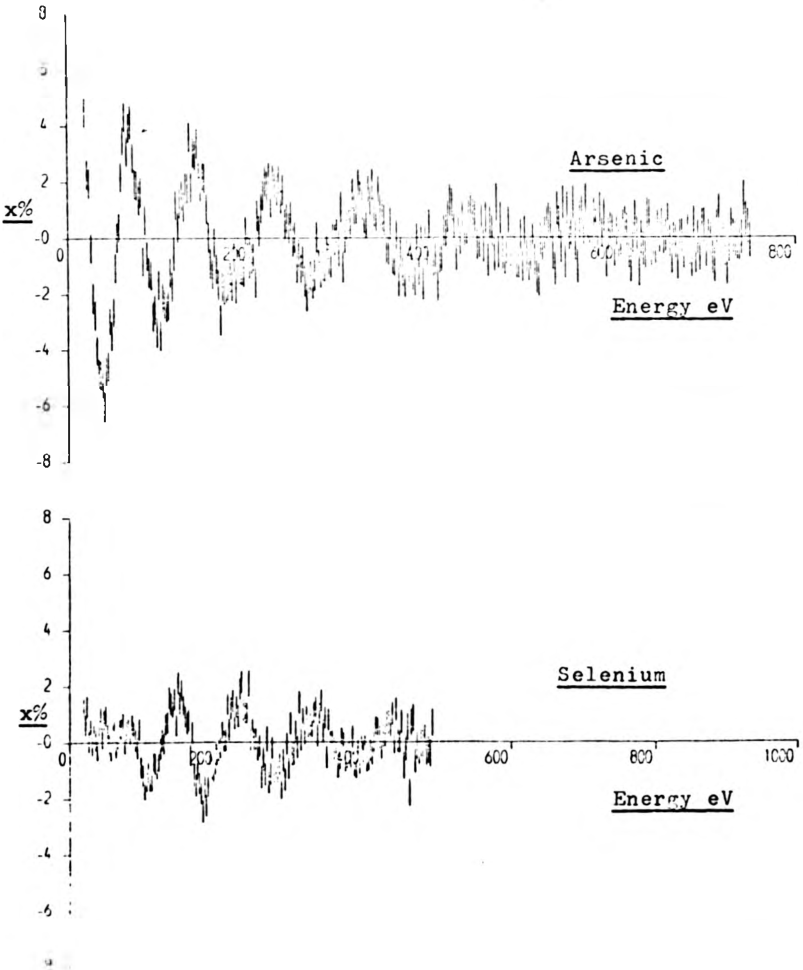

Fig.5.40. The fine-structure from the arsenic and selenium edge in $As_2S_3Se_3$.

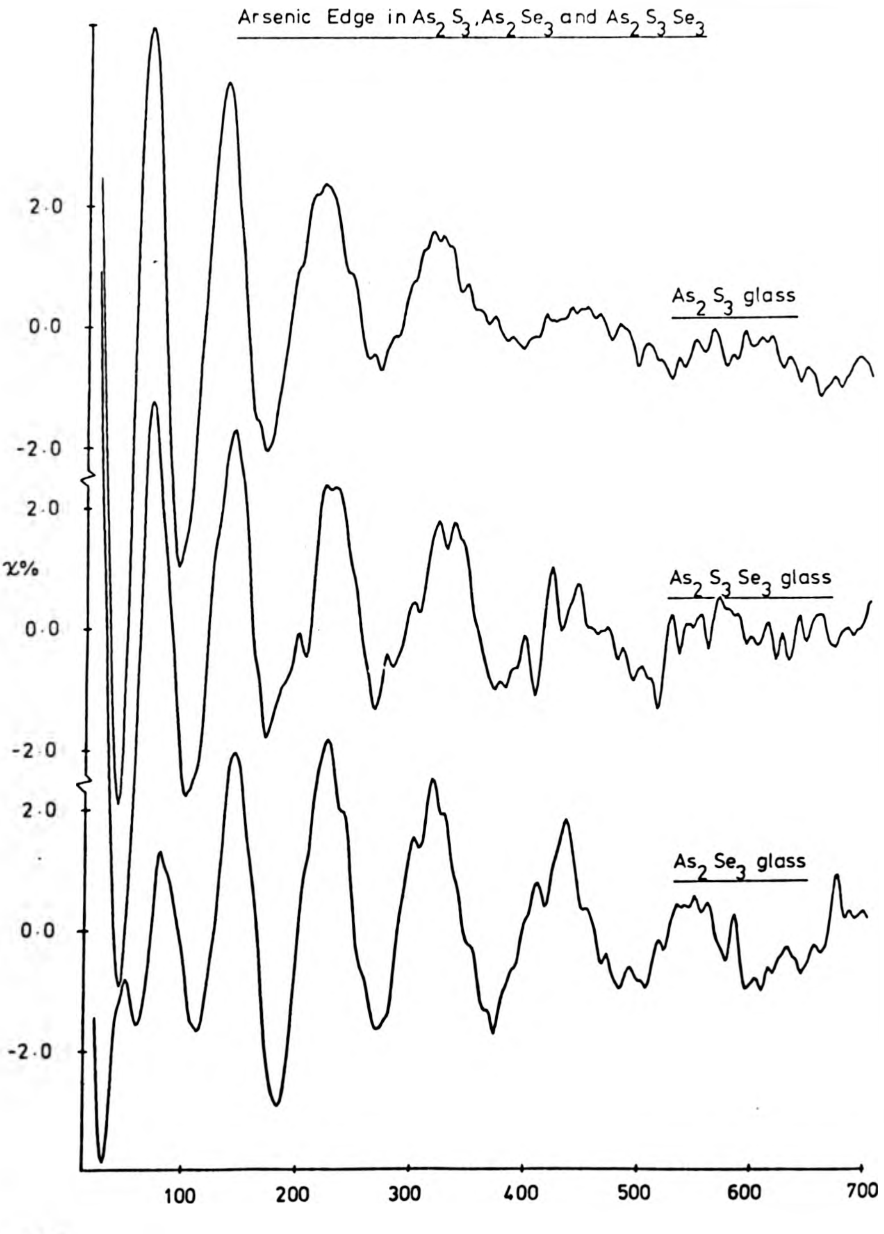

Fig.5.41. A comparison of the arsenic edges in the three chalcogenide glasses. These data were calculated using a Victoreen absorption coefficient above the edge and smoothed cubic splines.

studied chalcogen compounds, e.g. ZnS and Zn Se which have the same first neighbour structure,suggest that the difference of bond energy favours the dominance of sulphur in the first coordination sphere (Bond energy (ZnS-Zn Se) ~ 6 K cal/mole Phillips (1973)).

To test this idea, a glass of the composition $As_2 S_3 Se_3$ was made by fusing together the elements in the correct stochiometric proportions in a silica ampoule. The material was kept at 550° C for 36 hours and then air quenched. The result was a good quality glass, free from bubbles, which was dark red in colour. Samples were prepared for absorption measurements in the manner described previously. The arsenic and selenium spectra recorded for this material are shown in Fig. 5.38-5.40. Subsequent data analysis on this material required interpolation of the spectra and so the spline interpolated data with the Victoreen background subtraction was used. These data, together with those on the arsenic edges in $As_2 S_3$ and $As_2 Se_3$ glass are shown in Fig. 5.41. We can see the inadequacy of the Victoreen background subtraction in providing an EXAFS function which oscillates symmetrically about the energy axis. Unfortunately the statistics and range of the data are not up to the standard of the other spectra, but it is immediately obvious from the As edge that there is a considerable amount of sulphur bonding present in the first shell which is characterised by the slow decay of the envelope of the fine structure as one moves away from the edge. However, from Fig. 5.41 it can be seen that (a) the amplitude of the fine structure is not equal to the amplitude of the pure $As_2 S_3$ glass, and (b) the fine structure extends further from the edge. The latter point indicates that there is another contribution to the fine structure evident beyond 400 eV which probably comes from As-Se bonding. To analyse this spectrum we assume that the phase shift functions, inelastic loss and disorder parameters remain the same when transferring from pure As_2S_3 and As_2Se_3 to $As_2S_3Se_3$. Then, merely adding together the As_2S_3 and As_2Se_3 spectra with adjustable weighting coefficients can give the fine structure of $As_2S_3Se_3$. Unfortunately we have to compensate for the poor background subtraction. This has been accomplished by adding a cubic polynomial to the sum. Thus the expression used was

$$\chi_{(As_2S_3Se_3)}(E) = a\,\chi_{(As_2S_3)}(E) + b\,\chi_{(As_2Se_3)}(E) + c + dE + eE^2 + fE^3 \qquad (5.11)$$

where E is the photoelectron energy. The problem is now one of standard linear regression. The analysis was carried out using a regression package written by B.A. Monk (University of Warwick 1968 unpublished). The energy range over which the data were fitted was from 20 →,700 eV evenly sampled in energy over 200 data points. The results of the analysis are as follows:

$a = 0.67 \pm 0.02$

$b = 0.32 \pm 0.03$

$c = (5.8 \pm 2) \times 10^{-3}$

$d = (-6.0 \pm 2) \times 10^{-5}\ (eV)^{-1}$

$e = (1.3 \pm 0.7) \times 10^{-7}(eV)^{-2}$

$f = (6 \pm 6) \times 10^{-11}\ (eV)^{-3}$

If we evaluate the coefficients of the polynomial $c+d\,E+eE^2+fE^3$ it can be seen that this is a slowly varying function over the entire energy range and just represents the inadequacy of the Victoreen interpolation approximation to the atomic absorption.

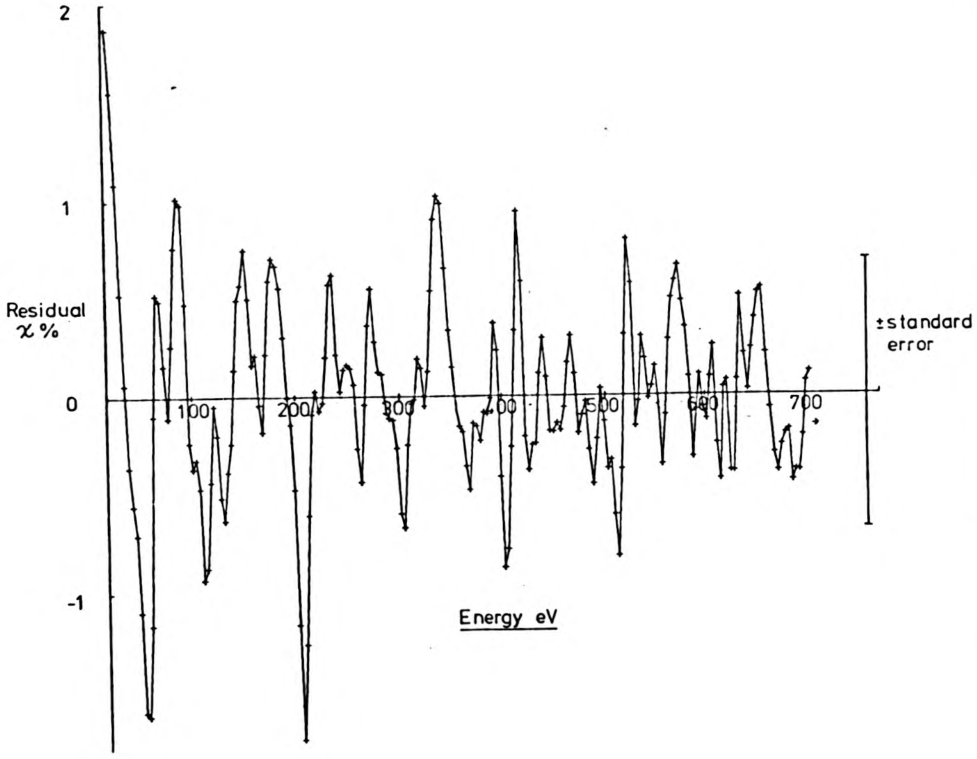

Fig.5.42. A plot of the residual fine-structure after subtracting the contributions from As_2S_3 and As_2Se_3. The small error can be attributed to the smoothing effect of the splines.

The coefficients a and b were left unconstrained and the sum of a+b = 0.99 ± 0.03 is remarkably close to one and supports our earlier assumption of the transferrability of arsenic-chalcogen bond characteristics from one glass to another. The individual coefficients themselves reflect the relative proportions of As-S and As-Se bonding. This ratio 67:32 or to within experimental error 2:1 may be significant in indicating a well defined As $S_{2/2}$ $Se_{1/2}$ unit. However this is speculation. A plot of the residual fine structure after fitting is shown in Fig. 5.42. The reason that most of the points lie inside the standard error for an individual point can be attributed to the effect of the cubic spline smoothing interpolation.

Fortunately, with EXAFS it is possible to discover still more about the structure by examining the selenium edge. Although the data are restricted in energy range, it is quite clear that the selenium edge closely resembles that in As_2 Se_3. At energies in excess of 100 eV from the absorption edge the structure rises to a maximum at ~ 200 eV and then decays. This is typical of the behaviour of scattering from atoms of the size As-Se, and, further, the amplitudes of the fine structure are roughly the same in both materials. There is no evidence for the slow, exponential-like decay typical of sulphur scattering. Thus it appears that sulphur is not present in the selenium first shell, and thus avoids bonding to selenium. We have to emphasise that the EXAFS technique samples the average arsenic and selenium site and so this does not rule out the possibility of phase-separation in this material. Electron microscopy and small angle X-ray scattering experiments appear to be the techniques which are most likely to shed light on this possibility.

To summarise, we have found:

a) arsenic bonds to sulphur and selenium in this glass in the ratio 2:1

b) sulphur avoids bonding to selenium

c) if we assume that the valency of each atom is fully satisfied, then we must have S-S and Se-Se links in the glass.

5.13 Preparation and Properties of As_2Te_3

There is only one type of crystal structure reported for the material As_2Te_3. Unlike As_2O_3 (Claudetite), As_2S_3 and As_2Se_3, the crystal structure of As_2Te_3 cannot be regarded as a layer lattice. The complete structure has been reported for As_2Te_3 by Carron (1963). Arsenic, instead of having its valency satisfied by three nearest neighbours, has half its sites octahedrally coordinated with six tellurium atoms. These have been called the O-sites by Cornet and Rossier (1973). The other arsenic sites are threefold coordinated pyramids with an arsenic atom at the apex bonded to three tellurium atoms, and these are called t-sites. The coordination of arsenic in the O-sites is thus greater than the normal value of three found in all of the other arsenic-chalcogen materials. This fundamental change of the local coordination is typical of the trends found when passing down the periodic table. A good example of this is given by the group IV elements Si,Ge and Sn, all three have tetrahedral coordination in the crystal phase, however Sn undergoes a semiconductor-metallic transition with temperature at 13.2° C when the tetrahedral bonding breaks down to produce a distorted octahedral environment. Similar trends are found in the chalcogenide elements. Selenium is essentially a valence material, i.e. it has its valency of two satisfied by the nearest neighbours in the chain. There is some evidence of inter-chain bonding, caused by the lobes of the p-orbitals between atoms in the chains projecting into adjacent chains. Selenium atoms in hexagonal selenium can be regarded as residing in a distorted octahedron consisting of two Se atoms in the same chain and four others in adjacent chains. Tellurium has a similar crystal structure, however, with increasing atomic number, the secondary bonding to adjacent chains is enhanced. This is reflected in decreasing anisotropy of such properties as thermal conductivity and the elastic constants (Stuke 1969). The O-sites of $As_2 Te_3$ can be regarded as an extreme case of large secondary bonding. The increase in secondary bonding in a material is accompanied by an increase in metallic properties and this accounts for the high conductivity of crystalline $As_2 Te_3$. The first neighbour distances in $As_2 Te_3$, taken from Carron's (1963) paper, are given below:

TABLE 5.9

Site	R Å	N Atoms	Site	R Å	N Atoms
T Sites	2.68	1	O Sites	2.93	1
	2.77	2		2.76	1
				2.90	2
				2.85	2

All atoms are
tellurium atoms

Local structure about arsenic in $As_2 Te_3$ according to Carron (1963).

The increase of metallic bonding also means a decrease of directionality in the bonding which is usually accompanied by a decrease in the glass-forming ability of the material. This is in fact the case with this material. Unlike $As_2 S_3$ and $As_2 Se_3$ which were difficult to crystallise, $As_2 Te_3$ is difficult to make glassy. This accounts for the sparsity of experimental measurements on this material compared to $As_2 Se_3$ and $As_2 S_3$. In fact much of the data that exists has been recorded on evaporated or sputtered films, and there is good evidence that films do not possess the same structure as glassy material. (De Neufville, Moss and Ovshinsky (1973)).

Attempts to make glassy $As_2 Te_3$ began by taking pieces of the elements of purity > 99.9999%, crushing them and mixing them in stoichometric proportions. The material was sealed under vacuum in a silica ampoule which was heated at 800° C for 24 hours. The ampoule was then cooled slowly to room temperature whilst still in the furnace, a process which took about 12 hours. The contents of the ampoule were examined by powder X-ray diffraction and were found to contain the lines from the compound $As_2 Te_3$ reported by Carron (1963). This phase will be referred to as the Carron phase. A particular search was made of the X-ray diffraction pattern for lines which may have been caused by non-stoichiometry, such as arsenic (orthorhombic and rhombohedral) and tellurium, with no success. Thereafter, small quantities of arsenic telluride ~ 2 grams were enclosed in an ampoule made from ½ mm thick silica. The shape of the ampoule was approximately 18 mm long by 8 mm wide and internal thickness was ~ 1 mm. The ampoule was sealed under a vacuum < 10^{-5} torr and then heated whilst maintaining some agitation. A first attempt to form the glass was made by quenching the ampoule from 800° C into liquid nitrogen following a procedure of Seager and Quinn (1974, unpublished). X-ray powder diffraction showed the contents of the ampoule to be crystalline but not of the phase described by Carron. This phase will be referred to as the high temperature phase of $As_2 Te_3$. A check on the composition was made by annealing the material in vacuum at 200° C for one hour. It was found that the

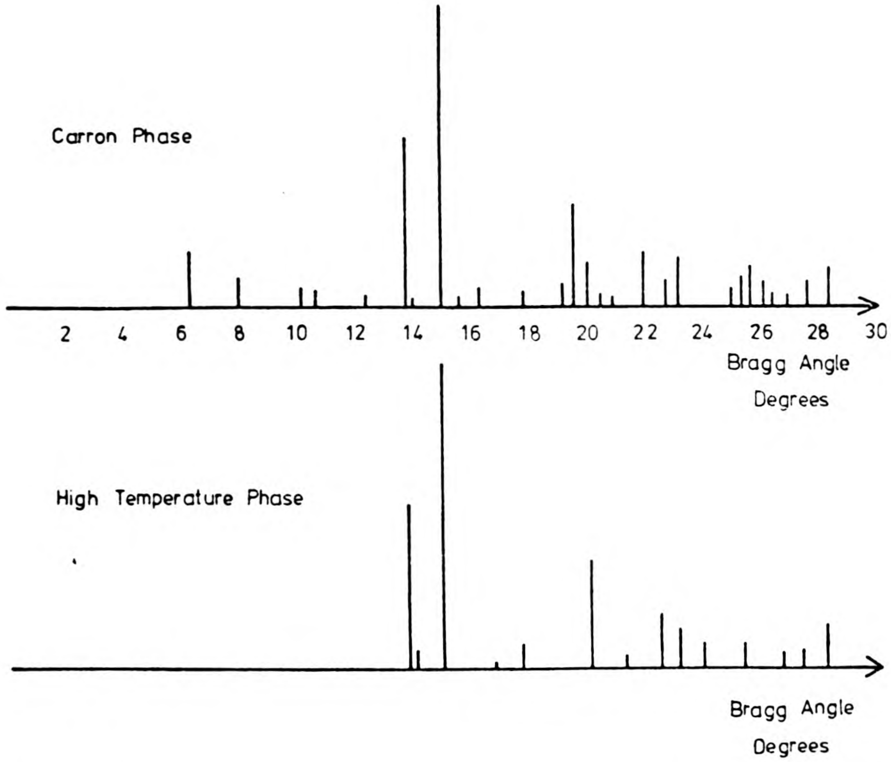

Fig.5.43. The X-ray diffraction lines of the two phases of As_2Te_3. Bar heights give relative intensities uncorrected for absorption or polarisation. The x-axis is in degrees and corresponds to Cu Kα radiation.

material reverted to the original Carron form. It is anticipated that this test will detect non-stochiometry of material such that an excess of tellurium of > 2% or arsenic > 4% would have been detected. The lines of the high temperature phase are given in table 5, and shown diagramatically together with those of the Carron phase in Fig. 5.43. All intensities are those which were recorded using a diffractometer and are uncorrected for polarisation and absorption. Qualitatively, the X-ray pattern of the high temperature form, possesses fewer lines than the Carron form. In particular the low-angle reflections 200, 201, 202 and ($11\bar{1}$, 400) are missing. There is only one phase of $As_2 Te_3$ commonly known which is the Carron form, however, Cornet and Rossier (1973a) have reported another phase in the As-Te system which occurs when arsenic-rich glasses crystallise. This phase has three fairly intense lines at d = 3.375 Å, 3.142 Å and 2.048 Å. Quinn (1974) has also reported a crystal of As-Te which has a fcc unit cell with a = 5.778 Å. This structure generates d-spacings of 3.330 Å, 2.880 Å, 2.030 Å ... none of these lines correspond to the diffraction pattern of the high temperature form of $As_2 Te_3$. It was hoped that the discovery of an intermediate crystal phase between crystal and glass could throw some light on the nature of the crystal-glass transition, similar to the way in which orthorhombic arsenic appears to be closer in structure to the glass than the rhombohedral form. (Smith, Leadbetter and Apling 1975).

Following these unsuccessful attempts, a glass was eventually formed by quenching the ampoule into an ice-water slurry. The mechanical properties of the glass are greatly different from those of either crystal forms. The glass is very brittle, and can be crushed easily into shiny pieces. The crystals on the other hand are very soft and malleable.

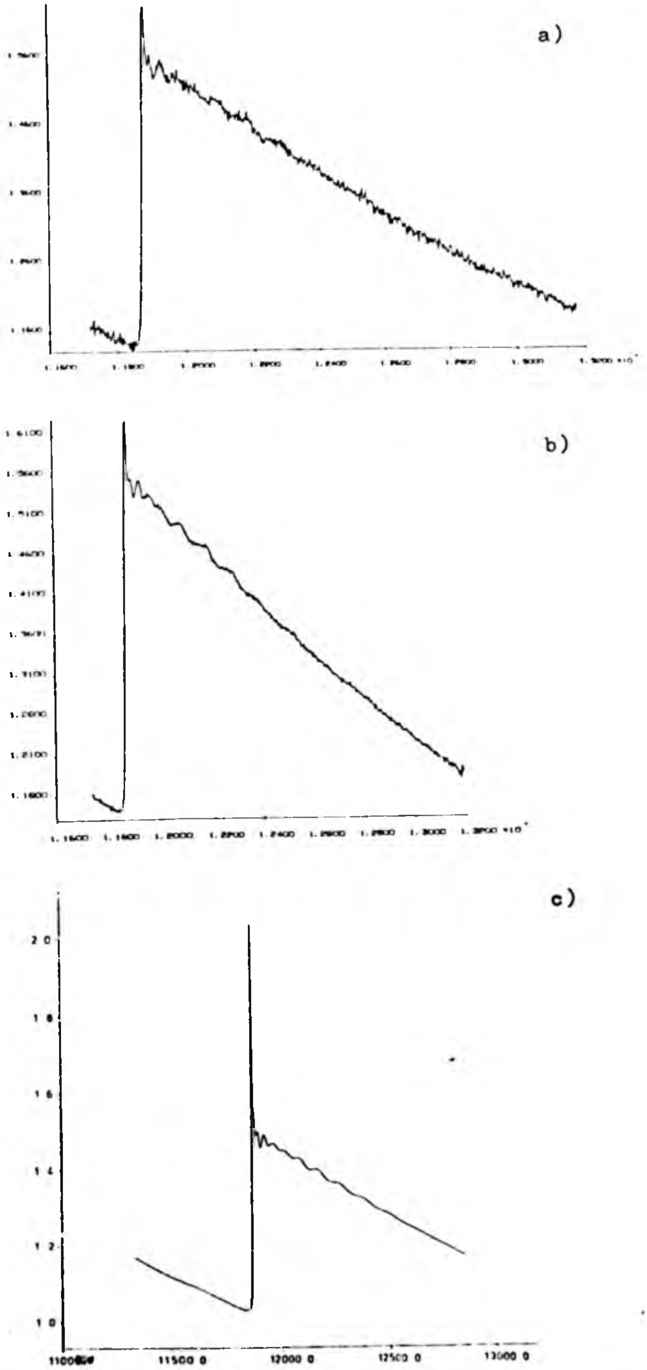

Fig.5.44. Three EXAFS spectra of As_2Te_3 glass. a) 10^5 counts accumulated per point b) 7×10^5 counts per point c) synchrotron spectrum.

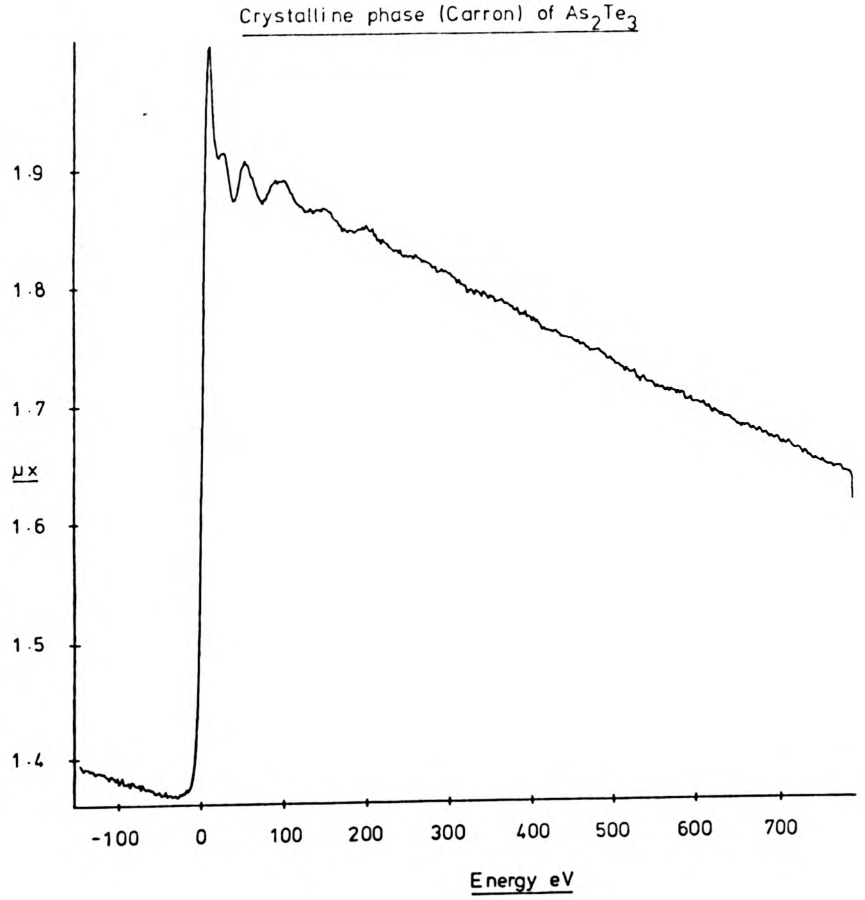

Fig.5.45. The raw arsenic K absorption edge spectrum of As_2Te_3 Carron form, taken with a conventional spectrometer.

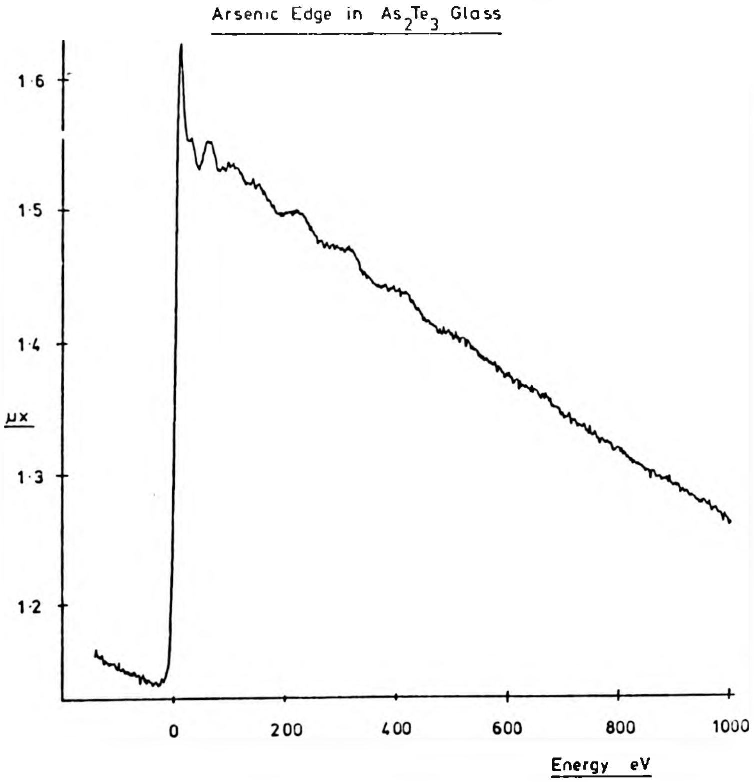

Fig.5.46. The raw arsenic K absorption edge spectrum of As_2Te_3 glass form, taken with a conventional spectrometer.

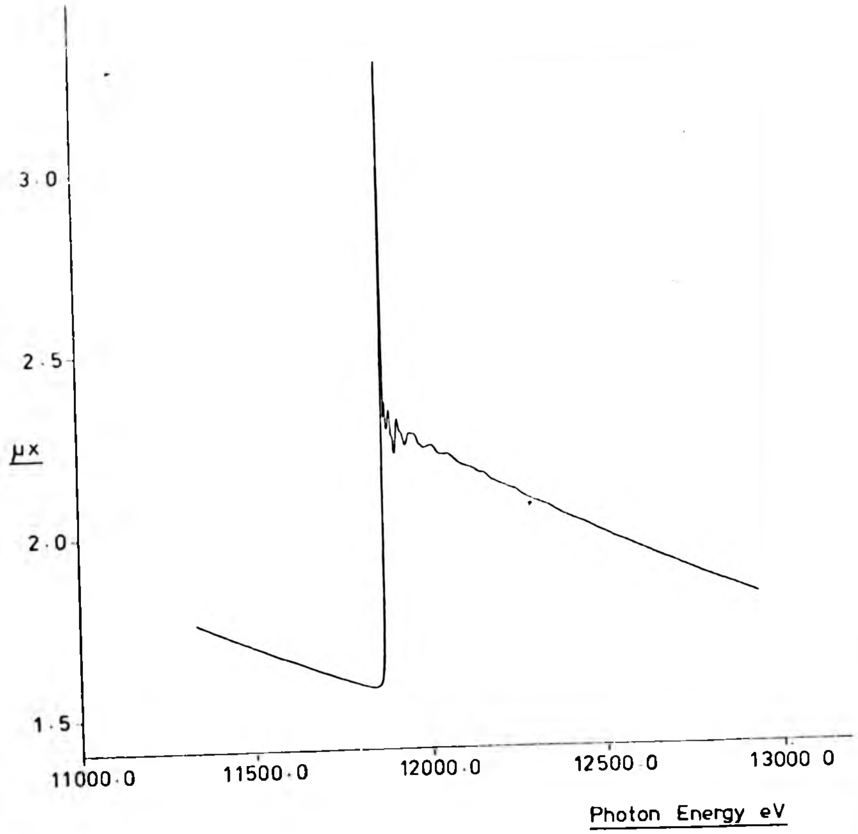

Fig.5.47. The raw arsenic K absorption edge spectrum of As_2Te_3 Carron form, taken using synchrotron radiation.

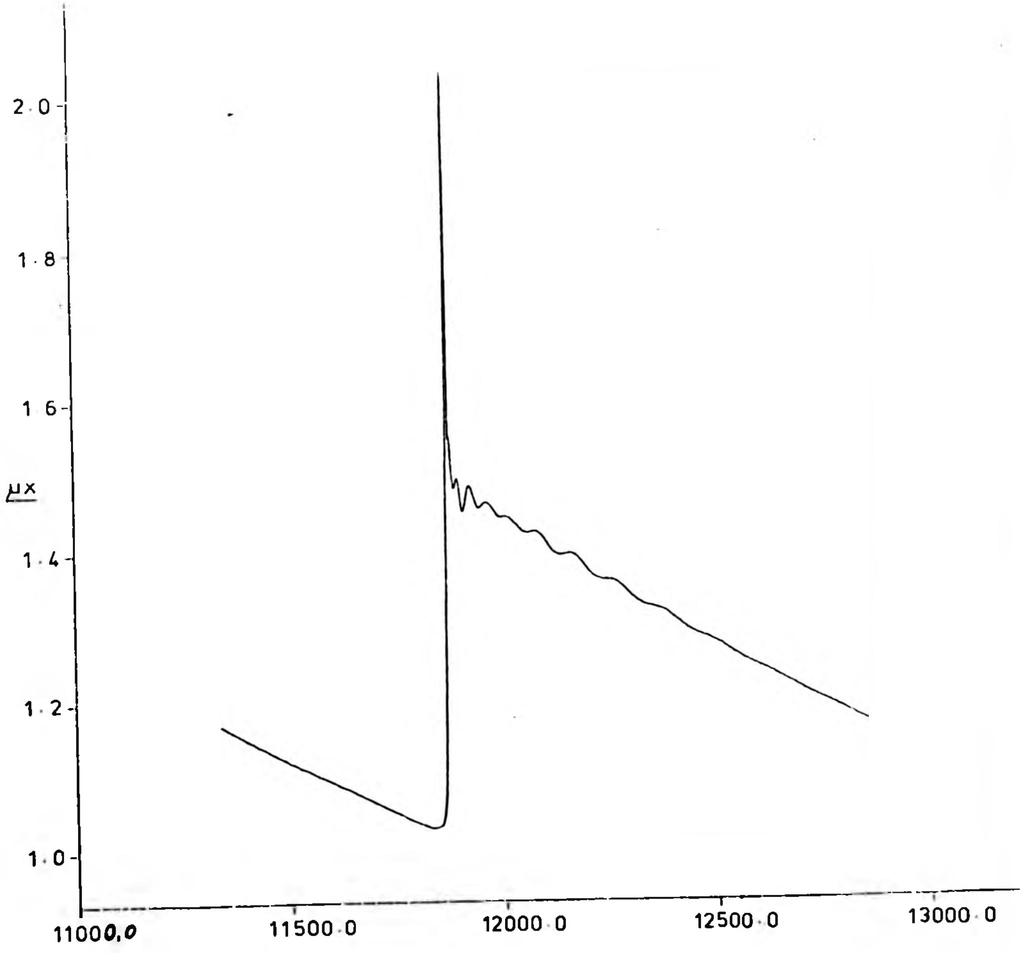

Fig.5.48. The raw arsenic absorption edge spectrum of As_2Te_3 glass, taken using synchrotron radiation.

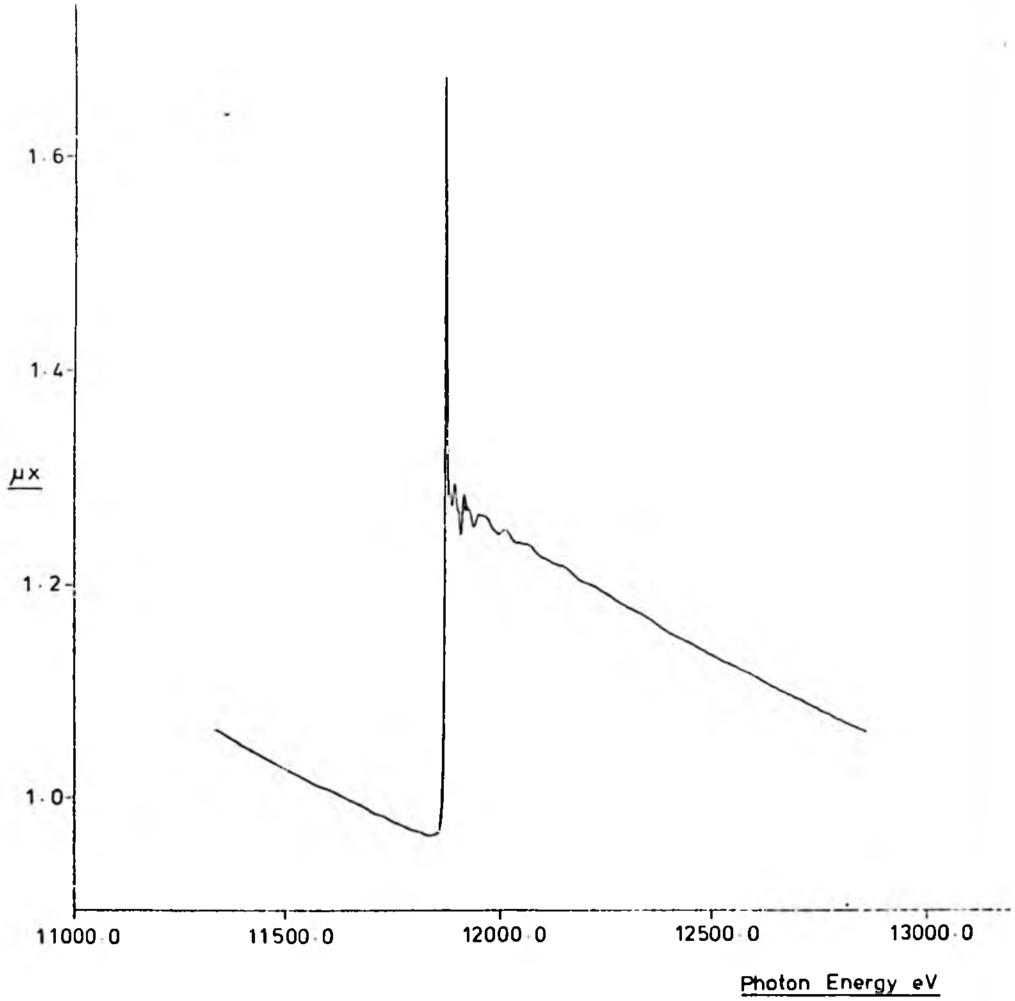

Fig.5.49. The raw arsenic absorption edge spectrum of As_2Te_3 High Temperature form, taken using synchrotron radiation.

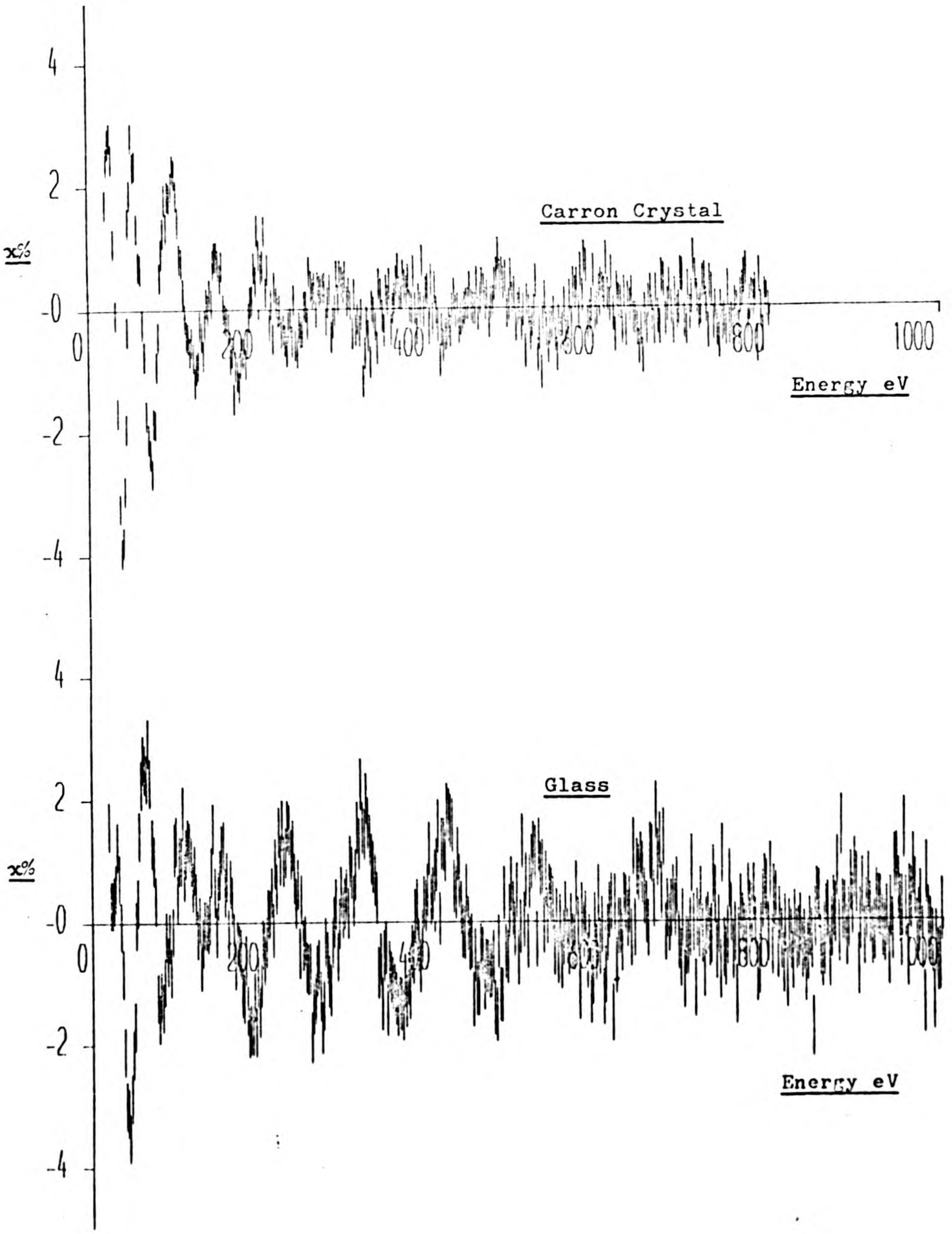

Fig.5.50. The fine structures of the Carron crystal and glass forms of As_2Te_3 using conventional apparatus.

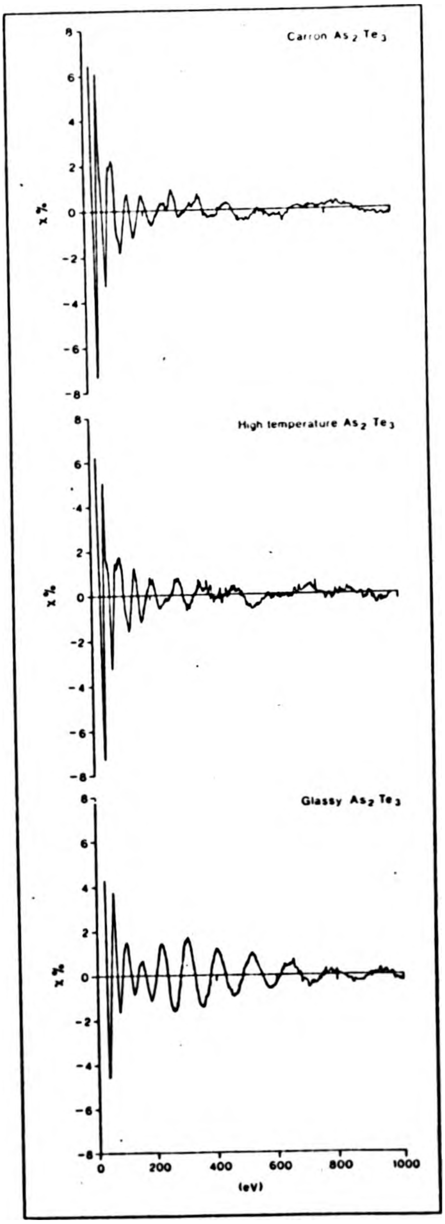

Fig.5.51. The fine structures of the three forms of As_2Te_3 taken using synchrotron radiation.

5.14 Discussion of the $As_2 Te_3$ Spectra

Tellurium has a large absorption at ~ 1 Å owing to its high atomic number. This makes the measurement of EXAFS in $As_2 Te_3$ the most difficult of the materials so far studied. It is thus appropriate at this stage to contrast the measurements of this spectrum taken with different apparatus. Fig. 5.44 shows three spectra of $As_2 Te_3$ glass, the first measurement is the result of accumulating a set of data, counting for 10^5 counts/point. There is little evidence of any fine structure present owing to the noise. This spectrum was the result of three days continuous counting. The next spectrum is the spectrum from a combination of seven individual runs of the spectrum. Now, the fine structure is clearly visible above the noise. The third spectrum was taken with synchrotron radiation from NINA using the apparatus built in collaboration with a group from Oxford University. The monochromator was a Si 111 channel cut crystal and the detectors were argon filled ionisation chambers. The resolution was dictated principally by the entrance slit to the spectrometer and yielded a resolution ~ 2 eV. The synchrotron was operating at 4 GeV 20 mA which provided ~ 10^8 photons/second through the monochromator. The time taken for the measurement was 1.3 hours. The product of increase of resolution × time × signal to noise ratio of the two spectra shows an improvement of ~ 3×10^4 of the synchrotron results over the results taken on the conventional apparatus. The raw absorption spectra are shown in Figs. 5.45 to 5.49, and the fine structure functions taken from these results are presented in Figs. 5.50 and 5.51. The two sets of data taken with different apparatus agree in phase and amplitude if we allow a small shift (~ 4 eV) of the synchrotron results to a higher energy with respect to the conventional measurements. We can also see that the fine structure obtained using the conventional apparatus is affected by resolution below 100 eV. Owing to the superior quality of the data from the synchrotron we will confine our discussion to the spectra in Fig. 5.51. It is clear from this figure that the amplitude of the fine structure in the glass is much larger and of a much simpler periodicity than that found in either of the crystals. This is clear evidence of a fundamental change in first neighbour coordination of arsenic between the crystal and glass. We can only make a qualitative comparison of these data and those taken by Sayers, Lytle and Stern (1974) on a sputtered film owing to the data processing that these authors have performed on their spectrum. We find that these authors also find that the fine structure is large in amplitude at high energies and this is in agreement with our results. It is also found that the first peak in their Fourier transform is somewhat narrower than that from lighter atom scattering. This is a consequence of the larger range of data available. The reduction in amplitude of the EXAFS in the crystal is expected to come from the interference of the various contributions to the fine structure from the range of first shell distances in the crystal. The fact that χ for the glass is much stronger than χ for either crystal results from a simplification of the first shell coordination in the glass. Thus we may say that the glass possesses a higher degree of radial order than the crystal.

It is worth pointing out that if the glass was a mixture of microcrystallites of both of the phases of $As_2 Te_3$ then the fine structure would be a weighted sum of the crystal fine structures, the weighting would then represent the amount of the crystal present. As the amplitude of the fine structure for the glass at high energies is much larger than that of the crystal phases then we can reject this hypothesis.

A comparison of the two crystal phases of $As_2 Te_3$ shows that there is very little difference in the local environment of arsenic in these materials. The major difference comes from a splitting of a peak in the fine structure of the Carron form at about 300 eV which is not as evident in the high temperature phase. This effect probably comes from a difference in a coordination shell other than the first, which appears well preserved.

An unexpected feature of the glassy $As_2 Te_3$ spectrum is the minimum in the envelope of the fine structure at about 130 eV. The behaviour of the envelope of χ in this region is unexpected because plots of $\frac{|f(\pi)|}{K}$, using both sets of phase-shifts, do not exhibit this deep minimum. There is some sign of a minimum in $\frac{|f(\pi)|}{K}$ at a much higher energy ~ 200 eV but it has nothing like the same strength as the minimum observed experimentally. It is clear that full interpretation of the glass spectrum should be able to explain this fact.

Owing to the complexity of the first shell radii in crystalline $As_2 Te_3$ it is not possible to perform the semi-empirical analysis which we found useful for $As_2 S_3$ and $As_2 Se_3$. Thus our interpretation must rely on fitting the experimental data using theoretical parameters.

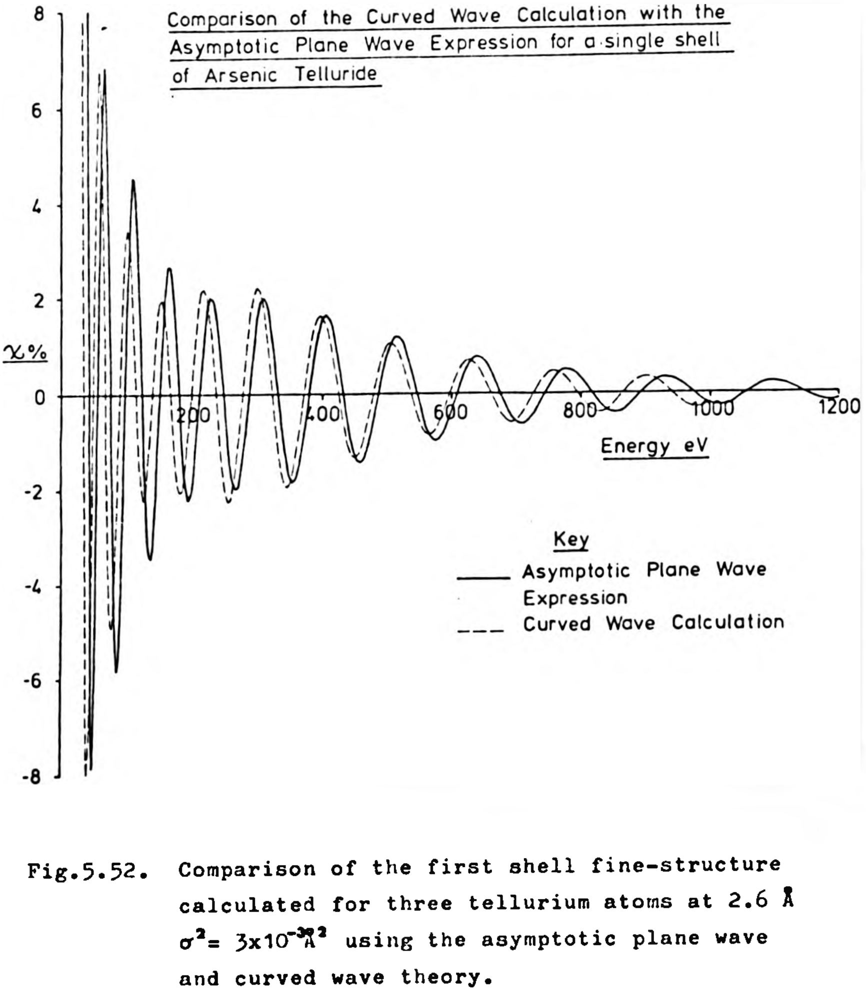

Fig.5.52. Comparison of the first shell fine-structure calculated for three tellurium atoms at 2.6 Å $\sigma^2 = 3\text{x}10^{-3}$ Å^2 using the asymptotic plane wave and curved wave theory.

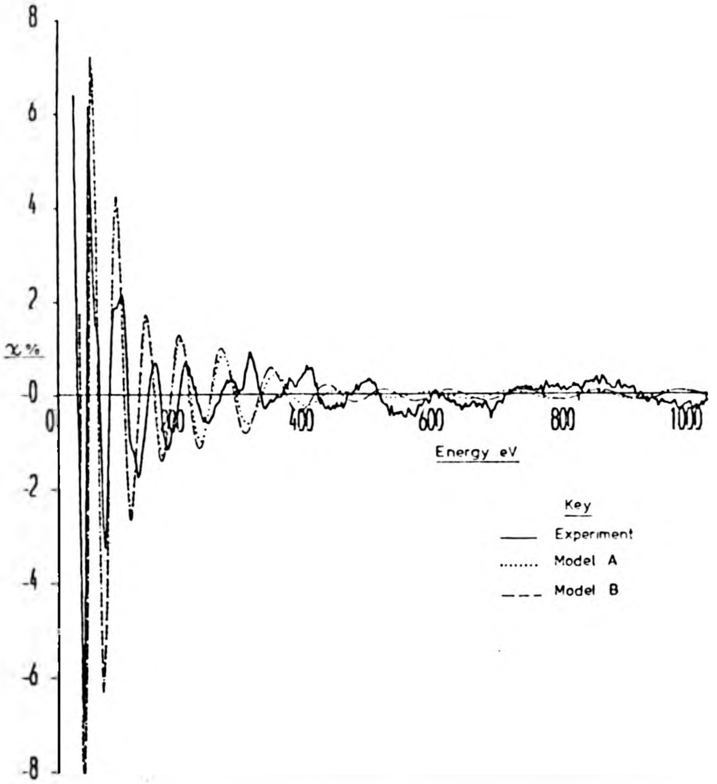

Fig.5.53. Comparison of the fine-structure calculated on the basis of the shell radii from the crystalline Carron phase with the theoretical spectrum.

5.15 Calculation of the $As_2 Te_3$ Spectra

As in the other chalcogenide glass systems, it is of interest to compare calculations of a model first shell structure using the asymptotic plane wave and curved wave theories. This comparison has been made in Fig. 5.52. It is immediately clear that the asymptotic plane wave theory is inadequate owing to the large ion-core size of tellurium. A second interesting feature is that the envelope of the curved wave calculation has developed a more pronounced minimum than that found in the asymptotic plane wave theory, this minimum has shifted to lower energies, ~ 150 eV. This is close to the minimum found in the experimental fine structure, but its strength is much less.

As a first step in the calculation of the glass parameters,it is wise to compare the calculated fine structure of the Carron phase whose first shell radius is known from Table 5.9 and compare this with the experimentally measured fine structure. Unfortunately we do not know the values of the Debye-Waller factors for each of the sites (T and O sites). Thus two calculations were performed using different sets of values and these are shown in Fig. 5.53. Despite the obvious presence of higher shell scattering in the crystal we can identify the dominant first shell scattering, and it can be seen that the calculated values using the Slater exchange phase shifts show a systematic shift in phase relative to the experimental spectrum. At low values of energy the curve is well reproduced, however at 300 eV above the absorption edge the phase of the calculated structure has become π radians out of phase. Also it is clear that the effects of a change of Debye-Waller factor cannot be responsible for this phase change as it takes place at too low an energy. This is a very disappointing result and clearly invalidates any structure

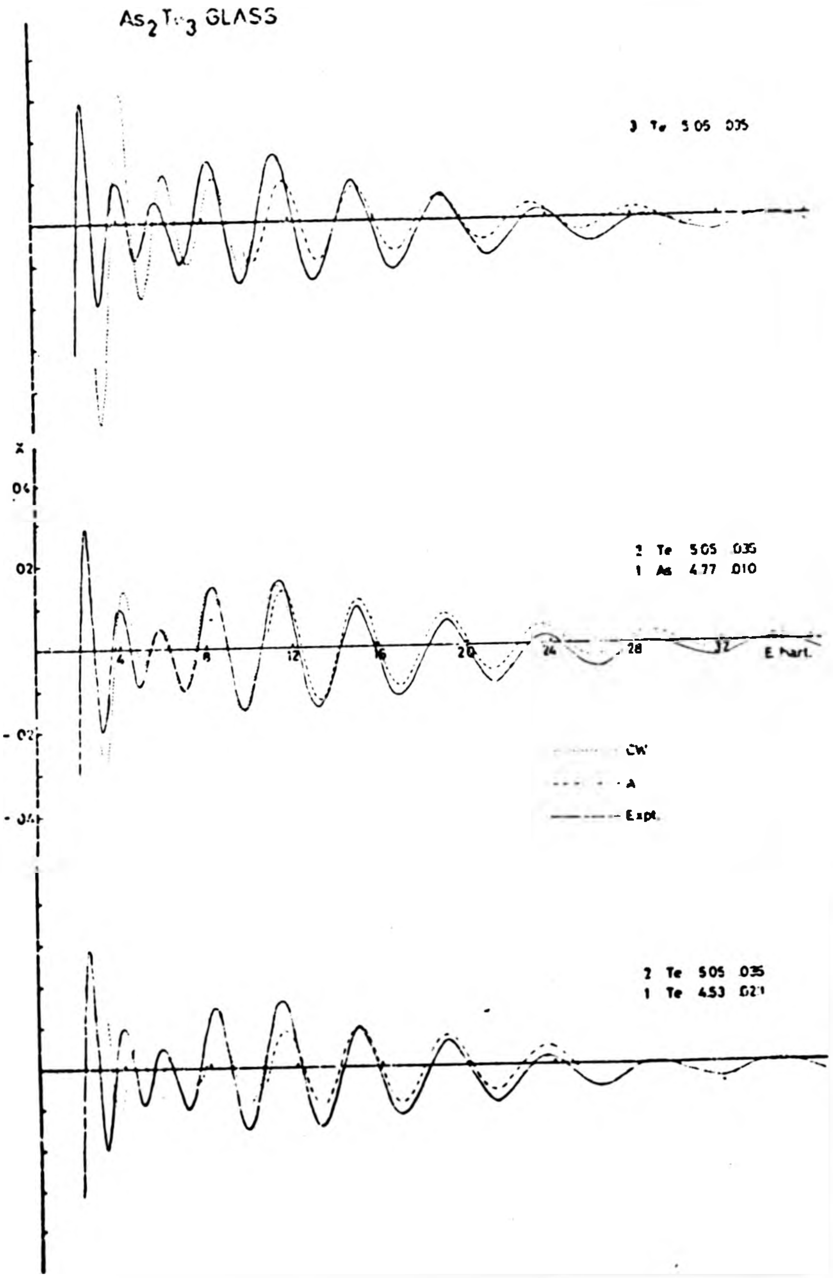

Fig.5.54. Fits to the experimental glass spectrum using Hartree-Fock phase-shifts and three separate models of the local order in the glass. Results of Gurman (unpublished).

determination for this system using the Slater exchange potentials. Gurman (unpublished) has however been able to reproduce the general phase of the crystal spectrum using the Hartree-Fock phase shifts, and has also fitted the glass spectrum; his results are shown in Fig. 5.54. The remarkable feature of these results is that it is necessary to include homopolar bonding to account for the strong minimum in the glassy spectrum. One uncomfortable aspect of these results is the wide variation of Debye-Waller factor found between the arsenic atom(0.0014 Å^2) and the tellurium atom (0.005 Å^2). This is strange as the ordering of the first shell of the glass is a clear indication of the onset of covalency rather than the metallic-like centres found in the crystal. Support for this idea comes from the reduction of the first shell distance to 2.67 Å (Te) and 2.52 Å (As). The T site in $As_2 Te_3$ has a mean As-Te radius of 2.74 Å and in crystalline arsenic the first shell is 2.51 Å, (although we expect some shortening of this distance in the amorphous case owing to the break-up of the extensive secondary bonding in rhombohedral As). Thus the onset of covalency should make the bond lengths rigid with a corresponding reduction in the Debye-Waller factor for all first neighbour atoms.

Gurman also finds no evidence of scattering from higher shells in the glass from his Fourier transform, this is in contrast to the Fourier transform of the data obtained with conventional apparatus data which showed peaks, presumably from noise components of the measured spectrum.

CHAPTER 6

Discussion and Conclusions

6.1 Discussion of the Experimental Apparatus and Technique of Measurement

Most of the results presented in this thesis have been obtained using a conventional X-ray spectrometer. These results are therefore limited, to some extent, in their usefulness. Both the resolution and the statistical accuracy of the results are inferior to those obtained with synchrotron radiation particularly close to the absorption edge. It would be useful to measure the shape of the EXAFS oscillations to attempt to detect the influence of possible higher shell scattering. This would show up in the asymmetry of the periodicity. Thus, there is a need for better quality data. We have found in Chapter 4, that the resolution was limited principally by the finite size of the source and receiving slits, and by the penetration of the X-rays into the crystal. The latter consideration prevents an increase of the acceptance angle of the crystal by grinding, as this will simultaneously degrade the resolution. One possible improvement in the system could be achieved by the elimination of the step scanning principle and alternatively recording each point of the spectrum simultaneously using a position sensitive detector. One possibility is a multiwire proportional counter (M. Breare, private communication). Given the same source and crystal, this would provide an effective increase of intensity of approximately 500. However, despite the possible improvements of a conventional source, it is very unlikely that spectrometers using bremstrahlung radiation will match the quality of data produced using synchrotron radiation.

Another aspect of experimental technique which needs closer consideration is the effect of specimen inhomogeneity. In particular, this influences the amplitude of the EXAFS function $\chi(E)$. This effect has been given little attention so far. It is important because it controls the accuracy to which the number and, to a lesser extent, the disorder of atoms in a coordination shell can be determined. Also, for many of the solids of interest in EXAFS, the only reasonable way to prepare specimens is to powder them and then cast them into a film. Even this process has its problems, such as the difficulties of grinding As_2S_3 crystals and As_2O_3 glass to a sufficiently fine powder. A typical apparent film thickness for the materials studied here is between 20μm to 30μm. Typical particle sizes for a material which has been crushed in a pestle and mortar were measured to be approximately 40μm in diameter, whereas those which have been milled are less than 4μm. It is difficult to quantify this effect owing to the unknown nature of the packing of particles. However, a model calculation can be made to give an idea of its importance. If we consider a film of mean thickness x_m with a variation of thickness in one dimension of $x'\cos y$, where y is a length of the film, then the mean intensity transmitted, I, when an incident intensity of I_0 falls on the film, is

$$I = \frac{I_0}{2\pi} \int_0^{2\pi} e^{-\mu(x_m + x'\cos y)}\, dy \qquad (6.1)$$

$$= I_0\, e^{-\mu x_m}\, J_0(\mu x') \qquad (6.2)$$

where

$$J_0(\mu x') = \frac{1}{2\pi} \int_0^{2\pi} e^{(-\mu x'\cos y)}\, dy \;. \qquad (6.3)$$

μ is the absorption coefficient, and J_0 is related to a Bessell function. It is easy to evaluate J_0 by direct numerical integration. The apparent absorption thickness product is then given by

$$(\mu x)_{app} = \mu x_m - \ln (J(\mu x')) \quad . \qquad (6.4)$$

If we consider an idealised absorption edge shown below

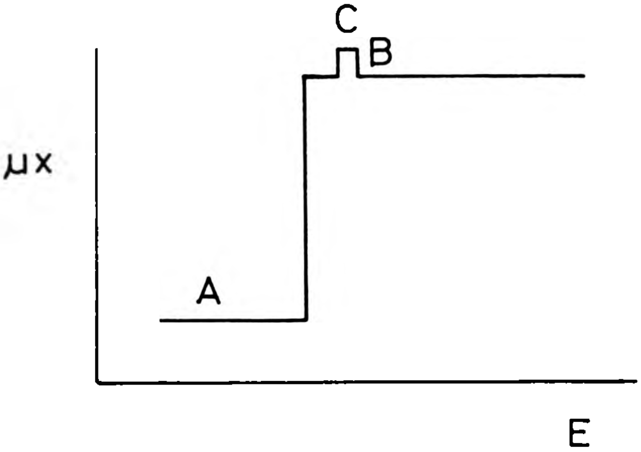

the fine structure is given by

$$\chi(C) = \frac{\mu x(C) - \mu x(B)}{\mu x(B) - \mu x(A)} \quad . \qquad (6.5)$$

Then substituting Eq. (6.4) into Eq. (6.5) will yield the apparent fine structure. The model predicts for the cases of As_2O_3 glass and As_2S_3 crystal with particle sizes of 40μm, which we equate to 2x', a reduction in the amplitude of fine structure of 12% (for χ = +10%) and 10% (for χ = -10%). For the 4μm powders, the effect is a 1% reduction in amplitude for both χ = + and - 10%.

Further, this reduction is to a first approximation independent of χ. The reason that the large particle size film does not have a larger reduction in χ results from the fact that whilst the fluctuations in absorption above the edge are reduced by inhomogeneity, so also is the magnitude of the edge itself. Although this model is crude, it does indicate the size of the effect and shows that coarse crushing of the material is inadequate if values of coordination number are to be extracted from the data. For finely milled material the correction is small and it is probably adequate to correct by scaling the EXAFS function by a constant. Owing to the coarse nature of the material in the $As_2 S_3$ crystalline and $As_2 O_3$ glass specimens it is likely that both spectra have reduced structure due to this effect. The magnitude of the reduced structure in these cases is approximately 20% and is consistent with the order of magnitude calculation performed above.

Unfortunately we cannot compare the EXAFS amplitude of our results with those of Sayers, Lytle and Stern (1974) as their amplitudes are not reported. Further, these authors also report difficulties in interpreting properties of the glass which are dependent on the amplitude of the signal. Further difficulties with the use of amplitude information in EXAFS studies have been noted by Hayes and Hunter (1977) who find that if they assume a constant mean free path of the photoelectron in the solid, then their results are consistent with five atoms in the first shell of germanium, rather than the assumed value of four. To account for this discrepancy, they suggest a possible increase in the mean free path when moving from the crystal to the glass. This explanation is unlikely, as the imaginary self-energy of the photoelectron is controlled by plasmon losses, which depend on the density of valence electrons, and to a lesser extent on core electron excitation, neither of which are expected to change when the local structure of the glass is the same as the crystal.

If the material to be studied requires accurate values of the amplitude of the signal and the specimen can only be made by powdering then the only alternative is to measure the EXAFS structure via the fluorescence signal. It is clear that further work of an experimental nature is needed to quantify the exact magnitudes of this effect. It is obviously not good enough to assume that the EXAFS structure has the correct magnitude on the basis of the macroscopic homogeneity of a sample.

6.2 EXAFS as a tool for Structure Research

In this section, the advantages and limitations of EXAFS are discussed in the light of the experimental and theoretical results. The information from EXAFS data can be divided into two parts a) the phase and periodicity of the signal and b) the amplitude of the signal. From the phase and periodicity, we can find the mean coordination shell distance of the emitter from the scattering shells. One of the factors affecting the accuracy to which this can be accomplished is the range of data over which the phase and periodicity are measured. The precision of conventional scattering experiments can be estimated from the range of data in terms of momentum transfer (Q) given to the scattering particles. This limitation of a finite range of data is reflected in the width of the Fourier transform peaks in real space, and thus in the precision to which the radius of the coordination shell can be established. Real space information from conventional scattering experiments is obtained by a Fourier transform such as:

$$4\pi\, r^2 \rho(r) = 4\pi\, r^2\, \rho_0 + \frac{2r}{\pi} \int_0^{Q_{max}} Q\, i(Q)\, \sin(rQ)\, dQ \qquad (6.6)$$

where $\rho(r)$ is the electron density, ρ_0 the average electron density, and $i(Q)$ is the coherent intensity for X-ray scattering; Q in this case is given by

$$Q = \frac{4\pi\, \sin\theta}{\lambda} \qquad (6.7)$$

(Klug and Alexander 1974).

Thus, for Cu Kα radiation Q_{max} is ~ 8 $Å^{-1}$. If we ignore the phase problem in EXAFS then a transform of the data is made with respect to 2k which is then equivalent to Q. If the experimental measurements are made to 1000 eV above the absorption then this corresponds to $k_{max} = 16$ Å^{-1} and the equivalent $Q_{max} = 32$ Å^{-1}. Thus the EXAFS data starts roughly at the finishing point of the X-ray diffraction data using copper Kα radiation. The large value of Q_{max} found in EXAFS experiments means that distances can be determined with great accuracy if statistically significant scattering can be observed to high energies. This condition is met well by the first shell scattering from heavy atoms such as selenium and tellurium, but to a lesser extent by sulphur and oxygen. The situation is different for higher shells, because disorder (both static and thermal) has the effect of multiplying the scattering signal by a term $\exp(-2\sigma^2 k^2)$. For the range of k investigated by EXAFS and with a σ^2 typical for second and higher shells, this is a rapidly decaying function which limits the effective maximum wavevector at which scattering from higher shells is significant above the noise. This effect is well exemplified by all of the glass data examined, except that for As_2O_3, in which the higher shell scattering is suppressed even for energies ~ 100 eV ($K = 5$ Å^{-1}). This is one of the present limitations of EXAFS, imposed essentially by a lack of theoretical certainty below 100 eV. To extend the theory of EXAFS to include the lower energy regions, is a non-trivial task because the phase shifts are expected to become much more environmentally sensitive, together with anticipated additional effects from multiple scattering and more complicated electron energy loss behaviour. However, we can compare the periodicity of first shell scattering between crystal and glass with high precision, owing to the freedom of systematic errors which results from the calibration of the spectra with respect to the emission lines of the X-ray tube. Together with the high Q range, this results in a precise estimate for the mean bond-length to nearest neighbours. The major limitation of the absolute accuracy of the nearest neighbour bond length of the glass is determined by the accuracy of the crystal structure. However, the figure of major significance to the property of glass is the relative difference in bond length.

Comparative methods, although more accurate, are only of limited use in situations where the crystal and glass have similar structure and also where the effect of higher shell scattering is small. The analysis used in Chapter 5 could be improved by a method suggested by Stern, Sayers and Lytle (1975) which involves transforming the data into real-space, isolating the first shell peak by setting the real-space transform to zero outside a window in r-space which surrounds the first peak, and then back transforming the data. Unfortunately, the problem with this technique lies in a suitable choice of window in real-space which includes all of the structure from the first shell and termination ripples, whilst excluding any structure from higher shells. In view of the quality of data it is doubtful whether the increase in accuracy resulting from this procedure would be significant. The alternative to comparison methods is the direct calculation of the EXAFS function theoretically. This approach is obviously of great advantage as the number of systems to which a comparative method can be applied is severely limited and these cases are often not the most rewarding to study. Further, this technique does in principal provide absolute values of Debye-Waller factors and bond lengths. The key parameter in interpreting the phase and periodicity of the EXAFS function is the total phase shift which ~~is~~ comprise~~d~~s ~~of~~ two parts, namely the outgoing phase shift from the emitter potential and the phase of the backscattering amplitude. From the phase-shift studies of Chapter 3, it was found that for the elements O, S and Se, the difference between the Hartree-Fock and Slater exchange phase shifts was mainly one of a constant phase difference. Comparing the theoretical EXAFS function with that calculated from both of the sets of the phase shifts, it is clear that the Slater exchange results are by far superior. As the results only differ by approximately a constant ($K > 6$ Å^{-1}, $E > 130$ eV) then both phase shifts give the correct periodicity but the phase differs for the case of the Hartree-Fock calculations. The situation changes abruptly for the heavy atom tellurium, for which it was found that the Slater exchange phase shifts fail to reproduce the observed structure. We note that the phase of the backscattering amplitude was predicted to be a strong function of wavevector k above 100 eV (approximately 5 Å^{-1}) for tellurium, unlike the other chalcogen atoms, and there appears to be some difficulty in describing this energy dependence using Slater exchange; however, Gurman's (unpublished) results suggest that under these circumstances the Hartree-Fock theory is more correct. Clearly it is desirable to calculate and measure the EXAFS for other materials with large coordinating atoms.

The agreement between theory and experiment becomes progressively better as the size of the scattering atom increases up to the best fit at arsenic selenide. This may be associated partially with the environmental dependence of phase shifts noted in Chapter 3. The selenium emitter potential phase shift η_I was calculated for a selenium atom surrounded by six other selenium atoms, and this environment most closely corresponds to that in $As_2 Se_3$. We also have an arsenic emitter and arsenic scatterer in $As_2 O_3$ (arsenolite third shell), however, the phase agreement is not as good as in As_2Se_3. The next step in improving this fit will be to use the appropriate selenium emitter phase shifts calculated in an oxygen environment. Lee and Beni (1977) have recently considered the problems of accurately calculating phase shifts. These authors find that they need to include an extra ingredient into the atomic potential caused by correlation effects. The phase shifts calculated are then used to produce impressive fits to a variety of experimental data obtained with a synchrotron. The accuracy achieved in crystalline material for the first shell is ~ 0.01 Å. The atoms studied in this paper are all of size less than selenium, and for copper and germanium the EXAFS function is calculated using the asymptotic plane wave expression. However, it is known that this produces a shift in phase for this type of atom; Lee and Beni have masked this effect by allowing the energy zero to be an adjustable parameter. Lee and Beni (1977) also give values for the phase of the backscattering amplitude for oxygen which can be compared with those calculated earlier with Slater exchange phase shifts. It is found that above 100 eV the phase difference between these results is less than 0.1 radians. Below this energy the phase difference between the two sets of results reaches about 1 radian at 50 eV. The agreement between these two sets of results for this material suggests that theoretical fitting of the experimental spectrum gives valid radii. The accuracy of fitting depends on the range of k over which significant scattering can be seen above the noise, and it is the aspect of the present work which is the major limitation on the accuracy of the shell radius, expecially in As_2O_3 and As_2S_3. The following estimates of the accuracy of shell radii are based on the data presented in this thesis on crystals, and an estimate of the phase difference between the theoretical fit and the experimental data:

Material	Shell	Accuracy
Arsenolite	1st	± 0.06 Å
	3rd	± 0.04
Orpiment	1st	± 0.03
As_2Se_3	1st	± 0.01

Here we are assuming that the published crystal structures are correct. Some of the discrepancies may well result from errors in the diffraction data. The information contained in the amplitude of the EXAFS is a composite of many effects as well as the structural information which is required. These factors are:-

1) The instrumental resolution, significant for fine structure close to the edge, particularly unresolved higher shell effects
2) Sample homogeneity, as discussed in Section 6.1
3) Wave curvature, which can be treated theoretically and is important particularly close to the edge for atoms of the size Se and Te
4) Shake up and shake off effects in the emitter which cause incoherence in the wavelength of a fraction of the emitted photoelectrons (Lee and Beni 1977). This is thought to reduce the theoretical amplitude by a factor of approximately 0.7 and remains constant for energies above 150 eV. These figures have been based on rare gases and has not been confirmed for atoms in a solid.
5) Inelastic loss, which is not a well established experimental parameter; however, if we assume that the theoretical model based on a constant imaginary self-energy of 4 eV is correct,

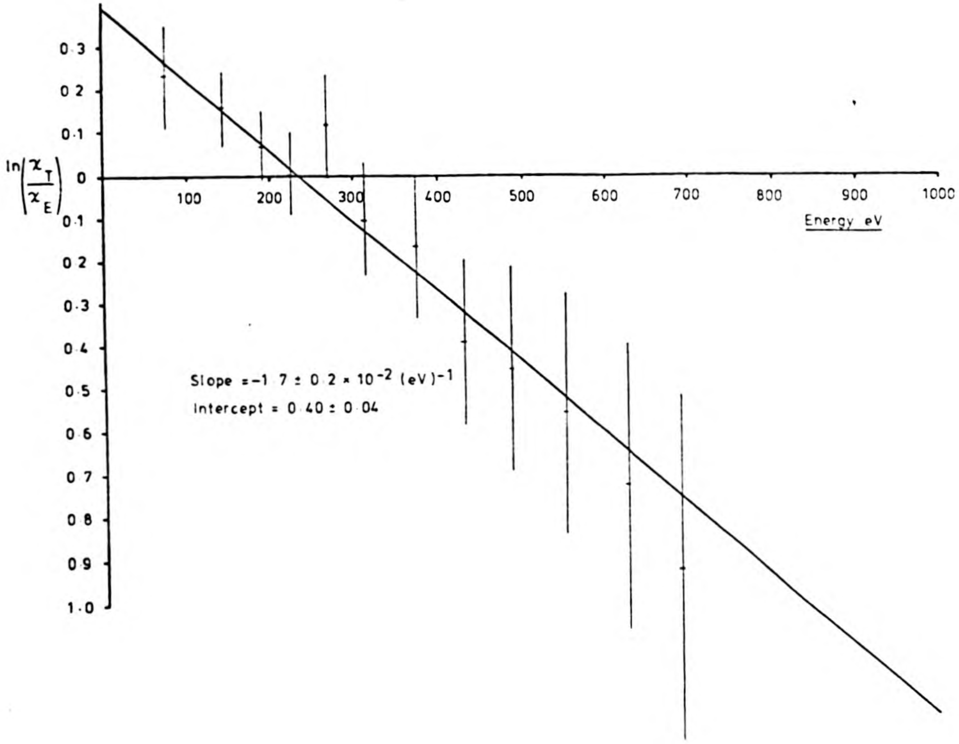

Fig.6.1. Plot of $\log_e$ of the ratio of the theoretical fine structure amplitude to the experimental amplitude against energy, for the arsenic edge in crystalline As_2Se_3.

and this is probably true for energies in excess of 100 eV, then at least for first shell scattering this parameter is not very energy-sensitive. For example, for the first shell of $As_2 Se_3$ from 200 eV to 1100 eV the amplitude variation is ~ 8%.

6) The accuracy of the phase shifts, these effects are confined to the low energy region as the Hartree-Fock and Slater exchange amplitudes agree at high energies. In view of the uncertainty of the magnitude of χ, in particular shake-up and shake-off effects, it is clear that the number of atoms in the coordination shells is a difficult parameter to assess. Possibly the only parameter that can be extracted is the Debye-Waller factor as this is exponentially dependent on energy, provided that a significant amount of scattering extends to high energies. From the materials studied here, the only data that can be tested adequately for the correctness of the absolute accuracy of the amplitude is the data on $As_2 Se_3$ crystal. The most significant factor in the list above, at energies in excess of 100 eV, is the shake-up and shake-off processes which have not been considered in the absolute calculations of the EXAFS processes in Chapter 5. As Lee and Beni (1977) have suggested that its effects are to multiply the theoretical function by a constant, also the Debye-Waller factor is exponentially dependent on energy, then a plot of $\ell n(\chi_T/\chi_E)$ against E should yield a straight line. Here, χ_T and χ_E are the theoretical and experimental EXAFS functions respectively, and E is the energy measured from the edge. This has been plotted in Figure (6.1) and it clearly shows that the theoretical amplitude is too large. The intercept at $E = 0$ is 0.40 ± 0.04 and this corresponds to an amplitude reduction of

67 ± 5% for the theoretical curve relative to experiment. Sample inhomogeneity can account for less than 5% of this value but clearly not the entire deficiency. Thus it appears that the shake-up and shake-off processes are responsible for about 30% of the photo-electrons losing coherence. This is also in agreement with Lee and Beni's estimate of about 30% based on the ionisation of rare gases. Obviously this has serious consequences for the other materials studied in this thesis. In particular, for materials which have only a limited range of scattering, such as $As_2 O_3$ and $As_2 S_3$, the energy dependence of the temperature term cannot be identified and consequently a reduction of the amplitude can easily be mistaken for an increased Debye-Waller smearing. Therefore, the values of the Debye-Waller factors found are probably an overestimate. The inclusion of this factor in a subsequent re-examination of the $As_2 Te_3$ data, for example, could well resolve the anomalies in the different Debye-Waller factors found by Gurman (unpublished) for As and Te bonding. A similar analysis of the $As_2 S_3$ glass spectrum also indicates that the theoretical curve over-estimates the magnitude of the EXAFS effect, although this data is not conclusive owing to the errors over the range of significate data which is much smaller than for $As_2 Se_3$. At present, there are no quantitative data on the contribution of shake-up and shake-off in solids and this is an obvious topic for study in the future. At least it suggests that our interpretation of the absolute values of the Debye-Waller factors are tentative.

Returning to graph (6.1) we can see that the slope is $-1.7(\pm 0.3) \times 10^{-3}$ $(\text{eV})^{-1}$ which corresponds to a reduction of the Debye-Waller factor used by $\Delta(\sigma^2) = -3.2(\pm 0.3) \times 10^{-3}$ Å^2; the actual Debye-Waller factor used in the theoretical calculation is 2.5×10^{-3} Å^2. Thus, at first sight, it appears that the temperature term has a positive exponent. This dilemma can be reconciled only if we re-examine the static displacement of atoms taken from the crystal structure of Vaipolin (1966). The interatomic distances are given in Chapter 5. The static displacement of atoms has a mean square variation of 2.5×10^{-3} Å^2 with an R factor of this determination of 13%. A study of the same material by Renninger and Averbach (1973) with the same R factor gives a static mean square variation of 6.4×10^{-3} Å^2. Thus it is not inconceivable that both of these crystal structures predict too much distortion to the arsenic chalcogen bond length. As a crude estimate, the total thermal and static displacement should contribute a total σ^2 of 1.8×10^{-3} Å^2.

It is instructive at this point to attempt a calculation of the factor σ^2 for the first shell of the arsenic-chalcogen distances. A realistic estimate is possible in this case owing to the availability of infra-red and Raman data. A remarkable feature of this data for the layer-lattice materials, As_2O_3 (Claudetite), As_2S_3 (orpiment) and As_2Se_3, is that all of the infra-red and Raman bands can be reproduced from material to material by scaling by a constant. Not only is this true for crystalline material but also for glass of the same composition. The scaling factors for both crystal and glass being approximately the same. This fact can be explained using a molecular model in which we assume that various structural units, although directly bonded, are vibrationally decoupled. The molecular units identified for chalcogenide glasses are the pyramidal units, consisting of the arsenic with three attached chalcogen atoms (AX_3, X denotes an O, S, Se or Te atom) and a unit which behaves in an analagous fashion to a water molecule, the X-As-X unit. Flynn, Solin and Papatheodorou (1977) have given an approximate expression for the A_1 symmetrical stretching mode frequency ν_1 based on Herzberg's (1945) analysis of a pyramidal molecule. Using a typical ratio of bond bending to bond stretching force-constants of 1 : 10, and bearing in mind that the X-As-X angle in the pyramidal molecule is ~ 100°, then to a good approximation

$$4\pi^2 \nu_1^2 = \frac{K_1}{\mu_1} \qquad (6.8)$$

where K_1 is the As-X stretching force constant and μ_1 is a reduced mass defined by

$$\frac{1}{\mu_1} = \frac{1}{M_X} + \frac{3\cos^2\beta}{M_{As}} \qquad (6.9)$$

where

$$\beta = \frac{2}{\sqrt{3}} \sin(\tfrac{1}{2}\alpha) \qquad (6.10)$$

α is the X-As-X bond angle in the pyramidal unit. Thus, if we can identify the A_1 mode, then we can obtain the force-constant K_1. The A_1 mode is strongly Raman active in the crystal and has been determined for many of the materials studied here, with the exception of As_2Te_3. For the latter material, infra-red data exists on glassy $As_{45}Te_{55}$, which has established that the infra-red bands of this material scale to those in As_2Se_3, and so we may use this scaling factor in conjuction with the known frequency of ν_1 of As_2Se_3 to obtain a value for the As-Te force constant. We note that the assumption made by

Taylor, Bishop and Mitchell (1975), that $As_2 Te_3$ consisted of interconnected As Te_3 pyramidal units, disagrees with the conclusions drawn from our EXAFS measurements. We can expect that the infra-red bands are still dominated by modes associated with As-Te bonds.

Material	$\nu_1 (cm^{-1})$	Type of Data	Source
Arsenolite	560	Crystal Raman	FSP
Claudetite	464	Crystal Raman	FSP
Orpiment	382	Crystal Raman	FSP and ZSW
$As_2 Se_3$	273	Crystal Raman	ZSW
$As_2 Te_3$	218	Scale from $As_2 Te_3$ Glass	TBM

FSP	Flynn, Solin and Papatheodorou	(1976)
ZSW	Zallen, Slade and Ward	(1971)
TBM	Taylor, Bishop and Mitchell	(1975)

Evaluating the population of these modes using the Bose-Einstien distribution function indicates that they are in the ground state at 77° K. Now it is of interest to calculate the mean-square relative displacement of a chalcogen atom with respect to the arsenic atom, and this can be done if we assume that the As-X bond stretching vibrations are independent and the chalcogen atom performs simple harmonic motion with the force constant obtained from the frequencies of Table (6.2) and the reduced masses of the arsenic and chalcogen atom. This approach assumes that the relative displacements are dominated by the bond stretching optical mode and ignores any acoustic mode contribution and also mixed stretching-bending modes which occur at a slightly lower frequency. This calculation should, however, provide a lower limit of the thermal vibrational contribution to the dynamical smearing of the fine-structure. The mean-square displacement of two atoms in their ground state can be calculated from the ground state wavefunction for simple harmonic motion (Schiff 1955) to be

$$\sigma^2 = \frac{h}{2\sqrt{\mu K_1}} \tag{6.11}$$

We can see from Equations (6.9) and (6.10) that if the X-As-X bond angle is 90°, then the reduced mass becomes simply the reduced mass of a pair of atoms. In fact, from crystal structure data, the bond angles are ~ 98°. We will ignore this difference from a right angle. This is not expected to make more than a 20% difference to the value of σ^2 and is thus within the spirit of this calculation. The values of σ^2 for the chalcogenide materials are given below

	σ^2 Å^2
As-O	2.6×10^{-3}
As-S	2.0×10^{-3}
As-Se	1.6×10^{-3}
As-Te	1.7×10^{-3}

The decrease of σ^2 as we move down the table results from the dominance of the reduced mass increase over the decrease of force constant K.

For $As_2\,Se_3$, we can see that the value calculated is comparable to the total (i.e. thermal and static) disorder, and thus we may conclude that the static variation of bond length is effectively zero. This is an attractive solution as it becomes easier to understand how the glass can process the same local structure as the crystal. If static disorder is present in the crystal, then this would be expected to be the result of weak interlayer interactions and/or steric effects within the twelve-membered ring system in the layers themselves. X-ray and neutron scattering studies (Leadbetter and Apling 1974), which are sensitive to cross-ring distances and the presence of layers, indicate that these possible constraints on the first shell distance would be relieved in the glass. Consequently, it therefore appears likely that the static and dynamic smearing should differ between crystal and glass, and this is contrary to the observed change. If, instead, we invoke the principle that the first neighbour distance is not affected at all by factors other than the arsenic-chalcogen covalent bond, then its preservation in the glass demands the same bond length, and consequently disorder effects are confined to small changes of bond-angle and the dihedral angle between molecular groups. These distortions require much less energy than bond stretching and thus explain the very high stability of $As_2 Se_3$ glass. Thus our conclusions concerning the effective Debye-Waller factor are plausible, and consequently any possible energy dependence of factors affecting the amplitude of the EXAFS signal is small. Therefore, it appears likely that energy-independent shake-up and shake-off processes are mainly responsible for a 30% loss of the EXAFS amplitude, and consequently this result supports the data on gases reported by Lee and Beni (1977). As a result, the absolute values of Debye-Waller factor found for the other materials are in doubt and clearly further work on a range of crystals of well-defined structure is highly desirable to quantify this effect.

Although the absolute magnitude of the amplitude of fine structure may be open to question, its energy behaviour is quite well defined. This is extremely useful and opens up the possibility of identification of the principal nearest neighbour atoms at a glance. This was used for the multicomponent glass $As_2 S_3 Se_3$ to show that the arsenic atoms were principally coordinated by sulphur and also that selenium avoided bonding to sulphur. Thus in the field of multicomponent glasses this information is expected to become very important. Further, the principal evidence for a split bonding of arsenic in $As_2 Te_3$ comes from the unexpected behaviour of the amplitude of scattering and thus this information is of considerable use, even in binary systems.

To summarise the comments made concerning the technique and its interpretation, we can say that comparative techniques are reliable in estimating bond length differences, number of coordinating atoms, and thermal and static smearing for first shell atoms, provided that a) a reasonable range of energy of EXAFS data can be observed; b) that the specimens can be made homogeneous; c) that we are certain of the type of atom in the shell; d) that a suitable, well-defined crystal standard structure is available. Absolute calculations are of value when the approximate structure of the first shell cannot be assumed and these calculations offer great promise, certainly for scattering atoms of the size of selenium or less where the phase shifts appear reasonably reliable.

6.3 Conclusions Concerning the Structure of Glass

This section concerns the conclusions drawn about the structure of the materials studied. It includes a comparison, where possible, with other experimental data on the same material. This section is subdivided according to material.

$As_2 O_3$

Our conclusions concerning the structure of $As_2 O_3$ glass are that the mean As-O bond length is the same (± 0.06 Å) as that found in arsenolite and also the As-As distance appears to be preserved to ± 0.03 Å from the cubic form. However, large concentrations of arsenolite molecules in the glass are not consistent with the data. This glass is anomalous with respect to the other chalcogenide glasses, in that neighbours from shells other than the first are observed. These results are in general agreement with those from X-ray scattering (Plieth, Reuber, Zschoerper 1969) where it is found that the X-ray pattern is reproduced by assuming that all atoms occupy the Claudetite lattice positions up to a radius of 3.4 Å, but beyond this distance only 1/6th of the atoms are in crystal positions, the rest being randomly distributed. In fact, the radial structure of Claudetite I has the same mean bond distances as those in arsenolite up to this radius. The preservation of the oxygen bond angle is confirmed by the Raman studies of Papatheodorou and Solin (1976) who also find that the mean oxygen bond angle is preserved in the liquid state. These authors also conclude that arsenolite molecules are not present in the glass despite the similarity of the Raman frequencies of glassy $As_2 O_3$ and arsenolite. This is in accord with the present study, but contrary to earlier Raman work (Cheremisinov 1968). Papatheodoron and Solin (1976) also conclude that the arsenic bond angle is larger in the glass (~114°) than all of the other phases (~ 100°). This is unusual in that NQR studies of $As_2 S_3$ and $As_2 Se_3$ (Rubenstein and Taylor 1974) have shown very small variations of this bond angle, i.e. $< 2°$, and also its magnitude is the same as in the glass. Clearly an As^{75} NQR study of the phases of $As_2 O_3$ would be of great interest.

It is difficult to reconcile the existence of higher shell scattering in arsenic oxide glass with the Raman data, however, as it is found that the "water molecule unit" As - O - As has an oxygen bond-bending force constant similar to that found in $As_2 S_3$ (Papatheodorou and Solin 1975). Consequently, we should expect that this would be liable to strain, and thus dampen scattering from the nearest neighbour arsenic shell. Support for a weak oxygen bond-bending force constant is given by the case of silica. This material exhibits large variations of the silicon oxygen bond angle which may have a range of over 30°. However, if we note the EXAFS data of Nelson, Siegel and Wagner (1962) on $Ge O_2$, then this also exhibits structure in the glass which does not belong to the first neighbour scattering at energies up to 300 eV from the edge. The distribution of oxygen bond angles, however, may be sensitive to annealing conditions. It was noted in Chapter 5, that $As_2 O_3$ glass is formed only by slowly cooling the melt, this may well anneal out the oxygen bond angle distribution.

Owing to the high range of momentum transfer, we cannot comment on the existence of any large structural units than those inside 3.3 Å. Unfortunately, it is the structure beyond this radius in which there is an interest and consequently this is a major shortcoming of the technique. It is possible, however, that an experiment with better signal to noise ratio and resolution could be analysed, and distributions of first and second shell atoms could be deduced, and thus, knowing the force constants from Raman studies, implication of higher shell disorder may be inferred.

$As_2 S_3$

From the results of Chapter 5 we established that the difference in the mean bond length to the first shell in crystalline and glassy $As_2 S_3$ is less than 0.02 Å, and the absolute magnitude of the shell radius in the glass was 2.25 Å ± 0.03 Å. From the discussions in Section (6.2), we note that the Debye-Waller factor indicates that the glassy disorder is comparable with, or less than the thermal disorder at nitrogen temperatures. Disorder is present between the molecular $As_2 S_3$ units; however, the results can be accounted for by assuming a disorder created by a spread of sulphur bond angles of half width > 5°.

The first shell radius can be compared with that determined from conventional scattering experiments. We must ignore data on $As_2 S_3$ films which have been shown by De Neufville, Moss and Ovshinsky (1973) and Apling, Leadbetter and Wright (1977) to have a different structure to the bulk glass. Leadbetter and Apling (1974) find a first neighbour peak in the glass at 2.28 Å using X-ray diffraction and 2.26 Å from neutron data. Our results may possibly differ from similar data taken at room temperature by up to 0.01 Å, assuming a thermal expansion coefficient (2×10^{-5} $Å^{-1}$). Thus our results are consistent with those of Leadbetter and Apling, however, they tend to support the bond length found from neutron data. These authors also discuss the variation of first shell distances and find a best fit with a Gaussian distribution with a mean square relative displacement described by $\sigma^2 = 10 \times 10^{-3}$ $Å^2$. Our results at nitrogen temperatures suggest that most of this distribution is merely thermal.

This highlights a fact which is almost universally ignored in diffraction studies of glass, and that is the contribution to widths of diffraction peaks made by thermal fluctuations. This suggests that many more diffraction experiments should be carried out at nitrogen temperatures if true glassy disorder is to be measured.

The small value of glassy disorder found in this study is supported by NQR data of Rubinstein and Taylor (1974) who found that the arsenic bond angle deviation was $< 2^\circ$ from that found in the crystalline state. Kobliska and Solin (1973) have found, however, that they cannot explain the width of the stretching Raman bands, if they assume a fixed arsenic valence angle, without assuming that there is a variation of radial force-constants of about ± 9%. This, in turn, suggests a static distortion of the As-S bond length which is twice that found in crystalline orpiment. Our results suggest that this is not correct. There is clearly an inconsistency in the NQR and Raman arguments, in that it has been established that the relative magnitudes of the stretching, arsenic bending, and chalcogen bending force constants are in the ratio 1 : 1/10 : 1/100 (Lucovsky and Martin 1972, and Flynn, Solin and Papatheodorou 1976).

Naively, we might expect that the disorder would therefore favour the weakest of these. Thus it seems unlikely that the chalcogen bond angle should be maintained. This flexibility permits the retention of bond length and arsenic bond angle.

The author has no experience of the sensitivity of the molecular model to chalcogen bond angle, however it appears likely that the success of the molecular model owes much to the fact that the chalcogen bond angle is nearly 90° and so the high energy stretching modes are orthogonal. We can well imagine that deviations of the chalcogen bond angle produce coupling between pyramidal units which will result in a spread of the stretching frequencies. This is the same spread that Kobliska and Solin (1973) attribute to a variation of force constant.

We have observed the disappearance of higher shell structure in $As_2 S_3$ glass which results from loss of correlation in the next nearest neighbour arsenic distance as we move from the crystal to the glass. A similar observation is not possible for conventional scattering experiments because the second peak of a radial distribution function contains contributions from chalcogen-chalcogen correlations. Distortion of the layers is detected, instead, by the absence of the cross-ring scattering distance which appears at 4.22 Å. Thus, we can state that the disorder of the material is a property which manifested within 4 Å of an individual atom. A microcrystallite model in which the crystal correlations are maintained over a short distance is thus not appropriate. With disorder in this short range, it seems unlikely that two distinct arsenic sites persist in the glass. This is contrary to the assumption made by Rubinstein and Taylor (1974) who postulated two non-equivalent sites in the glass to explain their nuclear spin relaxation data.

$As_2 Se_3$

Unlike $As_2 S_3$, we could not observe any scattering from shells other than the first, and thus our conclusions are limited to this shell only. It was found that the mean bond length of the glass was the same as that in the crystal to within 0.01 Å, and its absolute value was 2.40 ± 0.01 Å. This value is in good agreement with the conventional scattering data of Renninger and Averbach (1973) of 2.41 Å and Leadbetter and Apling (1974) whose X-ray results gave 2.42 Å and neutron results 2.40 Å; again our result favours the neutron data.

We cannot compare our values of static disorder ($\sigma_s^2 < 1 \times 10^{-3}$ Å^2) with those of any other study as the effects of temperature have not been deconvoluted from the other radial structure data. The suggestion of Sayers, Lytle and Stern (1974) that one of the three bonds to As in glassy $As_2 Se_3$ was homopolar cannot be denied on the basis of the EXAFS data. However, the bond length of a homopolar bond would be expected to be slightly different from that of the heteropolar bond, and thus the similarity of the bond lengths between crystal and glass makes the existence of As-As bonds in any large concentration unlikely. More concrete evidence for heteropolar bonding in this material comes from infra-red and Raman studies of Lucovsky, Galeener, Geils and Keezer (1977).

The small distribution of bond lengths and the small variation of arsenic bond angle found by Rubinstein and Taylor (1974) from NQR data again suggests that the chalcogen bond angle is responsible for the disorder in this material in a similar fashion to the cases of $As_2 O_3$ and $As_2 S_3$.

It is clearly of interest in this material to extend the temperature measurements to liquid helium values in an attempt to resolve more structure.

$As_2 S_3 Se_3$

We found in this material that the bonding of arsenic to the chalcogens favoured sulphur; however, some selenium also bonds to arsenic. The ratio of sulphur to selenium bonding was approximately 2 : 1 and an examination of the selenium bonding showed that this atom avoided bonding to sulphur.

The split bonding of arsenic in this material has been confirmed by Nemanich and Lucovsky (private communication) on the basis of infra-red reflectivity data. Their results also support the ratio of 2 : 1 although the exact ratio is difficult to determine using their data. An investigation of bonding of selenium in this material awaits a Raman study.

These results are unexpected because crude thermodynamic models suggest that the As-S bond should dominate the bonding to arsenic. The existence of split bonding to arsenic suggest that there is little difference in the heats of formation of $As_2 S_3$ and $As_2 Se_3$. However, this is contrary to the data of Mills (1974) where $\Delta H_{298} = 40.0 \pm 5$ Kcal/mole for $As_2 S_3$ and $\Delta H = 24.5 \pm 5$ Kcal/mole for $As_2 Se_3$. The difference between these figures - 15.5 Kcal/mole - is much greater than the thermal energy available at the melting point of the glass 550°C, which is approximately 4 Kcal/mole. Thus further comment requires more accurate thermodynamic data.

$As_2 Te_3$

Although difficulties arose in the interpretation of the $As_2 Te_3$ spectra on the basis of the hitherto reliable Slater exchange phase shifts, there is some evidence that the bonding in glassy $As_2 Te_3$ contains homopolar components. The major evidence for this comes from the minimum in the envelope of the fine structure at 150 eV in the glass spectrum. Despite difficulties of interpretation, two points can be definitely made. Firstly, the structure of the glass cannot be accounted for by a microcrystallite model; secondly, the bond lengths of the first shell have shortened when passing from the crystal to the glass. The shortening of the bond length when moving into the glassy state is characteristic of the break-up of secondary, or mesomeric bonding. Krebs (1969) quotes other cases, for example arsenic, in which the structure of the normal metallic form can be described by saying that each arsenic atom is in a distorted octahedral site. When arsenic is made amorphous, the three weakest bonds break, and the result is that arsenic then has a pyramidal basic unit the same as that found in $As_2 O_3$, $As_2 S_3$ and $As_2 Se_3$. This is also the most likely mechanism in $As_2 Te_3$ where the octahedral sites are mesomeric, disorder then encourages a strengthening of the primary bonding and a resultant shortening of this bond length. A decrease in the bond length has been observed using conventional scattering techniques by Fitzpatrick and Maghrabi (1971) and Cornet and Rossier (1973) on bulk $As_2 Te_3$. With increasing covalency we can also expect an enhanced quadrupole splitting of the nuclear levels and this has been observed using Mössbauer spectroscopy by Seregin and Vasilev (1972).

It is quite probable that the chemical ordering of the first shell cannot be inferred from scattering data of the quality used by Fitzpatrick and Maghrabi (1971) and Cornet and Rossier (1973) because the maximum value of momentum transfer is insufficient to produce resolution of different bond lengths in the glass. A good example of this is given by Cornet (1977) who used neutron data extending to 9.5 $Å^{-1}$ and was unable to resolve As-Te and Te-Te distances supposed to be present in $As_{25}\ Te_{75}$. A similar situation exists in Ge Te glass where Betts, Bienenstock, Keating and De Neufille (1972) have found the task of discovering the local coordination of atoms in this material impossible from a single X-ray diffraction experiment. Infra-red data of Taylor, Bishop and Mitchell (1975) have been interpreted in terms of the glass structure consisting of $As_2\ Te_3$ pyramids, although their data was taken with non-stoichiometric material ($As_{45}\ Te_{55}$) and the presence of As-As bonds was not detected. The lines observed were similar to those detected by Nemanich and Lucovsky (private communication) on $As_2\ S_3\ Se_3$ and merely signify the existence of As-Te bonds rather than pyramidal units.

Trends in macroscopic physical properties have been observed as a function of composition by Cornet and Rossier (1973) and from their data they conclude that $As_2\ Te_3$ glass is chemically ordered. However, a closer inspection of their data shows that different conclusions can be drawn. For example, the density of amorphous As-Te alloys shows no discontinuities at $As_{40}\ Te_{60}$, in contrast to the As-Se system (Hulls 1970). The glass transition temperature also exhibits no anomalies, again in sharp contrast to the As-S and As-Se systems (Myers and Felty 1967) and Tsuchihashi and Kawamoto 1971). The Vickers microhardness shows a slight inflection at $As_{40}\ Te_{60}$ but again this is a much less obvious anomaly than that found by Tsuchihashi and Kawamoto (1971) for As-S. Electrically the As-S and As-Se systems exhibit anomalies at or around the stoichiometric composition (Hulls 1970, Hurst and Davis 1974) but Ast (1973) reports no such change in the As-Te glasses. Further,Oberafo (1977) has studied the liquid state, with, again, no evidence of anomalous behaviour. Clearly if one looks at differences in properties between crystals and glasses then we can expect anomalous behaviour, but this should not be confused with the properties of the glass itself, which do not present strong evidence for exclusive heteropolar bonding.

It is tempting to extrapolate the properties of $As_2\ Te_3$ from the other members of the arsenic chalcogenide system where we know that heteropolar bonding dominates. This is probably the reason for the wide acceptance of a model of $As_2\ Te_3$ glass which only includes heteropolar bonding. Why should $As_2\ Te_3$ be different from the other members of the series? This question is probably most related to the progressive weakening of covalent bonds as the atoms doing the bonding become heavier. A rough idea of the stability of a compound to dissociation into its elemental constituents can be gained from the heat of formation of the compound. Values of the heat of formation of the crystals from the elements at 298° C have been given by Mills (1974) and these are $\Delta H(As_2\ S_3) = 40$ Kcal/mole, $\Delta H(As_2\ Se_3) = 27$ Kcal/mole and $\Delta H(As_2\ Te_3) = 9$ Kcal/mole. The thermal energy present in the solid at a melting temperature of 800° C, (RT), is approximately 6 Kcal/mole. This is comparable to the heat of formation for the case of $As_2\ Te_3$ whilst being much smaller for the other arsenic chalcogenides.

Thus, there appears to be strong evidence for the existence of As-As bonds in $As_2 Te_3$, and this is probably also true for the Ge-Te system also. Confirmation of the proposed structure could be obtained using high momentum transfer neutron data. However, we may soon gain greater confidence in the calculated EXAFS spectrum by fitting other systems which also contain heavy atoms.

General Remarks on the Structure of Glasses

The main feature of all of the glasses studied here is that they all have a well defined first shell which is not heavily disordered. Indeed, we can say that in the case of $As_2 Se_3$ the glassy disorder is very much less than the thermal contributions. Further, the glassy disorder starts immediately beyond the first coordination sphere and is consistent with a variation of chalcogen bond angle. Thus, from the EXAFS data, together with NQR infra-red and Raman data a picture emerges in which the glassy disorder in the first two shells of chalcogenide glasses is distributed principally in the chalcogen bond angle. This is true even if we include oxygen as a chalcogen atom. This behaviour is reminiscent of the structure of $Si O_2$ found by Mozzi and Warren (1969) who found a distribution of oxygen bond angles which varied continuously from 120° to 180° with a peak at 144°. Again, the principal molecular unit of a silicon atom surrounded by four oxygen atoms is well preserved. In this sense, the structures of chalcogenide and oxide glasses are very similar. Of course, this is only the beginning of a structural description, questions of the existence of larger structural groupings remain unanswered and it appears that EXAFS will not provide the solution to this problem. However, it can provide well defined structural constraints on the local glass structure and will clearly be of great interest in multicomponent systems.

REFERENCES

Adler D., Scientific American, May 1977, p.36.

Agarwal B.K. and Verma L.P., Proc.Phys.Soc.Lond.Solid St. (1968) 1, pp. 208-9.

Almin K.E. and Westgren A., Arkiv.Kemi.Min.Geol. (1942) 15, p.1.

Anikin R.V., Borovskii I.B. and Kozlenkov A.I., Bull.Acad.Sci. USSR Phys.Ser. (1967) 31, pp.1032-38.

Apling A.J., Leadbetter A.J. and Wright A.C., J.Non Cryst.Solids (1977) 23, pp.369-84.

Ashley C.A. and Doniach S., Phys.Rev.B (1975) 11, p.1279.

Ast D.G., J.Van.Sci.Technol. (1973) 10, pp.748-52.

Azaroff L.V., Rev.Mod.Phys. (1963) 35, p.1012.

Azaroff L.V. (ed.) X-ray Spectroscopy (1974), McGraw-Hill Inc.

Beattie I.R., Livingston K.M.S., Ozin G.A. and Reynolds D.J., J.Chem.Soc.A (1970) p.370

Becker K.A., Plieth K and Stranski I.N., Prog.Inorg.Chem. (1962) 4, p.1.

Beeman W.W. and Friedman H., Phys.Rev.B (1939) 56, p.392.

Bell R.J. and Dean P., Amorphous Materials (1970) p.443 (ed.) Douglas R.W. and Ellis B., Wiley - Interscience.

Beni G. and Platzman P.M., Phys.Rev.B (1976) 14, p.1514.

Bertin E.P., Principles and Practice of X-ray Spectrometric Analysis (1970) Plenum Press.

Betts F., Bienenstock A., Keating D.T. and De Neufville J.P., J.Non Cryst.Solids (1972) 7, p.417.

Bishop S.G., Amorphous and Liquid Semi-Conductors (1974) 2, p.977, (ed.) Stuke J. and Brenig W., Taylor and Francis.

Bondot P., Acta Cryst. (1974) A30, p.470.

Bötticher Von H., Plieth K., Reuber-Kürbs E. and Stranski I.N., Z.Anorg.Allgem,Chem. (1951) 266, p.302.

Boult C. and Ghosh B.N., Brit.J.App.Phys. (1965) 6, pp.1762-3.

Bragg W.L., James R.W. and Bosanquet C.H., Phil.Mag. (1921) 41, p.309.

Bragg W.L. and West J., Phil.Mag. (1930) 10, p.823.

Burbank R.D., Rev.Sci.Instrum. (1961) 32, p.368.

Carron G.T., Acta Crys (1963) 16, p.338.

Cauchois Y. and Mott N.F., Phil.Mag. (1949) 40, pp.1260-9.

Cheremisinov V.P., *Optical Methods of Investigating Solid Bodies* (1968) Consultants Bureau, New York.

Citrin P., Eisenberger P. and Kincaid B., Phys.Rev.Lett. (1976) 36, p.1346.

Clementi E. and Roetti C., Atomic Data and Nuclear Tables (1974) 14, Nos. 3-4.

Codling K., Repts.Prog.Physics (1973) 36, p.541.

Compton A.H. and Alison S.K., X-rays in Theory and Experiment (1935) D. Van Nostrand Co. Inc.

Cornet J., Structure of Non-Cryst.Mat. (ed.) P.H. Gaskell, Proc.Symp. Cambridge (1976) published 1977, Taylor and Francis Ltd.

Cornet J. and Rossier D., J.Non-Cryst.Solids (1973) 12, p.61.

Coster D. and Veldkamp J., Z.Physik (1931) 70, p.306.

Coster D. and Klamer G., Physica (1934) 1, pp.889-894.

Cramer S.P., Eccles T.K., Kutzler F., Hodgson K.O. and Martenson L.E., J.Am.Chem.Soc. (1976) 98 p.127.

Cramer S.P., Eccles T.K., Kutzler F., Hodgson K.O. and Doniach S., J.Amer.Chem.Soc. (1976) 98, p.8059.

Creveceour C. and De Wit H.J., J.Cryst.Growth (1972) 12, pp.334-6.

Dehmer J.L., J.Chem.Phys. (1972) 56, p.4496.

De Neufville J.P., Moss S.C. and Ovshinsky S.R., J.Non-Cryst. Solids (1973/74) 13, pp.191-223.

Doran D.G. and Stephenson S.T., Phys.Rev. (1957) 105, pp.1156-7.

Douglas R.W. and Ellis B., Amorphous Materials (1970) Wiley-Interscience.

Doyle P.A. and Turner P.S., Acta Cryst.A (1968) 24, p.390.

Eisberg R.M., Fundamentals of Modern Physics (1961) p.544, J. Wiley and Sons.

Enderby J., Amorphous and Liquid Semiconductors (1974) (ed.) J. Tauc, p.361, Plenum Press.

Ferrier R.P., Prado J.M. and Anseau M.R., J.Non-Cryst.Solids (1972) 8-10, p. 798.

Fitzpatrick J.R. and Maghrabi C., Phys.Chem.Glasses (1971) 12, p.105.

Flaschen S.S., Pearson A.P. and Northover W.R., J.Amer.Ceram.Soc. (1959) 42, p.450.

Flashen S.S., Pearson A.P. and Northover W.R., J.Am.Ceram.Soc. (1960) 43, p.274.

Flynn E.J., Solin S.A. and Papatheodorou G.N., Phys.Rev.B (1976) 13, p.1752.

Freeman L.A. , Howie A., Mistry A.B. and Gaskell P.H., The Structure of Non-Crystalline Materials, (ed.) Gaskell P.H., p.245, Proc.Symp. at University of Cambridge (1976), published 1977, Taylor and Francis.

Friedrich H., Sonntag B., Rabe P. and Schwarz W.H.E., to be published, see Koch E.E., Kunz C. and Sonntag B., Physics Reports (1977) 29C, p.155.

Gaskell P.H. (ed.) The Structure of Non-Crystalline Materials (1977) Taylor and Francis.

Glazov V.M., Chizhevskaya S.N. and Glagoleva N.N., Liquid Semi conductors (1969) p.273, Plenum Press, New York.

Greenwood D.A., Electronic and Structural Properties of Amorphous Semiconductors (1973) (ed.) Le Comber P.G. and Mort J., p.127, Academic Press.

Gurman S.J. and Pendry J.B., Solid St.Commun. (1976) 20, p.287.

Hannawalt J.D., Phys.Rev. (1931) 37, p.715.

Hartree D.R., Kronig R. De L. and Petersen H., Physica (1934) 1, pp.895-924.

Hayasi T., Sci.Rept.Tohoku Univ. First Sev. (1949) 33, p.123.

Hayes T.M. and Hunter S.H., The Structure of Non-Crystalline Materials, (ed.) Gaskell P.H., Proc.Symp. Cambridge (1976), published 1977, Taylor and Francis.

Hedin L., X-ray Spectroscopy (ed.) L.V. Azaroff (1974), p.230, Mc-Graw Hill, Inc.

Herman F. and Skilman S., Atomic Structure Calculations (1963) Prentice Hall.

Herzberg G., Molecular Spectra and Molecular Structure II, Infra-red and Raman Spectra of Polyatomic Molecules (1945) p.175, Van Nostrand.

Holland B., to be published (1977).

Hulls K., Ph.D. Thesis (1970) University of Warwick.

Hurst C.H. and Davis E.A., J.Non-Cryst.Sol. (1974) 16, p.343.

Ing B.S. and Pendry J.B., J.Phys.C. (1975) 8, p.1087.

International Tables for X-ray Crystallography (1962) Vol. III, Kynoch Press, Birmingham.

Klems G.J., Das B.S. and Azaroff L.V., Development in Applied Spectroscopy (1963) Vol. 2, pp.275-84.

Klug H.P. and Alexander L.E., X-ray Diffraction Procedures (1974), 2nd Ed., p.290.

Kobliska R.J. and Solin S.A., Phys.Rev.B (1973) 8 (2), p.756.

Kossel W., Z.Physik (1920) 1, p.119.

Kostarev A.I., Sh.Eksperim i Theov.Fiz. (1941) 11, pp.60-73.

Krebs H., J.Non-Cryst.Solids (1969) 0, pp.435-37.

Krogstad R.S., Ph.D Thesis, Washington State College (1955).

Kronig R. de L., Z.Physik (1931) 70, p.317.

Kronig R. de L., Z.Physik (1932) 75, pp.191-468.

Le Comber P.G. and Mort J., Electronic and Structural Properties of Amorphous Semiconductors (1973), Academic Press.

Leadbetter A.J. and Apling A.J., J.Non-Cryst.Solids (1974) 15, pp. 250-68.

Lee P.A., Phys.Rev.B (1976) 13, p.5261.

Lee P.A. and Pendry J.B., Phys.Rev.B (1975) 11, p.2795.

Lee P.A. and Beni G., Phys.Rev.B (1977) 15, p.2862.

Lindau I. and Spicer W.E., J.Electron Spectroscopy and Related Phenom. (1974) 3, p.409.

Loucks T.L., Agumented Plane Wave Method (1967) Benjamin Inc.

Lucovsky G.,The Physics of Selenium and Tellurium, (ed.) W.C. Cooper (1967) p.255, Pergamon Press.

Lucovsky G., Amorphous and Liquid Semiconductors 2 (1974) p.1099, (ed.) Stuke J. and Brenig W., Proc.Int.Conf. September 1973, published 1974, Taylor and Francis, and references cited therein.

Lucovsky G. and Martin R.M., J.Non-Cryst.Solids (1972) 8-10, pp.185-90.

Lucovsky G. and White R.M., Phys.Rev.B (1973) 8, p.660.

Lucovsky G., Galeener F.L., Geils R.H. and Keezer R.C., Proc.Conf. Structure of Non-Cryst.Mat., University of Cambridge, September 1976, (ed.) Gaskell P.H., published 1977, Taylor and Francis.

Lytle F.W., Developments in Applied Spectroscopy (1963) 2, p.285.

Lytle F.W., Phy.Non-Cryst.Solids, Proc.Int.Conf. Delft, Netherlands, (1964) pp.12-29, published 1965.

Lytle F.W., Acta Cryst. (1967) 22, p.321.

Lytle F.W., Science (1969) 165, p.416.

Lytle F.W., Sayers D.E. and Moore E.B., Appl.Phys.Lett. (1974) 24, p.45.

Lytle F.W., Sayers D.E. and Stern E.A., Phys.Rev.B (1975) 11, p.4825.

Mills K.C., Thermodynamic Data for Inorganic Sulphides, Selenides and Tellurides (1974) Butterworth.

Morimoto N., Mineralog.J. (Japan) (1954) 1, p.160.

Mott D.L., Ph.D thesis (1963) New Mexico State University.

Mott N.F. and Davis E.A., Electronic Processes in Non-Crystalline Materials (1971) Clarendon Press, Oxford.

Mozzi R.L. and Warren B.E., J.Applied Cryst. (1969) 2, p.164.

Myers M.B. and Felty E.J., Materials Research Bulletin (1967) **2**, pp.535-46.

Nagasima N., Sci.Repts.Tokuku Univ. (1966), **49**, pp.57-64.

Nelson W.F., Siegel I. and Wagner R.W., Phys.Rev. (1962) **127**, p.2025.

Nelson W.F., Siegel I and Wagner R., Developments in Applied Spectroscopy (1963) **2**, p.308.

Nordstrand R.A. Van, Non-Cryst.Solids (1960) (ed.) Fréchette V.D., p.168, North-Holland.

Nozière P. and Dominicus C.T., Phys.Rev. (1969) **178**, p.1097.

Oberafo A.A., J.Phys.C (1977) **8**, pp.469-78.

Padalia B.D. and Krishnan V., Phys.Rev.B (1975) **12**, p.443.

Papatheodorou G.N. and Solin S.A., Solid State Commun. (1975) **16**, p.5.

Papatheodorou G.N. and Solin S.A., Phys.Rev.B (1976) **13**, p.1741.

Parratt L.G., Phys.Rev. (1939) **56**, p.295.

Parratt L.G., Hempstead C.F. and Jossem E.L., Phys.Rev. (1957) **105**, pp.1228-32.

Pendry J.B., *Low Energy Electron Diffraction* (1974) Academic Press.

Pertlik F., Monatshefte Chemie (1975) **106**, pp.755-62.

Phillips J.C., *Bonds and Bands in Semiconductors* (1973) p.49, Academic Press.

Plieth K, Reuber E and Zshoerper K., Glastech.Ber. (1969) **42**, p.359. see Chem.Abs. **71** - 117372.

Pye L.D., Stevens H.J. and La Course W.C., *Introduction to Glass Science* (1972) Plenum Press.

Quinn R.K., Mat.Res.Bull. (1974) **9**, p.803.

Rawson H., *Inorganic Glass-Forming Systems* (1967) Academic Press.

Rechtin M.D. and Averbach B.L., J.Non-Cryst.Solids (1973) **12**, pp.391-421.

Rechtin M.D., Renninger A.L. and Averbach B.L., J.Non-Cryst.Solids (1974) **15**, pp.74-82.

Reinsch C.H., Num.Maths. (1967) 10, pp.177-83.

Renninger A.L. and Averbach B.L., Acta Cryst. (1973) B29, p.1583.

Rubinstein M. and Taylor P.C., Phys.Rev.B (1974) 9, p.4258.

Sandstrom A., Handbuch der Physik (1957) (ed.) S. Flügge, 30, p.78.

Sayers D.E., Lytle F.W. and Stern E.A., Report D180-14134-1, Boeing Scientific Research Lab. (1971) Seattle, Washington.

Sayers D.E., Lytle F.W. and Stern E.A., J.Non-Cryst.Solids (1962) 8-10, pp.401-7.

Sayers D.E., Lytle F.W. and Stern E.A., Amorphous and Liquid Semiconductors, (ed.) Stuke J. and Brenig W. (1974), 1, p.403.

Schaich W., Phys.Rev.B (1973) 8, p.4028.

Schiff L.I., Quantum Mechanics, 3rd Ed. (1955) p.71, McGraw-Hill.

Seager and Quinn (1974) (unpublished).

Seregin P.P. and Vasil'ev L.N., Sov.Phys. Solid State (1972) 13, p.2258.

Shaw C.H., Phys.Rev. (1946) 70, pp.643-45.

Shiraiwa T., Ishimura T. and Sawada M., J.Phys.Soc.Japan (1958) 13, p.848.

Shmidt V.V., Bull.Acad.Sci.USSR Phys.Ser. (1961) 25, pp.988-93.

Shmidt V.V., Bull.Acad.Sci.USSR Phys.Ser. (1963) 27, pp.392-97.

Short M.A., Rev.Sci.Instrum. (1960) 31, p.618.

Slater J.C., Phys.Rev. (1937) 51, p.840.

Slater J.C., Quantum Theory of Atomic Structure (1960) McGraw-Hill.

Slater J.C., Quantum Theory of Matter (1968) 2nd Ed. p.339, McGraw-Hill.

Smith P.M., Leadbetter A.J. and Apling A.J., Phil.Mag. (1975) 31, p.57.

Stephenson S.T., Handbuch der Physik (1957) 30 Springer Verlay, p.337.

Stern E.A., Phys.Rev.B (1974) 10, p.3027.

Stern E.A., Scientific American, April 1976, p.96.

Stern E.A., Sayers D.E. and Lytle F.W., Phys.Rev.B (1975) 11, p.4836.

Stuke J., The Physics of Selenium and Tellurium (1969) p.3, (ed.) Copper W.C., Pergamon Press.

Tauc J. (ed.), Amorphous and Liquid Semiconductors (1974) p.159, Plenum Press, New York.

Taylor P.C., Bishop S.G., Mitchell D.L. and Treacy D., Amorphous and Liquid Semiconductors 2 (1974) p.1267, (ed.) Stuke J. and Brenig W., Taylor and Francis.

Taylor P.C., Bishop S.G. and Mitchell D.L., Sol.St.Commun. (1975) 16, p.167.

Thomsen J.S., X-ray Spectroscopy (1974) (ed.) L.V. Azaroff, p.26, McGraw-Hill Book Co.

Tsuchihashi S. and Kawamoto Y., J.Non-Cryst.Solids (1971) 5, pp.286-305.

Vaipolin A., Sov.Phys.Cryst. (1966) 10, p.509.

Victoreen J.A., International Tables X-ray Cryst. (1962) Vol. III, p.161, Kynoch Press, Birmingham.

Vierling J., Gilfrich J.V. and Birks L.S., Appl.Spect. (1969) 23, p.342.

Warren B.E., X-ray Diffraction (1969) pp.328-9, Addison-Wesley Publ. Co.

White E.W. and McKinstry H.A., Adv.X-ray Anal. (1966) 9, pp.376-92.

Wilson A.J.C., Elements of X-ray Crystallography (1970) p.30, Addison-Wesley Pub. Co.

Wong J. and Angell C.A., Glass Structure by Spectroscopy (1976) p.669, Marcel Dekker Inc.

Wright A.C., Advances in Structure Research by Diffraction Methods (1973) 5,

Wright A.C. and Leadbetter A.J., Phys.Chem.Glass (1976) 17, p.122.

Wyckoff R.W.G., Cryst.Struc. (1964) 2, Interscience, p.26.

Zallen R., Slade M.L. and Ward A.T., Phys.Rev.B (1971) 3, p.4257.